Fractional quantum phenomena of 2DHGs within strained germanium quantum well heterostructures

By

Oliver Newell

Thesis submitted to the University of Warwick in partial fulfilment of the requirements for admission to the degree of Doctor of Philosophy in Physics

September 2018

Declaration

This thesis is submitted to the University of Warwick in support of my application for the degree of Doctor of Philosophy. All experimental data presented was carried out by the author, or (where stated) by specialists under the author's direction.

Abstract

Strained Ge modulation doped quantum well (MODQW) heterostructures facilitate a high mobility channel layer. Spatial separation of mobile carriers from the ionised dopants that supply them is key to increasing mobilities many orders of magnitude above bulk values.

Materials characterisation techniques are employed to asses and improve the buffer layers within the MODQW heterostructures. The efficacy of dislocation filter layers (DFLs) is investigated, along with annealing trials and suspended structures. A 4% enhancement in SiGe relaxation is reported utilising a Ge DFL, while optimum SiGe relaxation is obtained through balancing the opposing thermal and lattice mismatch within the Ge_{buff} layer.

Reverse linearly graded buffers demonstrate a grading rate of 350% μm^{-1}, while achieving a 4 nm RMS roughness. This represents an order of magnitude improvement on the quoted limits of forward linear grading rates. Suspended microwires are presented, providing isolation of channel layers from buffer layers. Strain mapping, using Micro-XRD at the Diamond Light Source, is employed to record strain development during microwire fabrication, resulting in a 0.9% increase in out of plane tensile strain upon suspension. The 150×15 µm microwires represent the first demonstration of suspending a Ge QW heterostructure.

Low temperature (300 mK), high magnetic field (37.5 T) Hall and resistivity measurements return the effective mass and mobility of composite fermions (CFs) within a 2DHG, along with well-developed FQHE oscillations. CF mobility is shown to contain greater thermal sensitivity compared to its bare electron counterpart. Fractional filling $\nu = 4/11$ is of great interest for its unknown origins and non-Abelian statistics, a potential observation is presented using a differentiated Hall signal. Inverted doping geometry returns the highest Ge MODQW room temperature mobility of 4,900 $cm^2V^{-1}s^{-1}$, assisted by a new contact process comprising Ar milling and Al/Ti/Au deposition, ideal for inverted structures.

Publications and conference presentations

1. M. Failla, J. Keller, G. Scalari, C. Maissen, J. Faist, C. Reichl, W. Wegscheider, O. J. Newell, D. R. Leadley, M. Myronov, J. Lloyd-Hughes, Terahertz quantum Hall effect for spin-split heavy-hole gases in strained Ge quantum wells, New J. Phys. **18**, 113036, (2016)

2. G. Colston, S. D. Rhead, V. A. Shah, O. J. Newell, I. P. Dolbnya, D. R. Leadley, M. Myronov, Mapping the strain and tilt of a suspended 3C-SiC membrane through micro X-ray diffraction, Materials and Design, **103**, 244-248, (2016)

3. F. Herling, C. Morrison, C. S. Knox, S. Zhang, O. J. Newell, M. Myronov, E. H. Linfield, and C. H. Marrows, Spin-orbit interaction in InAs/GaSb heterostructures quantified by weak antilocalization, Phys. Rev. B, **95**, 155307, (2017)

4. G. Colston, S. D. Rhead, V. A. Shah, O. J. Newell, I. P. Dolbnya, D. R. Leadley and M. Myronov, Structural thermal stability of suspended 3C-SiC membranes at very high temperatures, ICSCRM 2015, 16th Intl. Conf. Silicon Carbide and Related Materials, Giardini Naxos, Italy, Oct. 4-9, 2015 Materials Science Forum, 858, 274-277, (2016)

5. C. S. Knox, C. Morrison, F. Herling, D. A. Ritchie, O. J. Newell, M. Myronov, E. H. Linfield and C. H. Marrows, Partial hybridisation of electron-hole states in an InAs/GaSb double quantum well heterostructure, Semiconductor Science and Technology, **32**, 10, (2017)

6. O. J. Newell, C. Morrison, C. Rava, S. Wiedmann, U. Zeitler, M. Myronov, Fractional Quantum Hall Effect in high mobility compressive strained Ge Quantum Wells, UK Semiconductors Consortium Summer Meeting, Sheffield Hallam University, July 6th-7th (2016)

7. O. J. Newell, C. Morrison, C. Rava, S. Wiedmann, U. Zeitler, M. Myronov, Composite fermions in strained epitaxial germanium, ICSI 10, University of Warwick 14th-19th May (2017)

8. O. J. Newell, D. Leadley and M. Myronov, Growth of germanium dioxide exhibiting a very low density of interface traps on a strained germanium quantum well, ICSI 10, University of Warwick 14th-19th May (2017)

9. O. J. Newell, G. Colston, S. D. Rhead, V. A. Shah, I. P. Dolbnya, D. R. Leadley, M. Myronov, Strain alteration in a germanium quantum well heterostructure caused by its suspension. Under review.

CONTENTS

Chapter 1. Background 13
1.1. Introduction 13
1.2. Buffer layer theory and terminology 14
1.2.1. Critical thickness for crystaline semiconductors 14
1.2.2. Defect formation and propagation 15
1.2.3. Defect interactions within cubic semiconductor systems 16
1.2.4. Impact of strain on the surface profile of germanium 17
1.2.5. Drude Model 18
1.2.6. Effective mass within strained semiconductors 18
1.2.7. Modulation doping method for introducing charge carriers ... 20
1.3. Formation of a two-dimensional hole gas (2DHG) 21
1.4. Integer quantum Hall effect theory and basic formulae 23
1.4.1. Classical Hall effect 23
1.4.2. Quantum Hall effect theory and fundamental formulae 25
1.4.3. Shubnikov-de Haas oscillations 26
1.4.4. Broadening of plateaus within Hall resistance data 31
1.5. Fractional quantum Hall effect quasi classical interpretation 32
1.5.1. Composite fermion model for charge carriers of the FQHE ... 32
1.5.2. Fermionic and bosonic behaviour of composite fermions 34
1.5.3. Filling factor 1/2 35
1.5.4. Rotated field measurements of FQHE phenomena 35
1.5.5. Finite thickness corrections to the FQHE in 2DHGs 37
1.6. Electron hole symmetry displayed by states within the FQHE 37
Chapter 2. Material characterisation techniques 38
2.1. Transmission electron microscopy 38
2.1.1. Alligning the TEM in diffraction mode 39
2.1.2. Origin of kikuchi lines in TEM spectra 40
2.2. X-ray diffraction (XRD) equipment and theory 41
2.2.1. Reciprocal space 44
2.2.2. Reciprocal space mapping 45

2.2.3. Interpreting reciprocal space map plots 46
2.2.4. Calculating composition and strain using XRD 48
2.3. Atomic force microscopy 49
2.4. Post growth device fabrication 50
Chapter 3. Optimisation of buffer layers 52
3.1. Annealing study on thin SiGe/Ge/Si buffer layers 53
3.1.1. Annealing data plots for thin SiGe/Ge/Si buffer layers 56
3.2. Dislocation filter layer characterisation results 72
3.3. Compressively strained germanium DFL 74
3.4. Tensile strained SiGe DFL 84
3.5. Thin graded SiGe layers for comparison with DFLs 92
3.6. Conclusion 101
Chapter 4. Suspended structures materials characterisation results 104
4.1. Bulk material analysed prior to micro wire fabrication 106
4.2. Fabrication of suspended quantum well microwires 108
4.3. Strain mapping of suspended quantum well microwires 110
4.4. Conclusion 114
Chapter 5. FQHE transport results 116
5.1. FQHE measurements varying the angle of applied magnetic field 123
5.2. Surface Hall bar aligned at 45 degrees to the <110> 133
5.3. Effective mass of composite fermions within strained germanium 137
5.4. Carrier generation through sample surface illumination 149
5.5. Searching for the exotic state $\nu = 4/11$ 156
5.6. Conclusion 161
Chapter 6. Room temperature mobility transport results 164
6.1. Contact processing for inverted doping semiconductor heterostructures, demonstrated to produce high mobility RT results 165
6.2. High RT mobility transport results 170
6.3. Conclusion 180
Chapter 7. Further work 181
Chapter 8. References 182

Abbreviations

µ-XRD	Micro X-ray diffraction
2DHG	Two-dimensional hole gas
AFM	Atomic force microscopy
BF	Bright field
CF	Composite fermion
CMOS	Complementary metal oxide semiconductor
DF	Dark field
DFL	Dislocation filter layer
DOS	Density of states
FLG	Forward linear grading
FQHE	Fractional quantum Hall effect
FWHM	Full width half maximum
Ge_{buff}	Ge buffer layer
HFML	High field magnet laboratory
HH	Heavy hole
HT	High temperature
I-PBCS	In-plane biaxial compressive strain
I-PBTS	In-plane biaxial tensile strain
IQHE	Integer quantum Hall effect
LH	Light hole
LLL	Lowest Landau level
LT	Low temperature
MB	Matthews Blakeslee
MD_s	Misfit dislocations
MFR	Modifier Frank-Reed
MODQW	Modulation doped quantum well
MOS	Metal oxide semiconductor
MOSFET	Metal oxide semiconductor field effect transistor
O-PBCS	Out of plane biaxial compressive strain
O-PBTS	Out of plane biaxial tensile strain
QDF	Quantum dot filter
QW	Quantum well
RLG	Reverse linear grading
RMS	Root mean squared
RP-CVD	Reduced pressure chemical vapour deposition
RSM	Reciprocal space map
Si_{buff}	Si buffer layer
TDD	Threading dislocation density
TEM	Transmission electron microscopy
VDM	Van der Merwe

XRD	X-ray diffraction
X-TEM	Cross sectional transmission electron microscopy

Symbols

v	Filling factor
m^*	Mobility
N_{2D}	2D density of states
E_{glide}	Activation energy for dislocation glide
B	Applied magnetic field
d_{hkl}	Atomic plane spacing
l_{av}	Average misfit dislocation length
μ_B	Bohr magnetron
e	Charge on an electron
μ_{CF}	Composite fermion mobility
h_c	Critical thickness
ω_c	Cyclotron frequency
K	Dielectric constant
B^*	Effective magnetic field
m^*_{eff}	Effective mobility
ϵ^m_{eff}	Effective strain
m_e	Electron mass
R_{gr}	Grading rate
R_g	Growth rate
P_{Hall}	Hall carrier density
R_H	Hall coefficient
μ_{Hall}	Hall mobility
R_{xy}	Hall resistance
m_h	Hole mass
ϕ_0	Magnetic flux quantum
l_B	Magnetic length
ρ_{xx}	Magneto resistivity
μ	Mobility
τ_t	Quantum scattering time
N_{TD}	Threading dislocation density
τ_t	Transport scattering time
R_k	Von Klitzing constant

Chapter 1. Background

1.1. Introduction

This thesis investigates improvements to buffer layer quality, electrical testing is then conducted on the highest mobility device. Improving device quality is motivated by furthering electrical performance, however, what motivates an interest in high mobility materials?

High mobility materials are predicted to be the future for reducing the size and increasing the speed of transistors. Moores law describes the barrier for reducing transistor size while maintaining capability. For devices that surpass the 15 nm generation it is forseen that high mobility materials will provide the answer.

The motivation for studying Ge is its high hole mobilities compared to Silicon. Strained germanium quantum wells (QWs) provide significant further enhancements in mobility. The three primary advantages of strained Ge systems over Si/SiO_2 systems are: lower effective mass, ability to tune the band-structure and finally the strain induced energy band splitting. The primary method for inducing strain in Ge layers is heteroepitaxial deposition of Ge onto a SiGe layer, with a mismatched lattice constant. The advantages of SiGe is that it forms a stable alloy over the entire composition range, permitting strain tuning within the Ge layer. The SiGe buffer also permits integration of the strained Ge onto an industry standard (001) silicon substrate, facilitating integration into current industrial fabrication processing.[1]

Fractional quantum Hall effect (FQHE) measurements drive the forefront of our understanding into a relatively unknown area. The FQHE, explained through composite fermion (CF) theory [2-7], gives an unusual opportunity to observe the blending of particle and condensed matter physics. The striking behaviour of an electron transforming into a boson [8], through binding with magnetic flux, renders the FQHE a unique merging of particle and solid-state physics. The stringent requirements of cryogenic temperatures, high magnetic fields and high mobility materials means that the FQHE within Ge is reported in only a few publications.

Quantum well (QW) heterostructures and their constituent buffer layers are required to achieve the mobilities needed for a FQHE observation. QW heterostructures permit ultra-pure, undoped semiconductor channel layers to be populated with carriers. Their design is broadly based on placing a narrow band gap semiconductor between two wide band gap semiconductors. The energy band offset between neighbouring layers of the heterostructure creates potential energy barriers at the layer interfaces, resulting in an energetically favourable layer or QW [9]. An external supply of charge carriers that move into the layer by diffusion can be achieved through modulation doping or gating [10, 11]. Biaxial compressive strain alters the band structure of Ge and leads to the formation of very high two-dimensional hole gas (2DHG) mobility within a QW, up to 1,500,000 $cm^2V^{-1}s^{-1}$ and 4,500 $cm^2V^{-1}s^{-1}$ at low and room temperatures, respectively [12-14]. The mobilities quoted show a dramatic improvement, contrasted to the value of $\leq$1,900 $cm^2V^{-1}s^{-1}$ found in bulk Ge.

1.2. Buffer layer theory and terminology

Buffer layers permit growth of materials on substrates with which they have a high level of lattice mismatch. Gradual relaxation of the lattice constant, from that of the substrate to that of the channel material, facilitates the transition in lattice constant. Thereby, avoiding an abrupt change which would prevent ordered layer by layer growth. Defects are the mechanism through which crystalline materials can release strain. Defects within buffer layers are therefore essential. The goal within buffer layers is to prevent the defects from propagating up and creating scattering centres within the active channel layers.

1.2.1. Critical thickness for crystaline semiconductors

The critical thickness (h_c) describes the minimum thickness of a strained layer that is required to generate dislocations and initiate relaxation. The Matthews and Blakeslee (MB) model is the most widely recognized model for predicting h_c. The MB model defines h_c as the thickness at which a grown in defect would be in mechanical equilibrium. This method looks at two forces and calculates at what layer thickness they are equal. The first force is the driving force on the dislocation from mismatch strain at the interface. This is balanced against the drag force on a dislocation, which is provided by the Peierls barrier. The Peierls barrier is the force required to displace materials from an un-slipped plane, permitting glide of a dislocation. Once the driving

force for dislocations has overcome the drag force then dislocations can glide, creating misfit segments that elongate with further glide. This initiates the start of relaxation and dictates the critical thickness h_c.

There are limitations with the MB model. It does not account for the requirements of defect formation, only balancing thermodynamic properties. Therefore, it is possible to grow a metastable layer that is thicker than the MB critical thickness. This is observed when growing low temperature SiGe layers (<750 °C). With higher quality substrates, less defects are present at the substrate/epilayer interface prior to relaxation. As the MB model relies on grown in defects existing prior to relaxation, discrepancies are observed between experiment and theory. For low temp growth and/ or high resistance substrates the MB model will underestimate h_c. People and Bean have provided a solution. Their model considers the energetics of nucleating a dislocation half loop at the growth surface. This does not rely on pre-existing threading dislocations. The energy barrier for nucleating half loops is higher, hence it is more likely at higher temperatures. With point source nucleation and higher temperature growth covered by the People and Bean model, it neatly covers the growth conditions over which the MB model proved insufficient.

1.2.2. Defect formation and propagation

The most common defect formed within a relaxing SiGe system is a 60° dislocation. Many extensive studies of 60° dislocation glide within $Si_{1-x}Ge_x$/Si (001) layers have been published [15-18]. People and Bean, [19] published a formula for the glide velocity within SiGe:

$$v_g = B \in \exp(-E_g/KT) \quad (1.1)$$

Where v_g is the glide velocity, $\in$ the mismatch strain, E_g the thermal activation barrier for glide and B is a constant. It was discovered that the activation barrier scales with composition as $E_g = (2.16 - 0.7\text{x})$ eV, with higher Ge content lowering the energy barrier, permitting dislocation glide [15].

Dislocation glide is required not only to promote interaction and annihilation but also to prevent a high threading dislocation density (TDD). Dislocations commonly form by nucleating a half loop at the growth surface, this extends through glide down to the SiGe/Si interface. As the threading arms continue to glide away from each other, the misfit between them is elongated.

Increased glide reduces pinning, the result is that less defects are required for equivalent relaxation.

Reports show that strain relaxation is kinetically limited, there is a limit on how fast dislocations can glide [17]. This presents dislocation nucleation as a bottleneck for further strain relaxation. Within the SiGe growth temperature range, low strain mismatch dislocation nucleation cannot occur [20-22]. Alternatively, dislocation nucleation occurs at defect sites [21, 22]. Dislocations can nucleate from pre-existing dislocations [23-25] or potentially nucleation can occur through surface roughening [26-29]. The dominance of a dislocation source type depends on the growth conditions of the epitaxial layer. Thin layers suppress multiplication mechanisms due to the low density of pre-existing dislocations. Large mismatch strain promotes dislocations from surface roughening and surface steps. At low mismatch strain, large energy barriers preventing dislocation nucleation exist. If the low mismatch layers are thick enough dislocation interaction following glide will be the dominant nucleation mechanism.

1.2.3. Defect interactions within cubic semiconductor systems

Stach et al [30] conducted direct, real time HR-TEM observations of CVD growth. This recorded dislocation motion and interacting during growth and annealing of SiGe/Si (001) material. Within this ground-breaking work Stach made multiple important discoveries. Stach's work focussed on gliding threading dislocations encountering orthogonal misfit dislocation segments.

Stach found that for low strain values all interactions resulted in dislocation pinning. This remains true, independent of the Burgers vectors. However, for thicker layers, pinning was seen to be increasingly Burgers vector dependant. With perpendicular Burgers vectors deterring pinning events, while parallel Burgers vectors induced pinning events. It was shown that a threading dislocation encountering a misfit segment resulted in two new defects with a 90° bend in each. The new right-angle defects could either continue to glide or were pinned due to mutual repulsion, it was believed that the outcome may be determined by the initial angle of approach of the two defects.

Investigating the impact of both growth and annealing temperature, Stach discovered that the stress required to free a pinned threading dislocation is higher than the stress energy that could prevent the initial pinning event. From Stach's work we learn that initial high levels of mismatch stress can be advantageous for reducing threading dislocation pinning. The initial relaxation under high stress is crucial, high stress provides energy to overcome the interaction energy barriers and defect line tension, promoting glide and reducing pinning.

1.2.4. Impact of strain on the surface profile of germanium

Surface roughening provides an alternative mechanism for strain relaxation. At high temperatures and large lattice mismatch, relaxation through surface roughening becomes energetically favourable. At lower temperatures and reduced lattice mismatch, relaxation through the modified Frank-Rhead method is favoured [31]. This form of relaxation has a thermodynamic origin, a kinetic barrier must be overcome before the roughening is initiated, this explains why it occurs at higher temperatures. SiGe, as an alloy, has a susceptibility for surface roughening. The larger Ge adatoms will preferentially migrate to the peaks of surface undulations, with the smaller Si adatoms moving to the troughs [32]. The final issue with roughening is that the undulations in strain create areas with reduced dislocation nucleation barriers. These act as sources of dislocation nucleation and multiplication [33, 34]. Therefore, wherever possible, to the maximum extent feasible, lowering the growth temperature is advantageous.

Ge and Si layers relaxing under compressive strain, display increased surface roughness, compared to those relaxing under tensile strain. Figure 1.1 shows the surface steps in an

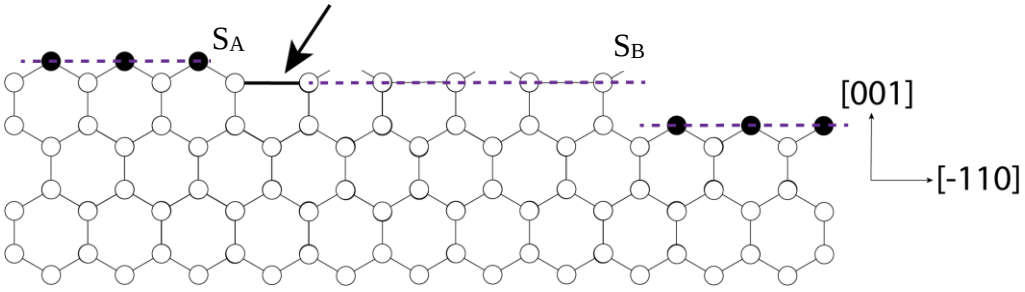

Figure 1.1 Diagram of single-height steps (S_A) and double-height steps (S_B) for a (100) orientated surface of Si or Ge. Image recreated from [35] . Arrow marks location of tensile bonded dimer responsible for strain dependant surface roughening.

unstrained (001) orientated Si or Ge surface (image recreated from reference [35]). Within Figure 1.1 S_A represents a single height surface step and S_B represents a double height surface step. The crucial aspect is the bonded dimer at the edge of a single height step, highlighted by the arrow within Figure 1.1. For single height steps this dimer is always located along the step edge making up part of the step itself. These special dimer bonds contain extra tensile strain, increasing the rigidity of single steps. The strain dependent surface roughening relates directly to this special dimer bond. Tensile strain further increases the energy within this dimer, increasing the energy barrier for step formation, however, compressive strain reduces the energy in this dimer, lowering the energy barrier for step formation. The double step responds to compressive or tensile strain equally, as such it does not impact the outcome. As you cannot have the double steps without single steps the single step becomes the limiting factor. This explains why layers relaxing under tensile strain display reduced surface roughening [35].

1.2.5. Drude Model

The Drude model describes charge carrier transport as classical particles moving through a periodic lattice. The electron – lattice interaction is considered through the creation of the effective carrier mass m^*. Electron collisions are accounted for by considering a scattering constant τ, which represents the average time between two collisions. Different scattering processes can be present, each with a different response to external variables such as temperature. For more information on scattering processes in heterostructures see reference [36]. The Drude model is only valid in situations where Landau quantization can be neglected, this requires small magnetic fields where the Landau levels will be overlapping.

1.2.6. Effective mass within strained semiconductors

The mobility of charge carriers is inversely proportional to their effective mass, as shown by the formula below.

$$\mu = \frac{e\tau}{m^*} \qquad (1.2)$$

Where τ is the transport scattering time, e the charge on an electron, m^* the effective mass and μ the mobility. There are two main ways to extract mobility. Either from the conductivity of the semiconducting material, referred to as the conductivity mobility. Alternatively, through the Hall effect, referred to as the Hall mobility. These two mobilities differ by the Hall factor.

The advantage of using the conductivity mobility is that the Hall scattering coefficient need not be known. All that is required is the majority carrier density and the resistivity of the semiconductor material. Properties of common bulk semiconductors are displayed in Table 1.1 below.

	Ge	Si	GaAs
m_e^*/m_e	0.22	0.33	0.067
m_h^*/m_e	0.29	0.55	0.62
$\mu_e/\mathrm{cm^2V^{-1}s^{-1}}$	3900	1500	8500
$\mu_h/\mathrm{cm^2V^{-1}s^{-1}}$	1900	450	400

Table 1.1 Transport properties of common bulk semiconductors at 300 K [9].

It is commonly observed that electrons display a higher mobility than their hole counterparts. The effective mass of holes within bulk Ge is notably smaller than in almost all other semiconductors. The room temperature mobility of holes in bulk Ge is $1900\ \mathrm{cm^2V^{-1}s^{-1}}$ Which exceeds the $1500\ \mathrm{cm^2V^{-1}s^{-1}}$ representing electrons in bulk silicon [9]. These fundamental properties explain the suitability of Ge within the CMOS industry.

Similarly, to Si, the valence band of Ge consists of multiple sub-bands. At the zone centre (k = 0) the valence band of Ge consists of the heavy hole (HH) band, light hole (LH) band and the split-off band. The split-off band so named as it is separated in energy due to the spin orbit interaction. Note that within Figure 1.2 the split off band is located at lower energies than is depcited within the graph. Figure 1.2 concisely depicts the impact on the Ge valence band of biaxial strain. Firstly, both compressive and tensile uniaxial strain result in a splitting of the LH and HH valence bands. In an unstrained layer these two bands are degenerate at the Γ point, overlaying each other in energy space. During pseudomorphic growth of Ge on SiGe the Ge lattice is biaxially compressed to match the reduced in-plane lattice constant of SiGe. Simultaneously the out of plane lattice constant will increase to maintain Poisson ratio. This deforming of the crystal breaks the degeneracy of the LH HH bands. Compressive strain increases the energy of the heavy hole band while reducing the energy of the light hole band. The strain dependent energy gap reduces unfavourable intervalley scattering events, thereby

increasing the mobility of the strained Ge system. This process is described as mass inversion, intuitively named as the HH becomes lighter than the LH [37].

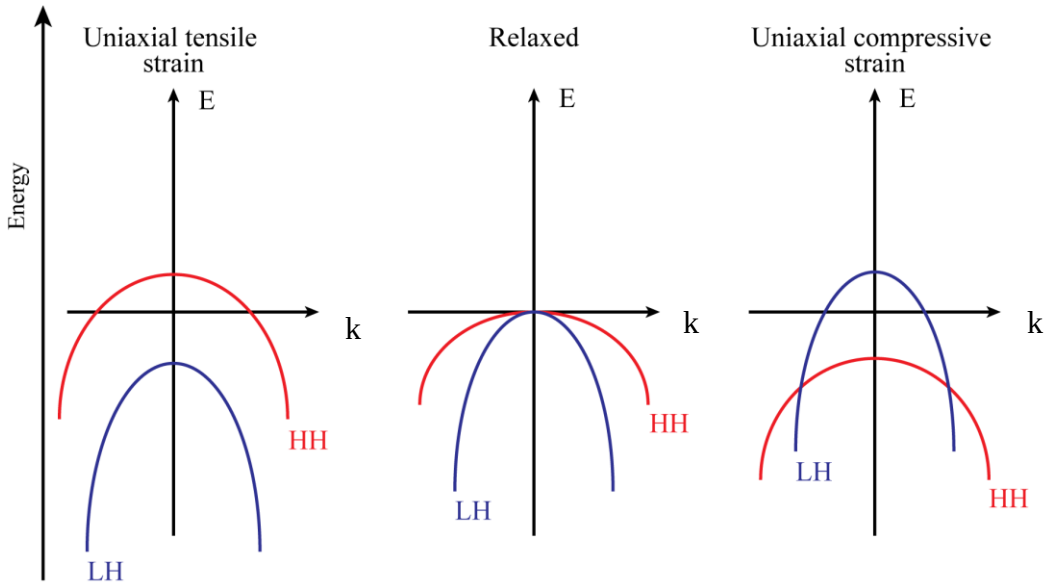

Figure 1.2 Impact of tensile and compressive strain on the Ge valence band. Light Hole (LH) and heavy hole (HH) energy bands split on application of strain. Parabolic approximation is used to display bands, image is not to scale.

1.2.7. Modulation doping method for introducing charge carriers

Elemental semiconductors are electrical insulators at low temperatures. Free carriers are not available to transport electrical current, with potential free carriers localised in the covalent bonds that form the crystal lattice. Free carriers can be introduced by adding impurities, called dopants. The dopants insert into the lattice, providing the excess charge carriers required for electrical conduction at low temperatures. Although dopants provide the required carriers, they also are themselves scattering sites for the newly introduced carriers.

Within a 3D structure, the scattering from ionized dopants cannot be avoided. However, when carriers are localized to a 2D plane, we can spatially and energetically separate the carriers from the ionized impurities that donated them. This separation is achieved by a spacer layer which is shown in Figure 1.3. Separation of the dopants and carriers is referred to as modulation doping.

1.3. Formation of a two-dimensional hole gas (2DHG)

When carrier holes are confined in a potential well, restricting and thus quantizing their motion in one direction. One effectively achieves a two-dimensional sheet of charge carriers, referred to as a 2DHG. At cryogenic temperatures and with smooth interfaces, carriers can travel distances on the order of microns before scattering off phonons, impurities or other electrons. The primary systems in which 2DHG behaviour is studied include QWs, superlattices and MOS structures [38, 39].

Germanium has a smaller band gap than silicon. The band gap for SiGe has been shown to be a linear interpolation of the gaps for Si and Ge [40]. At the interface between a SiGe buffer and a Ge channel layer the valence band maximum resides in the material with higher Ge content, regardless of strain. By varying the SiGe composition the discontinuity in band gap can be tuned.

The formulae, modelling and assumptions of classical physics are applicable to 3D semiconductor materials. To observe quantum phenomena, the building blocks of macroscopic behaviour, low dimensional electron systems are studied. This is carried out at cryogenic temperatures preventing the small responses being masked by thermal noise. Also, reduced temperatures increase the distance a carrier can travel between scattering events, referred to as the mean free path. Experimentally this means the carriers retain their quantum phase for macroscopic distances. Without the extended scattering times it would not be feasible to produce devices small enough to display quantum effects. Low dimensional systems are produced through geometric confinement. Within this work, confinement refers to restricting carrier movement in one direction, resulting in a 2D plane of carriers referred to as a 2D hole gas (2DHG).

In a 3D universe, achieving 2D confinement requires the surface of an object. Alternatively, an interface between two substances and a force to keep objects there. An analogy is a snooker table and balls. The balls reside in air and cannot move through the table, gravity holds them in place within a 2D plane. Currently the smoothest 2D plane, produced to confine charge carriers, is the interface between two similar semiconductor layers.

The layer structure used to produce 2D confinement within this work is shown in Figure 1.3 (a). Note the charge carriers, holes in this example, are localized at the interface between the $Si_{0.2}Ge_{0.8}$ and the strained Ge layer. This is analogous to the air and snooker table example. The force in this example is provided by the electrical attraction between the carrier holes and the ionized donors present in the Boron doped supply layer. Figure 1.3 (b) shows why the holes cannot pass into the spacer layer, just as the snooker balls do not pass through the table. It is due to the valence band energy being higher in the spacer layer. There is a potential energy barrier preventing the carriers from moving into the spacer layer. Carriers reside within the strained Ge layer within a potential energy well. It is the attraction to the boron doped supply layer that makes the well triangular, localizing the carriers to the 2D interface between the spacer and strained Ge layer. To really stretch the snooker table analogy, what would be ideal is something more akin to an air hockey table, where the friction is greatly reduced between the carrier and the interface. Therefore, great efforts are made to produce smooth, highly crystalline growth interfaces within the heterostructures developed.

Carriers are scattered by the surface roughness of the interface to which they are localized. Scattering also occurs from random impurities and lattice/ phonon vibrations. To mitigate this samples are cooled to temperatures in the 10s or 100s of mK range. These temperatures reduce

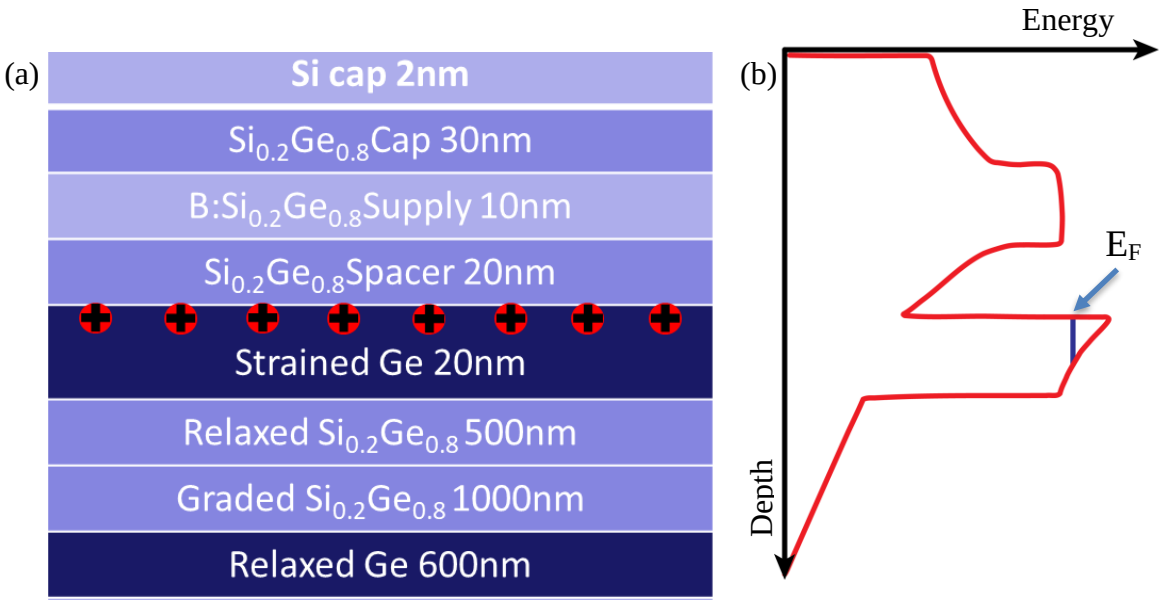

Figure 1.3 (a) Example of layer structure that produces 2D system. (b) Impresion of valence energy band for the strained Ge MOD QW strucutre shown on the left.

lattice vibrations and the consequential scattering to an acceptable level, when compared to scattering from residual impurities. This permits observation of "clean" charge carrier behaviour governed only by interactions, both carrier-carrier and with their surroundings. Lower concentrations of impurities and smoother interfaces permit a deeper probe of fundamental physical interactions. This initiated the technological race to produce highly crystalline materials [8].

1.4. Integer quantum Hall effect theory and basic formulae

1.4.1. Classical Hall effect

A magnetic field, B, applied perpendicular to the 2DHG causes the carriers to move in circular orbits (unless they meet at an edge where they are reflected). The Lorentz force given by; $\vec{F} = -e(\vec{v} \times \vec{B})$ acting at a right angle to the direction of carrier motion, within the 2D plane, maintains the circular orbits.

Applying a current (I_{AC}) along the Hall bar and a magnetic field (B) perpendicular to the Hall bar, following the geometry shown in Figure 1.4, induces a Hall voltage across the Hall bar, depicted as resistance R_{xy}. The Hall voltage arises as carriers are split depending on their charge. For instance, positive carriers performing clockwise rotation and negative carriers performing anticlockwise. Scattering events interrupting the cyclotron orbit of carriers lead to positive and negative carriers being separated to opposite edges of the Hall bar, inducing the measured Hall voltage. The magnitude and sign of the voltage provides information on carrier density, carrier type and mobility. Hall measurements provide a robust method of probing charge carrier properties with macroscopic magnetoresistance measurements. The properties extracted are universal and geometry independent, allowing them to be compared across widely varied material systems. The Hall measurement is very robust, to the extent that it is unaffected by drilling holes through the mesa. Due to the cyclotron motion any holes in the mesa act as scattering events and the cyclotron motion continues.

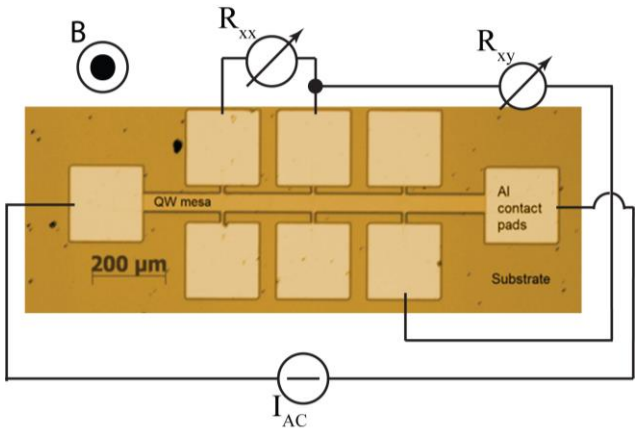

Figure 1.4 SEM image of Hall bar with added wiring diagram for measurement set up. Orientation of applied magnetic field displayed with scale bar.

Important fundamental formulae required for extracting values from Hall and resistivity measurements are included below. The Hall coefficient R_H is equal to the gradient of a Hall resistance Vs applied magnetic field plot.

$$R_H = \frac{\Delta\rho_{xy}}{\Delta B} \qquad (1.3)$$

Where $\Delta\rho_{xy}$ is the difference in Hall resistance between two measurements and ΔB is the difference in applied field for the same two measurements. Care must be taken to ensure the gradient is taken from a linear region of the Hall signal. The Sheet carrier density of a 2DHG is given by:

$$p_{Hall} = \frac{1}{e \times R_H} \qquad (1.4)$$

The Hall mobility of a 2DHG is given by:

$$\mu_{Hall} = \frac{R_H}{\rho_{xx}(0)} \qquad (1.5)$$

Where $\rho_{xx}(0)$ represents the value of longitudinal resistivity without an applied magnetic field [36]. The measured resistance of a semiconductor is influenced by the application of a magnetic field. As explained above the application of a magnetic field causes carriers to deviate from their average drift velocity in the orientation of applied current. This increases the measured resistance and is referred to as magnetoresistance. Magnetoresistance varies depending on the sample geometry, to compare different materials sample geometry is divided out to produce the geometry independent property- magnetoresistivity.

1.4.2. Quantum Hall effect theory and fundamental formulae

An example of a typical Hall and resistivity plot is displayed in Figure 1.5. The sample is set up under the conditions described in section 1.4.1. and the resistivity (R_{xx}) and Hall resistance (R_{xy}) are measured in the geometry depicted within Figure 1.4. In a simplified manner the typical plots such as Figure 1.5 are easily interpreted. A constant current is applied along the Hall bar (Figure 1.4) while a magnetic field (orientated normal to the sample surface) is continuously ramped in magnitude.

While this is occuring one measures two voltages, one parallel to the current and one perpendicular to the current. The parallel voltage is converted into resistivity and gives R_{xx}, as shown in Figure 1.4. The perpendicular voltage is converted into resistance and gives R_{xy}, also as depicted in Figure 1.4.

The features, comprising oscillations in R_{xx} and step like plateaus within R_{xy}, displayed in Figure 1.5 originate from the interplay of charge carriers and energy bands. The sample set up only requires an applied current, two voltage measurements and a steadily ramped magnetic field.

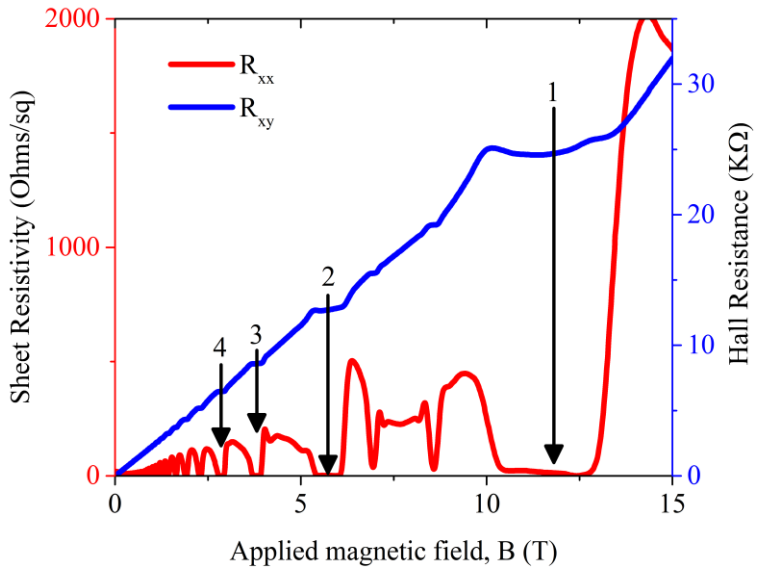

Figure 1.5 Resistivity and Hall data collected during a 0 to 15 T magnetic field sweep. Selected filling factors for the integer quantum Hall effect are labelled. Horizontal plateaus in Hall resistance are clearly visible.

The features in Figure 1.5 occur at predictable values of magnetic field, depending on carrier density and mobility. This holds true regardless of the material or geometry of the sample measured. The locations of the features are termed filling factors, for reasons that will be explained subsequently. Selected filling factors are labelled within Figure 1.5 for clarity. At each filling factor the Hall resistance displays a flat plateau and the Sheet resistivity displays a minima, which for an ideal sample would equal zero resistivity. The filling factors for the integer quantum Hall effect are all integers and the filling factors for the fractional quantum Hall effect are all Fractions.

Low temperature (< 0.3 K), high field (> 10 T) Hall measurements of a 2D system will not return the linear Hall response expected from a bulk 3D system. Instead, the Hall response shows a step wise dependence on magnetic field, displayed in Figure 1.5. The value of R_H calculated from the plateaus in Hall resistance is accurate to a few parts per billion. This highly accurate value can be measured in any 2D system regardless of the material or carrier density, this has led to the Hall resistance being declared as the resistance standard from which all other resistances can be calibrated. It was Klaus von Klitzing that first discovered the remarkably accurate constant $R_K = h/e^2 = 25812.807\ \Omega$ (the von Klitzing constant). The constant can be measured from the quantised Hall resistance plateaus, where the Hall resistance value for each filling factor v equals:

$$R_{xy} = \frac{1}{\nu} \times \frac{h}{e^2} \qquad (1.6)$$

Where h is planks constant, e the charge on an electron and v the filling factor.

The periodic circular motion of charge carriers within the 2DHG can be modelled as a one-dimensional harmonic oscillator displaying the frequency $\omega_c = eB/m^*$ termed the cyclotron frequency. The oscillatory motion within the 2D plane forms a discreet set of achievable energy levels with a discreet set of permitted energies. Each energy level is separated by a characteristic energy $\hbar\omega_c$. The energy levels are called Landau levels.

1.4.3. Shubnikov-de Haas oscillations

Shubnikov-de Haas (SdH) oscillations are oscillations in longitudinal resistivity that occur when continuously ramping the applied magnetic field. An example of SdH oscillations can be

seen in Figure 5.5. The oscillations provide an essential tool to investigate the fundamental physical interactions that carriers are experiencing within a sample. The oscillations appear due to two effects, firstly, the discrete set of allowed energy levels (Landau levels). Secondly, the directly proportional relationship between applied magnetic field and the density of states (DOS).

Within Figure 1.6 each curve represents an individual Landau level, the area inside each Landau level represents allowed energy states for a charge carrier. The red colour fill represents which states are populated by charge carriers and the black dashed line shows the Fermi energy. Figure 1.6 (a) shows the situation where Landau levels overlap causing a continuum of states, the location of the Fermi level at the highest occupied energy state is shown by the dashed line. Figure 1.6 (b) shows two completely filled Landau levels and the Fermi energy residing in the forbidden energy gap in-between Landau levels. When the Fermi energy resides in a forbidden energy gap, carriers are not free to contribute to conduction. Counterintuitively, this causes the resistance minima within SdH oscillations, as seen in Figure 5.5. This is explained by chiral motion conduction which is explained subsequently.

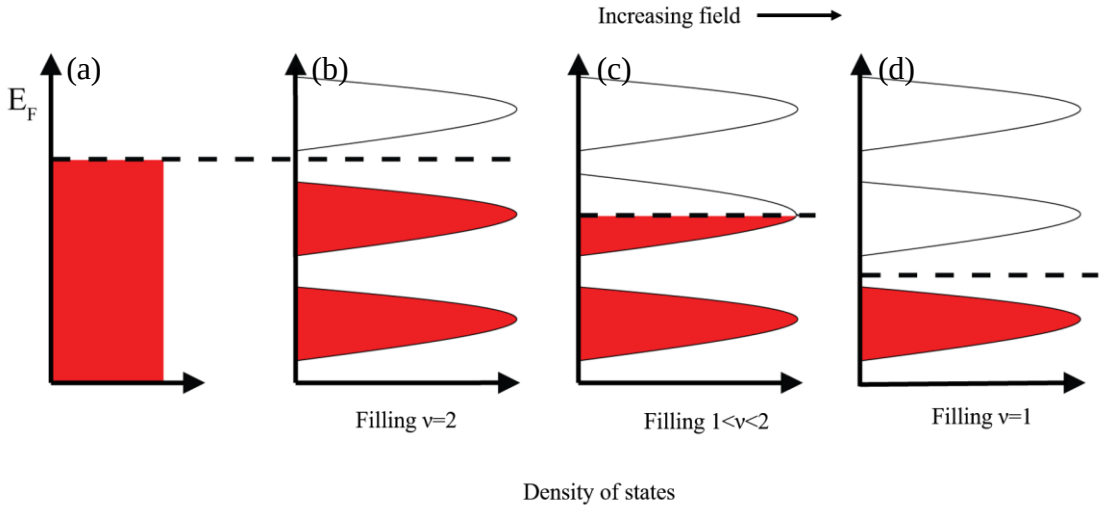

Figure 1.6 Schematic diagram showing how increasing applied field increases the density of states, resulting in all carriers residing in the lowest Landau level. Y axis displays energy, X axis displays density of states. Direction of increasing applied field is labelled. The relationship between filling factor and Landau level filling is labelled on the X axis.

Figure 1.6 (c) displays that as we increase the applied magnetic field the density of states increases. The increase in available states within each Landau level causes carriers to depopulate higher energy Landau levels, subsequently occupying lower and lower energy Landau levels. The result is shown in Figure 1.6 (d) where the DOS has reached a value that permits all charge carriers to reside within the lowest energy Landau level. This describes filling factor 1 and is labelled on Figure 1.6. The oscillations in resistance occur when the Fermi energy crosses a forbidden energy region, between Landau levels. This occurs as the DOS increases, carriers depopulate higher energy levels, moving to subsequently lower energy Landau levels. Once all carriers reside within the lowest energy Landau level no further forbidden energy gaps exist. Therefore, within the integer quantum Hall effect regime, no further oscillations are predicted when increasing magnetic field above filling factor one. As is shown subsequently, further oscillations do occur, fractional quantum Hall effect theory is required to explain these results.

As mentioned previously, when an integer number of Landau levels are full, and the Fermi energy resides in a forbidden energy gap, minima in longitudinal resistivity are observed. This occurs due to the conduction only occurring along the edges of the sample. With the Fermi energy within a forbidden gap, carriers are localized to length scales dictated by their cyclotron orbit. This is shown for the charge carriers at the centre of the mesa in Figure 1.7, however, the carriers on the edge of the sample do not complete a full cyclotron orbit. Carriers in the edge channels contribute to conduction by skipping along the edges of the sample, analogous to

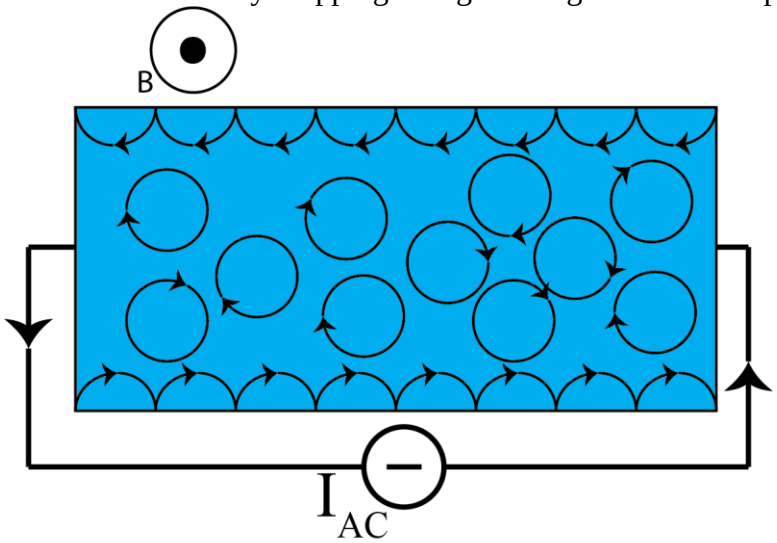

Figure 1.7 Schematic diagram of how chiral edge motion leads to conduction devoid of backscattering,, blue rectangle represents the mesa of a Hall bar or equivalent conduction path.

skimming stones on a pond. This method of conduction is devoid of backscattering, such as would be seen for bulk conduction, this explains how an absence of free carriers within the centre of the mesa can cause a deep minimum in longitudinal resistivity.

In a high magnetic field charge carrier's complete multiple orbits between scattering events. Projecting the cyclotron motion onto a 2D plane, orthogonal to the 2DHG, displays carrier motion as a simple harmonic oscillator. It is effective to represent the circular motions as two linear harmonic oscillators perpendicular to each other (with a π/2 phase shift) both with angular frequency ω_c. Within the high field regime where $\hbar \cdot \omega_c > k_b \cdot T$ carrier motion becomes quantised into discrete energy levels, called Landau levels. The energy of the Landau levels is given by:

$$E_n = \hbar \cdot \omega_c \cdot \left(n + \frac{1}{2}\right) \quad n = 0,1,2, \ldots \tag{1.7}$$

The radius of the cyclotron orbit is also quantised and referred to as the Larmor radius or magnetic length l_B,

$$r_L = l_B = \sqrt{\frac{\hbar}{e \times B}} \tag{1.8}$$

Increasing the applied magnetic field reduces the cyclotron radius and increases the radial velocity. When one includes the spin of charge carriers each Landau level splits into two distinct levels. The energy levels are then given by:

$$E_n = \hbar \cdot \omega_c \cdot \left(n + \frac{1}{2}\right) + g \cdot s \cdot \mu_B \cdot B \quad n = 0,1,2, \ldots \tag{1.9}$$

Where ω_c is the cyclotron frequency, g the Lande g-factor, s the spin, μ_B the Bohr magnetron and B the applied magnetic field. When moving onto the fractional quantum Hall effect (FQHE) at very high magnetic fields, spin is often ignored as it is assumed that all levels are spin polarised. The density of states for each level can be expressed as:

$$n_{2D} = e \times \frac{B}{h} \tag{1.10}$$

Which explains the magnetic field dependence of the density of states displayed within Figure 1.6. Following on from equation 1.10 the number of occupied levels is given by:

$$v = \frac{p_s}{n_{2D}} = \frac{h \times p}{e \times B} \tag{1.11}$$

Therefore, as the applied field (B) increases, the number of occupied levels (v) decreases. As explained previously at integer filling values the fermi energy resides in the forbidden gap. This produces the zero conductivity and zero resistance state, where carriers progress through chiral motion devoid of backscattering [41]. The characteristic Shubnikov de Haas oscillations of the quantum Hall effect can be modelled as the product of three units. The full derivation can be found in [42] and [43].

$$\frac{\Delta\rho_{xx}(B)}{\rho_{xx}(0)} = 4 \cdot cos\left(\frac{2 \cdot \pi \cdot E_F \cdot m^*}{\hbar \cdot e \cdot B}\right) \cdot exp\left(-\frac{\pi \cdot m^* \cdot \alpha}{e \cdot B \cdot \tau_t}\right) \cdot \frac{\psi}{\sinh(\psi)} \quad (1.12)$$

Where

$$\psi = \frac{2 \cdot \pi^2 \cdot k_B \cdot T \cdot m^*}{\hbar \cdot e \cdot B} \quad (1.13)$$

Where τ_t is the transport scattering time, $\rho_{xx}(0)$ is the magnetoresistance at zero magnetic field, $\Delta\rho_{xx}(B)$ is the amplitude of the SdH oscillations and α describes the ratio of the classical scattering time (τ_t) to the quantum scattering time (τ_q), given by $\tau_q = \tau_t/\alpha$. For a 2DHG the Fermi energy is given by:

$$E_F = \frac{\pi \cdot \hbar^2 \cdot p_s}{m^*} \quad (1.14)$$

The two unknown variables within formula 1.12 are m^* and α. Which are determined by measuring repeated field sweeps while incrementing temperature. An iterative process involving linearizing the exponential growth component then settles on an equilibrium value for m^* and α, as shown in [44].

The first term in formula 1.12 describes the periodic ρ_{xx} oscillations, the period of which is proportional to 1/B. The second term describes the exponential growth component of the envelope for SdH oscillations, this growth increases relative to the applied magnetic field also depending on relaxation time and effective mass. The final term is the most important, it permits the extraction of the effective mass of charge carriers. This final term depends on applied magnetic field, effective mass and importantly temperature. Varying the temperature alters the amplitude of the SdH oscillations but importantly does not impact anything else. Incrementing the temperature of repeated magnetic field sweeps thus facilitates an extraction of the effective mass by measuring the resulting change in peak amplitude.

1.4.4. Broadening of plateaus within Hall resistance data

In theory the plateaus observed in the Hall resistance should not be broadened, as is observed in the sample data of Figure 1.5. When the applied magnetic field causes an integer number of Landau levels to be filled the longitudinal resistivity should show a delta function peak and the Hall voltage should show a similarly instantaneous plateau. Broadening occurs due to imperfections in the 2DHG. It is assumed that the system is perfectly 2D, realistically energetic hills and valleys exist along the interface. These are created by defects, impurities and steps in the surface atoms. When a Landau level is being populated with carriers some carriers get trapped by defects, these carriers no longer contribute to conduction and behave equivalently to cutting holes through the 2D layer. As explained in section 1.4.1 for the classical Hall effect, these holes have no impact on the measured results. Carriers within the energetically flat part of the Landau level negotiate a path around the hills and valleys.

The hills and valleys provide a reservoir of carriers that can be fed into the energetically flat region of the Landau level, maintaining the flat region at full capacity, which maintains the Fermi level within an energy gap. While the reservoir of trapped carriers feeds the energetically flat region the Hall resistance remains at its quantized value, this extends the Hall plateau for finite stretches of magnetic field. Ironically without defects there would be no plateau broadening and one would not be able to observe the integer quantum Hall effect (IQHE).

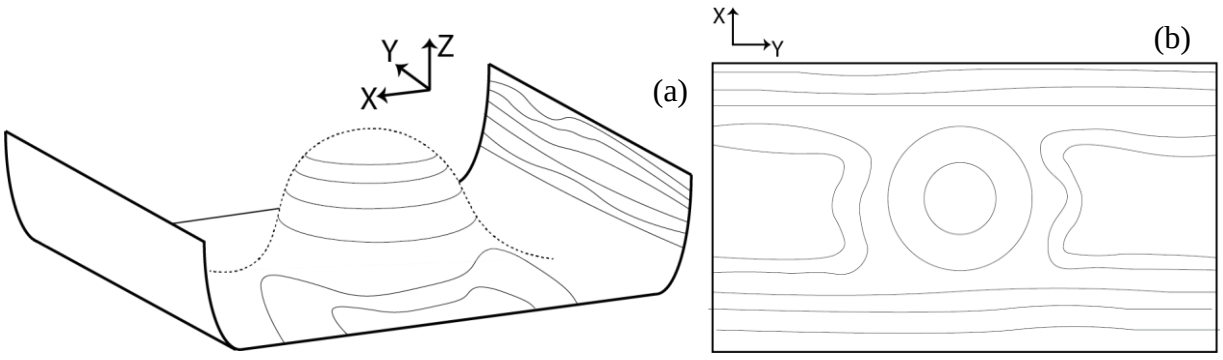

Figure 1.8 (a) Diagram showing continuous edge state energy levels and localized central energy levels of the Hall effect. (b) shows the view from above of the energy levels with the continuous conducting edge states.

1.5. Fractional quantum Hall effect quasi classical interpretation

When the DOS is such that all carriers reside within the lowest energy Landau level, corresponding to filling factor $\nu = 1$, further increasing applied field results in the lowest energy Landau level being only fractionally filled. No further energy gaps are predicted by the IQHE. Features that occur when the lowest energy Landau level is partially filled are explained by the fractional quantum Hall effect (FQHE). The IQHE is termed a single-particle effect, all features of the IQHE can be explained by considering an individual charge carrier moving through a magnetic field. This is not the case with the FQHE. The FQHE is termed a many-particle effect as it originates from the interaction between charge carriers. It is the large number of unfilled states within the last electron Landau level that permits the FQHE to occur. Within the IQHE, carriers were closely packed and had no means by which to avoid their mutual repulsion. Within the FQHE, carriers avoid each other in the most energetically advantageous manner. Within the FQHE charge carriers reduce their mutual repulsion, forming a complex many body problem to model. One interpretation of the FQHE is to consider the formation of composite particles named composite fermions [8].

1.5.1. Composite fermion model for charge carriers of the FQHE

The intuitive thought process for understanding composite fermions begins by considering a 2D plane of electrons. Quantum mechanically individual electrons are indistinguishable, their location is smeared uniformly over the entire 2D plane. The electrons are commonly described as a featureless liquid. When a magnetic field is applied it can be considered as creating small whirlpools or vortices within this uniform lake of charge. One vortex is created per magnetic

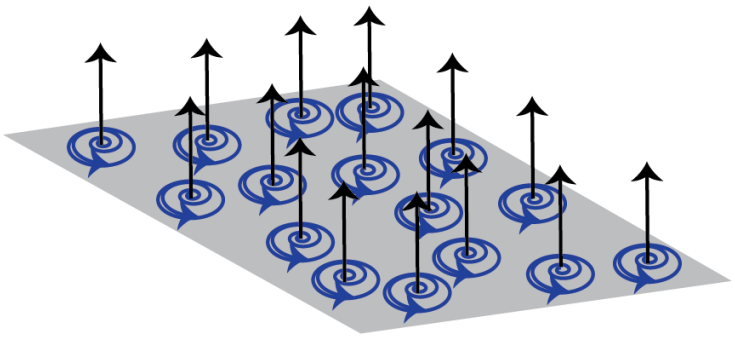

Figure 1.9 Diagram showing magnetic field impinging on a 2D electron system. One vortex is formed per magnetic flux quantum ϕ_0.

flux quantum ϕ_0, as is shown diagrammatically in Figure 1.9. It is worth noting that magnetic field is itself not quantized. Magnetic flux quanta are the elementary units in which a magnetic field interacts with a system of electrons.

Within each vortex electronic charge is displaced, equal to zero at the centre while recovering to the average background at the vortex edge. The size of the vortex is approximately the area which would contain one magnetic flux quantum ($area \times B = \phi_0$) This permits each vortex to be considered as carrying one quantum of magnetic flux. The vortices, just as in the electron case are spread uniformly over the 2D plane. The probability of finding either an electron or a vortex is completely uniform over the plane. This is the foundation of how the system can reduce its overall energy. Electrons and vortices represent opposing objects, one being a package of charge and the other an absence of charge. Placing electrons directly onto vortices is energetically advantageous. The dip of the vortex represents the displacement of every other background electron, this provides shielding keeping other charges at a distance and reducing mutual repulsion.

At $\upsilon = 1$ there is one vortex per electron. At magnetic fields above $\upsilon = 1$ there are a larger number of vortices than electrons, the system can reduce its electrostatic Coulomb energy considerably by placing more than one vortex on each electron. Increasing the number of vortices bound to each electron produces greater shielding, resulting in a greater reduction in the mutual repulsion.

The movement of electrons is no longer dictated by the Pauli exclusion principal, instead a correlated motion is initiated that is driven by opportunities for reducing the Coulomb energy. The process of picturing a composite particle made of electrons and vortices remains the most visual and intuitive means to understand composite fermions (CFs) and the FQHE. Within the literature CFs are often described as electrons bound to magnetic flux quanta, this is an equivalent description to the vortex analogy.

The composite fermions behave differently to bare electrons. At specific values of magnetic field, all the applied field is incorporated into the composite particles via flux quantum attachments. From the CFs perspective there is no externally applied magnetic field. This is

observed during measurements with CFs performing straight trajectories in high magnetic fields. Whereas, bare electrons in this environment would follow tight circular orbits.

The effective mass of CFs is unaffected by the effective mass of the underlying electrons. The mass originates entirely from the interaction energy of many particles and bares no relation to the effective mass of any one individual electron. The calculated mass will vary with the value of applied magnetic field.

1.5.2. Fermionic and bosonic behaviour of composite fermions

Electrons are fermions and obey the Pauli exclusion principal, as such they sequentially fill one state after the other. Bosons obey Bose-Einstein statistics and prefer being in the same state, usually referred to as a Bose-condensate. Fermions have half integer spin and bosons have integer spin. It is possible to combine fermions to produce bosons.

When a mutual position exchange occurs between two bosons, within a larger Bose-condensate system, the wavefunction is multiplied by +1. For fermions, this exchange multiplies the wavefunction by -1. Essentially fermions and bosons behave very differently under mutual exchange of constituent particles.

Composite fermions switch between bosonic and fermionic behaviour depending on the number of flux quanta bound to the composite particle. Each flux quantum attached adds an extra "phase twist" during mutual position exchange. As a result, an electron bound to an odd number of flux quanta becomes a composite boson (CB). Whereas, an electron bound to an even number of flux quanta becomes a composite fermion.

At $\upsilon = 1/3$ the lowest Landau level (LLL) is 1/3 full, the electron fluid contains three vortices for every one electron. The mutual repulsion energy between electrons is reduced by each electron binding to three flux quanta, keeping all other electrons optimally at bay. The odd number of flux quanta attached renders the particle as a CB. With all the field incorporated into the CB via flux quantum attachments, the CB resides in an apparent zero magnetic field environment. As expected for bosons in zero apparent magnetic field, the system Bose-condenses into a new ground state with its own energy gap, characteristic of such a

Bose-condensate. The energy gap explains the features that occur at field values above filling factor 1. Further increase in applied magnetic field above $\upsilon = 1/3$ creates excess vortices, these cannot bind to any electrons as it would disrupt the symmetry of the system. The excess vortices represent a charge deficit of 1/3 of an electronic charge. As a charge deficit (vortex in the electron lake) they behave as quasi-holes. The 1/3 charged particles are free to move throughout the 2D plane and transport current. They have been detected via multiple experimental means.

Fractions at $\upsilon = 1/5,\ 1/7$ can be explained by the same method, by attaching 5 and 7 flux quanta per electron. The quasi particles (excess vortices) in this case have charge $e/5, e/7$ respectively.

1.5.3. Filling factor 1/2

The $\upsilon = 1/2$ state behaves very differently to the $\upsilon = 1/3$ state. When the LLL is exactly half full two flux quanta bind to each electron. As mentioned previously each flux quanta adds an extra phase twist corresponding to an extra -1 multiplier under mutual position exchange. This renders the system at $\upsilon = 1/2$ as a system of composite fermions (CFs). All applied field has been incorporated via flux quantum attachments. As fermions residing in an apparent zero field environment, the CFs fill up successively higher energy states until all CFs have been accounted for. The process is analogous to electrons at $B = 0$. Indeed, comparing the IQHE at $B = 0$ and the FQHE at $\upsilon = 1/2$ returns a very similar structure of longitudinal resistivity.

Around $\upsilon = 1/2$ as the field is increased or decreased away from half filling, the FQHE for CFs, in an effective field which is the difference from that at $\upsilon = 1/2$, can be considered equivalent to the IQHE of electrons. Carriers are excited across energy gaps and oscillations in longitudinal conductivity ensue. This thought process reduces a complicated many particle system to a simple system made up of composite particles.

1.5.4. Rotated field measurements of FQHE phenomena

Laughlin's initial all-encompassing wavefunction, put forward to explain FQHE physics, assumes complete spin polarization [45]. This assumption has a logical basis. Spin polarization occurs when the Zeeman energy, $g\mu_B B$, exceeds the Coulomb energy, $e^2/\varepsilon l_0$. The Coulomb

energy scales as $B^{1/2}$, so at sufficiently high magnetic field values, it appears logical that the system would be fully spin polarized. It was later discovered that the ground state at $\nu = 2/5$ is not spin polarized. This provided the exciting prospect that a fraction could vary depending on the value of magnetic field it is observed at. Fractions will appear at different magnetic field values depending on the carrier density. This highlights a motivation for gated samples. Observing unpolarized to polarized phase transitions, induced through gated carrier density manipulation, remains an area of investigation within the field.

The tilted field technique, first introduced by Fang and Stiles [46], is a method of probing the spin degree of freedom within transport measurements. The technique rotates the applied magnetic field with respect to the sample normal. This takes advantage of the fact that spacing between Landau levels depends solely on the perpendicular component of applied field with respect to the sample normal. The spin flip Zeeman energy however scales with the total magnetic field B_{tot}. Through tilting the sample each energy scale can be varied independently.

Some fractions contain both polarized and unpolarized configurations for their ground states. Adding an in-plane component of magnetic field favours the spin polarized state and can drive the system from unpolarized to polarized while observing the same fraction. The tilted field technique involves varied angles of applied magnetic field. The technique assumes only the field component parallel to the sample normal impacts the Landau level energies. Thusly the assumption is also made that a field applied perpendicular to the sample normal (in the plane of the 2DHG) will only impact the Zeeman energy. The assumption that a parallel field will only affect the Zeeman energy relies upon perfect 2D confinement for a 2DHG. In a realistic system, the 2DHG has a finite thickness, which is affected by the in-plane magnetic field, and correction factors have been suggested [47, 48].

Measuring at high tilt angles is important. Consider the Landau level fan, at high tilt angles the Fermi level is far away from any points of coincidence. A measurement of the energy gap at high angles provides an accurate measure of m^* without interference from g^*.

1.5.5. Finite thickness corrections to the FQHE in 2DHGs

When an in-plane component of magnetic field is present it exerts an extra Lorentz force on charge carriers. This secondary Lorentz force acts perpendicular to the cyclotron orbits within the 2D plane. The force acts to deform the wavefunction of the subband. Initial experiments, such as those by Fang and Stiles, used rotated field to extract the g factor for 2D electrons, assuming the effect of this perpendicular force was negligible [46]. Subsequently, J. Hampton and Eisenstein went on to show that an in-plane field compresses the charge distribution closer to the interface. This was demonstrated to be a large enough effect that it could be measured experimentally. Measurement was achieved by recording the capacitance between an inversion layer and a topside metal gate contact. This work confirmed that a parallel component of magnetic field acts to reduce the finite thickness of the 2D carrier gas. Hampton also discovered that samples with higher carrier density, where a second subband is populated, show a higher initial rate of compression. This is interpreted as the higher level depopulating, leading to a halving of the finite thickness of the 2D sheet [49].

1.6. Electron hole symmetry displayed by states within the FQHE

In 1987 Haug et al [50] discovered that for 1/3 filling the activation energy, extracted via temperature dependence, decreased slightly when the applied field was rotated. In the same experiment it was found that for 2/3 the opposite effect occurred, with an increase in activation energy during an equivalent field rotation. This describes electron hole symmetry breaking. The phenomenon is explained through permitting spin reversal in the ground state, this accounts for breaking the electron hole symmetry.

In an ideal system it was first shown by Halonen et al [51] , through modelling of finite systems in a periodic rectangular geometry, that within the LLL when a perpendicular *B* field is applied electron-hole symmetry should be maintained. Work by Chakraborty [52] altered Halonen's modelling to represent a triangular potential confinement instead of a parabolic potential well. Chakraborty also explored the impact of rotated fields on the electron hole symmetry. It was discovered that electron and hole FQHE states behaved differently under field rotation. This agreed with experimental results such as those by Furneaux et al [53].

Chapter 2. Material characterisation techniques

2.1. Transmission electron microscopy

Transmission electron microscopy (TEM) is a transmission imaging technique. A focused beam of electrons is directed through a thin (~100 nm) sample. The electrons that pass through the sample irradiate a phosphor screen, converting the electron image into a visible image. To capture the image the phosphor screen is substituted for a CCD. TEM provides information on the crystal quality, layer thickness, defect density, composition and topography of materials.

Prior to imaging, samples must be thinned until they are electron transparent. This is achieved through mechanical grinding using abrasive SiC paper, followed by ion milling and polishing within a precision ion polishing system. This equipment uses a low energy (2 - 4 keV) argon beam to slowly erode the surface. Reference [54] provides an extensive description of the TEM sample preparation process used within this work.

Contrast in TEM images represent the variation in electron absorption over the sample. A TEM image is a conversion of electron absorbance into greyscale, providing an optical method to observe density variation within solid materials.

The resolution of conventional optical microscopes is limited by the wavelength of light. This is not the case with TEM, with wavelengths of 0.0025 nm commonly used, the limiting factor to TEM resolution (~ 0.1 nm) is imperfections in the focusing lens. Calculating the wavelength of the electron beam represents an exercise commonly conducted in undergraduate physics courses. It was Louis de Broglie who initially explained that matter could propagate as a wave, with the wavelength of a particle given by: $\lambda = h/mv$ where λ is the wavelength of a particle, h planks constant, m the particle mass and v the particle velocity. For the electrons the velocity is determined by the accelerating voltage given by: $v = \sqrt{2eV/m}$ where v is the electron velocity and V the accelerating voltage. Therefore, the formula for calculating the classical wavelength of an electron beam is: $\lambda = h/\sqrt{2meV}$. However, electrons within a TEM can reach up to 70% the speed of light at an accelerating voltage of 200 KeV. This means that

a relativistic correction will have a notable impact on the true wavelength value. When including a relativistic correction, the wavelength of the electron beam is given by:

$$\lambda = \frac{h}{\sqrt{2meV}} \times \frac{1}{\sqrt{1 + \frac{eV}{2mc^2}}} \quad (2.1)$$

Where c is the speed of light. Inputting values for electrons accelerated at 200 KeV returns a wavelength of 0.0025 nm, which is where the value quoted above for resolution comparison originates from.

2.1.1. Alligning the TEM in diffraction mode

The samples imaged in this work are crystalline. Therefore, when the electron beam passes through the sample some beam paths are diffracted and some are transmitted. The TEM can then be placed into two different conditions, bright field (BF) and dark field (DF). BF is when an aperture is added that only allows transmitted (un-diffracted) electrons to pass. Whereas, DF is when the added aperture only permits some diffracted electrons to pass (which diffracted beams are selected should be specified). The image in either BF or DF displays the variation in diffraction contrast over the samples surface, highlighting features that may not be previously visible. When there is a large intensity in the diffracted beam there is a corresponding reduction in intensity from the transmitted beam. This explains why feature contrast is extensively improved when using an aperture.

When the TEM is switched into diffraction mode it involves an internal adjustment of the projector lens. Lenses in a TEM use electromagnetic fields to focus the electron beam, behaving similarly to conventional optical lenses. On selecting diffraction mode, the projector lens transfers the image from the back focal plane (converging of rays before the image plane) onto the phosphorus viewing screen. At the back focal plane parallel rays intersected, hence in diffraction mode an array of spots is observed. Each spot corresponds to a specific reflection from a plane within the sample crystal. In standard imaging mode what is observed are reflections from all planes, superimposed on top of each other. Diffraction mode separates these reflections into spots, the spots are located based on their position relative to the incident beam angle. By selecting electrons reflecting from a specific plane, while rejecting others, contrast of specific features is achieved.

Dislocations are only visible when the planes displaced by the dislocations cause diffraction of the electron beam. When a dislocation causes a disturbance in a crystal lattice it is quantified by the Burgers vector, b. When the diffraction condition g is perpendicular to the Burgers vector, $g \cdot b = 0$, the dislocation is not visible in the TEM image. This is called the invisibility criterion [55].

2.1.2. Origin of kikuchi lines in TEM spectra

To align the TEM to obtain a specific diffraction condition, Kikuchi lines are used. When the electron beam is diffracted a grid pattern of spots is observed. The diffraction spots will either fade or become brighter as the crystal orientation is altered, however their location remains fixed. This displays which spots correspond to a plane that is fulfilling the Bragg condition. Kikuchi lines display a different behaviour, unlike the diffraction spots the Kikuchi lines will move across the phosphor screen as the crystal orientation is altered. The contrasting behaviour of diffraction spots and Kikuchi lines stems from their separate sources.

The diffraction spots represent electrons from the incident beam that have been elastically scattered. The Kikuchi lines represent electrons that have been in-elastically scattered and subsequently diffracted.

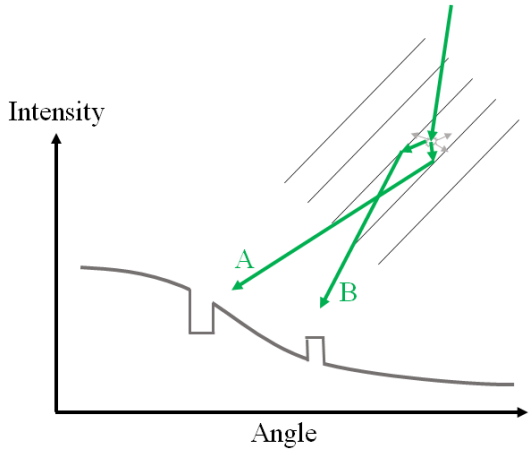

Figure 2.1 Diagram displaying how Kikuchi lines are formed from secondary diffraction of electrons originating from an inelastic scattering event.

When an inelastic scattering event occurs, electrons are produced that have a different wavevector to the incident beam (as depicted in Figure 2.1). Most of these secondary electrons contribute to the background intensity of the diffraction pattern. However, some secondary electrons will fulfil the Bragg condition, diffracting from the planes within which the inelastic source lies. These paths are labelled A and B within Figure 2.1. The impact of A and B on the background intensity is shown in the graph at the bottom of Figure 2.1. One path is lower in intensity and one is higher. These discontinuities within two dimensions form a pair of Kikuchi lines.

2.2. X-ray diffraction (XRD) equipment and theory

X-ray diffraction (XRD) is a non-destructive method for measuring the in and out of plane lattice parameters within a crystal. For the Si, Ge and SiGe used within this thesis, XRD provides the composition, strain and relaxation of each layer within a heterostructure. When fully strained layers are measured, thickness fringes can also provide accurate information on layer thicknesses [56]. This also provides a highly accurate method for calibrating TEM scale bars and thickness calculations. Many comprehensive guides to the aspects of XRD exist [57-59].

The laboratory based XRD measurements were performed on a Panalytical X'Pert PRO Materials Research Diffractometer (MRD). The set up uses a Cu anode, operating at 45 kV and 40 mA. Detailed diagrams of this specific set up including explanations of all features are available from multiple sources [54, 55, 60]. Figure 2.2 displays a diagram of the XRD experimental set up, including the locations of the principal diffraction axes, omega and two-theta. The set up lends itself to the study of layers with varied composition and strain. By using a diffraction and acceptance slit combined with a Ge analyser crystal, a small region of reciprocal space is collected by the detector, this is termed triple axis diffractometry [61]. Through combining multiple ω-2θ scans, for a range of ω values, a section of reciprocal space can be mapped, for example data see Figure 3.5. Reciprocal space is based on a coordinate system where each point in space represents a crystal plane. Performing a Fourier transformation of a crystal lattice produces the reciprocal lattice, for a full explanation see reference [57]. Within reference [57] the Ewald sphere diagram succinctly explains how the geometry for meeting Bragg's diffraction condition works, it displays how an atomic plane within a crystal is

represented by a single point in reciprocal space. See also Figure 2.3 and the following explanation.

Within the lab based XRD conducted, the reflections used are 004 for symmetric measurements and 224 for asymmetric measurements. Si and Ge have a face centred cubic base structure arranged as a diamond cubic crystal structure. To determine which reflections to study during X-ray diffraction, the form factor (scattered intensity for an isolated atom) and structure factor (scattered intensity for a plane of atoms) are combined providing an intensity value, dependent on the reflection condition, for the material in question. These provide the selection rules for the Miller indices of reflections that will be present and those that will be absent or attenuated. It is possible to look up tables that display the relative intensity of the primary reflections for diamond cubic crystals, there are also a set of selection rules for this type of crystal, i.e. that the Miller indices (h, k, l) must be all odd or all even. Also, that (h+k+l) = 4n i.e. a multiple of four will result in twice the intensity of (h+k+l) = 2N+1 and finally that reflections where (h+k+l) = 2N will be absent. Both the look up tables and full derivations of the integrations that produce the selection rules can be found in reference [61], or alternatively in most undergraduate crystal physics textbooks.

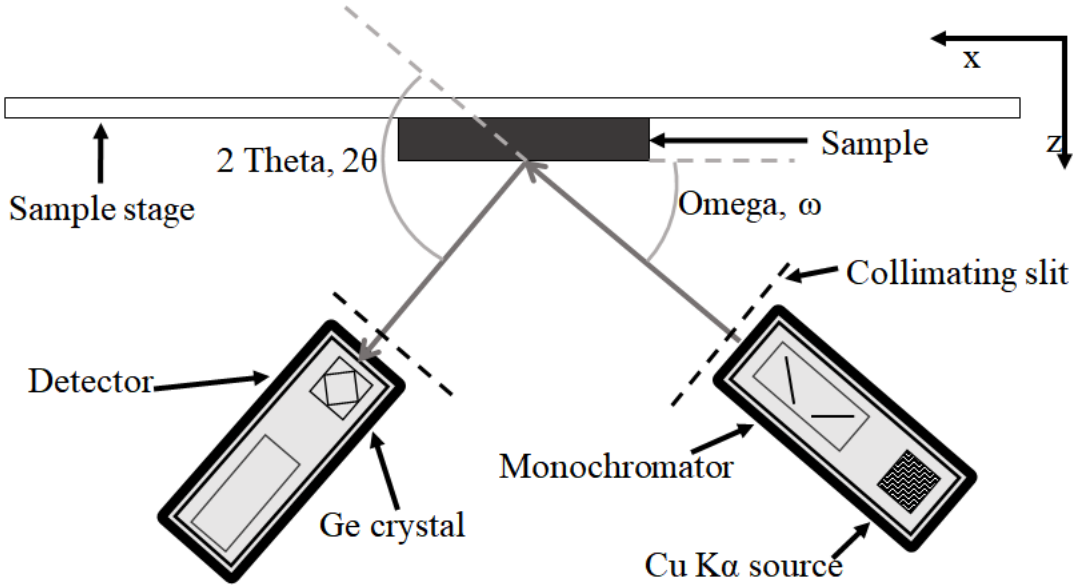

Figure 2.2 Schematic diagram of lab based HR-XRD at the University of Warwick.

Combining reciprocal space maps of symmetric and asymmetric reflections, permits determination of the strain and composition of SiGe alloys. This also permits independent extraction of epilayer tilt. This refers to the angle between the vectors normal to the epilayer and substrate surfaces. For an in depth explanation of the calculations that convert diffraction angles into lattice parameters, with a focus on SiGe alloys, see Capewell [32].

The limitation of lab based XRD is the intensity of the source and following that, the minimum spot size achievable. Measurements requiring high surface resolution, for example studying the suspended microwires within Chapter 4, require μXRD. This involved time granted on beamline B16 at the Diamond Light Source (DLS) facility, on the Rutherford Appleton site. B16 is a bending magnet source operating at 2-25 keV, complete with a five circle diffractometer and Polaris area detector, for more information on the synchrotron and specifically beamline B16 see reference [62]. The high intensity beam at the DLS is focused to the small spot sizes required using beryllium compound refractive lenses (CRL), advantages of the technique can be found here [63], whereas, the original paper containing the first report of CRLs can be found here [64]. It was previously believed that focusing X-ray beams using refractive lenses was unfeasible; however, now the body of work using the technique continues to grow.

μXRD mapping of SiGe islands and nanostructures has already been reported [65-67]. Within lab based XRD, the asymmetric reflection collected was the 224, whereas, at the Diamond synchrotron the asymmetric reflection collected was the 115. By comparing the form factors for each reflection one can calculate that the 224 reflection will return 45% higher intensity than the 115 [61]. The reason for using the 115 at the DLS was an equipment limitation, the large Polaris flight tube was poorly designed for high angle measurements. Fortunately, the X-ray source at the DLS has a very high intensity, meaning the counting times were negligibly affected by using the 115 reflection. There will, however, be a small reduction in accuracy when measuring the in-plane lattice parameter a_x when using the 115 instead of the 224 reflection. This occurs as the 115 is closer to the (001) plane, meaning a larger component of the reflection is out of plane rather than in plane. Ideally one would always use the 224 as the asymmetric reflection for a (001) FCC crystal.

2.2.1. Reciprocal space

Taking a Fourier transform of the crystal lattice returns the reciprocal lattice. Each point in reciprocal space represents a set of crystal planes. The formulas that convert the lattice basis vectors into the reciprocal lattice basis vectors are given below.

$$b_1 = 2\pi \frac{a_2 \times a_3}{a_1(a_2 \times a_3)} \quad (2.2)$$

$$b_2 = 2\pi \frac{a_3 \times a_1}{a_2(a_3 \times a_1)} \quad (2.3)$$

$$b_3 = 2\pi \frac{a_1 \times a_2}{a_3(a_1 \times a_2)} \quad (2.4)$$

Fortunately, as the Ge crystal system is face centred cubic the angle between any of the unit cell lattice vectors are 90°. This makes the value of the cross products in formulas 2.2, 2.3 and 2.4 equal to one, therefore the formula can be simplified to:

$$b_1 = \frac{2\pi}{a_1} \quad (2.5)$$

$$b_2 = \frac{2\pi}{a_2} \quad (2.6)$$

$$b_3 = \frac{2\pi}{a_3} \quad (2.7)$$

The Ewald sphere (displayed in Figure 2.3) is most commonly used to visually display how the diffraction of X-rays from a crystal lattice results in the reciprocal lattice, also how the Bragg condition is fulfilled geometrically.

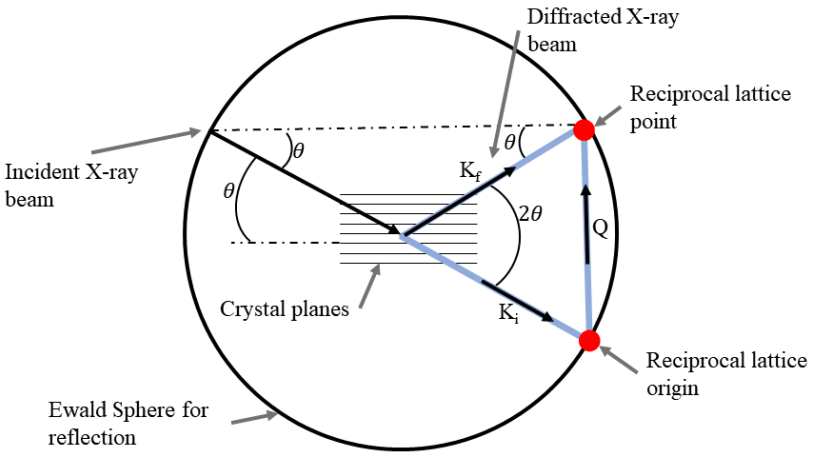

Figure 2.3 The Ewald sphere, displaying the geometric basis of X-ray diffraction.

The Ewald Sphere explains geometrically when the Bragg conditions are met. The sphere is constructed with a radius of $2\pi/\lambda$. The sphere is located with the incident X-rays entering radially. This fixes the origin of reciprocal space on the circumference of the sphere. When a reciprocal lattice point also lies on the circumference (as depicted in Figure 2.3) the Bragg conditions are met, permitting diffraction. The diffraction vectors in Figure 2.3 is equivalent to the diffraction conditions:

$$k_f - k_i = Q \quad (2.8)$$

Where k_f is the diffracted wave vector, k_i is the incident wave vector and Q the scattering vector. This is an equivalent form for the Bragg conditions.

The XRD data is produced by scanning lines through areas of reciprocal space. As shown in Figure 2.2 Omega (ω) describes the angle between the sample surface and the incident beam. While two theta (2θ) describes the angle between the incident and diffracted beam. If a layer is known to be fully strained, a rocking curve measurement can be performed, and composition information can still be extracted. This measurement traces a straight line through reciprocal space, for a symmetric (004) scan Si, Ge and SiGe peaks will all lie on this line in reciprocal space. A rocking curve is conducted by fixing the ratio of $\omega/2\theta$, while scanning around the selected peak. As the scan is conducted the detector will have to move twice as fast as the stage to maintain the fixed ratio. With symmetric scans no information about the in-plane lattice parameter (a_x) is collected. The out of plane lattice parameter (a_z) is dependent on both strain and composition. Therefore, it is only with fully strained layers that one can determine composition with the rocking curve measurements.

2.2.2. Reciprocal space mapping

If the material is partially relaxed a reciprocal space map is required to measure and deconvolute the strain and composition values. Reciprocal space maps are made up of a series of $\omega/2\theta$ scans, taken over a range of ω values

The white region within Figure 2.4 (adapted from [61]) shows the regions of reciprocal space that it is possible to probe for a (001) orientated crystal. The region labelled ω <0 is forbidden,

as to access this reflection the incident beam would have to enter below the surface of the sample. Similarly, the region labelled $\omega > 2\theta$ is a forbidden reflection as the diffracted beam would be required to exit below the sample surface. The upper forbidden region is inaccessible as the X-ray wavelength is too long.

A symmetric (004) scan is performed to calculate the out of plane lattice constant a_z. This also provides a value for the crystallographic tilt of the layers. An asymmetric (224) scan then provides a value for the in-plane lattice constant a_x. With both a_x and a_z the composition and strain of the layer can be deconvoluted and calculated. It is assumed that both in-plane lattice parameters are equivalent (a_x, a_y). This assumption can be made due to the homogeneous in-plane bi-axial relaxation of a cubic crystal. For comprehensive calculations on extracting lattice parameters from a reciprocal space map (RSM) see section 2.2.4 and reference [32].

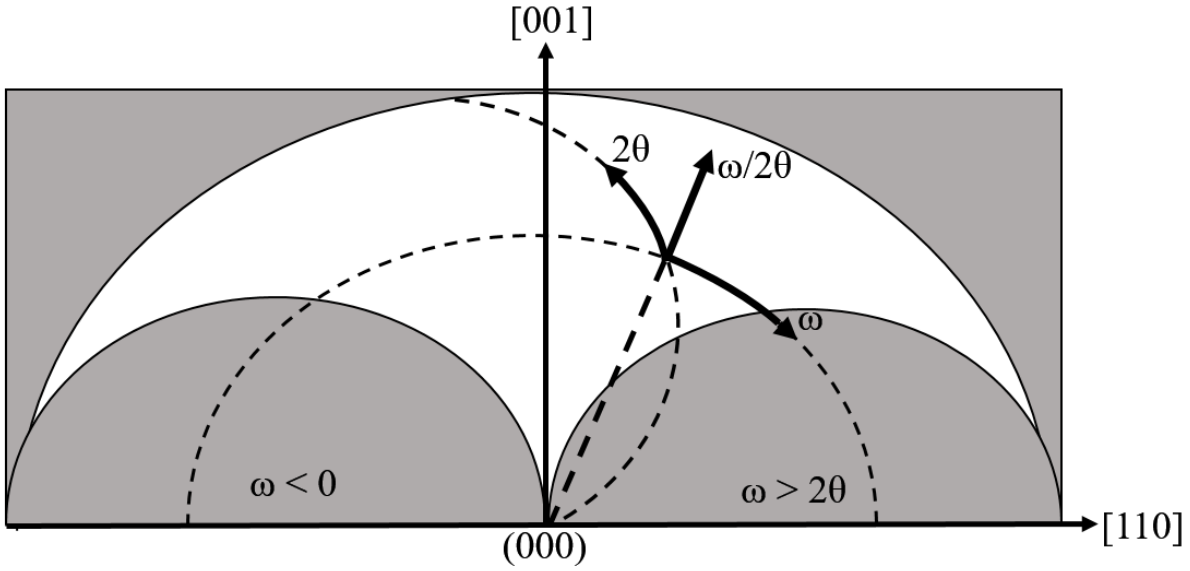

Figure 2.4 Diagram showing how changes in ω, and θ (source and detector angles) translate into movements through reciprocal space. Adapted from [32].

2.2.3. Interpreting reciprocal space map plots

Figure 2.5 provides an example of a typical reciprocal space map plot. This comprises two data sets, the (004) and the (224), displayed on separate axes. The (004) is a symmetric reflection, providing information on the out of plane lattice parameter (normal to the sample surface). If unsure on miller indices and index notation see reference [57]. The key information to be determined from the 004 scan is the presence or absence of crystallographic tilt. This is

when deposited epilayers are not parallel to the sample substrate. Absence of crystallographic tilt is displayed though alignment of peaks in Q_x, within the (004) data.

The (224) data is an asymmetric reflection, as such it contains information on both in plane and out of plane lattice parameters. Using the (004) data one can deconvolute the symmetric aspect from the (224) data, permitting extraction of both the in-plane and out of plane lattice parameters.

The RSM axis are in reciprocal space units, therfore a larger Q_x translates to a smaller in-plane lattice constant, inversley a smaller Q_x translates to a larger in-plane lattice constant. The same holds true for the Q_z axis, only relating to the out of plane lattice constant. The location of the bragg peaks within Figure 2.5 (relative to where a fully relaxed peak is expected to occur for bulk Ge, SiGe and Si) depend on the amount and type of strain within the crystal epilayers.

The Bragg peaks of tensile layers will appear above the black dashed line within Figure 2.5, with compressive layers appearing below. The distance from the dashed line displays the magnitude of the strain present. The black cross between Ge QW and Ge_{buffer} in Figure 2.5 shows

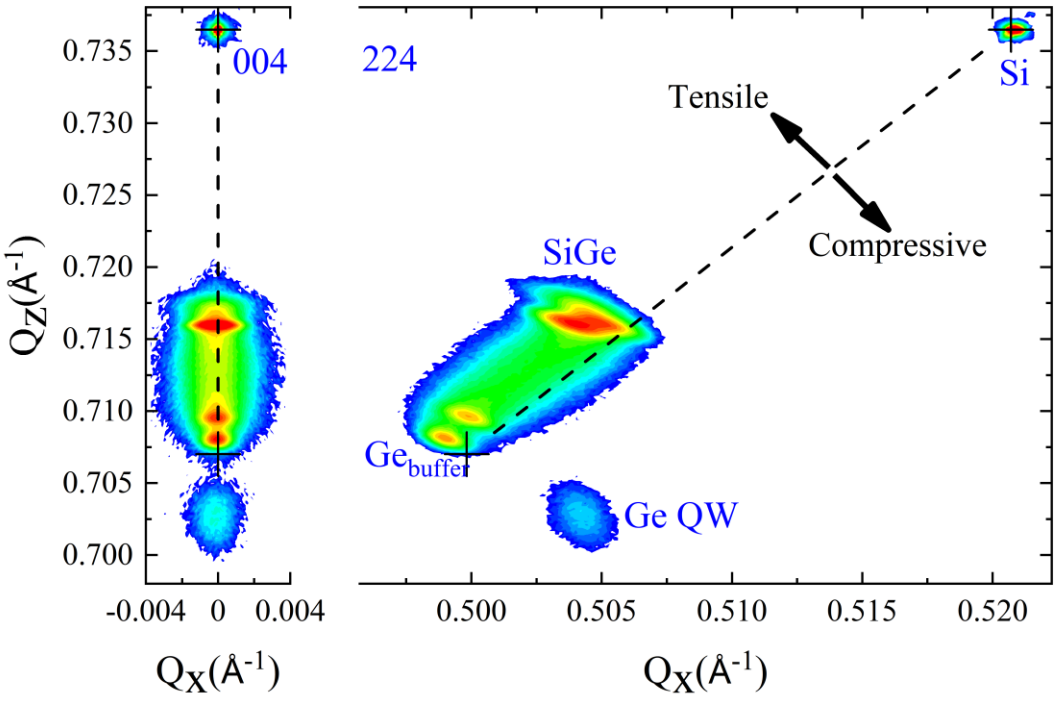

Figure 2.5 Example XRD data of a reciprocal space map. Bragg peaks for SiGe, Ge Buffer layer, Ge quanutm well and Si substrate are labelled. Plot displays a symetric 004 and assymetric 224 scan on separate axis.

where a fully relaxed Ge peak would occur. The QW is below the dashed line, showing that it contains in-plane biaxial compressive strain (I-PBCS). The $Ge_{buffer,}$ depicted above the dashed line contains in-plane biaxial tensile strain (I-PBTS).

2.2.4. Calculating composition and strain using XRD

The key formula that links the measured angle of diffraction to the spacing of atomic planes is the Bragg equation:

$$2d_{hkl}sin\theta = \lambda \quad (2.9)$$

Where d_{hkl} is the spacing between atomic planes, θ the diffraction angle and λ the wavelength of the incoming radiation. There may be crystallographic tilt (ϕ) of the epilayers to be accounted for. This value can be measured from the angular offset between the Si_{sub} and the epilayers. The value of tilt is subtracted from the measured Bragg angle, providing the true diffraction angle for the epilayer:

$$\theta_{epi}^{measured} = \theta_{epi} - \phi \quad (2.10)$$

Where $\theta_{epi}^{measured}$ is the measured Bragg angle, θ_{epi} is the true Bragg angle and ϕ is the tilt of the epilayers with respect to the Si_{sub}.

In-plane compression results in out of plane expansion. This is a measured response, conserving energy and matter. The resultant tetragonal distortion follows Possion's law. During elastic deformation the in and out of plane lattice parameters (a_x and a_z respectively) are related to the relaxed lattice parameter, a(x) by:

$$a(x) = a_x + \frac{1-\upsilon}{1+\upsilon}(a_z - a_x) \quad (2.11)$$

Where υ represents Poisson's ratio. To calculate a_x and a_z, d_{hkl} must be calculated for two non-parallel planes. For FCC cubic crystals this is normally the 004 as a symmetric peak and either the 224 or 115 as an asymmetric peak. The formulas below can be used to calculate the lattice constants, they are simplified by dividing out values for the Si_{sub}. This cancels the terms in 2λ. Measuring relative to Si is useful as the Si_{sub} is known to be fully relaxed.

$$a_z = a_{Si}\left[\frac{sin(\theta_{sub}^{004})}{\sin(\theta_{epi}^{004})}\right] \quad (2.12)$$

And

$$a_x = \left(\sqrt{h^2 + k^2}\right)\left[\frac{\lambda}{2\sin(\theta_{epi}^{224})\sin(\phi)}\right] \quad (2.13)$$

Using the value for the equivalent relaxed lattice constant a(x) calculated in equation 2.11, it is possible to calculate the composition. This is achieved by solving the correction to Vergard's law:

$$a(x) = a_{si}(1-x) + a_{Ge}x + 0.02733x^2 - 0.0278x \text{ Å} \quad (2.14)$$

Relaxation is defined as:

$$\text{Relaxation} = 100 \times \left(\frac{a_x - a_{Si}}{a(x) - a_{Si}}\right) \quad (2.15)$$

If the value of relaxation is above 100% it means the layer is tensile strained. If it is under 100% then it is compressively strained [32, 68].

2.3. Atomic force microscopy

Atomic force microscopy (AFM) uses a thin (20 nm) silicon nitride tip scanned across a sample surface to record a map of the surface morphology. AFM measurements provide a root mean squared (RMS) value for the surface roughness of samples. The Veeco Multimode AFM used within this work provides a resolution of 0.2 nm in Z and 4 nm in x and y. The root mean square (RMS) roughness describes the density of surface features, while the Z range provides information on their magnitude. The tip is located on the end of a thin flexible cantilever. The sample is placed beneath the tip on a piezo stage, allowing precise movement in x, y and z directions. A laser is reflected off the back of the cantilever onto a photo detector, measuring the degree of bending of the cantilever. This provides feedback that can modulate the height of the piezo stage to apply a constant force as the tip scans the sample.

In contact mode, the piezo stage is raised until the sample is in contact with the tip. A constant force is maintained between the tip and the sample while the sample is rastered (the tip remains stationary; the sample is moved) over the area to be mapped. To maintain a constant force the sample stage height (z) is adjusted to counteract features on the sample surface. The changes in Z height are recorded and provide a topological map of the sample surface.

2.4. Post growth device fabrication

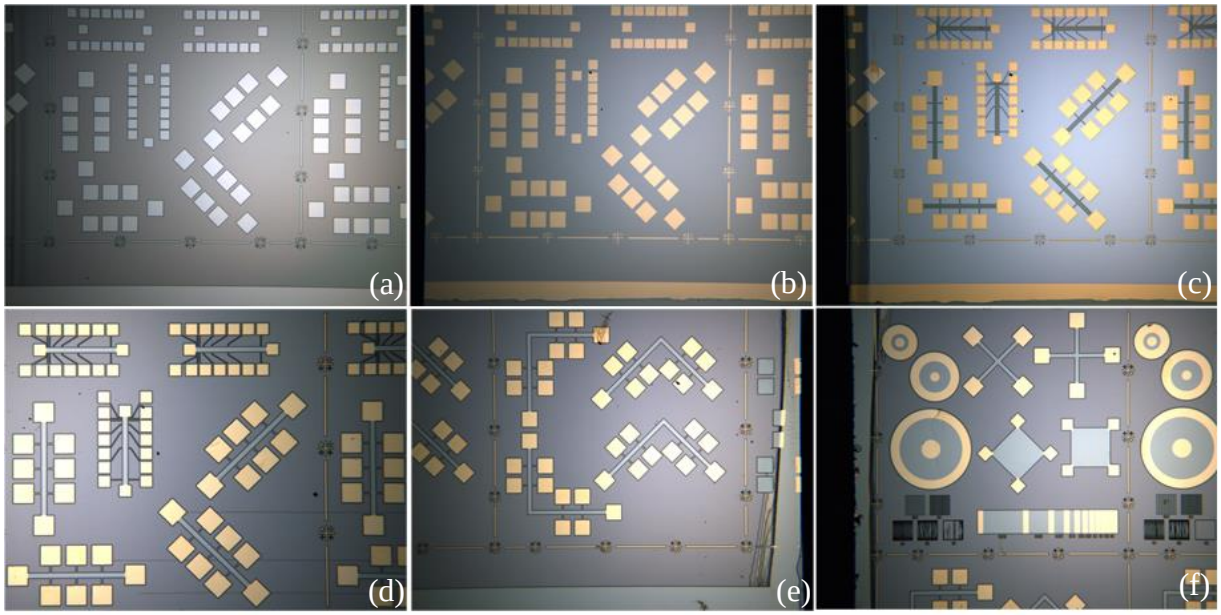

Figure 2.6 Optical images of fabrication steps for producing Hall bars.

Device fabrication was conducted within a class four clean room environment. Optical images of each step are displayed in Figure 2.6 and a table of the steps within the process is shown in Table 2.1. Each contact pad is 200×200 µm.

Process steps	Notes
(a) Prime, spin, bake, expose, reverse bake, flood expose and develop a -ve photo resist (AZ512E) to expose windows for the contact pads.	Sensitive to humidity, failure to open windows fully will result in no contact adhesion.
(b) Argon mill 70 nm, back fill with Al/Ti/Au using E-Beam evaporation. Lift off photo resist in acetone then IPA.	Milling requires calibration, depth varies with SiGe concentration. Rule of thumb is 7 nm per minute at an accelerating voltage of 500 KV
(C) Prime, spin, bake, expose and develop a +ve resist (S1813) to protect mesa.	PR must be >1.5 µm thick to prevent dry etching removing all photoresist, exposing mesa to etch.
(d, e, f) Dry etch material surrounding mesa down to the Si_{sub}, remove photoresist using acetone then IPA.	If ICP etching hardens photo resist, warm N-Methyl-2-pyrrolidone (NMP) provides an aggressive resist stripper.

Table 2.1 Process steps for fabricating a Hall bar geometry device. Letters within brackets link explanations to optical images within Figure 2.6.

The optical images of Hall bar fabrication display the array of devices contained on the Hall bar mask. These include repeats of Greek cross, TLM, CTLM, L shaped Hall bar, VDP and Hall bar geometry with varied spacing between the contact arms. TLM and CTLM devices provide the contact resistance deconvoluted from the material resistance, L shaped Hall bars asses orientational asymmetry of transport properties while unequivocally maintaining an identical current in both surface orientations, finally the Hall bar and VDP devices facilitate Hall and resistivity measurements. After using this mask, the advice for designing a new mask would be to have groups of devices. Each group would contain one of each type. For example, a Hall bar next to a Greek cross a CTLM and a TLM. This provides the advantage of being able to test different geometries and validate the contact quality with one small piece of wafer. It is also indisputable that the TLM and Hall bar received identical processing steps. Having a mask where devices are grouped by type means that TLMS to check contacts and Hall bars to test devices are on separated pieces of wafer. Even though every care is taken to repeat identical fabrication on each sample it cannot be indisputably proved.

Chapter 3. Optimisation of buffer layers

Progress with FQHE observations relies on continued development of sample fabrication. This requires high quality 2D systems, a process demanding improvement to existing buffer layer technology. This chapter is focussed on investigating the possibility of thinner buffer layers (<1μm), facilitating the deposition of high Ge content ($x > 0.5$) $Si_{1-x}Ge_x$ layers onto Si (001) substrates.

Advances with high-K dielectric integration on germanium has sparked renewed efforts developing advanced Ge MOSFET devices [69, 70]. The fields of germanium based spintronics and photonics are also constantly expanding [71]. Aspects of these growing fields require fabrication of low dimensional structures, post heterostructure deposition. In the field of low dimensional systems, thinner buffer layers are particularly advantageous. This provides one motivation for attempting to produce thinner buffer layers ideally with comparable quality to current, thicker buffer layers (>3μm). Other motivations behind thinner buffer layers include increased heat dissipation and avoiding microcracks [72-76]. The work within this chapter aims to investigate the impact of different growth temperatures and post annealing steps to increase threading dislocation mobility, with a final goal of producing a buffer layer that is thinner while maintaining comparable crystal quality.

Constant composition SiGe on Si, with the lowest RMS roughness and TDD, are currently grown at temperatures <600° C and are subjected to multiple annealing cycles increasing relaxation and promoting defect interaction [77]. The literature on high Ge content ($x > 0.5$) $Si_{1-x}Ge_x$ is limited, due to the large lattice mismatch with commonly used Si substrates. Constant composition SiGe on Si suffers from dislocation pile up and pining, this leads to only partial relaxation being achieved (<85%), prohibiting a fully relaxed layer [55]. The buffer layers within this chapter use an intermediate Ge_{buff} to reduce the lattice mismatch, at the SiGe heterointerface, and absorb many of the misfit dislocations. The Ge_{buff} should act to reduce the dislocation pile up making relaxation within higher Ge content, constant composition, SiGe layers possible.

3.1. Annealing study on thin SiGe/Ge/Si buffer layers

The basic layer structure, for all samples in this chapter, is shown in Figure 3.1. An industry standard Si (001) wafer is loaded into the RP-CVD system. A 100 nm Ge layer is initially deposited, this aspect separates this work from other published studies. Predominantly, attempts at a constant composition SiGe buffer on Si deposits SiGe directly onto Si. The lattice mismatch in this case induces compressive strain which needs to be relaxed via dislocations. The growth plan here however deposits an almost fully relaxed intermediate Ge layer. Now, lattice mismatch acts to induce tensile strain within the SiGe layer, this also requires relaxation via defects. It is known that tensile strain aids in reducing surface roughening [35]. The insertion of the Ge underlayer should aid in reducing surface roughening.

$Si_{1-x}Ge_x$ at 650	400 -1000 nm
Ge	~100 nm
p^- (1-30 ohm cm) - Si (001)	

Figure 3.1 Basic layer structure for thin buffer layer study. Si (001) wafer is loaded into the RP-CVD. Intrinsic Ge is deposited followed by varied compositions and thicknesses of SiGe. Individual parameters for each sample are displayed within Table 3.1 labelled by the corresponding sample number.

Figure 3.2 is included to show the method and trend returned when calibrating SiGe composition. The samples that provide the results of Figure 3.2 are all thin, fully strained SiGe grown at low temperatures. The SiGe is deposited onto Si (001) substrate with an intermediated 600 nm Ge_{buff} layer. Fully strained SiGe is used for this calibration as it makes extracting the composition and thickness values using XRD easier and faster. Fully strained layers only require a single rocking curve to determine an accurate composition and thickness. The results in Figure 3.2 show how thickness and SiGe composition vary when Ge precursor flow is fixed while the Si precursor flow is incrementally increased. During CVD growth each desired composition is tuned individually, however collecting plots such as Figure 3.2 give a good starting point for beginning composition calibration. The parabolic fits are only added as a guide for the eye.

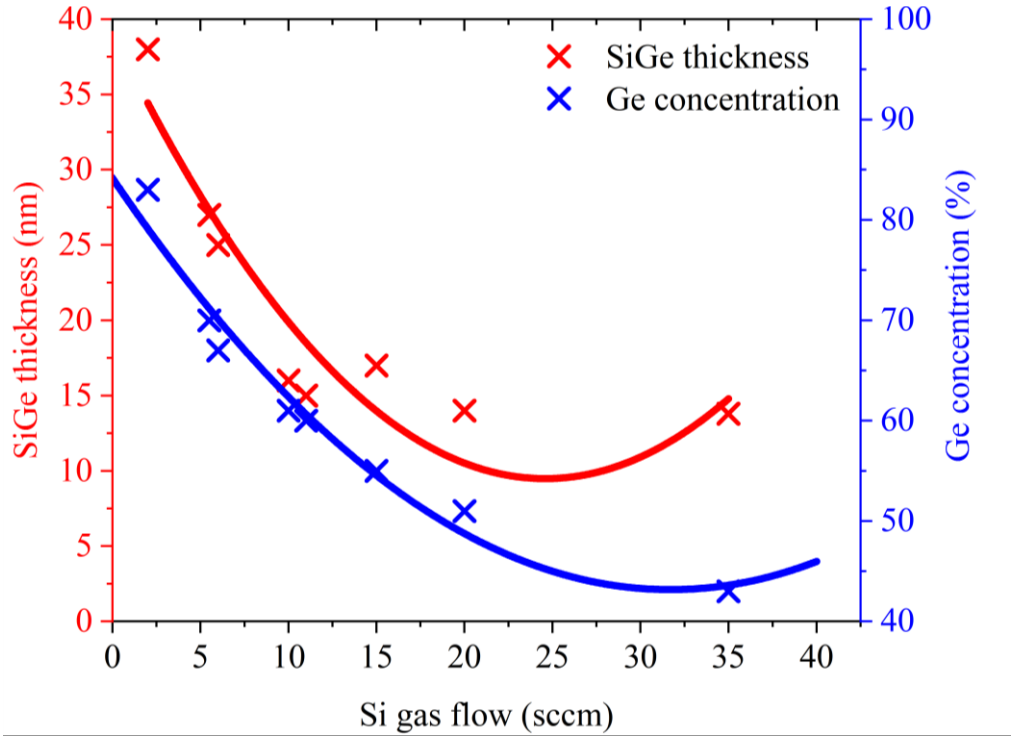

Figure 3.2 Low temperature, fully strained SiGe. Samples 17-278, 280, 281, 282, 283, 284, 17-304, 306. Si Gas flow vs SiGe thickness and Ge concentration.

Table 3.1 lists the incremental variations on the basic growth plan. Material characterisation results are listed beside each sample number. Samples are ordered into four groups with each group focussed on investigating one aspect of buffer layer fabrication. RMS roughness values were extracted using atomic force microscopy measurements. The composition and relaxation values are extracted through XRD reciprocal space mapping, using the method as described in section 2.2.4

	Sample	Composition	Growth temperature (°C)	Growth time (s)	Anneal Temperature (°C)	RMS roughness (nm)	SiGe Relaxation (%)
Group 1	17-074	$Si_{0.20}Ge_{0.80}$	650	129	700	5	109
	17-075	$Si_{0.03}Ge_{0.97}$	650	129	800	6	108
	17-076	$Si_{0.21}Ge_{0.79}$	650	129	900	3	108
	71-077	$Si_{0.21}Ge_{0.79}$	650	129	-	2	108
	17-078	$Si_{0.28}Ge_{0.72}$	650	189	700	3	109
	17-079	$Si_{0.28}Ge_{0.72}$	650	189	800	4	109
	17-080	$Si_{0.29}Ge_{0.71}$	650	189	900	3	109
	17-081	$Si_{0.29}Ge_{0.71}$	650	189	-	2	110
	17-082	$Si_{0.45}Ge_{0.55}$	650	600	700	3	109
	17-083	$Si_{0.45}Ge_{0.55}$	650	600	800	4	109
	17-084	$Si_{0.45}Ge_{0.55}$	650	600	900	4	109
	17-085	$Si_{0.45}Ge_{0.55}$	650	600	-	2	108
Group 2	16-067	$Si_{0.08}Ge_{0.92}$	650	120	-	3	106
	16-068	$Si_{0.19}Ge_{0.81}$	650	120	-	4	108
	16-069	$Si_{0.26}Ge_{0.74}$	650	120	-	11	108
	16-070	$Si_{0.30}Ge_{0.70}$	650	120	-	13	110
	16-077	$Si_{0.29}Ge_{0.71}$	650	80	850	7	110
	16-078	$Si_{0.20}Ge_{0.80}$	650	80	850	3	109
	16-079	$Si_{0.11}Ge_{0.89}$	650	80	850	2	106
	16-080	$Si_{0.33}Ge_{0.67}$	650	120	850	10	106
	16-081	$Si_{0.35}Ge_{0.65}$	650	120	850	15	109
	16-115	$Si_{0.20}Ge_{0.80}$	850	80	-	3	106
	16-116	$Si_{0.11}Ge_{0.89}$	850	80	-	3	108
	16-139	$Si_{0.24}Ge_{0.76}$	850	120	850	10	112
	16-140	$Si_{0.20}Ge_{0.80}$	850	120	850	3	107
	16-142	$Si_{0.25}Ge_{0.75}$	850	120	850	4	109
	16-207	$Si_{0.20}Ge_{0.80}$	550	120	-	3	108
	16-208	$Si_{0.14}Ge_{0.86}$	550	120	-	9	105

Group 3	17-226	$Si_{0.30}Ge_{0.70}$	650	900	700	-	105
	17-227	$Si_{0.20}Ge_{0.80}$	650	900	700	-	103
	17-228	$Si_{0.10}Ge_{0.90}$	650	900	700	-	103
	17-229	$Si_{0.39}Ge_{0.61}$	650	900	700	-	105
	17-230	$Si_{0.46}Ge_{0.54}$	650	900	700	-	106
	17-231	$Si_{0.50}Ge_{0.50}$	650	900	700	-	106
	17-232	$Si_{0.56}Ge_{0.44}$	650	900	700	-	104
Group 4	17-029	$Si_{0.10}Ge_{0.90}$	650	600	-	<2	103
	17-030	$Si_{0.21}Ge_{0.79}$	650	600	-	<2	103
	17-031	$Si_{0.29}Ge_{0.71}$	650	600	-	<2	105
	17-032	$Si_{0.39}Ge_{0.61}$	650	600	-	<2	105

Table 3.1 Material characterisation results for samples from groups one to four. Composition and relaxation values determined from XRD reciprocal space mapping, RMS surface roughness determined by AFM measurements. 105% relaxed refers to over relaxation, therefore a layer that contains 5% tensile strain.

3.1.1. Annealing data plots for thin SiGe/Ge/Si buffer layers

Annealing is reported to reduce TDD within both group IV and III-V materials [78-81]. Annealing increases the velocity of dislocations leading to increased annihilation events. The aim remains to produce thinner (<1 µm) fully relaxed SiGe buffer layers on Si (001) substrates. To pursue this goal 12 samples (group 1) were produced following the growth plan displayed in Figure 3.3.

The bar chart within Figure 3.3 displays the relaxation of the SiGe layer with respect to the Si_{sub}. Relaxation values were measured using X-ray diffraction. Relaxation values were calculated from 004 and 224 Bragg reflections, using Expert Epitaxy software (method as described in section 2.2.4). All 12 samples are produced in the layer structure shown in the top right of Figure 3.3. Each anneal was carried out for a duration of five minutes within the RP-CVD chamber, after material deposition. All SiGe layers are 400 ± 100 nm in thickness, with some thickness variation occurring for samples of different composition. The thickness of samples with identical composition was comprehensively calibrated previously (data not shown here), this was achieved by capturing TEM images of multilayer samples, within which each

layer represents a different growth time. Thickness values for the samples within Figure 3.3 were verified using FTIR measurements. This also gave a thickness uniformity value for the four-inch wafers. The FTIR measurements use an automated wafer stage to record 32 sample locations arranged in a cross geometry, this gave an average uniformity of between 2 and 5% for the group 1 wafers. For each composition three annealing temperatures of 700, 800 and 900 °C were tested. There was also a control sample for each composition, where no annealing was conducted.

The results are displayed in Figure 3.3. For all compositions and annealing temperatures 11 of the 12 samples show 1% variation in relaxation, with no clearly identifiable pattern or trend. With all 12 samples displaying <2% variation. Compared to results for high Ge content SiGe on Si (001) [82], achieving 101-109% strain relaxation in a 400 nm SiGe buffer layer is already a notable achievement, the goal however remains 100% relaxation. When first developing the Ge underlayer it was possible to achieve a wide range of compressive and tensile relaxation by

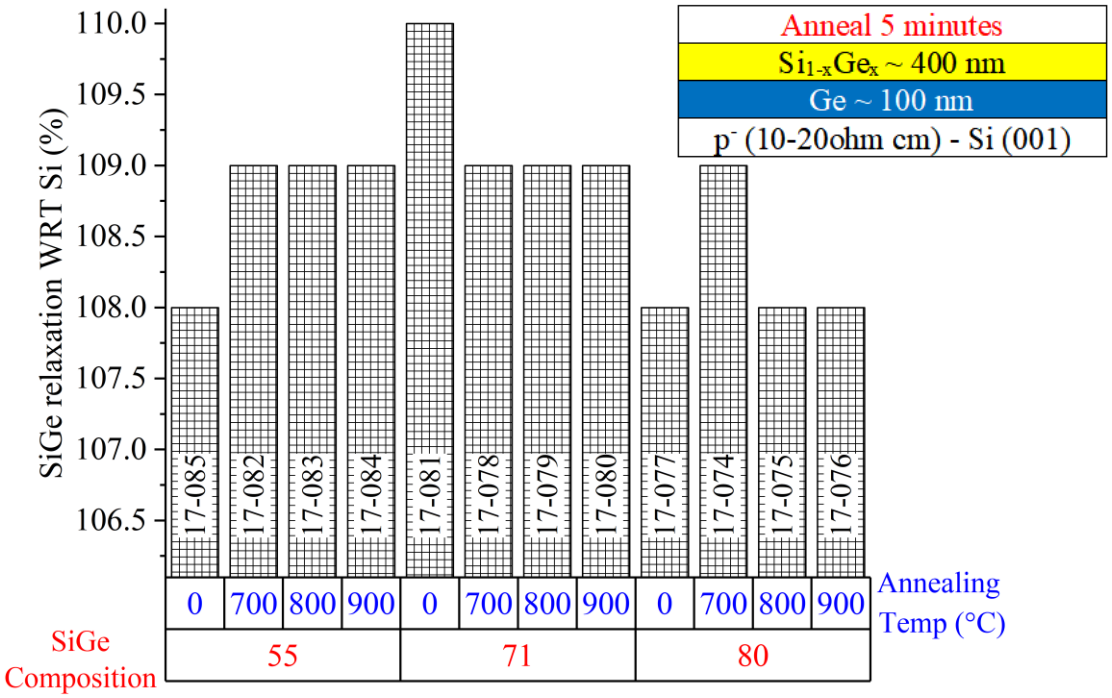

Figure 3.3 Basic layer structure of all samples within Group 1 (top right). Relaxation of SiGe layers WRT Si are measured by XRD and displayed on the Y axis. Multiple compositions of SiGe are included with 55, 71 and 80% Ge content (Centre left). Each composition was annealed at three different temperatures. Annealing temperatures of 700, 800 and 900° C are tested including an unannealed control sample.

varying the temperature, precursors and growth times [55, 83]. When attempting to reproduce this by varying the same parameters for SiGe/Ge/Si (001) it seems the SiGe strain state is unresponsive. The group 1 samples provide a bench mark, attempts to push the relaxation further within the thin buffer layers is presented in the results for subsequent groups.

The data for group 2 samples (as listed in Table 3.1) is displayed in Figure 3.4. The aim for group 2 was to investigate if changing the SiGe growth temperature would render the SiGe material more responsive to the post growth annealing. As shown in Figure 6.3 both higher (850° C) and lower (550° C) growth temperatures have been trialled, for varied SiGe compositions. Half the samples have been subjected to a five minute anneal at 850° C while the remaining half are as grown. Another change introduced within group 2 was to increase the thickness of the SiGe layers to 700 ± 100 nm. Overall group 2 produced more promising results, with an increase in the average relaxation wrt Si (001). The improvement in relaxation occurred for all samples regardless of annealing treatment or growth temperature, this suggests that the improvement is due to the increased thickness to 700 ± 100 nm aiding in relaxing the induced strain. Figure 3.4 displays that the annealing is still not providing any clear assistance in relaxing

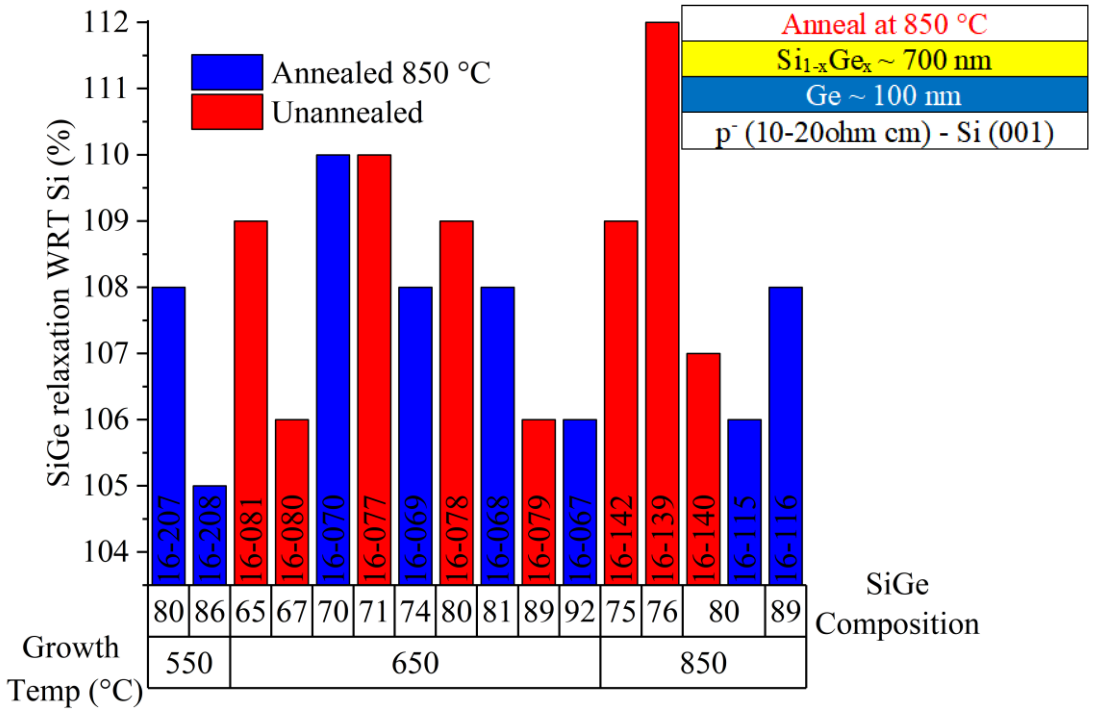

Figure 3.4 Group 2, Relaxation of SiGe wrt Si (001) as measured by XRD. Samples include varied growth temperature of SiGe and varied composition of SiGe. Red columns were annealed at 850° C for 5 minutes, blue columns are un-annealed.

the SiGe material. This is regardless of varying the composition or growth temperature of the material. Comparing annealed and un-annealed samples, with similar ±1% composition and identical growth temperatures, shows that annealing at 850° C returns identical or less relaxation of the SiGe layer. Within these growth conditions the results show that annealing either has negligible or a detrimental impact on strain relaxation, with the tensile strain value often being increased by the annealing step.

The example XRD data in Figure 3.5 displays the peak positions of each layer within reciprocal space, from which tilt, composition and strain of the Si, SiGe and Ge layers can be determined. The symmetric scan (left) shows the absence of tilt within the layers, recognisable by the alignment of all Bragg peaks in the vertical Q_x plane. In the asymmetric scan (right) the black line and red cross have been added for visual clarity. The red cross shows the location where fully relaxed crystalline germanium would appear. The cross is almost located at the centre of the measured germanium Bragg peak in Figure 3.5, displaying that the 100 nm Ge layer grown directly onto the Si_{sub} is almost fully relaxed. This is challenging to achieve as the closer a layer is to full relaxation the less energy there is to drive defect motion. Calculations show that the Ge layer includes 1% tensile strain. This is due to thermal expansion mismatch between Si and Ge. The angled black line is added to show the region that a fully relaxed SiGe

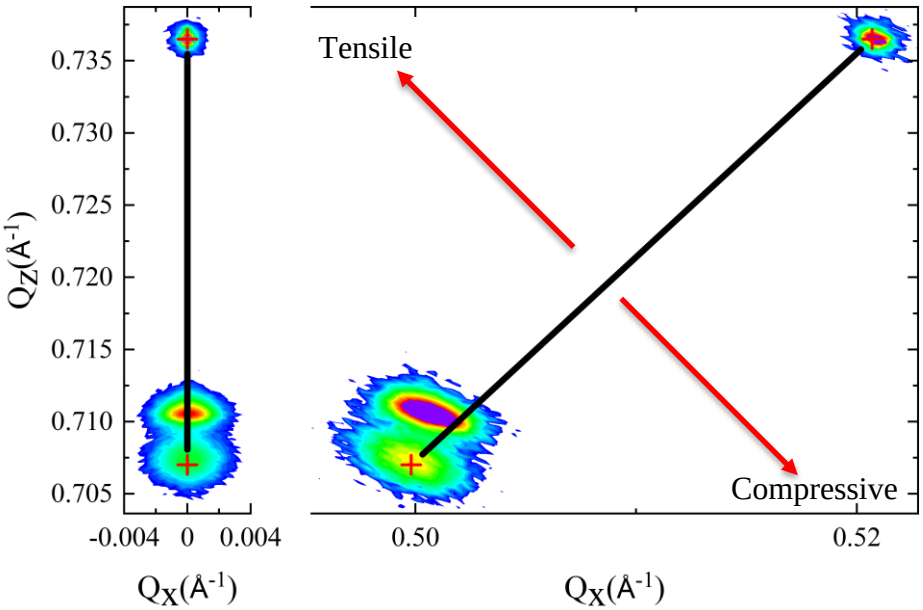

Figure 3.5 XRD data for sample 16-067, (left) symmetric 004 reflection. (right) asymmetric 224 reflection. SiGe grown at 650 ˚C.

alloy would occupy on the plot. Tensile strained SiGe peaks will appear above the black line and compressively strained peaks below the line, as indicate by the labels. For this SiGe sample grown at 650° C, with no annealing, the result is tensile strained SiGe. The exact composition is calculated as $Si_{0.08}Ge_{0.98}$, as is shown in Table 3.2. This data for sample 16-067 is primarily shown as a comparison for the following data of sample 16-115.

Sample 16-115 is an identical layer structure as 16-067, with similar composition, but the growth temperature has been increased from 650 to 850° C. From Figure 3.6 it is observed that the higher growth temperature did not induce additional strain relaxation within the SiGe peak. Analysis performed within the X-pert Epitaxy software package shows that growth at 650° C and 850° C both produce a SiGe layer with 6% residual tensile strain. The marked change that has occurred when growing the SiGe at the higher temperature of 850° C is displayed by the Ge underlayer. It appears the Ge has undergone an increase in tensile strain, observed as an increase in Q_z within Figure 3.6. This is justifiable, due to the thermal mismatch between the Ge and the Si_{sub}. Further investigation via TEM displays that the Ge layer has suffered inter-diffusion, caused by increasing the overall thermal budget.

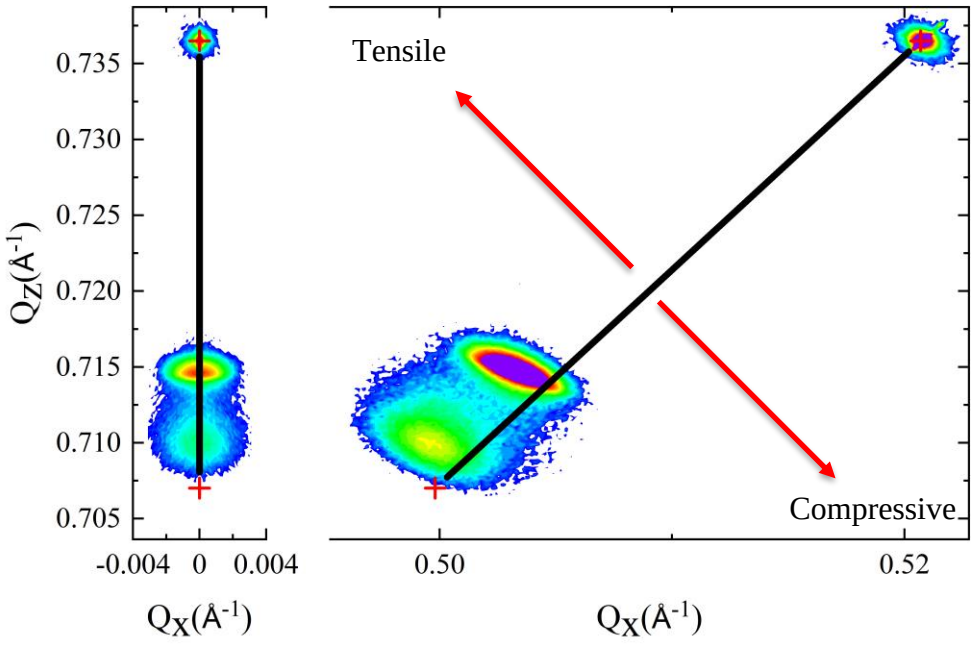

Figure 3.6 XRD data for sample 16-115 (left) symmetric 004 reflection. (right) asymmetric 224 reflection. SiGe grown at 850° C. Counting time increased from one to three seconds per point, to counter reduced diffracted beam intensity.

The atomic resolution TEM images, within Figure 3.7, show the Ge layer is no longer a uniform layer with well-defined interfaces. The counting time for XRD measurements had to be increased from one second to three seconds. This was required to counteract the reduction in diffracted beam intensity, caused by the intermixing of the Ge layer. Increasing the thermal budget for the structure, by increasing the growth temperature of the SiGe layer, has caused inter-diffusion. Work on Ge-Si inter-diffusion has been conducted previously [84], this work predominantly focused on thin (11 nm) multilayer structures. Therefore, what we have observed is that there is a critical temperature between 650 and 850° C. Exposing the ~ 100 nm Ge layer to this critical temperature during SiGe growth combined with a two minute anneal, causes the Si to diffuse into the Ge. The TEM images from the lower growth temperature SiGe layers are displayed in Figure 3.8.

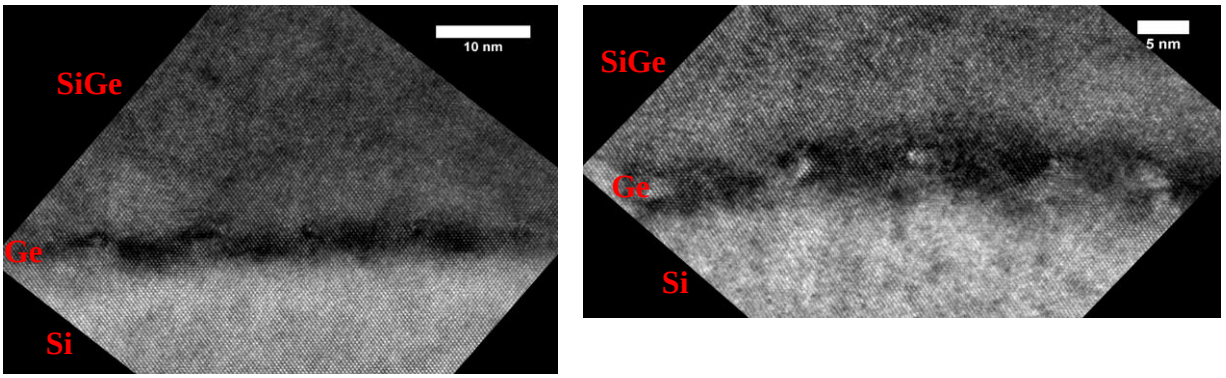

Figure 3.7 TEM images of sample 16-115. Images highlight inter-diffusion of Ge underlayer with surrounding material. Interdiffusion caused by raising SiGe growth temperature from 650 to 850° C.

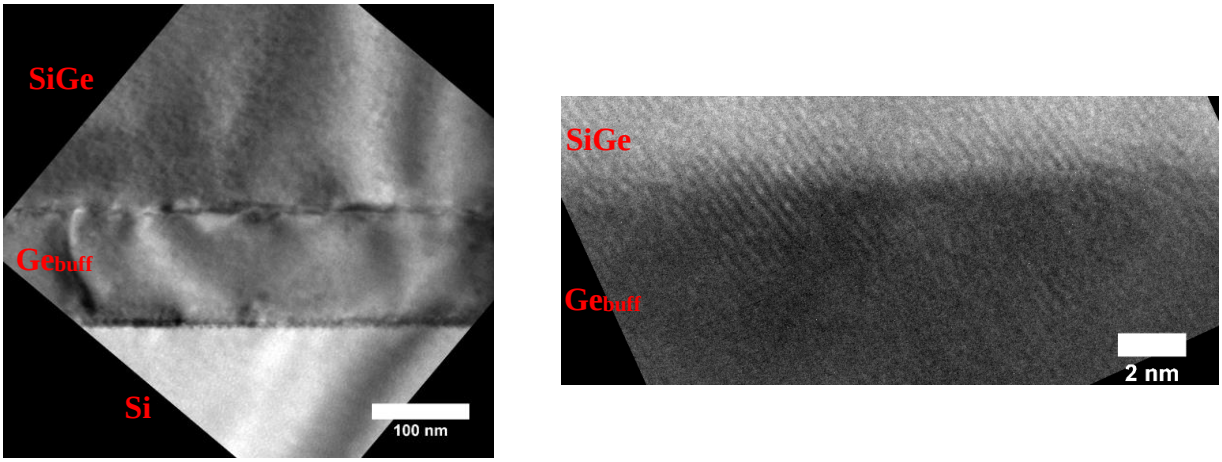

Figure 3.8 TEM images of sample 16-067. Images highlight higher quality Ge-SiGe interfaces generated by the lower (650° C) growth temperature of the SiGe layer.

The TEM images presented in Figure 3.8 display the Ge/SiGe interface grown at the lower growth temperature of 650° C. These images confirm that the lower growth temperature preserves the high-quality interface characteristics, in contrast to the high temperature growth shown in Figure 3.7. The atomic resolution image (right) shows atomic planes continuing across the interface between the Ge and SiGe.

Further investigation shows that all samples, from groups 1 and 2, annealed at 800, 850 and 900° C show intermixing between the Si and Ge layers. Increasing temperature causes increased interdiffusion, all 800° C anneals mix the Ge layer producing a SiGe layer with $95 \pm 1\%$ Ge concentration, whereas a 900° C anneal causes greater Si-Ge intermixing producing an $84 \pm 2\%$ Ge content SiGe layer. The post deposition annealing steps performed are clearly causing intermixing within the heterostructure and removing the strong compositional interface between the Ge and SiGe. This will also be affecting the large misfit dislocation network that previously resided at this interface. It is striking that this severe intermixing has had such a minor impact on the relaxation of the SiGe layer above the Ge. It is also observed in the atomic resolution images of Figure 3.8 that the SiGe lattice is highly crystalline and relatively unaffected by the intermixing beneath it. There are applications, particularly in photonics where the underlying Ge_{buff} layer is problematic. Without the Ge layer, 86% relaxation and above for high Ge content SiGe on Si (001) is highly challenging. If annealing breaks up the uniform Ge_{buff} layer without negatively impacting the SiGe layers above this could prove to be a useful technique, presenting the heterostructure design as suitable for photonics applications. It would be pertinent to investigate what happens to the mismatch induced strain between the SiGe and Ge layers when the Ge undergoes large intermixing post deposition. Depositing various thicknesses of Ge, between SiGe and Si (001), then annealing until thoroughly intermixed provides a new style of grading. This would be highly controllable. An advantage could be that the system will always find its lowest energy configuration.

Figure 3.9 shows group 3 where the growth time has been kept constant at 15 minutes and the composition has been varied. The lower growth temperature of 650° C has been selected along with the lowest annealing temperature of 700° C. These conditions were not observed to cause intermixing within groups 1 and 2. The corresponding increase in thickness that is caused

by changing the precursor ratios is also included on the x-axis. The results in Figure 3.9 confirm what we already knew, that thicker growth layers provide better relaxation.

Table 3.3 is presented for a direct comparison between selected samples from groups 1 and 3. All samples within Table 3.3 experienced the same growth conditions (650° C) and annealing temperature (700° C). Group 3 displays higher average relaxation of SiGe, when compared to groups 1 and 2. This is true for samples 17-230, 17-231 and 17-232 which are thinner than the samples within groups 1 and 2. An aspect of group 3 is providing increased SiGe relaxation when compared to earlier groups. Comparing all the results for both groups the strong differential factor is that the Ge underlayer has a higher relaxation % for the improved group 3. Samples 17-227 and 17-228, although displaying the greatest thickness, importantly also contain compressively strained Ge underlayers. Interestingly the compressive Ge_{buff} layers do not increase the RMS roughness for sample 17-227 and 17-228, which is the common reason to avoid compressive underlayers.

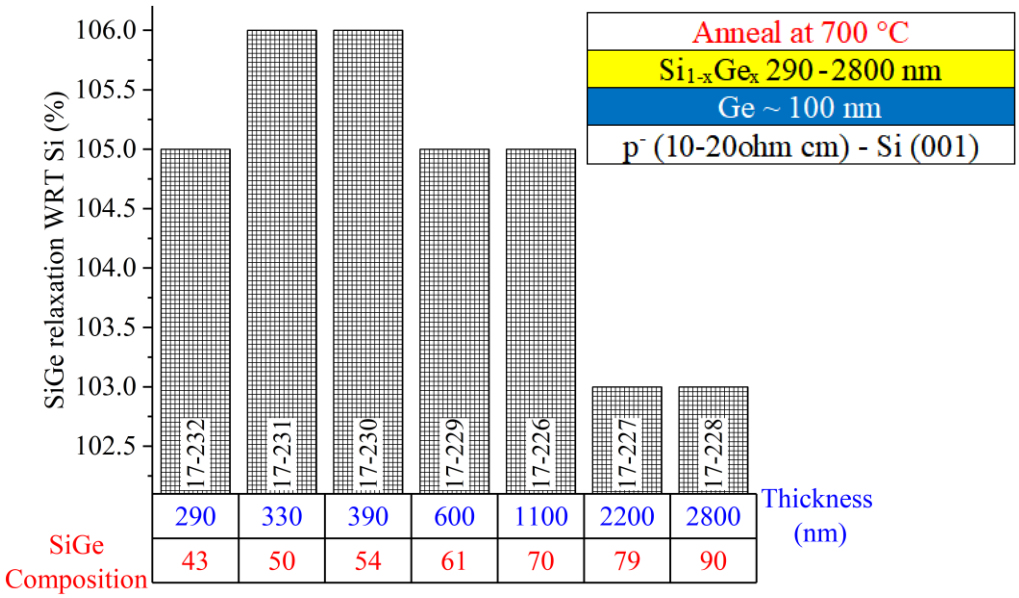

Figure 3.9 Group 3, All samples annealed at 700° C for 5 minutes, SiGe composition is varied from 43% Ge up to 90% Ge. SiGe growth time is kept constant at 15 mins but thickness is varied due to changes in composition.

	Group 3			Group 1
	17-230	17-231	17-232	17-082
Composition	$Si_{0.57}Ge_{0.43}$	$Si_{0.50}Ge_{0.50}$	$Si_{0.46}Ge_{0.54}$	$Si_{0.45}Ge_{0.55}$
SiGe thickness (nm)	290	330	390	400
SiGe relaxation (%)	105	106	106	109
Ge relaxation (%)	100	100	100	104
Ge thickness (nm)	60	80	70	100

Table 3.3 Direct comparison of selected samples from groups 1 and 3. Aim is to highlight the assistance that a compressively strained Ge underlayer could provide in relaxaing the subsequent SiGe epilayer. The SiGe within the group 3 samples is thinner, however, they display increased relaxation when compared to the samples from group 1.

Table 3.3 shows by direct comparison of samples with equivalent growth and annealing conditions, the advantages of increased relaxation within the Ge_{buff} layer. Tensile strained Ge_{buff} layers appear detrimental to the relaxation of the subsequently deposited SiGe.

The results for Group 4 are displayed in Figure 3.10. The aim of this group was to validate the theory that a compressively strained intermediate Ge_{buff} layer, between the Si_{sub} and SiGe layer, assists in reducing the tensile strain within the SiGe epilayer. All the Ge_{buff} layers within the samples of group 4 contain 3% compressive strain, giving a relaxation value of 97%. The results are shown in Figure 3.10. The results show that a consistently high level of SiGe relaxation is shown for all four samples, unlike the variation and up to 10% tensile strain we observed in groups 1 and 2. Comparing sample 17-032 from Group 4 to sample 17-229 in group 3 provides a promising result. The SiGe layer within 17-032 (with a compressive Ge_{buff}) is 100 nm thinner and displays an equivalent relaxation, without the 700° C anneal.

Comparing sample 17-030 to sample 17-227 is another example of the advantage of a compressive Ge_{buff} layer. Sample 17-030 is 800 nm thinner yet displays the same level of relaxation, the key difference being that sample 17-030 has a 3% compressive Ge layer beneath whereas 17-227 has a 100% relaxed Ge_{buff} layer beneath. An important parameter to check is the surface roughness, historically compressive underlayers have been avoided due to the predicted increase in RMS roughness. AFM measurements on all samples within group 4 display a sub 2 nm RMS roughness, the true value was lost within the resolution limitations of the AFM. This displays that either the 3% compressive strain within the Ge_{buff} is not increasing surface roughness, or that subsequent tensile strained SiGe layer is counteracting any increase in roughness. Whichever possibility is true, the compressively strained Ge_{buff} is demonstrated as an effective method for relaxing a SiGe layer on a Si (001) substrate.

The difficulty in reducing the tensile strain within the SiGe layers is interpreted in the following way: The lattice mismatch strain between SiGe and Ge is imparting tensile strain within the SiGe. The thermal mismatch strain is also imparting tensile strain within the SiGe. With both factors providing tensile strain into the SiGe layer it is difficult to fully relax the SiGe without using thick layers. We developed techniques to relax the Ge on Si_{sub} with buffer layers thinner than 100 nm. This was made possible because the Ge is given tensile strain from thermal mismatch but compressive strain from lattice mismatch (with Si_{sub}). By balancing the two effects

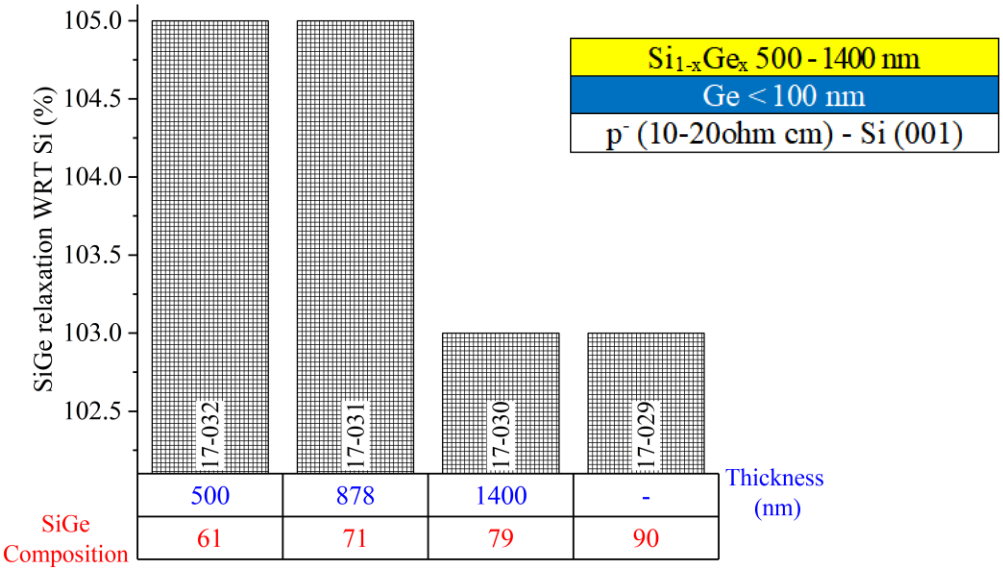

Figure 3.10 Group 4, SiGe relaxation wrt Si all samples grown at 650° C without annealing. The key feature for this group is that all samples contain a Ge_{buff} layer with 3% compressive strain.

the Ge can be relaxed using thin layers. This presents two options for further improvements with the SiGe relaxation. Either work on reducing the thermal mismatch by using lower temperature growth, alternatively produce a further relaxed Ge underlayer perhaps even a compressively strained Ge underlayer. The Ge_{buff} layers within Figure 3.3 all contained ~4% tensile strain. Further relaxed Ge will provide the SiGe with an equivalent situation to the one that achieved 100% relaxed 100 nm Ge on Si_{sub}. The lattice mismatch from compressively strained Ge will impart compressive strain within the SiGe while the thermal mismatch from the Si (001) underlayer will impart tensile strain. By balancing the two effects thin relaxed SiGe layers can be produced.

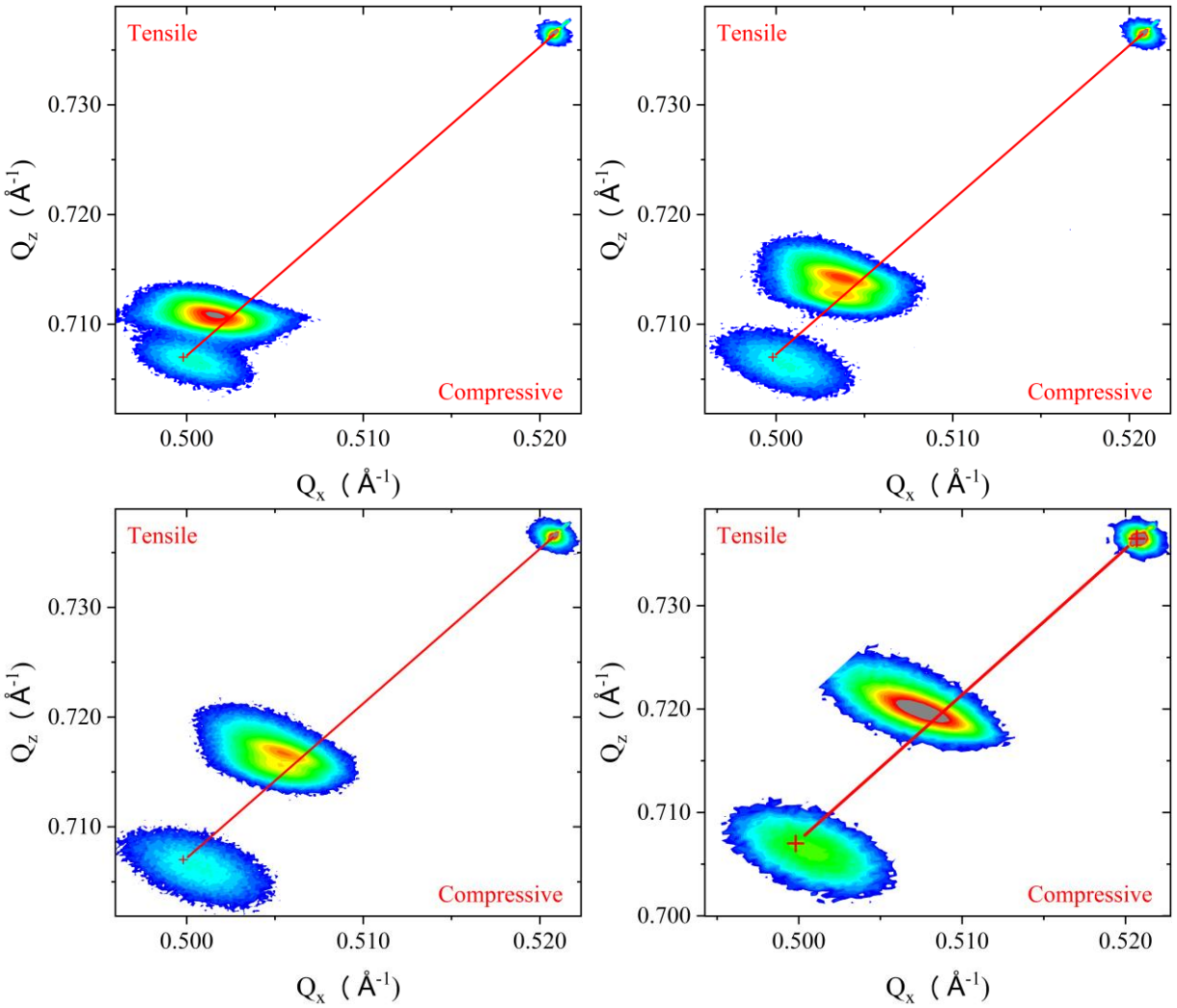

Figure 3.11 XRD results for group 4 samples with 3% compressive strain within Ge buffer layer. (top left) 17-029, (top right) 17-030, (bottom left) 17-031 and (bottom right) 17-032.

A striking feature of the XRD data for the group 4 samples, that is not observed in the other XRD results for the other 58 samples analysed in this study is displayed in Figure 3.11. The feature that the compressed Ge_{buff} produces, is the asymmetry of the SiGe peak for sample 17-029, which develops into a new inter-compositional layer for samples 17-030 and 17-031. There is a notable absence of the splitting for sample 17-032. This group of samples are not annealed so this phenomenon cannot be assigned to the high temperature intermixing that was observed with groups 1 and 2. The growth temperature is 650°C of which there are many examples within this study that all show clear SiGe-Ge interface properties. The samples are also thin which maintains the overall thermal budget lower than identical samples within the study. The only differentiating feature and possible cause of the extra layer appearing for this group is the compressive Ge underlayer. The intermixing displayed within the XRD results of Figure 3.11 is not substantial enough to be observed in the cross sectional TEM (X-TEM) results shown in Figure 3.12.

The compressive strain enhancement of Si-Ge interdiffusion was first reported by LeGoues et al in 1989 [85]. Following this original work publications disagreed if strain enhanced the diffusion or not. Cowern and Theiss published work agreeing that compressive strain did enhance the Si-Ge interdiffusion [86, 87] in 1992 and 1996 respectively. Opposing views denying a change in the activation energy for diffusion were subsequently published by Hollander et al, Gillin et al and Baribeau [88-90]. The most recent publications on this agree with the original work by LeGoues, stating that compressive strain does enhance the Si-Ge interdiffusion, these recent publications are by Aubertine et al and Xia et al [91-94]. These

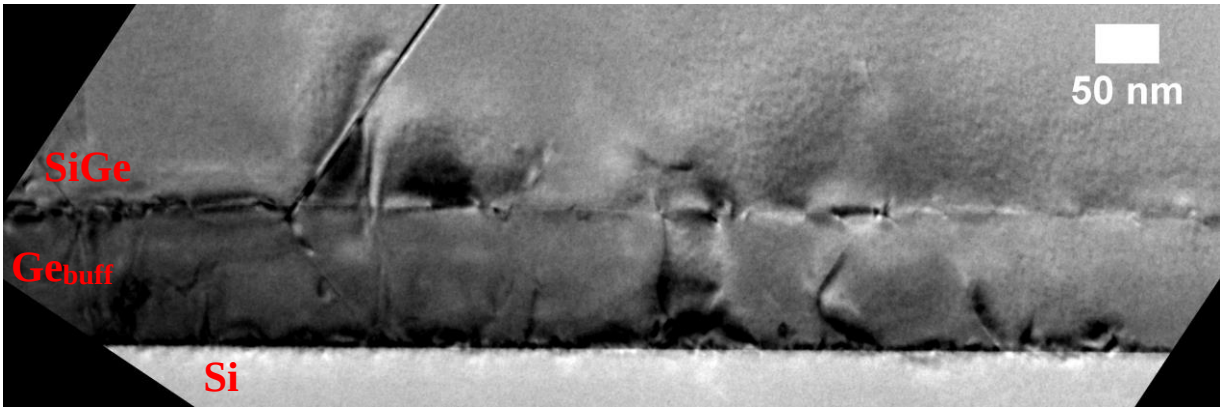

Figure 3.12 X-TEM image of sample 17-31, displaying that the intermixing viewed in the XRD results of Figure 3.11 are not substantial enough to be observed within TEM results.

references all refer to Si-SiGe diffusion as this is the only literature available that covers the impact of strain on diffusion within this material system. As such the literature only covers low Ge content SiGe <56% as high Ge content SiGe on Si is seldom attempted.

A more recent 2013 paper presents theoretical and experimental results for the intermixing of strained and relaxed SiGe, investigating how the level of strain impacts the interdiffusion driving force, this paper concludes that compressive strain does increase the interdiffusion driving force [95]. This publication acknowledges that confusion in this field arises from convolution of the impact of defects, temperatures and Ge concentration gradients. The results presented in Figure 3.11 show that the compressively strained Ge layer has increased interdiffusion in the Si/Ge/SiGe heterostructure. Considering earlier groups with identical growth conditions but tensile strained Ge it can be said with some conviction that it is not the magnitude but the type of strain that is important. 2% compressive strain will cause a significant increase in interdiffusion whereas 2% tensile strain does not cause a noticeable increase in interdiffusion. This suggests that it is not the excess energy of having strain present, that is important, instead some fundamental difference between a tensile and compressively strained crystal lattice.

Work by Cowern et al concluded that Si-SiGe interdiffusion is driven by vacancies over interstitials [86, 96]. Combine with this the theoretical work of Aziz et al, stating that; biaxial compressive strain in SiGe favours vacancy formation [97]. One could conclude that the compressive strain is supplying excess vacancies which is driving increased Ge-SiGe interdiffusion. This forms a possible answer to the appearance of the interstitial layer driven by the compressively strained Ge under layer. The structures studied by Cowern and Aziz are not identical to our situation, as such this is only a possible solution and not a firm conclusion. It does however explain the observations we are reporting and fits very neatly with the factors that appear to drive the intermixing observed.

Relaxing a fixed amount of strain within a thinner layer generates a higher density of defects. Interactions between defects can render them less mobile preventing relaxation of lattice misfit strain [32]. The issue is more prevalent in constant composition layers as most defects form close to the lower interface. Graded buffer layers act to reduce the defect pinning found in

constant composition buffers. Thin graded layers with a high grading rate were produced corresponding to sample numbers 17-325 to 17-328. The layer structure for each sample is displayed within Figure 3.13. The aim was that grading would act to spread the generation of defects and reduce dislocation pile up, improving dislocation mobility.

The layer structure diagrams within Figure 3.13 show that a 500 nm graded layer has been inserted. As stated the aim of this is to investigate a potential increase in relaxation through increasing dislocation mobility. Sample 17-328, Figure 3.13 (d), contains two grading steps. Firstly, grading from Ge to $Si_{0.2}Ge_{0.8}$ then from $Si_{0.2}Ge_{0.8}$ to $Si_{0.3}Ge_{0.7}$ this attempts to spread the required defects over an even greater area, further reducing the impact of defect pinning. It can also be seen that compared to previous groups the Ge layer has increased in thickness. The aim was to increase Ge relaxation, avoiding the residual tensile strain displayed by previous groups. The six-fold increase in Ge thickness was intended to relax the Ge within a different mode. As previously explained, the success in producing thin (100 nm) fully relaxed Ge relies upon balancing the compressive strain from lattice mismatch, with tensile strain from thermal mismatch. By producing a 650 nm Ge_{buff}, the goal was that the Ge would be consistently fully relaxed, without needing to strike this delicate balance. The graded samples probe the contribution of defect pinning to the difficulties in relaxing the residual tensile strain. It is clear that the graded samples are starting to stretch the limits (especially sample 17-328) of what could be classed as a thin buffer layer, which was the motivation behind this chapter.

(a)

SiGe70	
Graded SiGe70	
Ge	~1050 nm
p- (10-20ohm cm) - Si (001)	

(b)

SiGe70	~500 nm
Graded SiGe70	~500 nm
Ge	~650 nm
p- (10-20ohm cm) - Si (001)	

(c)

SiGe70	~500 nm
Graded SiGe70	~500 nm
Ge	~650 nm
p- (10-20ohm cm) - Si (001)	

(d)

SiGe70	~500 nm
Graded SiGe70	~200 nm
SiGe80	~500 nm
Graded SiGe80	~300 nm
Ge	~650 nm
p- (10-20ohm cm) - Si (001)	

Figure 3.13 Heterostructure designs to test if grading can remove potential defect pile up. Sample numbers are (a) 17-325 (b) 17-326 (c) 17-327 and (d) 17-328. Sample 17-327 is grown with no interupts, in contrast to sample 17-326.

The XRD results within Figure 3.14 show that the insertion of a graded layer has not had an impact on reducing the last few percent of tensile strain within the SiGe layer. It can be seen from the colour gradient streak between the Ge and SiGe peaks that grading has occurred. The XRD data returns very similar results to the constant composition samples within groups 1 and 2. It is also seen that producing a thicker (600 nm) Ge layer has not induced any further relaxation compared to the initial 100 nm layer. Relaxation values for the Ge layers within Figure 3.14 are all either 104 or 105% relaxation. This reaffirms that for Ge on Si striking the balance between lattice and thermal mismatch strain is the best option. The results for SiGe relaxation are 107%, 110%, 108% and 110% for (a) to (d) respectively. This displays relaxation equal to the worst of the constant composition SiGe layers reported within groups 1 and 2. This does not rule out the impact of defect pinning, but it does show that the structures within Figure 3.13 do not provide any increased relaxation. Potentially different grading rates, growth temperatures or layer structures could provide a better solution. The graded layers returned smooth surfaces, with the RMS roughness of all four samples below 4 nm.

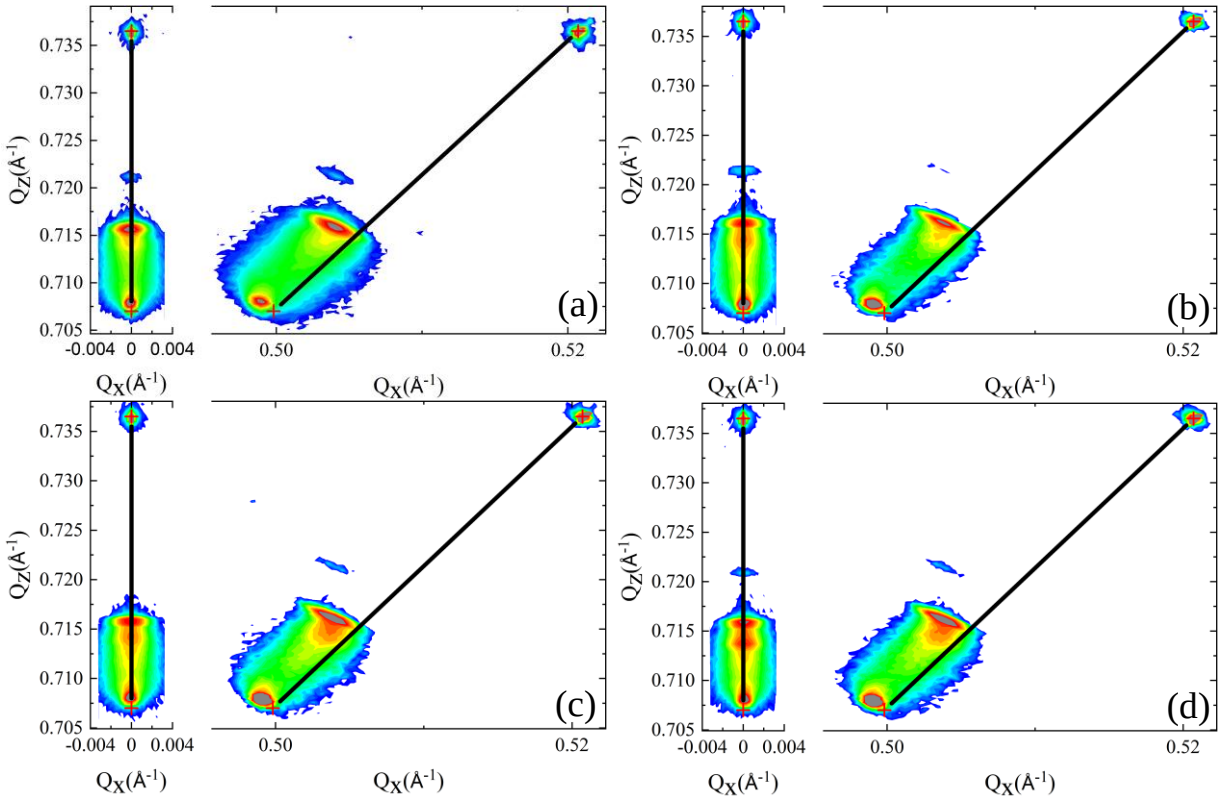

Figure 3.14 XRD data for graded buffer layers presented in Figure 3.13. Sample numbers are (a) 17-325 (b) 17-326 (c) 17-327 and (d) 17-328

The thin buffer layer study has shown that it is possible to produce 105% relaxed SiGe layers under a micron thick, grown at 650° C on a Si_{sub}, utilizing a <100 nm interstitial Ge_{buff} layer. Producing a 100 nm low temperature-high temperature (LT-HT) Ge layer deposited onto Si took extensive research and calibration efforts. Through varying the thickness of the Ge layer, a range of compressive and tensile strain values are achievable. This is primarily made possible by the competing effects of lattice mismatch strain and thermal mismatch strain between the deposited Ge and the Si_{sub}. The lattice mismatch strain acts to induce in-plane compressive strain within the Ge layer, whereas, the thermal mismatch strain acts to induce in-plane tensile strain within the Ge layer. As we grow thicker Ge layers, past the critical thickness, the lattice mismatch strain is relaxed, and the thermal mismatch becomes dominant resulting in tensile strain. In thinner layers the lattice mismatch strain is dominant, resulting in compressively strained Ge [55, 83].

The next stage was to utilize this Ge layer on Si to provide a platform on which thin fully relaxed SiGe can be produced. The motivation was that the Ge would localize many of the defects required to transition from Si to $Si_{1-x}Ge_x$, x = 70, 80, 90. This has been demonstrated to work through TEM observations such as Figure 5.3. The Ge_{buff} layer is also in place to allow the SiGe to relax under tensile strain. It is documented SiGe relaxing under compressive strain leads to increased surface roughening [35]. Therefore, the Ge layer will help improve surface roughness, interestingly our results show that a small amount of compressive strain (3%) did not increase the final RMS surface roughness.

This study has found that within thin (~ 400 nm) SiGe layers on a 100 nm Ge_{buff} layer, deposited onto a Si (001) substrate, the dominant strain inducing effect is not lattice mismatch but in fact thermal mismatch induced strain. As has been shown the relaxation of the SiGe is consistently around 106%. Variations of SiGe composition, thickness, growth temperature, annealing temperatures and annealing times have shown to have minimal impact on the SiGe relaxation. If the dominant strain mechanism was lattice mismatch induced strain there should be a variation in strain with SiGe composition, also a variation of relaxation with annealing temperature would be expected.

Increasing SiGe annealing temperatures to 800° C has been reported previously to improve crystallinity, relaxation and surface roughness [98]. The observation of a metastable SiGe layer that replicates its strain state under multiple alternative growth conditions, highlights the dominant mechanism observed is thermal mismatch strain. Further progress with the structures tested will hinge on reducing this thermal mismatch strain. Low temperature growth is a clear option. The group ethos is always working towards commercially viable solutions, as such the low growth rates that result from LT growth seem preventative to commercial acceptance.

3.2. Dislocation filter layer characterisation results

Section 3.1 looked at improving thin buffer layers through varying growth and annealing temperatures, the aim was to increase defect interaction and annihilation. Another option is to use thin filtration laters, called dislocation filter layers, to increase defect interaction and annihilation.

The function of dislocation filter layers is to reduce the threading dislocation density. This is primarily achieved through mutual annihilation of threading dislocations. The typical defect reduction mechanism is an array formation of misfit dislocations at the filter layer interfaces, this occurs as the threading segments are encouraged to glide perpendicular to the growth direction, driven by the misfit stress within the filter layers. This mechanism was originally described by Matthews [99, 100].

The mechanisms behind high TDD is not completely understood. Currently a model that can predict the TDD within any material system doesn't exist. What is known is that TDD correlate with the size of the 3D islands that form during the first stage of layer growth [6] Matthews suggested a mechanism for the formation of defects through the coalescing of the initial isolated islands, it concluded that small rotational misalignments of these islands generate defects upon merging. The defects provide scattering centres and reduce carrier mobility, making methods of reducing TDD advantageous for device performance.

This chapter aims to test alternatives to constant composition SiGe buffer layers. Seven samples have been produced with sample numbers 17-490 to 17-496. Each sample replicates

the structure displayed at the top of Figure 3.15, with one variable altered. The substrate for all samples is a Si (001) wafer. A relaxed Ge layer of 350 ± 5 nm thickness is deposited directly onto the substrate. The Ge layer utilizes the low temperature-high temperature growth technique to improve crystal quality. The Ge on Si layer structure is identical in all seven samples within the study. After the relaxed Ge_{buff} some samples within the study differ from others. 17-495 and 17-496 are then graded from Ge to $Si_{0.3}Ge_{0.7}$ and completed with a constant composition $Si_{0.3}Ge_{0.7}$ layer, as seen in Figure 3.27 and Figure 3.29 respectively. Sample 17-496 has double the compositional grading rate of 17-495. Samples 17-490 and 17-491 trial the efficacy of Ge dislocation filter layers (DFLs) within a SiGe buffer layer. As seen in the layer diagram of Figure 3.15, five repeats of 2 ± 1 nm Ge and 10 ± 1 nm $Si_{0.3}Ge_{0.7}$ are deposited. The five fully strained Ge layers each separated by a $Si_{0.3}Ge_{0.7}$ layer can be seen in Figure 3.15 (e). The fully strained Ge layers represent the dislocation filter layers, the aim is that they will interact with threading dislocations and reduce the threading dislocation density (TDD). This will increase dislocation mobility, increase relaxation and reduce surface roughening. The variable altered between 17-490 and 17-491, which both contain Ge DFLs, is a doubled thickness of strained Ge layers within 17-491. Samples 17-493 and 17-494 also contain dislocation filter layers, the variation is that the filter layers are now of $Si_{0.4}Ge_{0.6}$ composition. Again, the distinction between the two samples is a double thickness filter layer within 17-494. The final sample, 17-492, represents a control sample. It is a constant composition $Si_{0.3}Ge_{0.7}$ layer of equivalent thickness to the other samples within the study.

Within a cubic diamond lattice, the dislocation direction and its Burgers vector are aligned in <110> directions. This situation limits the number of perfect dislocations that can be present within the material system. A perfect dislocation is one in which the lattice translation vector **b** is the shortest permitted lattice vector (i.e. the distance between two equivalent atoms in the closest packed plane). The three basic types of perfect dislocation are a pure edge dislocation, a 60-degree dislocation and a screw dislocation, for more detail see section 1.2.

3.3. Compressively strained germanium DFL

Repeat ×5

Relaxed $Si_{0.3}Ge_{0.7}$	~100 nm
Strained Ge	2 nm
Relaxed $Si_{0.3}Ge_{0.7}$	10 nm
Anneal	10:00 min
Relaxed $Si_{0.3}Ge_{0.7}$	~100 nm
Anneal	10:00 min
Relaxed HT-Ge	350 nm
Relaxed LT-Ge	
p^- (1-30ohm cm) - Si (001)	

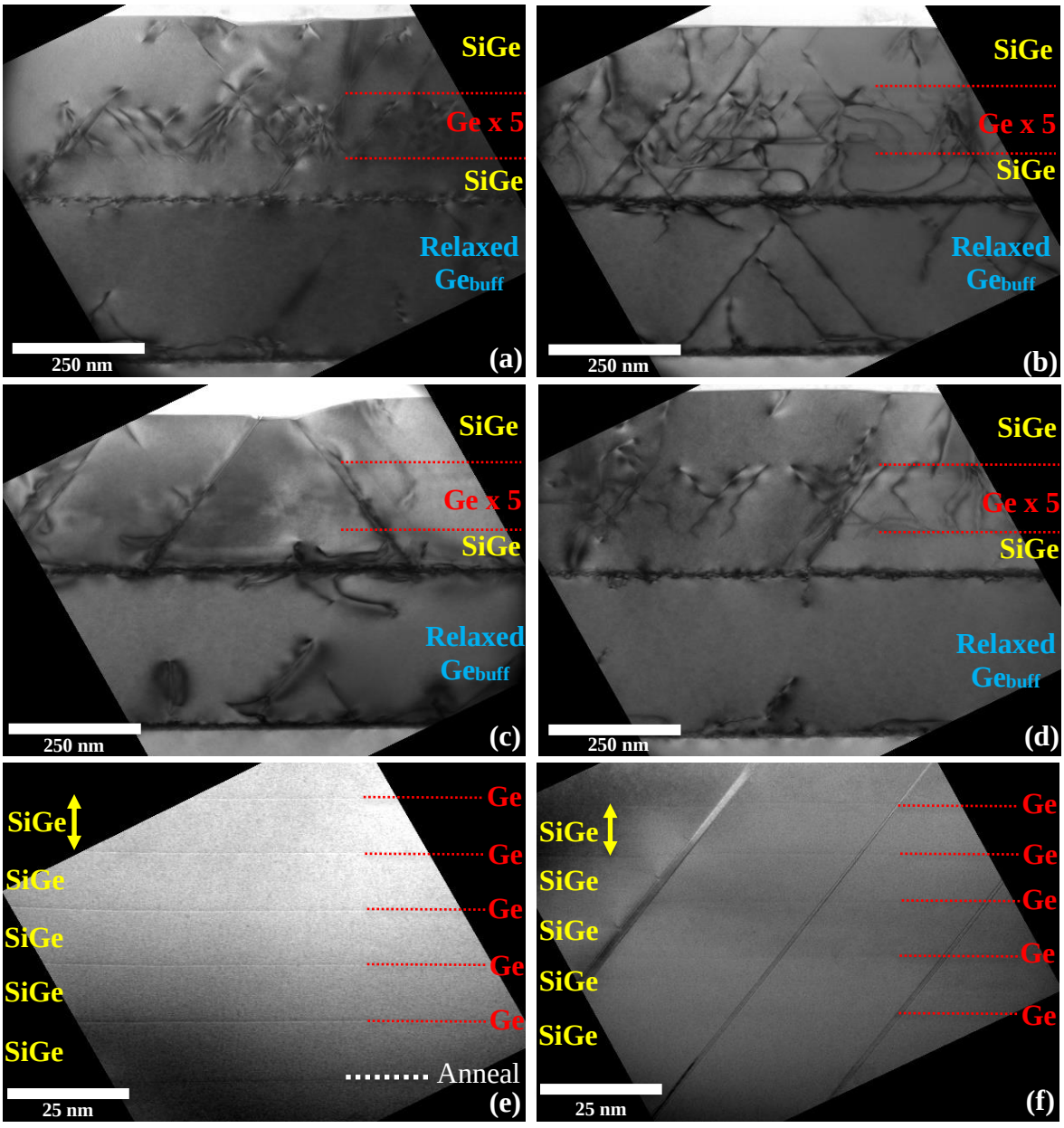

Figure 3.15 Sample 17-490. X-TEM images of buffer layers, investigating impact of Ge dislocation filter layers. Schematic daigram of heterostructure includes layer thicknesses and annealing times.

Images (a) to (d) within Figure 3.15 represent repeat images along the cross-sectional length of sample 17-490. Images (e) and (f) are higher (120 K×) magnification, showing the strained Ge DFLs. The five compressively strained Ge filter layers can be observed in Figure 3.15 (e) and (f). Both images are taken on a JEOL 2100 TEM in bright field, double tilt, 004 condition at 120 K× magnification. The Ge layers are 2 ± 1 nm thick with the spacing between filter layers equal to 10 ± 1 nm. The full stack of five filter layers and spacings is 60 ± 2 nm thick. Below the filter layers in Figure 3.15 (e) a darker interface is observed, resembling a 6th filter layer. This is interpreted as segregation caused by the annealing step. The intermediate annealing step causes Ge to rise to the surface, due to the preferential surface segregation of Ge [101].

Within SiGe, surface segregation is driven by an imbalance in the surface tension of the two constituent elements [102, 103]. The result is that Ge diffuses to the surface, reducing the overall surface energy of the structure. For SiGe this process is also driven by the atomic size difference, with the radius $r_{Ge} = 0.137$ nm and $r_{Si} = 0.132$ nm [104, 105]. Experimental and theoretical reports exist, covering both amorphous and crystalline SiGe, confirming segregation occurs when annealing SiGe films [106, 107]. A universal temperature for initiating segregation cannot be quoted, it is dependent on composition, strain, growth rate and is also suppressed by hydrogen terminated surfaces [106]. Published works mainly cover low ($x < 5$) Ge content $Si_{1-x}Ge_x$, the $Si_{1-x}Ge_x$ samples studied here have high Ge content ($x > 6$). A reduction in segregation temperature is expected for the decreased Si content SiGe within the study, resulting in the samples showing increased tendency for segregation.

Images (a), (b) and (d) within Figure 3.15 show dislocations being created at the interface of the lowest Ge DFL. All three images were taken in a dark field, double tilt, 220 condition at 25 K× magnification. It appears successive Ge layers do not produce similarly significant numbers of defects. Instead defects, initiated at the lowest Ge interface, propagate through the filter layers and terminate on the uppermost Ge filter layer. This behaviour suggests that it is not relaxation of the thin 2 ± 1 nm Ge layers that has initiated the extended defects (this is logical as the thickness is well below h_c). Instead it is more likely that the added mismatch strain or interruption of growth has produced the extended defects within the SiGe spacer layer, proceeding the first Ge filter layer. Figure 3.15 (c) shows a reduced number of threading dislocations, the strain has instead been released through large stacking faults that propagate

through the entire SiGe structure and reach the sample surface. Stacking faults are also observed within Figure 3.15 (f). The interaction with the surface has caused visible surface roughening.

Sample 17-490 appears to have a high number of spontaneously generated defects in the constant composition layer above the DFLs. It is possible that separate defects have interacted at this point producing a single defect that appears to self-nucleate. The multiple contributing defects will not appear in the image if they satisfy the invisibility criteria. It is also possible, that the crystal contains a nucleation source, most likely introduced unintentionally during growth. Possible sources can include oxide precipitates [108], carbon contamination [15, 109] or <114> stacking faults [21]. Nucleation sources are one reason why 60 degree misfits are often observed in clusters, implying a type of multiplication effect, not dissimilar to a Frank-Read source [110].

Defects within Figure 3.15 are propagating at 60° to the surface along the <110> directions. The origins of this behaviour can be explained by fundamental material parameters. The highly directional bonds of the Ge crystal result in a large Peierls barrier (the Peierls stress representing the force required to move a dislocation in a plane of atoms within the unit cell) retarding dislocation motion, this also increases the probability of dislocations aligning in the <110> close packed direction.

The SiGe layer contains many partial dislocations. To lower their intrinsic energy dislocations split into two partials with stacking faults in between them (a stacking fault is a two-dimensional lattice defect which is required to be bounded by a 1D partial. Stacking faults can be seen in Figure 3.15. This is not unexpected, multiple authors have published results showing that the stacking fault energy in Si and Ge is relatively low (~50-70 mJ m^{-2}) [33, 111]. Work by Yonenaga et al investigated the impact of composition on stacking fault energy within SiGe alloys. His systematic study found that there is a decrease in stacking fault energy as the composition of SiGe moves towards pure Si, meaning an increase in the ease of stacking fault formation [112]. Yonenaga's conclusions suggest that the high Ge ($x > 6$) content SiGe within this chapter will show reduced densities of stacking faults compared to a low Ge content SiGe buffer.

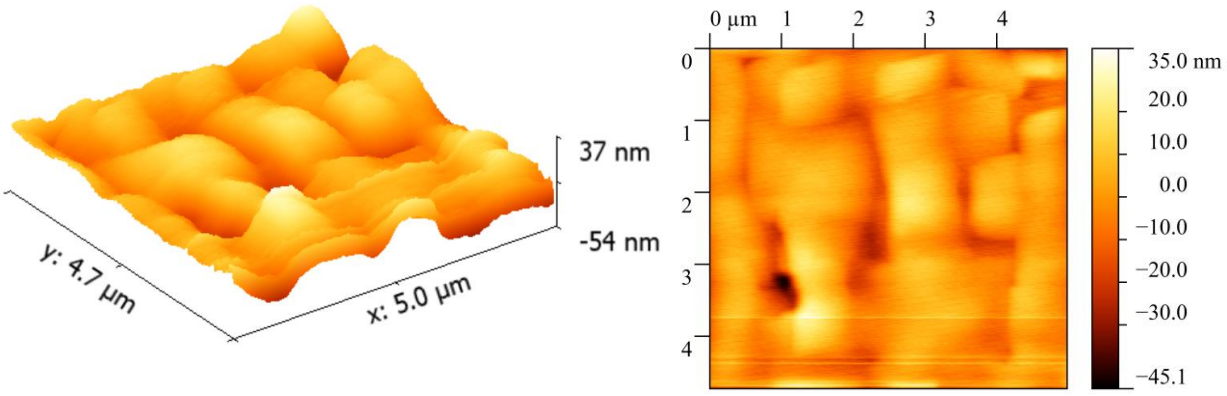

Figure 3.17 Representation of 3D surface profile (left), produced from AFM data. (right) colour map of surface height variation. Sample 17-490 demonstrating lattice relaxation assisted by strained Ge DFLs.

Figure 3.17 displays a representation of the surface profile of sample 17-490, produced from AFM data. The surface profile has a root mean squared (RMS) surface roughness of 11 ± 1 nm. For context on this value, the thick (> 3 µm) buffer layer within the million-mobility sample (13-335 reported within Chapter 5) has an RMS value of <3 nm. However, empirically strain relaxation within such a thin layer can commonly produce RMS values >20 nm. Within context, the RMS value for this surface is not the desired 3 nm, but better than expected. The surface features are aligned along the x direction, forming troughs and ridges. These features are aligned along the <110> surface orientations, demonstrating cross hatching, resulting from relaxation via the modified Frank-Read mechanism [24, 113].

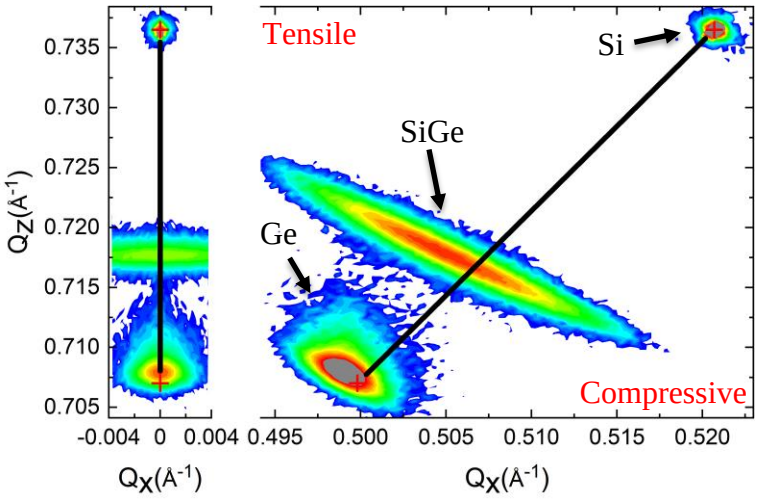

Figure 3.16 Reciprocal space map of sample 17-490. Results display relaxation state assisted by strained Ge DFL.

The relaxation values for the Ge and SiGe layers are 105% and 104% respectively. These are calculated from the data within Figure 3.16 using the X'Pert Epitaxy software package. The composition of the SiGe is also verified as $Si_{0.30}Ge_{0.70}$. Interestingly this is the only sample within this chapter and the previous chapter that displays higher relaxation within the SiGe than the underlying Ge. In terms of thermal expansion mismatch the SiGe has a lower linear thermal expansion coefficient compared to the Ge. If it was assumed that all lattice mismatch strain was relaxed, one would expect to obtain less tensile strain in the SiGe compared to the Ge layer. This was not observed to occur throughout the previous chapter focussing on thin constant composition SiGe layers. Meaning that lattice mismatch is still contributing to the resultant tensile strain within the SiGe layer. What this does suggest is that the Ge DFL structure within sample 17-490 is assisting in relaxing the lattice mismatch strain. It certainly shows that the Ge DFLS are not having a negative impact on the relaxation of the 260 ± 5 nm SiGe layers, also that this is one design to develop further.

Considering dislocations thermodynamically, it is not possible for them to terminate within a crystalline semiconductor. Therefore, defects terminate on the surface or edges of a sample. Misfit dislocations do not often terminate at the edges of a sample (other than in low dimensional geometries), so they must find a different method to terminate: through forming a closed loop, ending in a precipitate (defect), at an interlayer surface or by forming two threading arms that propagate to a surface [114].

Work by P. Germain studied the average length of misfit dislocations within germanium. The relationship discovered was:

$$l_{av} = {}^{8f_m}/_{N_{TD}B} \qquad (3.1)$$

Where l_{av} is the average length of a misfit dislocation, f_m is the lattice mismatch, N_{TD} is the threading dislocation density and B is the Burgers vector. Drawing a parallel between this discovery and research into quantum dot filters (QDF) [115, 116] presents a possible line of future investigation. It has proved vital for the efficacy of QDF to tune the size of the dots to maximize their interaction with threading dislocations. Applying this to DFLs, an investigation on the optimum length and therefore density of misfit dislocations could be an interesting area of further work. Knowing the optimum conditions for maximum interaction energy between

MDs and TDs would inform where to locate the DFLs within a buffer layer. It could also lead to DFLs where the degree of relaxation is tuned to the TDD that requires filtering, potentially with sets of DFLs that vary in composition, thickness or mismatch strain with respect to the distance from the substrate. Using equation 3.1 for pure Ge on Si (001) gives an average misfit dislocation length of 8 μm [117]. The average dislocation length is limited by blocking and annihilation, caused by other dislocations lying within the same plane. Misfits expand through lateral glide of their threading arms during strain relaxation. They will continue to expand until they are hindered by the repulsive effects of a neighbouring defect with identical Burgers vector, alternatively they can be stopped by the strain field of a crossing misfit. This highlights the advantage of grading, utilized in samples 17-496 and 17-495. The grading spreads the misfit network through a three-dimensional space. Allowing misfits to glide and reduce blocking and pining of the generated defects.

Repeat ×5

Relaxed $Si_{0.3}Ge_{0.7}$	~100 nm
Strained Ge	~3 nm
Relaxed $Si_{0.3}Ge_{0.7}$	10 nm
Anneal	10:00 min
Relaxed $Si_{0.3}Ge_{0.7}$	~100 nm
Anneal	10:00 min
Relaxed HT-Ge	350 nm
Relaxed LT-Ge	
p^- (1-30ohm cm) - Si (001)	

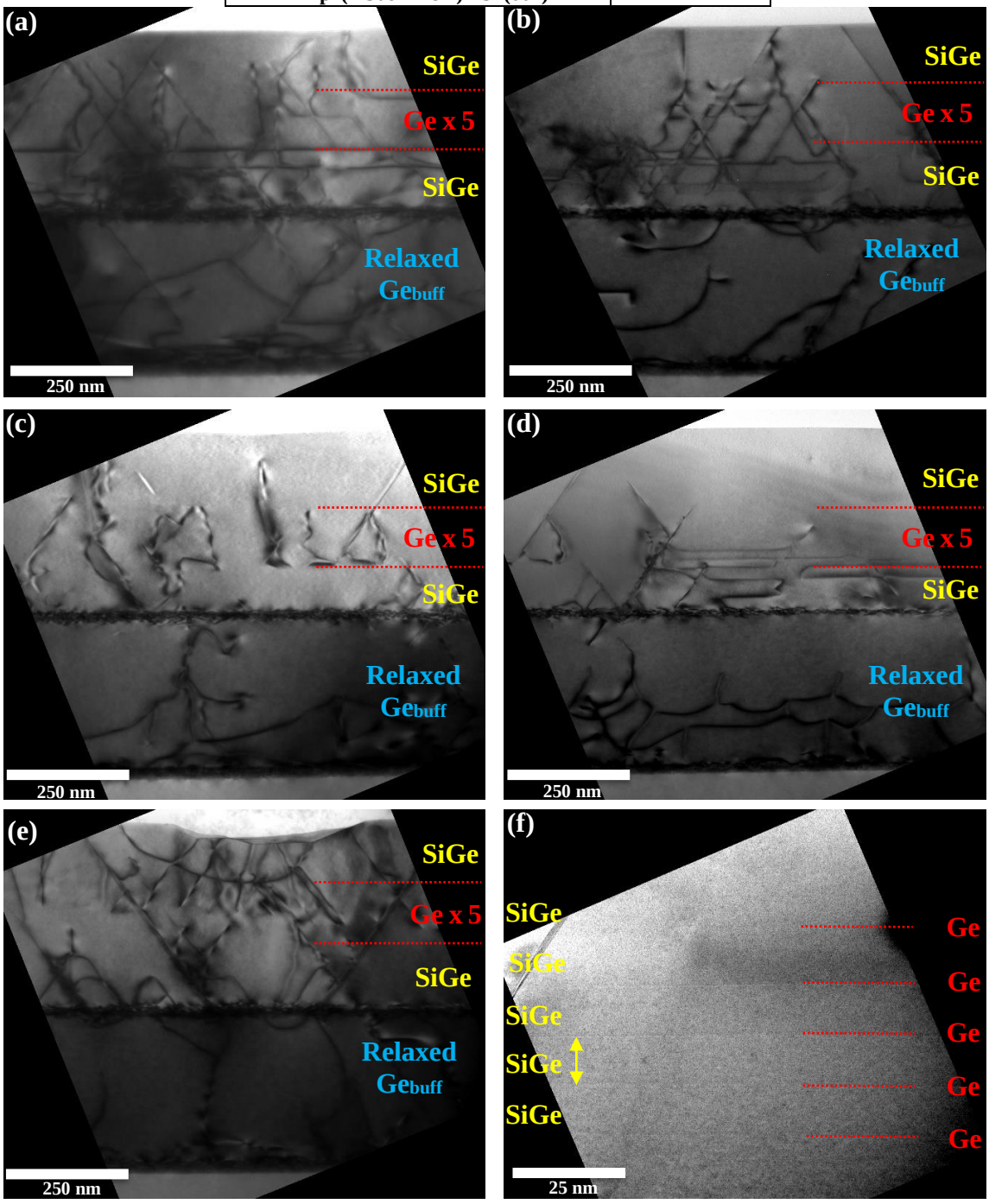

Figure 3.18 Sample 17-491. X-TEM images of buffer layers, investigating impact of Ge dislocation filter layers. Schematic diagram includes layer thicknesses and annealing times.

Sample 17-491 presented in Figure 3.18. replicates sample 17-490 presented in Figure 3.15 the variation; an extended growth time of the compressively strained filter layers. The growth time of the Ge layers is extended from 2 to 5 seconds. Direct comparison of the two structures, through a selection of TEM images, suggest that the thicker Ge layers display increased confinement of dislocations within the filter stack, primarily through formation of closed loops. Image (d) shows loops that have terminated at the interface of the first Ge filter layer. It is seen that dislocations have propagated along the interface at 90° to the growth direction. On interacting with other defects, they have formed closed loops. This can also be seen at the lower annealing interrupt. This is an advantageous interaction between DFLs and propagating defects, resulting in increased confinement of defects closer to the substrate. This does not necessarily mean that the thicker layers will display improved relaxation or surface roughness.

Increased confinement can lead to defect starvation which hinders relaxation. Defect starvation describes a critical defect density, below which the low number of defects reduce relaxation. The reduction occurs as fewer defects interact due to their low density and large distribution throughout the sample. Initially the predicted impact of defect starvation was much larger than the experimental findings [118]. However, this was later explained as being due to the ratio of mobile to sessile defects being maintained during relaxation, as opposed to the initial hypothesis where a larger proportion of sessile dislocations develop.

Dislocation glide, leading to interactions and closed loops is an ideal process to reduce the density of defects. Image (c) within Figure 3.18 displays a prime example of how defects can be terminated in closed loops. The image shows defects which appear at the interface of the lowest Ge filter layer, subsequently change propagation direction, eventually interacting and terminating in a closed loop at the interface of the final Ge filter layer. The relaxed Ge_{buff} layer shown in Figure 3.18 (d) is 330 ± 5 nm thick. It also stands as a prime example of dislocation interaction and annihilation. The image shown in Figure 3.18 (e) shows detrimental dislocation behaviour within SiGe. The large cluster of defects has not been able to glide and self-annihilate, resulting in propagation to the sample surface. The defect network has caused surface roughening. The aim of the TEM measurements is a relative comparison between samples, to ascertain which display the most favourable dislocation filtering behaviour. Knowledge of

which buffer design displays the most potential can be used to direct further development and research efforts.

Within the TEM images of Figure 3.18, especially image (d), the magnitude of the dislocation confinement within the relaxed Ge layer is apparent. The efficacy of relaxation and TDD reduction within the relaxed Ge_{buff} is down to the LT HT growth. The initial LT growth step relaxes a large amount of mismatch stress at the Si-Ge interface. Much of this relaxation occurs through a Lomar dislocation network [83]. The advantage of Lomar dislocations is that they propagate at 90° to the growth direction. The dense network of dislocations at the Si-Ge interface results in a low dislocation density in the following growth. This low density reduces dislocation blocking resulting in less resistance to glide. This improves defect interaction and annihilation, the results of which are displayed in Figure 3.18 (d).

The relaxation values for the Ge and SiGe layers are 105% and 108% respectively. These are calculated from the data within Figure 3.19 using the X'Pert Epitaxy software package. The composition of the SiGe is also verified as $Si_{0.30}Ge_{0.70}$. Broadening of the SiGe peak, perpendicular to the inserted black line is apparent. The broadening for SiGe is noticeably larger than for the Ge. This agrees with the TEM observations showing the increased defect density within the SiGe compared to the Ge. The orientation of the maximal broadening for the SiGe peak, within reciprocal space, represents ω broadening in real space. The broadening is

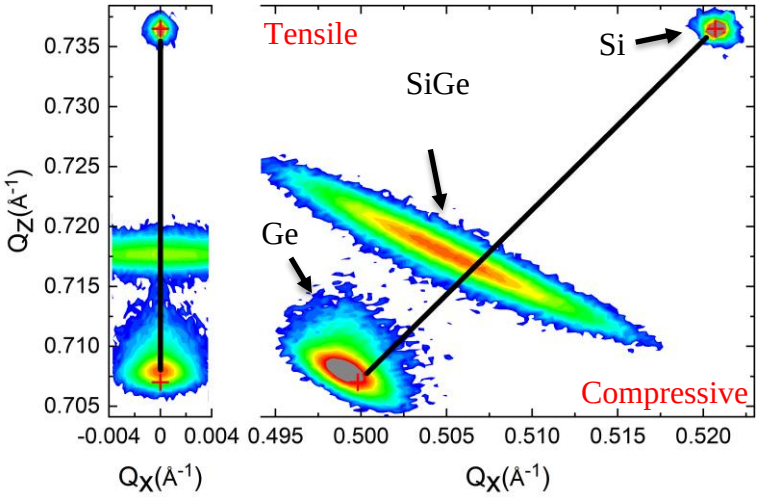

Figure 3.19 Reciprocal space map of sample 17-491. RSM displays relaxation assisted by strained Ge DFL.

produced by mosaic tilt or mosaicity within the sample. This is distinct from layer tilt described within Chapter 4. Layer tilt describes macroscopic tilt of epilayers within the heterostructure. Mosaic tilt describes microscopic regions within epilayers that deviate from the bulk crystallographic alignment. Defects and the strained regions surrounding them cause such mosaicity, with clusters of defects contributing significantly to the peak broadening in reciprocal space. It is not possible to accurately extract quantitative defect density values from the broadening of the single asymmetric RSM within Figure 3.19. To extract quantitative information multiple asymmetric RSMs of successive (h k l) orders must be obtained, the FWHM of broadening in each scan must be plotted within a Williamson Hall plot [119]. This plot deconvolutes the multiple contributions to peak broadening to extract quantitative information on defect densities from XRD RSM data [120-122].

Figure 3.20 is a representation of the surface of sample 17-491, produced using AFM data. The RMS roughness value calculated from Figure 3.20 is 10 ± 1 nm this is a marginal improvement on the 11 ± 1 nm for sample 17-490, crucially lying within the uncertainty. When assessing the DFLs using XRD and AFM, the thinner strained Ge DFL layers are superior. This is due to their increased relaxation (4% greater than the thicker layers) and comparative surface roughness. The TEM analysis, however, displays improved defect confinement and a greater number of closed defect loops within the thicker Ge layers. It is possible that the observed increase in defect confinement within TEM images has resulted in reduced defect densities, therefore reducing relaxation through reducing defect interactions. It must also be understood

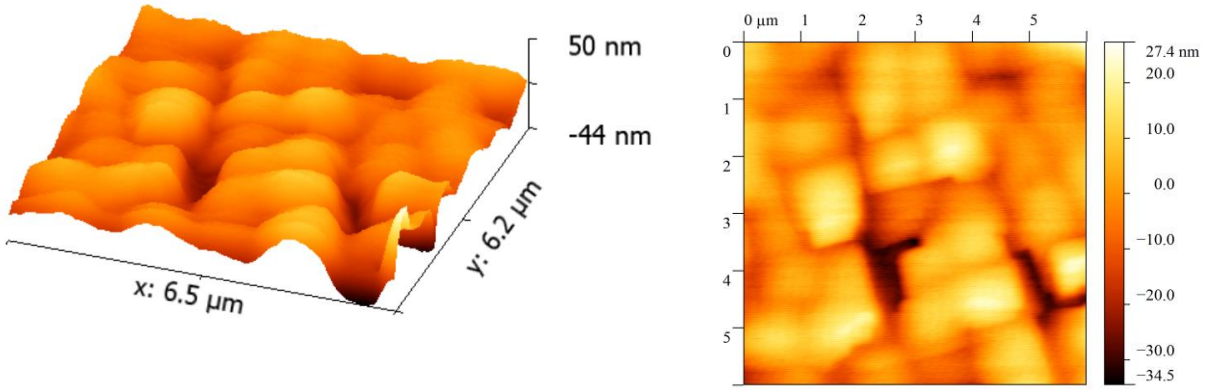

Figure 3.20 Representation of 3D surface profile, produced from AFM data. Sample 17-491 demonstrating lattice relaxation assisted by strained Ge DFLs. 17-491 demonstrates impact of increased DFL thickness compared to previous sample.

that TEM results must be analysed with care, ideally backed up by supporting characterization techniques. TEM images show only small regions within a larger sample. Accumulating large numbers of images and presenting a representative selection (as displayed above), does not represent a statistically significant volume of an entire wafer, unlike XRD and AFM measurements.

3.4. Tensile strained SiGe DFL

Sample 17-493, displayed in Figure 3.21, replicates the structure of the previous two Ge DFL samples. The variation being; the composition of the filter layer has changed, with a $Si_{0.4}Ge_{0.6}$ layer inserted instead of the Ge. The important difference with the $Si_{0.4}Ge_{0.6}$ filters is that they are tensile strained, as opposed to the Ge filter layers that were compressively strained. Direct comparison of TEM images for Ge and SiGe filter layers display a weaker interaction between SiGe DFLs and extended defects. Figure 3.21 (b) highlights the weak interaction, resulting in ineffectual filtering of dislocations. A weak interaction is inferred by minimal direction changes in defects, limited glide along <110> planes (observed as 90° misfit segments) and finally the high TDD present at the sample surface. This reduction in filtration for $Si_{0.4}Ge_{0.6}$ can be explained by the reduction in lattice mismatch strain. It is believed to be mismatch strain that aids interaction with dislocations and alters dislocation propagation [118, 123, 124].

×5	Relaxed $Si_{0.3}Ge_{0.7}$	4:16
	Strained $Si_{0.3}Ge_{0.7}$	0:08
	Relaxed $Si_{0.3}Ge_{0.7}$	0:43
	Anneal	10:00
	Relaxed $Si_{0.3}Ge_{0.7}$	4:16
	Anneal	10:00
	Relaxed HT-Ge	4:06
	Relaxed LT-Ge	4:28
	p^- (1-30ohm cm) - Si (001)	

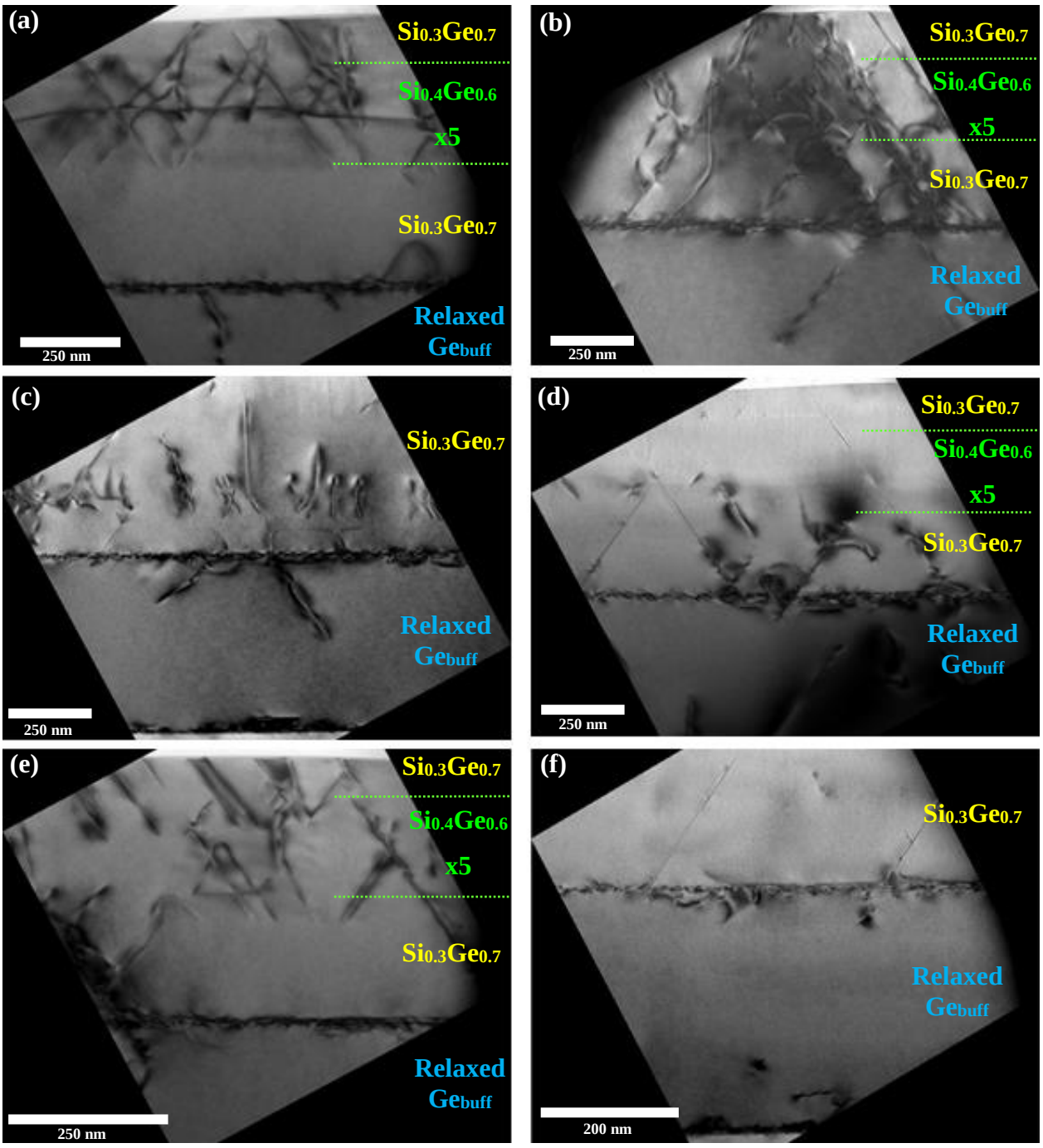

Figure 3.21 Sample 17-493. X-TEM images of buffer layers, trialing impact of dislocation filter layers. Schematic diagram of heterostructure included with growth times.

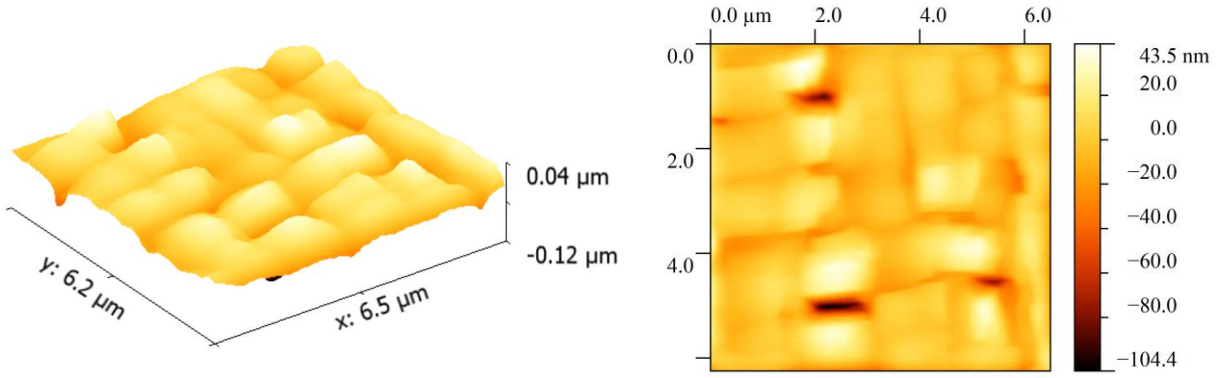

Figure 3.22 Representation of 3D surface profile, produced from AFM data. Sample 17-493 demonstrating lattice relaxation assisted by strained SiGe DFLs.

For the Ge filter layers, the lattice parameter of the whole structure was that of $Si_{0.3}Ge_{0.7}$, with fully strained compressive Ge interlayers. For the SiGe filters the lattice parameter of the stack is the same, however, the interlayers are fully strained tensile $Si_{0.4}Ge_{0.6}$. The Ge DFLs contain increased lattice mismatch strain energy having to deform to absorb a 30% concentration discontinuity. Whereas, the SiGe DFLs only need to absorb a 10% concentration difference. It may prove that using a DFL of $Si_{0.6}Ge_{0.4}$ would have provided enhanced filtering, matching that shown by the Ge interlayers. Fewer closed dislocation loops are observed for the SiGe DFLs. Images for the SiGe DFLs themselves have not been achieved. Imaging the SiGe DFLs proved unachievable due to the low contrast (due to similar densities) between the two SiGe concentrations.

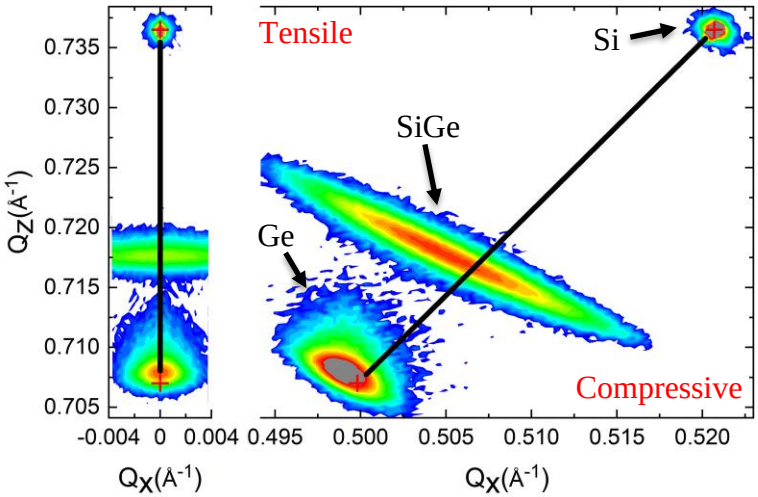

Figure 3.23 Reciprocal space map of sample 17-493. Results display relaxation assisted by strained $Si_{0.4}Ge_{0.6}$ dislocation filter layers.

The calculated RMS roughness for Sample 17-493, from the data within Figure 3.22, is 16 ± 1 nm. This is rougher than both the Ge DFLs and rougher than the thicker SiGe DFL. The cross-hatching pattern observed within the smoother Ge DFLs is not as clear in the SiGe DFLs. The initial motivation for the SiGe DFLs, was utilizing the strain enhanced smoothing effect; the process by which surface energetics of tensile strain impedes surface roughening, resulting in smoother surfaces [35]. Comparing the tensile SiGe and compressive Ge DFLs, suggests that strain enhanced smoothing is not a dominant effect. The compressively strained DFLs provide a 40% smoother surface, in terms of RMS roughness. Explanations for this outcome include: the DFLs are too thin to impact the surface roughening through the strain enhanced smoothing effect, alternatively, the $Si_{0.4}Ge_{0.6}$ induced greater surface roughening than the Ge DFLs. In response to the first hypothesis, no literature appears to exist investigating the impact of thickness on the efficacy of strain enhanced smoothing in SiGe. However, it seems reasonable that as this is a process that relies on an energy barrier retarding surface step formation, the larger the number of layers deposited the greater the impact of the process.

Relaxed $Si_{0.3}Ge_{0.7}$	4:16
Strained $Si_{0.4}Ge_{0.6}$	0:15
Relaxed $Si_{0.3}Ge_{0.7}$	0:43
Anneal	10:00
Relaxed $Si_{0.3}Ge_{0.7}$	4:16
Anneal	10:00
Relaxed HT-Ge	4:06
Relaxed LT-Ge	4:28
p^- (1-30ohm cm) - Si (001)	

×5

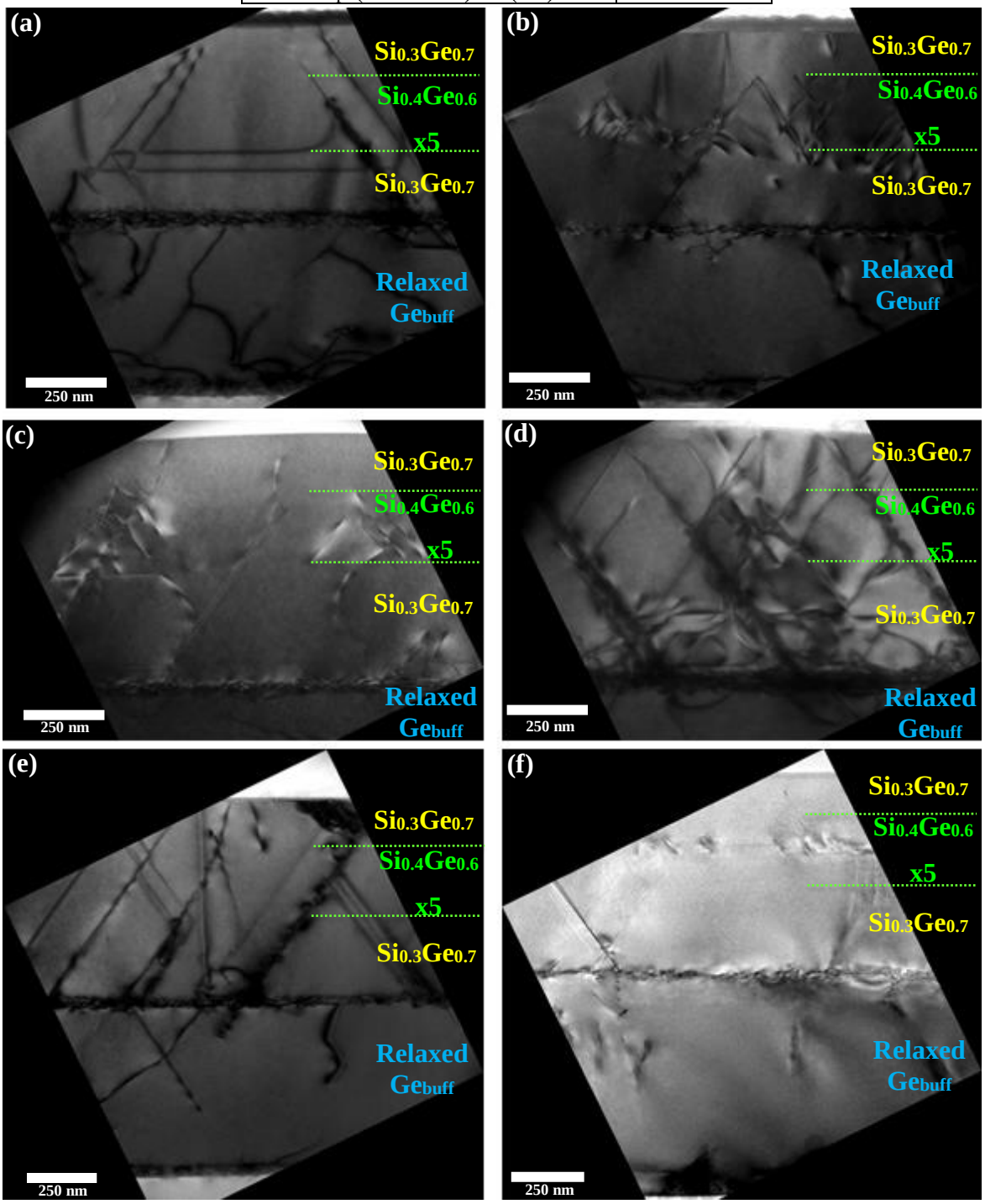

Figure 3.24 Sample 17-494. X-TEM images of buffer layers, trialing impact of dislocation filter layers. Schematic daigram of heterostructure included with growth times.

Sample 17-494, presented in Figure 3.24, replicates sample 17-493, they differ only in the extended growth time of the $Si_{0.4}Ge_{0.6}$ filter layer. In 17-494 the growth time for the filter layer, is extended from 8 seconds to 15 seconds. Direct comparison of TEM images reveals minimal difference in how the defects are interacting with the filter layers. Again, as with the thinner SiGe filters, less interaction is observed compared to the Ge DFLs. Also, a reduction in the appearance of closed defect loops compared to the Ge DFLs. Increasing the thickness of the $Si_{0.4}Ge_{0.6}$ layers does not display a detrimental impact. It is not apparent that any increases in relaxation are contributing to a higher generation of defects within the DFLs themselves. This motivates further work pursuing higher levels of misfit strain within the SiGe DFLs and thicker filter layers.

Figure 3.26 is a representation of the sample surface for sample 17-493, produced using AFM data. The RMS value extracted from Figure 3.26 is 13 ± 1 nm. This is a significant (20%) improvement over the thinner SiGe DFL. However less relaxation was achieved within the thicker SiGe DFL, which is likely to be the dominant factor producing smoother surfaces. The same trend appears for both the SiGe and Ge DFLs. With the thicker layers providing less relaxation and smoother surfaces. If the filter layers were in the regime where they had exceeded the critical thickness (h_c) and begun to relax plastically, one would expect an increase in surface roughening, therefore it seem unlikely that this is the situation observed here. Assuming the DFLs to be fully strained, a thicker strained layer interacts with a longer section of a defect arm

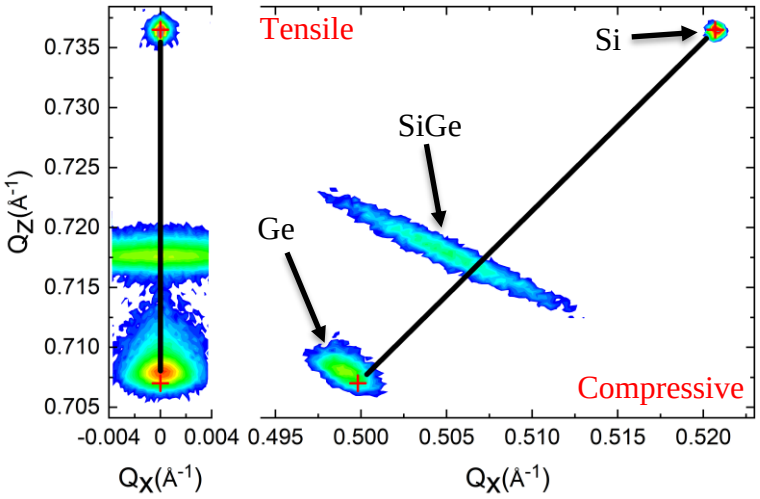

Figure 3.25 Reciprocal space map of sample 17-494. Results show relaxation assisted by $Si_{0.4}Ge_{0.6}$ dislocation filter layers.

threading through the filter layer. One would therefore expect a greater increase in glide for thicker filter layers providing they are below the critical thickness, however that is not what has been observed. These measurements undeniably display very early stages of this study. The trend should be tested with multiple samples increasing filter layer thickness incrementally. A limit is expected where increased TDD from the relaxation of the filter layers negates the increased filtering provided by increased mismatch strain.

Through comparing the SiGe and Ge filter layers, it is apparent that the Ge layers are superior. This can be interpreted in two ways, either the increased lattice mismatch for the Ge layers provides the advantage, or the alternating sign of the strain for the $Ge/Si_{0.3}Ge_{0.7}$ provides the advantage. For both possibilities it appears that the strain enhance smoothing effect for tensile strained layers is not a dominant effect. The advantages of alternating the sign of strain in dislocation filter layers is explained in a publication by Simpson et al [125]. Simpson studied strained layer superlattices and stated that to increase relaxation, each layer within the superlattice needed to alternate the strain value from tensile to compressive. This maintained the average lattice constant of the buffer layer, while encouraging dislocations to glide back and forth. The motivation is that this increases the likelihood of two dislocations segments meeting and annihilating.

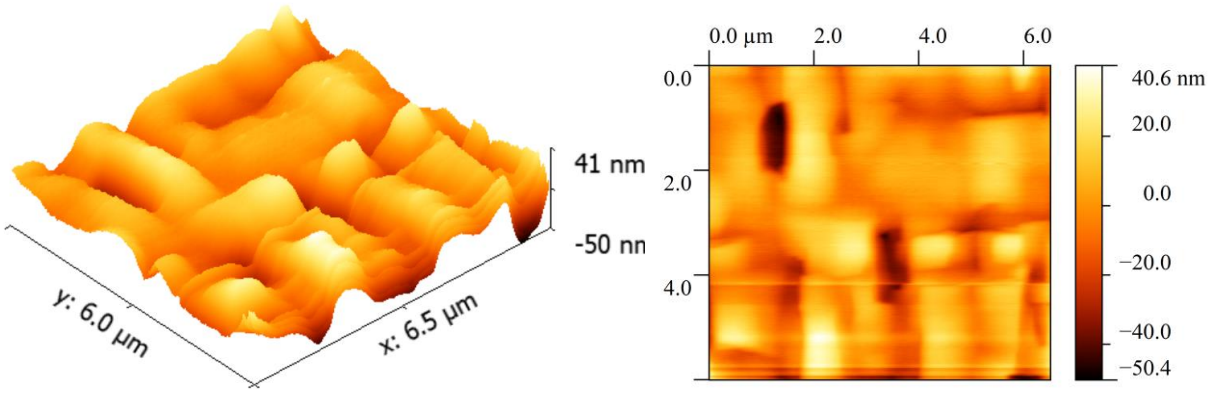

Figure 3.26 Representation of 3D surface profile, produced from AFM data. Sample 17-494, demonstrating lattice relaxation assisted by strained SiGe DFLs. 17-494 demonstrates impact of increased DFL thickness compared to previous sample 17-493.

To determine if the increased lattice mismatch is providing the enhancement one would need to produce a $Si_{0.6}Ge_{0.4}$ strained filter layers, within a $Si_{0.3}Ge_{0.7}$ buffer. The advantages of alternating strain type, between adjacent layers, on dislocation filtration has already been suggested [125, 126]. This work referred to strained layer superlattices. It was hypothesised that alternating the internal stresses of adjacent layers would increase interaction and mutual annihilation of defects. At the time it was believed that a fundamental limitation of this method rendered it ineffectual, it was believed that a reduction in mobile threading dislocations resulted in this relaxation process fading, as the encounter probability of dislocations reduces [118]. This limitation was later relaxed as it was demonstrated by Ward that there is an exchange between mobile and sessile TDs, leading to a balancing of the population and continued reduction of TDD [118]. Further work is therefore required to determine the exact process behind the superior properties of the strained Ge DFLs within this study

3.5. Thin graded SiGe layers for comparison with DFLs

Relaxed $Si_{0.3}Ge_{0.7}$	7:06
Anneal	10:00
Graded $Si_{0.3}Ge_{0.7}$	4:16
Anneal	10:00
Relaxed HT-Ge	4:06
Relaxed LT-Ge	4:28
p^- (1-30ohm cm) - Si (001)	

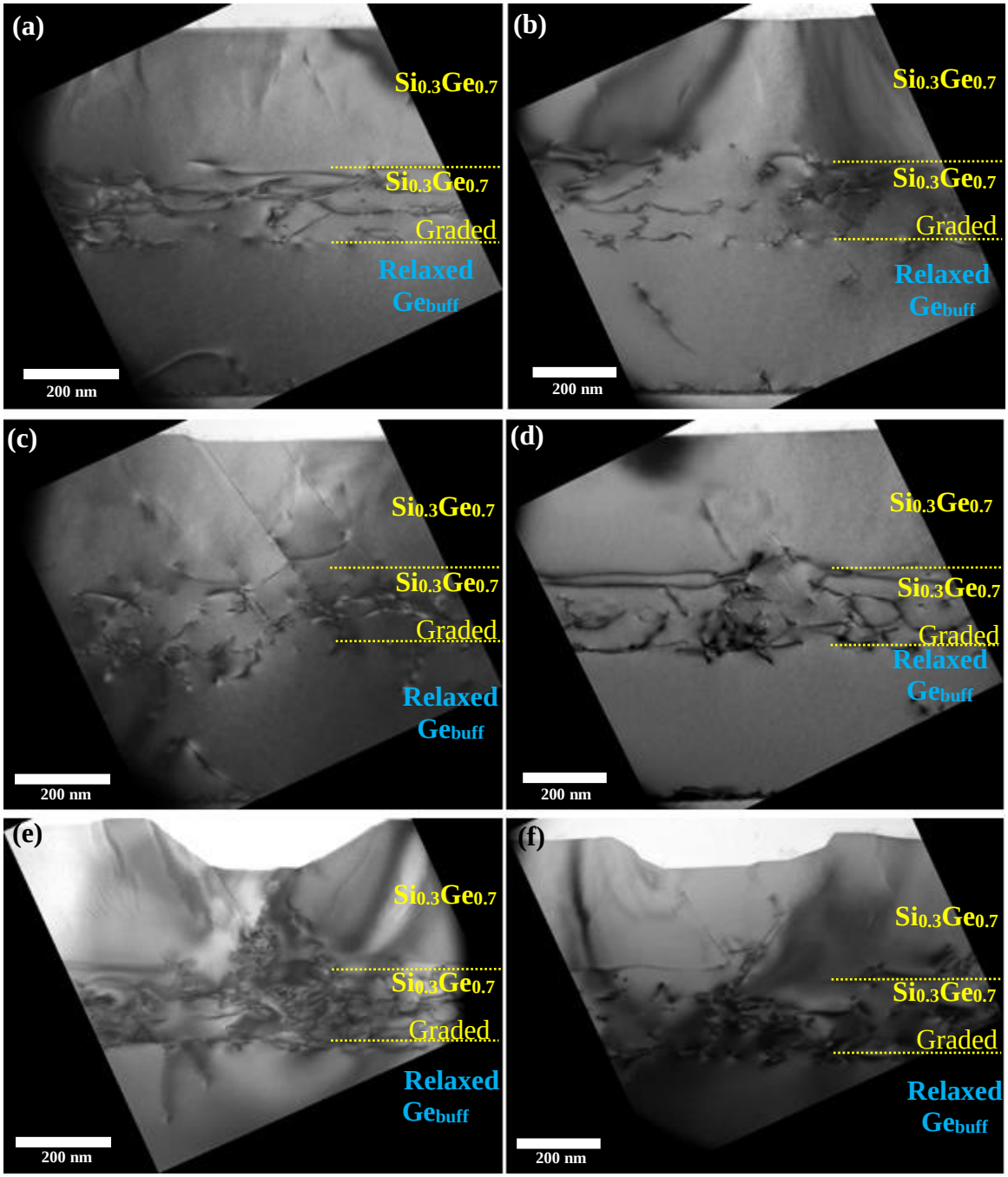

Figure 3.27 Sample 17-495. X-TEM images of buffer layers, trialing impact of graded layers. Schematic diagram of heterostructure included with growth times.

Figure 3.27 displays the first of two graded buffer layers. The overall thickness of the samples is comparable to the DFLs to aid comparison between the two techniques. Multiple types of relaxed SiGe buffer layers exist. Predominantly their application is facilitating deposition of strained Ge and Si channel layers onto Si substrates. Currently the best results are from compositionally graded SiGe buffer layers. During growth, the Ge concentration (x), in the $Si_{1-x}Ge_x$ alloy, is increased with increasing film thickness [127]. The grading trend is usually described as either step-like or linear. The main advantage of grading is that the dislocations are introduced gradually. The layer is considered as multiple low mismatched interfaces. Therefore, the misfit dislocations are gradually introduced during the growth.

The Linear grading technique has demonstrated much lower TDDs and higher dislocations mobilities, compared to constant composition buffer layers [110, 128-130]. The perceived negative of grading is the expected increase in surface roughening through cross hatching. One challenge with executing graded layers is selecting a grading rate. Fitzgerald et al [131] reported that a faster grading rate leads to a reduced critical thickness. This results in generation of dislocations closer to the substrate interface, causing greater surface roughening. For SiGe on Si, the higher the final Ge concentration, the higher the TDD, despite an identical grading rate [127]. This result is attributed to the strain fields of multiple misfit dislocations combined with the resultant surface roughening, resulting in dislocation blocking. However, with the insertion of the Ge underlayer this rule may be altered. Blocking the propagation of threading dislocations results in dislocation pile up [132]. Graded buffer layers have been shown to return lower TDD and smoother surfaces with slower grading rates. The clear issue with slow grading rates is fully relaxed layers are required to be overly thick, this brings its own array of issues as described in Chapter 4.

Fitzgerald et al [131] produced a detailed study regarding forward linear grading of SiGe. The modelling found three main control variables: Temperature, grading rate and growth rate. Each of these parameters is interdependent within CVD growth. The dependence found for controlling graded materials is shown below:

$$\rho = \frac{2R_g R_{gr} exp\left(E_{glide}/KT\right)}{bBY^m \in_{eff}^m} \quad (3.2)$$

Where R_g is the growth rate, R_{gr} the grading rate, E_{glide} the activation energy for dislocation glide, K the Boltzmann constant, T the growth temperature, b the Burgers vectors of 60° dislocations, B a constant related to the initial velocity, Y the Young's modulus for the SiGe layer and $\in_{eff}^{m}$ is the effective strain in the system and m is an exponent which is generally between 1 and 2 [55, 130].

There appears to be general agreement that the optimum forward grading rate in SiGe is 10% per micron [131]. The measure of ideality in this case is reduced TDD and RMS roughness. Isaacson et al [129] reported on high Ge content ($x > 0.6$) graded SiGe buffer layers. The report attempted to study the impact of varying the growth rates and grading rates, initially the hypothesis was that a high grading rate, but slow growth rate would give dislocations equivalent glide times as a slower grading rate. Longer misfit segments increase the amount of relaxation per defect, reducing the overall number of defects required. To promote longer defects when grading, high temperatures and low growth rates are advantageous. The aim of this method is to allow glide to keep pace with the demand for relaxation. The advantage being, that a faster grading rate permits thinner buffer layers. What Isaacson instead discovered is that higher grading rates (for forward linear grading) result in surface roughening and increased TDD even with a slower growth rate. With a non-planar surface, defects were seen to interact with the surfaces as well as previously trapped dislocations, resulting in dislocation pile up [133, 134].

Linking Isaacson's results back to equation 3.2, the results do not disprove equation 3.2. Instead it suggests there is a strong influence of the growth rate R_g and grading rate R_{gr} on the effective strain $\in_{eff}^{m}$ through surface roughening. High grading rates cause surface roughening, reducing the effective strain. This causes dislocation pile up, further reducing the effective strain. Reducing the effective strain inhibits dislocation glide necessitating a higher TDD for equivalent relaxation. following this reasoning, to increase the grading rate, but maintain a low TDD, a method to suppress surface roughening is paramount.

Much of literature covers forward linear grading of low ($x < 0.5$) Ge content SiGe. Forward linear grading describes grading that increases germanium content with thickness. The difference with the grading presented in samples 17-495 and 17-496 (Figure 3.30 and Figure 3.29 respectively), is that it displays reverse linear grading. This describes grading that reduces

the Ge content with increasing thickness. This reverse grading process on Si (001) is facilitated by the relaxed Ge_{buff} grown directly onto the Si (001). A key advantage, linking directly to the conclusions of Isaacson, is the reduced surface roughening observed with reverse grading. This occurs, as explained in section 1.2.4, due to tensile strain enhanced smoothing. This process explains why layers relaxing under tensile strain display smoother surfaces than those relaxing under compressive strain. The first reports of reverse linearly graded SiGe buffer layers show that the grading rate could be increased to 61% per micron while still achieving Frank VDM growth, as opposed to the 3D Stranski-Krastanov growth mode. The 61% per micron growth rate returned an RMS surface roughness of 4 nm.

Figure 3.26 (e) and (f) show examples of pits in the surface of sample 17-495. Surface roughening is observed in these samples as a competing mechanism for strain relaxation. The form of this type of surface roughening can be pits or straight edged grooves within the sample surface [27]. The pits provide high stress regions, as such the energy barrier for dislocation nucleation is extremely small [28]. Surface roughening of this type is commonly accompanied by a cluster of dislocations, like the situation displayed in Figure 3.27 (e) and (f). A simple method for reducing the likelihood of strain relaxation through surface roughening is to reduce the growth temperature. This reduces the surface mobility of the adatoms which suppresses the surface roughening process, facilitating relaxation through the more desirable modified Frank-Read (MFR) mechanism [24]. Reducing temperature is not a complete solution for growth quality. For CVD growth, quality is affected by many interdependent parameters, including temperature, pressure, precursor reactivity and carrier gas ratios.

AFM results (Figure 3.28) show relaxation by the MFR mechanism, identifiable by the visible crosshatch pattern. The crosshatching arises from the surface steps formed by 60-degree dislocations piling up. This explains the orientation of the crosshatch ridges along the <110> directions, following the directions of the misfit dislocations below the sample surface. The RMS surface roughness extracted from AFM measurements for sample 17-495 is 6 ± 1 nm. This is lower than all dislocation filter layers tested, representing an 85% improvement on the control sample (17-492); a constant composition SiGe layer of equivalent composition and thickness. The grading rate within 17-495 is 200% per micron, this far exceeds the 10% per micron recommended by other authors [129-131]. This is very unexpected, it was initially assumed that

the dominant issue would be surface roughening. It is important to remember that the literature almost exclusively covers forward grading, whereas, the data presented is for reverse grading. An author that does investigate reverse grading, Vishal Shah [55], reported 50 nm RMS roughness for a grading rate of 200%. The comparatively low RMS value (6 ± 1 nm) for sample 17-495 is therefore unexpected.

Comparing the low RMS roughness measured, to the TEM images (e) and (f) within Figure 3.27 exhibits inconsistencies. The pits within Figure 3.27 are clearly not representative of the full wafer. The RMS value for sample 17-495 in Figure 3.28 was calculated from three repeat scans of a 20×20 µm area, whereas the TEM image covers a 400 nm section of the surface. Assuming the sample to be ~100 nm thick, the TEM images within Figure 3.27 cover an area of 0.08 μm^2 compared to the 1.6 mm^2 sampled with the AFM. The images of the pits do however highlight the issue of dislocation clustering causing surface roughening, to exclude them would be detrimental.

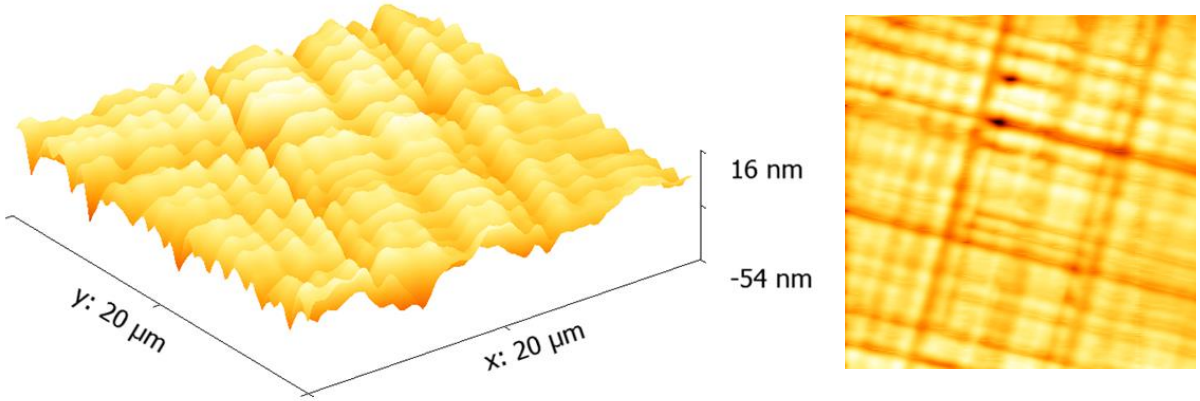

Figure 3.28 Representation of 3D surface profile, produced from AFM data. Sample 17-495, displaying cross hatching pattern on sample surface.

Relaxed $Si_{0.3}Ge_{0.7}$	7:06
Anneal	10:00
Graded $Si_{0.3}Ge_{0.7}$	2:00
Anneal	10:00
Relaxed HT-Ge	4:06
Relaxed LT-Ge	4:28
p^- (1-30ohm cm) - Si (001)	

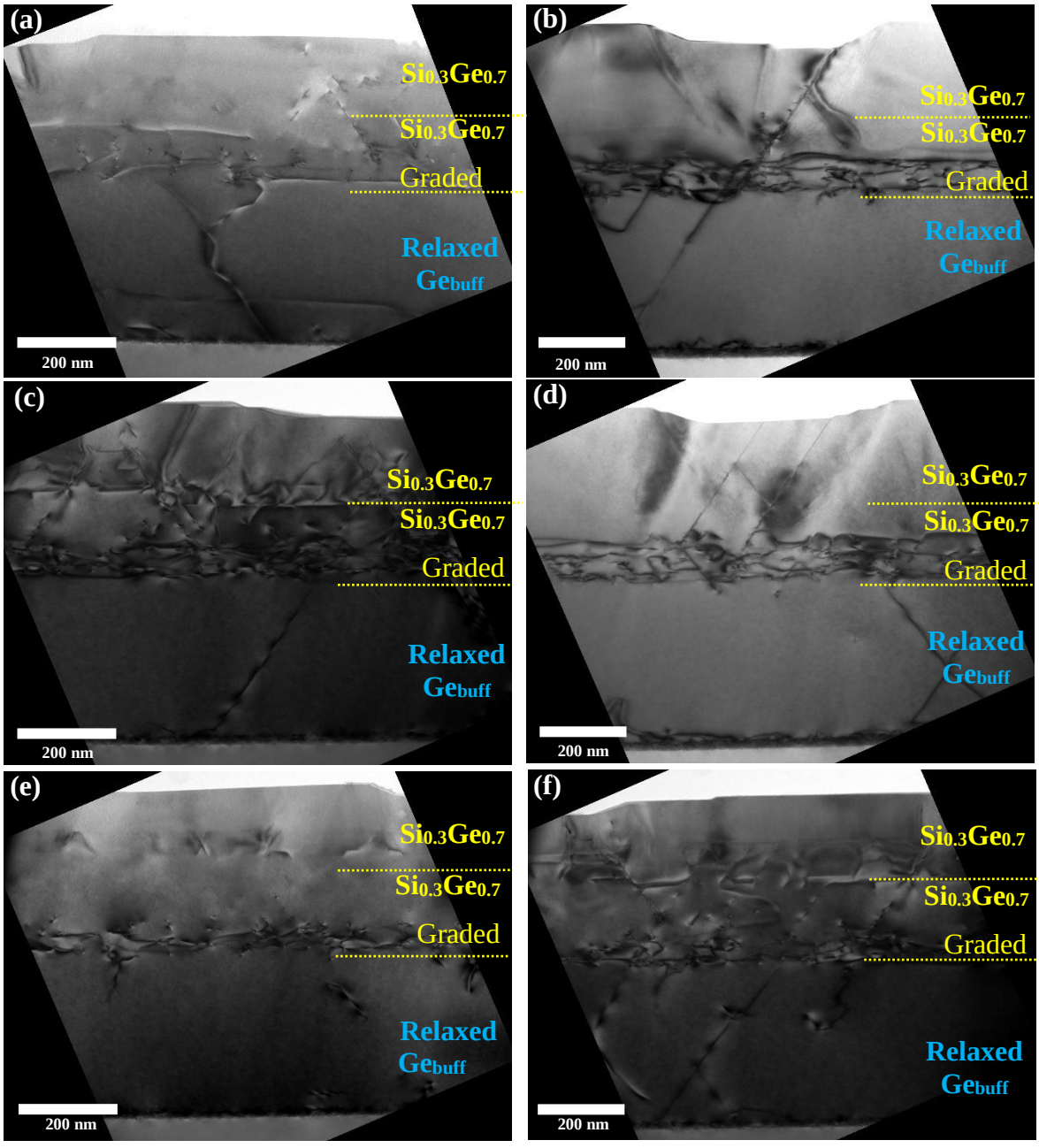

Figure 3.29 Sample 17-496. X-TEM images of buffer layers, trialing impact of graded layers. Schematic diagram of heterostructure included with growth times

The TEM images for sample 17-496, shown in Figure 3.29, represent the second graded buffer layer. The alteration is that 17-496 has double the grading rate of sample 17-495. It is difficult from the TEM images collected to measure exactly the thickness of the graded layer. However, an estimation puts the grading rate at $350 \pm 50\%$ μm^{-1}. Reaffirming what has been stated earlier this far exceeds the 10% μm^{-1} quoted as optimum for forward linear grading [129-131]. $350 \pm 50\%$ μm^{-1} is far outside the range investigated by Isaacson et al and Fitzgerald et al [129-131] for optimum grading rates. Sample 17-496 has a higher grading rate and a reduced RMS roughness compared to 17-495, this is the opposite of expectations. The RMS value calculated for sample 17-496 is 3 ± 1 nm. For context this value is comparable to the state of the art, >3 µm buffer layers, within high mobility materials [135-137].

The design of the graded buffer layers attempts to make full use of the advantages of grading. Initiating grading at the Ge-SiGe interface attempts to prevent high TDD and pile up along with the dislocation blocking that commonly occurs at this interface. An alternative approach could be to grade from pure Ge to $Si_{0.4}Ge_{0.6}$ then to include a constant composition $Si_{0.3}Ge_{0.7}$ layer. The introduction of this discontinuity in lattice constant could be advantageous. It has been shown that a buried misfit dislocation network can aid in TDD reduction [138]. The misfit network provides a large interaction cross section for grown in defects. It can facilitate defect interactions through encouraging climb and the built-in misfit stress.

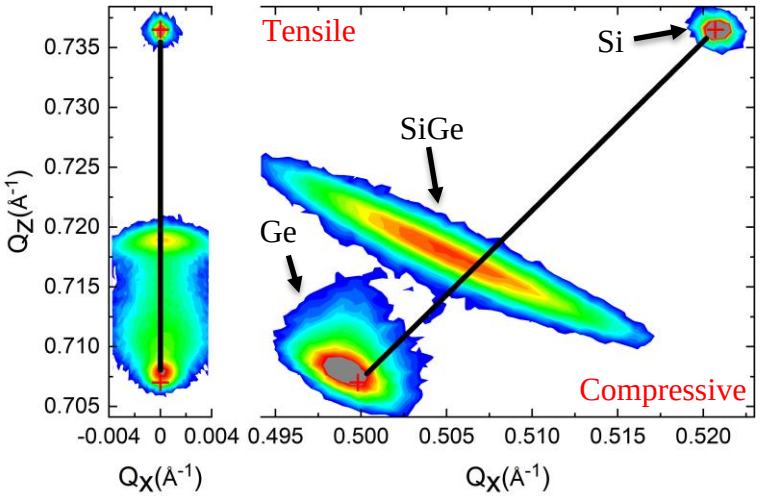

Figure 3.30 Reciprocal space map of sample 17-495. Results display relaxation assisted by linear grading.

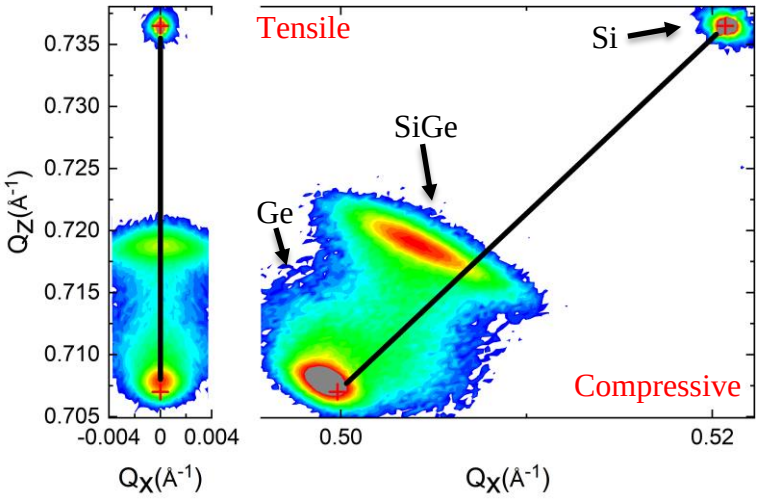

Figure 3.31 Reciprocal space map for sample 17-496. Results show relaxation assisted by a graded SiGe layer.

Table 3.4 compiles relaxation values (from XRD) and RMS values (from AFM) measurements, for all filter layer and graded samples. The control sample listed at the bottom of Table 3.4 is grown to match as closely as possible to the DFL and graded samples. The difference being it is a simple constant composition $Si_{0.3}Ge_{0.7}$ layer. This control sample facilitates comparison between itself and each of the buffer layer types demonstrated within 3.2. As strained crystal layers increase in thickness the strain energy exceeds the defect nucleation energy barrier, with consequential relaxation. A control sample must be used to observe the magnitude of relaxation that would have occurred in the absence of filter layers or graded layers.

DFL type	SiGe Relaxation WRT Si (%)	RMS surface roughness (nm)	Sample #
Ge thinner	104	11	17-490
Ge thicker	108	10	17-491
SiGe thinner	106	16	17-493
SiGe thicker	110	13	17-494
SiGe graded slower rate	111	6	17-495
SiGe graded faster rate	115	3	17-496
Control	108	20	17-493

Table 3.4 Comparing the $Si_{0.3}Ge_{0.7}$ relaxation WRT Si_{sub}. Values determined from reciprocal space map of 004 and 224 reflections.

The results show that, in terms of the relaxation achieved, the thinner SiGe and Ge DFLs have outperformed the thicker layers. The Ge DFLs have outperformed the SiGe DFLs. The thinnest Ge DFL has provided 104% relaxation of the SiGe layer, WRT the Si_{sub}. This is compared to 108% relaxation within the control sample. The 104% relaxation achieved in the thinnest Ge layer is remarkable, within a SiGe layer that is only 350 ± 5 nm thick. For context, in section 3.1.1, 104% relaxation of SiGe is better than was achieved for any of the 400 ± 5 nm samples within the annealing study. 104% relaxation represents a 4% improvement on the control sample, grown with identical parameters but without the filter layers. The 4% residual tensile strain is due to the thermal mismatch of the Ge and Si expansion coefficients. As discussed as the outcome of section 3.1.1 the best way to overcome this is to reduce the thickness of the Ge_{buff} layer so that it is not fully relaxed. Achieving relaxation in a SiGe layer that is only 350 ± 5 nm has empirically proved to be difficult [139]. Clearly from the TEM images the buffer layers display a high density of clustered dislocations. Relaxation within such a thin layer provides the opportunity for subsequent growth of a fully relaxed, reduced defect density SiGe layer of up to 650 nm. This could have the potential for a 1 µm relaxed SiGe buffer with a TDD that is suitable for device processing. A 1 µm buffer provides a potential reduction in the thickness of SiGe virtual substrates for Ge integration on Si. In their current condition the DFLs are not suitable for device applications due to their high surface roughening, the graded layers show impressive surface smoothness but have not achieved comparable relaxation.

Comparing the $Si_{0.4}Ge_{0.6}$ DFLs to the control sample it is observed, in terms of relaxation, that the $Si_{0.4}Ge_{0.6}$ filter layers are detrimental to strain relaxation. Both provide an increase in the resultant tensile strain within the $Si_{0.3}Ge_{0.7}$. The SiGe filters were displaying less interaction with propagating defects, compared to the Ge interlayers. Potentially, extra tensile strain within the heterostructure, provided by the $Si_{0.4}Ge_{0.6}$ layers is resulting in a larger resultant tensile strain for the entire stack. Combining this with the reduced interaction between $Si_{0.4}Ge_{0.6}$ layers and propagating defects, results for the $Si_{0.4}Ge_{0.6}$ DFLs show that considerable further development is required.

Another notable aspect of the thinnest Ge DFL is the relaxation of the SiGe compared to the Ge_{buff} layer beneath it. With all samples in section 3.1.1, the SiGe contains a larger or equivalent amount of tensile strain compared to the Ge_{buff}. With the thinnest Ge DFL the SiGe contains 1%

less tensile strain than the Ge_{buff}. Combining this result with improved relaxation, wrt the control sample, highlights the efficiency of the Ge DFLs for strain relaxation.

3.6. Conclusion

Reducing buffer layer thickness increases heat dissipation, avoids microcracks and improves the ability for fabrication of low dimensional devices. The difficulty with thin buffer layers is that it places the active conduction channels closer to the high density of defects that are common near to the substrate-buffer layer interface. To reduce TDD, close to the upper epilayers, efficient relaxation of buffer layers is required, along with promoting defect interaction and termination.

Constant composition SiGe buffer layers provide the simplest buffer layers for depositing strained Ge on Si (001) substrates. The constant composition layers require less calibration than the more complex graded layers and contain less variables requiring tuning. Multiple annealing trials at 700, 800 and 900° C on varied compositions of SiGe (with 60, 70 and 80% Ge content) were conducted. The growth temperature of the SiGe was also varied prior to annealing, resulting in a relatively large study including 60 samples. The overwhelming conclusion was that annealing on these thin <700 nm SiGe layers provided no marked advantages, regardless of other parameters varied, on the contrary it was frequently detrimental, causing increased tensile strain through increased thermal mismatch. The higher growth temperature, increased from 650° C to 850° C was shown through TEM images to cause severe intermixing between the SiGe and Ge layers, although interestingly this didn't appear to have a notable impact on the subsequent SiGe growth, verified using TEM and XRD measurements.

A positive result produced, is an optimised method for increasing relaxation within a Si_{buff}/Ge_{buff}/SiGe stack. This was identified through reducing the thickness of the Ge_{buff}. By thinning the Ge_{buff} a balance can be struck between thermal mismatch induced tensile strain and lattice mismatch induced compressive strain. This provides enhanced control over the final relaxation state of the Ge_{buff} and consequently the SiGe epilayer. A small batch of samples containing 3% compressive strain within the Ge_{buff} demonstrated enhanced SiGe relaxation, compared to samples with a tensile strained Ge_{buff}, this remained true even when the samples

with the tensile Ge_{buff} contained thicker SiGe layers. XRD measurements displayed a disadvantage of the compressive Ge_{buff}, namely enhanced intermixing between the Ge and SiGe layers, producing an extra Ge rich SiGe XRD peak. However, this intermixing is believed to be minimal as TEM images display no signs of the increased intermixing.

Reducing TDD can either focus on tuning growth parameters, introducing less defects, or attempt to reduce the dislocation population after defects have been produced. The latter is referred to as dislocation filtering. Within this chapter, four simple dislocations filter layer designs were tested, the aim was that one design would stand out as superior to the rest and could guide further research and development. Two samples with Ge DFLs were produced, one with thicker and one with thinner Ge layers. The other two samples utilised $Si_{0.3}Ge_{0.6}$ DFLs, again with varied DFL thicknesses. In terms of relaxation the Ge DFLs outperformed the SiGe DFLs. With the thinnest Ge DFL providing a 4% relaxation enhancement compared to a control sample of equivalent thickness without filter layers. The explanation proposed for enhanced relaxation within the Ge DFLs is that enhanced lattice mismatch strain increases the driving force for dislocation glide. Also, that alternating between compressive and tensile strain increases the likelihood of defect interactions.

There are a limited number of reports on reverse linear grading within the literature (describing grading where the Ge content increases with thickness). However, much research exists on forward linear grading, where the generally agreed optimum grading rate was limited to 10% per micron. The reverse linear grading reported here demonstrates a greatly increased grading rate of 350% per micron, while maintaining an ideal RMS roughness of 4 nm. One limitation is the incomplete relaxation achieved, which requires a solution. It was originally shown that reverse linear grading (RLG) could achieve higher grading rates than forward linear grading (FLG) when a grading rate of 60% with an RMS roughness of 4 nm was reported [55]. This work however extends the limits of grading rate yet further, opening the possibility of thinner buffer layers through rapidly graded virtual SiGe substrates.

When approaching buffer layer enhancement from a purely materials base, the DFLs provide an interesting challenge and theoretically the potential for reductions in TDD. When assessing the DFLs in a devices-based context, such as insertion into a MODQW heterostructure, a flaw

of Ge DFLs is highlighted. The Ge DFLs are thin and strained. They are also situated within a SiGe layer. This provides the exact conditions of the Ge QW that is to be deposited above the buffer layers. As such, once the device is fabricated and cooled the result is that each DFL could act as a parallel QW. Producing an undesired multiple QW system. The only clear method to circumvent this issue is to introduce an adapted form of the suspended microwire method demonstrated within Chapter 4.

Chapter 4.Suspended structures materials characterisation results

Chapter 3 investigated thinner buffer layers, firstly through varied annealing and growth temperatures and secondly using DFL's. This chapter demonstrates a method with the potential to circumvent the difficulties of defect density reduction. This method involves physical removal of the buffer layer, which previously supported the epilayers. These are referred to as suspended structures.

Current areas of research on Ge require fabrication of low dimensional structures on Si, examples include optical detection and lasing [140]. To realize these devices, buffers are required that do not rely on thick layers to dissipate threading dislocations. Currently low TDDs (3×10^6 cm^{-2}) are achieved by producing thick (~4 μm) buffer layers. One disadvantage of these thick layers is that they promote micro cracks due to the thermal mismatch between Si and Ge. Ge has a larger thermal expansion coefficient, with the coefficient for Ge = $5.84\cdot10^{-6}$ ° K^{-1} and for Si = $2.61\cdot10^{-6}$ ° K^{-1}. When Ge is deposited onto Si in the reduced pressure chemical vapour deposition (RP-CVD) reactor, deposition temperatures for relaxed Ge are ~650° C. At this temperature both Si and Ge lattices are expanded by a factor determined by their expansion coefficients, meaning Ge is expanded further from its natural lattice spacing than Si.

When growth is complete, the sample cools, Si and Ge are then covalently bonded. Both layers contract until the thicker Si layer reaches its natural lattice constant. The Ge layer that had initially expanded further has not yet reached its bulk lattice parameter, the Si is preventing it from fully relaxing. This is termed thermal mismatch strain. For the Ge layers deposited onto Si, the result is persistently 4% tensile strain within the Ge layer. 4% strain occurs if the lattice mismatch induced strain, originating from the different lattice parameters of Ge and Si, has been fully relaxed. Cracking occurs either as the material is cooled to room temperature or during post growth material processing, such as cleaving, annealing or device formation [72-76]. When the residual strain within the Ge epilayers is larger than the energy required to form two new interfaces, cracks will form. The cracks will not terminate until they meet a surface or an interface. If cracks do not penetrate the active channel they still cause electrical deterioration of devices. The prospect of cracking demonstrates devices as unreliable for commercial

applications. Additionally, thick high Ge content SiGe buffers induce self-heating effects due to the high thermal resistivity.

A key goal for Ge technology is cost-effective deposition of epitaxial Ge on industry standard Si (001) wafers, an essential component for ultra-large-scale integration (ULSI) of Ge into current industrial fabrication lines. Growth of III-V materials on Si has received much of research efforts to date. Difficulties with III-V integration originate from the large lattice mismatch, causing high threading dislocation densities (TDD). Si and Ge have 4.2% lattice mismatch and form a stable SiGe alloy over the full range of compositions. This enables epitaxy of an intermediate SiGe buffer on a Si_{sub} to permit highly crystalline Ge integration on Si. Buffers for Ge on Si integration are progressing with dislocation densities of 3×10^{6} cm^{-2} reported [141]. This chapter presents suspended microwires as a possible solution to achieve industry compatible Ge QW integration on Si. Previously, fabrication of a suspended microwire, containing a Ge QW had not been reported.

Research that recognizes the demand for thinner SiGe buffers is already published by Cecchi et al [139]. Cecchi utilizes compositional steps and grading at a low growth temperature of 475°C. The strain mapping results of suspended microwires, presented below, will support current ongoing work fabricating suspended Hall bar geometry devices.

Suspended devices can provide electrical, thermal and structural independence from the substrate material. One common method for fabricating suspended material is to machine from the backside of the substrate to produce suspended material on the wafer surface [142, 143]. Front side micromachining (defining boundaries on the front side and removing material from beneath the active channel) is more compatible with CMOS integration. Front side micromachining is commonly achieved in one of two ways. Either, using multiple isotropic and anisotropic dry etch processes. Where commonly a sacrificial protective oxide layer needs to be deposited, producing the potential issue of high temperature processing steps [144]. Alternatively, wet etchants are used in combination with sacrificial oxide layers located below the active layer. Depositing a highly crystalline channel layer above an oxide layer is not conducive to high quality growth [145]. The method presented for suspending material has the

advantage of using a cheap, readily available, asymmetric wet etchant, that does not require a sacrificial oxide layer.

Devices have previously been produced from suspended Ge. Nam et al produced tensile strained 1.6 µm Ge membranes, reducing the band gap to increase light emission efficiency [146]. Also Audet et al produced Fabry-Perot optical modulators operating at GHz frequencies, on a Ge membrane [147]. Within our group, research has focused on large (up to 3.5 mm^2) square Ge membranes. Quality and suitability has been demonstrated within multiple publications, firstly displaying improved RMS roughness and crystalline quality of the suspended membranes, using AFM and vibration techniques [148]. Secondly, using XRD and plan view TEM, it was confirmed that the membranes were perfectly flat and that the underlying misfit dislocation network had been removed [149]. Finally, electrical measurements confirmed removal of the misfit dislocations network, demonstrated by the increase in electrical isolation of over two orders of magnitude [143]. The chapter that follows is the latest work exploring the advantages and capabilities of suspended Ge devices. The work displays suspending not only bulk Ge, but an entire SiGe/Ge/SiGe quantum well heterostructure. To our knowledge, currently no publications exist reporting a suspended microwire containing a strained germanium quantum well.

4.1. Bulk material analysed prior to micro wire fabrication

Prior to fabricating the suspended microwires (using sample 13-333), x-ray diffraction measurements were conducted on the bulk material. The results of which are shown in Figure 4.1. The black cross between Ge QW and Ge_{buffer} in Figure 4.1 shows where a fully relaxed Ge peak would occur. The QW is below the dashed line, showing it contains in-plane biaxial compressive strain (I-PBCS). The $Ge_{buffer,}$ depicted above the dashed line contains in-plane biaxial tensile strain (I-PBTS). I-PBCS within a Ge QW is advantageous due to the mobility increase it causes. Strain increases mobility in Ge by reducing the density of states (DOS) effective mass. Monte Carlo transport simulations show that 1% strain variation can reduce the DOS mass by as much as 0.15 m_0 [150]. Application of I-PBCS to Ge has another advantage, it removes the degeneracy of the light hole (LH) and heavy hole (HH) valence bands. Band separation increases mobility by limiting interband scattering. Simulations report that 2% strain

can cause up to 0.1 eV energy separation between bands [150]. These simulations highlight the importance of strain and the motivation for a study focusing on strain changes caused by suspending heterostructure material.

When designing the high mobility QW heterostructures with a broad array of applications in mind, it would be advantageous to achieve fully relaxed SiGe and Ge_{buff} layers. The lattice parameter of fully relaxed buffer layers is less likely to alter during subsequent high temperature processes, making fully relaxed buffer layers more stable. Another reason for wanting to remove the I-PBTS (from buffer layers), is that it promotes crack formation. As shown in section 3.1, relaxing the last few percent of residual I-PBTS within Ge_{buff} remains challenging.

Producing suspended QW wires requires a small amount of residual tensile strain within the buffer layers. It is not possible to produce bulk strained Ge wires from compressively strained material. The compressive strain causes the wires to bend and warp when supporting material is removed. A direct comparison of tensile and compressively strained bulk Ge membranes has been published [151], the rough corrugated surface of the compressively strained membrane is clearly visible.

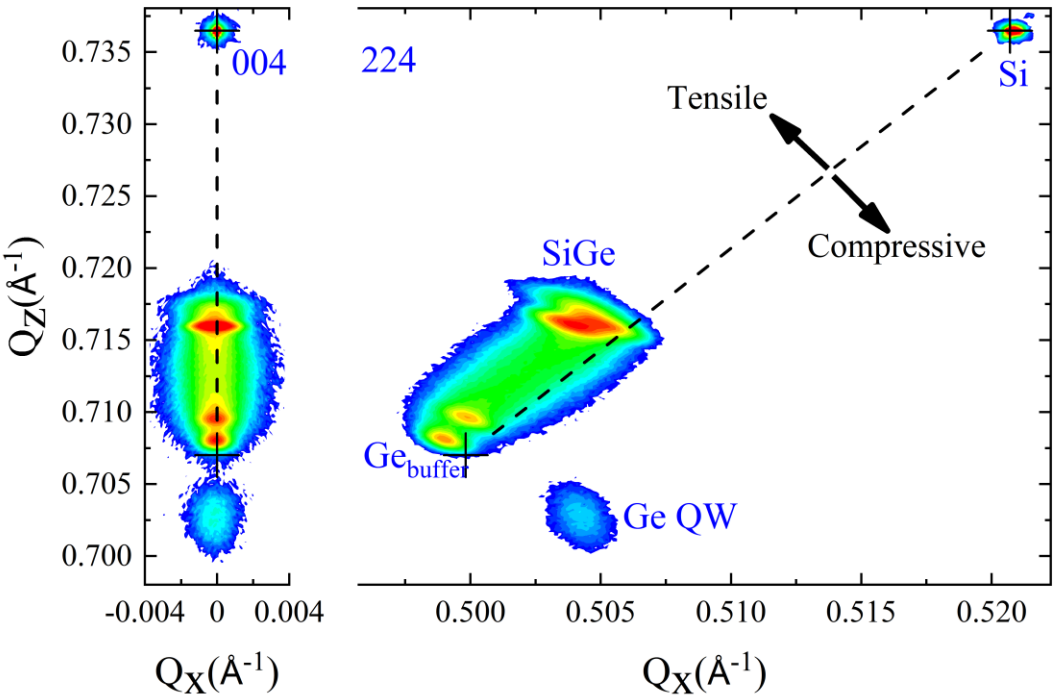

Figure 4.1 Reciprocal space map of bulk material prior to fabrication of suspended wires. Position where fully relaxed Si and Ge would appear marked with black crosses and connected by dashed line.

4.2. Fabrication of suspended quantum well microwires

The bulk material (for sample 13-333) was produced within an industrial type RP-CVD reactor at the University of Warwick. The material is deposited on an n- Si (001) wafer. Initially, a 600 nm intrinsic Ge layer is deposited. This layer has required intensive prior research to optimise growth of a thin crystalline layer with 4.2% lattice mismatch [152]. The buried Ge_{buff} layer facilitates the advantages of reverse linear grading (RLG) to be utilized over standard forward linear grading, for more detail see [55]. The RLG starts from pure Ge and grades up to $Si_{0.3}Ge_{0.7}$. Above this is deposited $Si_{0.3}Ge_{0.7}$/Ge/ $Si_{0.3}Ge_{0.7}$, as shown in Figure 4.2. To accommodate the 3% lattice mismatch, the 20 nm Ge layer deforms elastically to include 0.9% I-PBCS, the advantages of which were explained in section 4.1.

The discontinuity in energy bands in a $Si_{0.3}Ge_{0.7}/Ge/Si_{0.3}Ge_{0.7}$ stack, enhanced by I-PBCS causing a narrowing of the band gap in Ge, leads to a square potential well. The insertion of a delta doped boron layer above the Ge active channel modifies the electric potential, forming a triangular potential well with the carriers localised to the Ge/spacer layer interface. Modelling on Nextnano (completed by Maksym Myronov) calculates the depth of the well as ~250 meV. The structure is completed with a 3 nm Ge cap to prevent subsequent unwanted alteration of the structure during device processing.

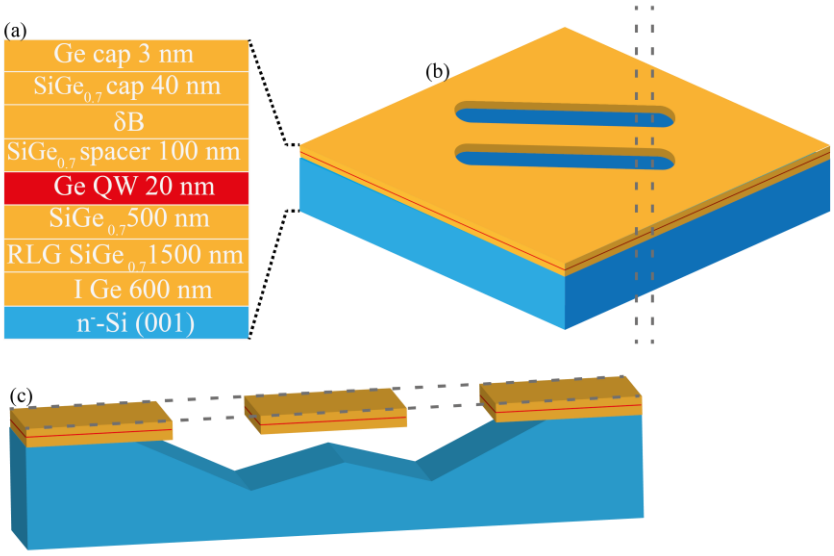

Figure 4.2 (a) Schematic diagram of heterostructure layers for sample 13-333. (b) Schematic diagram of one individual microwire showing location of expanded cross section. (c) Expanded cross section of micro wire, highlighting the under etching that occurs along the 111 planes.

Microwire arrays were fabricated from the bulk material in a top down process. Photoresist was applied to the surface to define the wire locations. Exposure and development was completed using standard photolithography techniques. To etch down through the heterostructure (orange layers of Figure 4.2) to the Si_{sub}, inductively coupled plasma (ICP) etching was used. The etchant gases comprised a mix of SF_6 and O_2. This resulted in 3 µm deep pits that form the side walls of the microwires. ICP etching is required to penetrate the Ge layers as they are highly resistant to tetramethylammonium hydroxide (TMAH) etching. Finally, the sample was submerged in a 25% wt. TMAH bath for 12 hours at 90° C. This etchant selectively etches the Si {001} planes while etching is restricted by the {111} planes. The TMAH connects the dry etched pits, etching underneath the buried 600 nm Ge_{buff} layer which now forms the

bottom face of the microwires. Each microwire is left suspended between Si supports at either end.

4.3. Strain mapping of suspended quantum well microwires

Micro X-ray diffraction (μ-XRD) measured the tilt and strain state of both a suspended wire and the surrounding bulk material. Micro Raman, which is a common technique for extracting strain values, cannot deconvolute strain from crystallographic tilt. However, XRD provides the ability to calculate strain and tilt independently, providing a more accurate value for strain. Extracting tilt from strain measurements is notably important for suspended structures, as large tilt variations occur at the transition from bulk to suspended material. Another advantage of μ-XRD is the small (~2.5 μm) spot size achieved by focusing the incoming X-ray beam using a compound refractive lens. This permits high resolution of surface structures such as the microwires presented in this chapter.

The SEM image in Figure 4.3 displays the black etch pits where the epilayers have been removed by a dry etch and subsequent wet etch process. The pits join beneath the intermediate material which forms the suspended microwires. Scale bars show the size of the microwires as 150×15 μm. The green dashed square shows the sampling location area of the data presented in Figure 4.5. The red dashed line shows the sampling location of the line scan data presented within Figure 4.6.

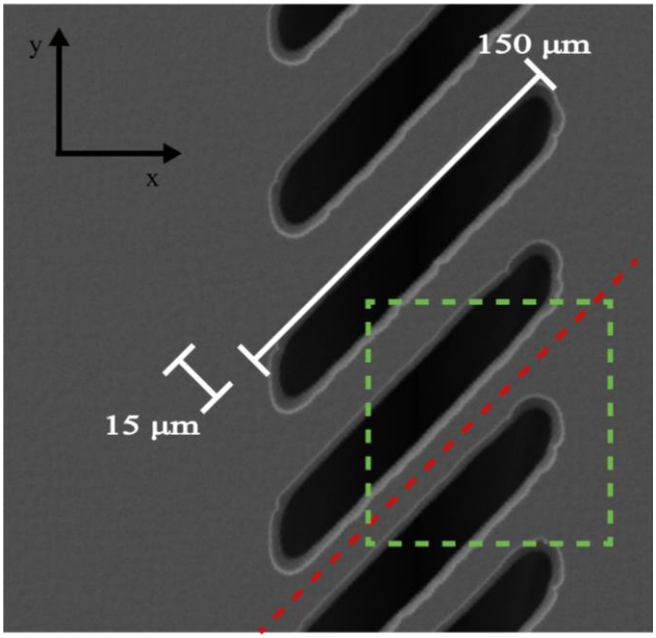

Figure 4.3 SEM image of suspended QW Microwires. Scale bars for widths and lengths of wires is included. Red dashed line displays location of XRD line scan. Green dashed square shows location of XRD area map.

The µ-XRD measurements were conducted at the DLS on beamline B16. The set up included a five-circle diffractometer combined with a PILATUS 300 K area detector. X-rays of wavelength 14.6 keV (0.849 Å) were focused to a spot size of ~2.5 µm. The small spot size combined with a (~0.5 µm) high precision (x, y, z) translational stage permitted the microwires to be rastered through the beam producing an area map of strain variations over the sample surface, presented in Figure 4.5.

The PILATUS area detector instantaneously captures a range of 2θ and γ values, including reflections for SiGe, Si and Ge (see Figure 4.4). A 90×90 µm surface area was scanned in 3 µm steps. The area scan was repeated 137 times, incrementing ω by 0.01° between each scan.

The format of collected data is an intensity profile (for each spatial point in the area map) as a function of ω, γ and 2θ. An intensity profile as a function of ω and 2θ, f(ω,2θ), was produced by compressing along the γ coordinate axis. Fitting gaussians to f(ω,2θ) provides ω and 2θ values for all Bragg peaks. To obtain γ information compression was repeated along ω, producing f(γ,2θ). Using standard formulae [153] peak positions were converted to inverse

lattice coordinates, atomic spacing units and finally strain values. All data that follows refers to the (115) reflection with a tilt correction applied calculated from the symmetric (004) reflection.

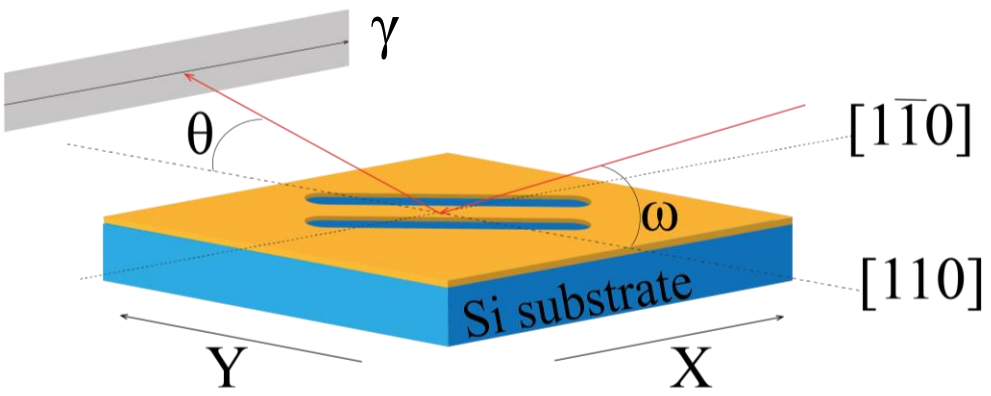

Figure 4.4 Schematic diagram of sample orientation for µ-XRD measurements. Relation between coordinate axis, diffraction angles and crystallo-graphic planes included.

The 90×90 µm strain map in Figure 4.5 covers both bulk and suspended material. The colour map scale covers perpendicular strain values from 0.92 to 1.03%. White areas of the colour map represent where dry etching removed all deposited layers, etching down into the Si_{sub}. Yellow areas of the colour map represent the suspended microwires where TMAH has etched underneath the heterostructure, removing an upper region of the Si_{sub}. Blue regions, depicting lower strain values, represent the bulk material, unaltered since deposition. It is clear from Figure 4.5 that the suspended material has a larger component of out of plane strain compared to the bulk material. The maximum strain shift calculated represents a 0.9% increase in out of plane tensile strain. This corresponds to a small increase of the desirable IPBCS.

Previous work [149, 153] on suspending bulk material has reported decreased IPBCS. The Ge QW reported here displays the opposite behaviour; on suspension, an increase of IPBCS occurs. The strain change observed diverges from previous results due to the buried tensile strained Ge_{buff} layer. Prior to suspension the 600 nm Ge_{buff} contained 1.04% tensile strain. When the Si_{sub} supporting the Ge_{buff} is etched away the in-plane lattice parameter of the Ge_{buff} decreases, reducing the tensile strain contained within the Ge_{buff} to 0.04%. Prior to etching the thermal mismatch between the Si_{sub} and Ge_{buff} was maintaining the Ge_{buff} in a tensile strained state. Once the Ge_{buff} is released form the Si_{sub} it effectively becomes the new substrate for the

heterostructure, relaxing towards its bulk lattice parameter. The Ge QW and SiGe layers contract with the Ge_{buff} exhibiting a decreased in-plane lattice parameter. This is the source of the increasing IPBCS within the Ge QW layer due to suspension of the microwires. Previous published work on bulk Ge wires reported strain variation across the width of the wires, with higher relaxation at the edges compared to the centre line. This is not observed in this current work. This is interpreted as a thickness dependant effect. The bulk Ge wires were 60-700 nm thick, whereas the devices here are >3 µm thick. The extra thickness in this case is required to produce a high-quality reverse linearly graded buffer layer.

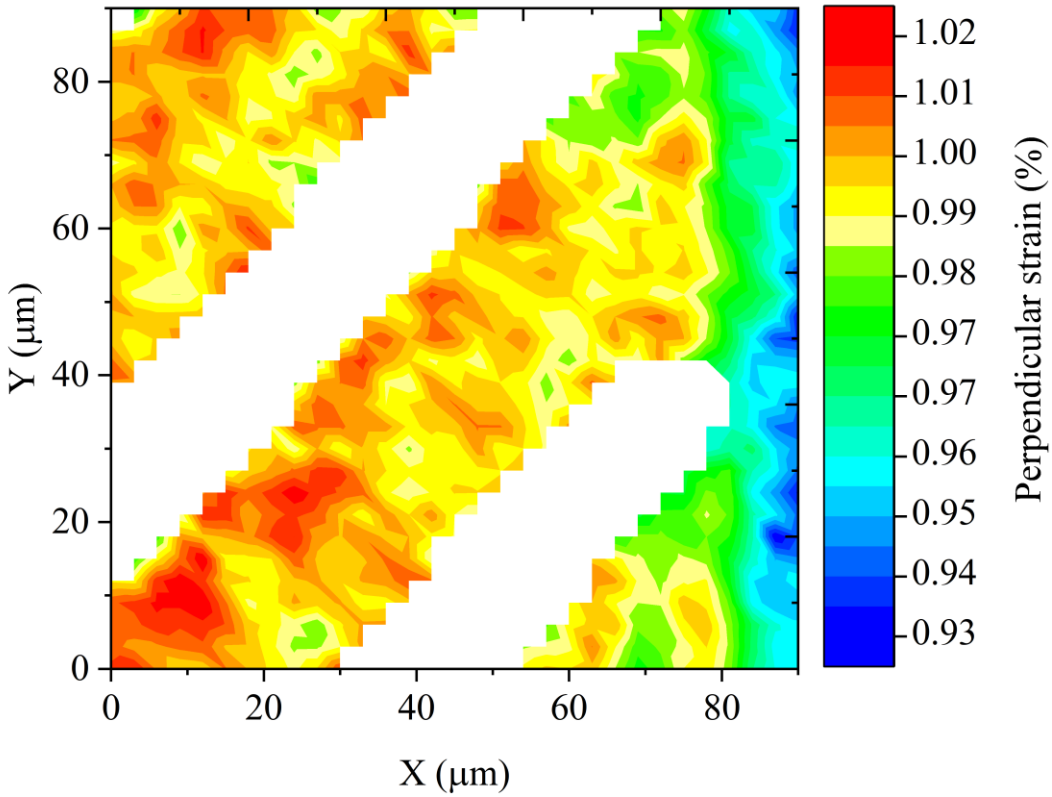

Figure 4.5 Real space area scan of suspended Ge QW microwires. Color map shows variation in the out of plane tensile strain for the 20 nm Ge QW, calculated from the (115) reflection. Tilt corrected, calculated from the (004) reflection.

The red line scan shown in Figure 4.6 traces from bulk material along the entire wire and back onto bulk. The location of the line scan is shown in Figure 4.3. Line scan results confirm the area map data with a 0.7 - 0.9% increase in out of plane tensile strain, corresponding to an increase of desirable in-plane compressive strain, on suspension. The results show that strain variation is symmetrical at both ends of the micro-wire. The blue (area map) data sampled from

identical real space coordinates as the red line scan display good agreement, confirming the validity of the measurements.

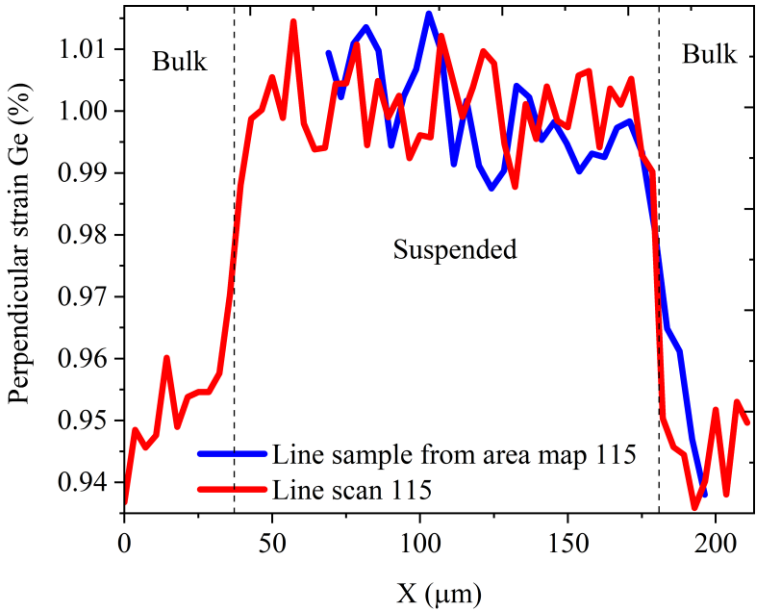

Figure 4.6 μ-XRD line scan along microwire shown in red. Plotted parameter is out of plane tensile strain for Ge QW layer. Blue line displays data sampled from the area map in Figure 4.5. Blue data is sampled from the same real space coordinates as the red line scan. Sampling regions for both sets of data shown in Figure 4.3.

4.4. Conclusion

Suspended structures isolate epilayers from the substrates they are deposited upon. This can provide electrical, thermal and even partial strain isolation. Electrical isolation can aid in reducing parallel conduction and remote impurity scattering, both of which degrade the electrical transport properties of epilayers. The high-resolution micro XRD performed at the Diamond Light Source is key to spatially resolving the strain variations. Facilitating comparison of the strain state within the suspended micro-wire and the bulk material supporting the wire.

Reducing the tensile strain within the Ge_{buff} by suspending the microwires reduces the chance of microcrack formation. Attempting to suspend a Ge QW invites complications, as explained previously the QW layer must contain IPBCS. Compressively strained bulk material cannot be suspended as the strain would cause the material to warp and crumple when the supporting substrate was removed. The buried Tensile strained Ge_{buff} provides a solution to this problem.

The tensile strained Ge_{buff} layer relaxes, reducing its tensile strain, when the Si_{sub} supporting it is etched away. This process firstly removes the issue of crack formation due to residual tensile strain. Secondly it preserves and slightly enhances the biaxial compressive strain with the QW layer. This will cause a small increase in mobility, more importantly without the buried tensile strained layer it would not be possible to suspend a compressively strained channel layer.

The top down process for fabricating suspended QW microwires is non-destructive and readily scalable to full wafer processing. The method presented is applicable to any material system comprising a heterostructure with residual tensile strain, avoiding crack formation is an advantage of this method. The suspended microwires within this chapter represent the first demonstration of suspending a heterostructure containing a strained Ge QW.

Chapter 5. FQHE transport results

Previous chapters focus on improving buffer layer technology within MODQW heterostructures. These structures are designed to provide high mobility channel layers, ideal for highly sensitive electrical measurements. The FQHE requires high mobility samples, where mobile charge carriers experience minimal scattering events. This chapter displays FQHE measurements of the current highest mobility Ge QW. The results displayed represent the deepest probe of the FQHE, within Ge, to date.

The quantum Hall (QH) effect arguably contains some of the most intriguing and elegant phenomena within physics. Research efforts within this area continue to gather momentum, with both theoretical and experimental research driving the forefront of our understanding. Examples of current topics of great interest include topological insulators [154], which stems from the quantum Hall effect. The quantum anomalous Hall effect [155], which describes the quantum Hall effect with an absence of Landau levels. Lastly the quantum spin Hall effect [156]. This describes the flow of spin currents instead of charge currents. These areas represent the most

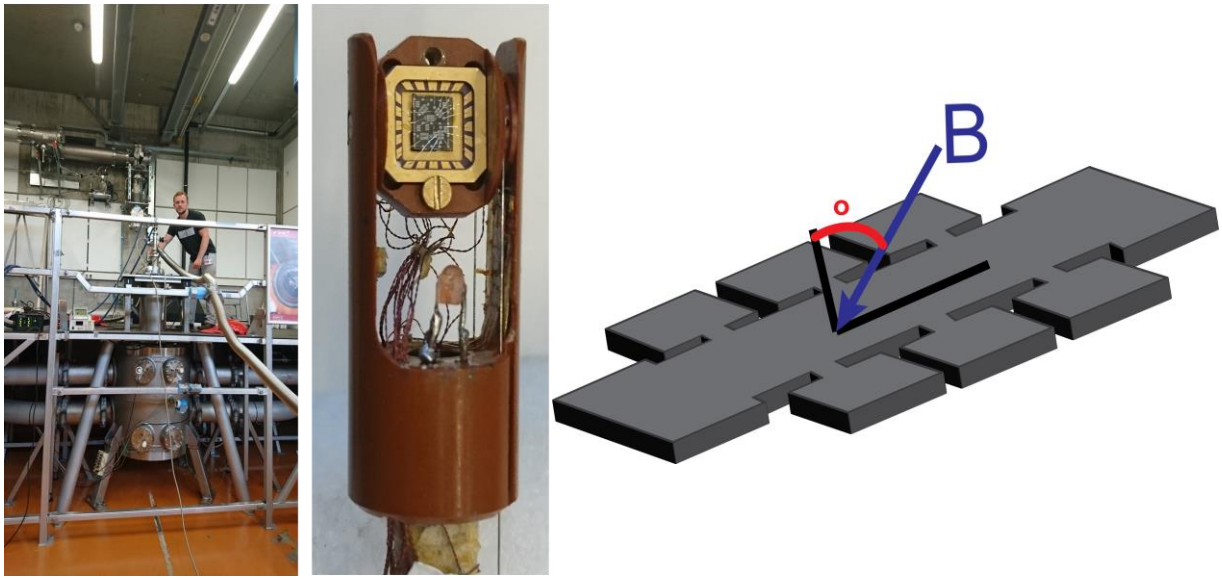

Figure 5.1 Optical images of equipment setup at HFML, Radbound University, Nijmegen. (left) Water cooled Bitter magnet with top loading cryogenic sample rod inserted. (right) Schematic diagram of the 0 degree hall bar alligned along <110>, convention for labelling angle of rotation between sample normal and incident magnetic field (B) is included. (middle) Rotating sample holder with infrared LED. Chip package containing sample is loaded. Sample inside chip package shows the different surface orientations of Hall bar that are all wire bonded.

recent branches of the QH effect to be developed. Since its discovery nearly 40 years ago research into the underlying physics of the QH and FQHE has not ceased. There remain many unanswered questions, especially relating to the FQHE. To date, an all-encompassing theory explaining all experimental observations has not been achieved.

The FQHE, explained through composite fermion (CF) theory [2-7], gives an unusual opportunity to observe the blending of particle and condensed matter physics. The striking behaviour of an electron transforming into a boson [8], through binding with magnetic flux, renders the FQHE a unique merging of particle and solid-state physics.

FQHE measurements require low temperatures and high magnetic fields. All FQHE measurements were conducted at the High Magnetic Field Laboratory (HFML) in Nijmegen. The equipment, shown in Figure 5.1, permitted continuous magnetic field sweeps from 0 to 25 T at a base temperature of 350 mK. Six Stanford research lock-in amplifiers were used, facilitating resistivity and Hall measurements, conducted on two Hall bar surface orientations simultaneously. The measurement theory is explained in section 1.4.1. The ability to rotate the sample in situ provides a means to probe extra degrees of freedom within FQHE states. Sample rotation maintains the total applied magnetic field (B_{tot}) and therefore the Zeeman energy, while reducing the perpendicular component of applied field (B_{perp}), therefore reducing the gap energies. Field rotation measurements are demonstrated within section 5.1. Illuminating the sample surface with an LED alters the carrier density at low temperatures (as displayed in section 5.4). The extra degree of freedom, varying the carry density, while fixing all other parameters provides information on carrier density limited processes.

Sample 13-335 is used for all FQHE measurements, it currently represents the highest mobility Ge 2DHG. The layer structure of sample 13-335 is displayed in Figure 5.2. The carrier mobility, as determined from thermal activation measurements of low field SdH oscillations, is $1{,}300{,}000\ \mathrm{cm^2V^{-1}s^{-1}}$, as published in [13]. This mobility value demonstrates the efficacy of MODQW heterostructures at increasing the Ge mobility from its bulk value of $1900\ \mathrm{cm^2V^{-1}s^{-1}}$. The carrier density as determined from the period of SdH oscillations in inverse magnetic field coordinates is $p_s = 3 \times 10^{11}\mathrm{cm^{-2}}$, as published in [13].

Figure 5.2 displays the structure of the 1.3 million mobility sample, 13-335. Its design is classed as a MODQW heterostructure, the advantages of which are explained in section 1.2.7. The buffer layer comprises a fully relaxed intrinsic Ge layer, followed by a reverse linearly graded SiGe buffer layer. Further work on developing graded SiGe buffers is presented in 3.2. A 30 nm spacer separates the boron doped supply layer from the 2DHG that forms within the QW layer. This permits diffusion of carriers into the QW layer at raised temperatures, while introducing an energy barrier forming a QW at reduced temperatures. The SEM image within Figure 5.2 shows the orientation of Hall (R_{xy}) and resistivity (ρ_{xx}) measurement probes during the measurements that follow. An optical image within Figure 5.2 displays multiple orientations of Hall Bar on the sample surface, facilitating simultaneous transport measurements along different crystallographic axes.

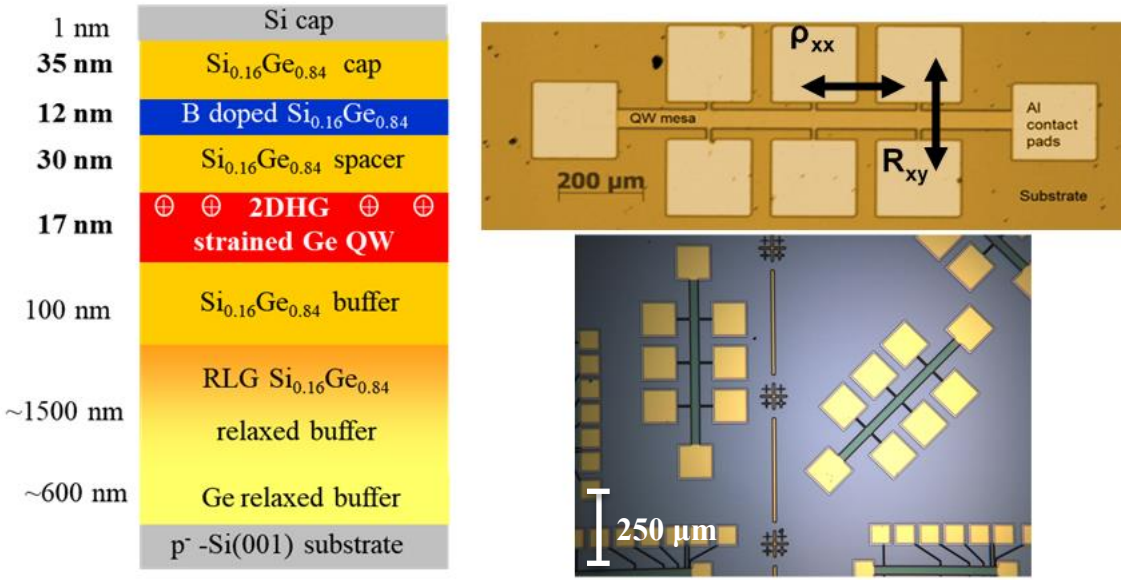

Figure 5.2 (left) Schematic diagram of layers within sample 13-335. Circles containing plus sign represent the positive charge carriers of the 2DHG. (top right) SEM image of one Hall bar, orientation of measurement probes for Hall and resistivity measurements are added. (bottom right) Optical image showing two orientations of Hall bar located on the heterostructure surface.

As displayed in the TEM image of Figure 5.3 sample 13-335 represents a thick 2.4 µm sample. This facilitates the low defect density upper layers of the sample. Remote impurity scattering from defects near the QW reduces mobility, hence why great care is taken to produce high crystal quality buffer layers beneath the QW. The reverse linearly graded SiGe buffer displays superb defect confinement. Defects that have propagated perpendicular to the growth

direction can be observed. This is fundamental for reducing defect densities in subsequent epilayer growth.

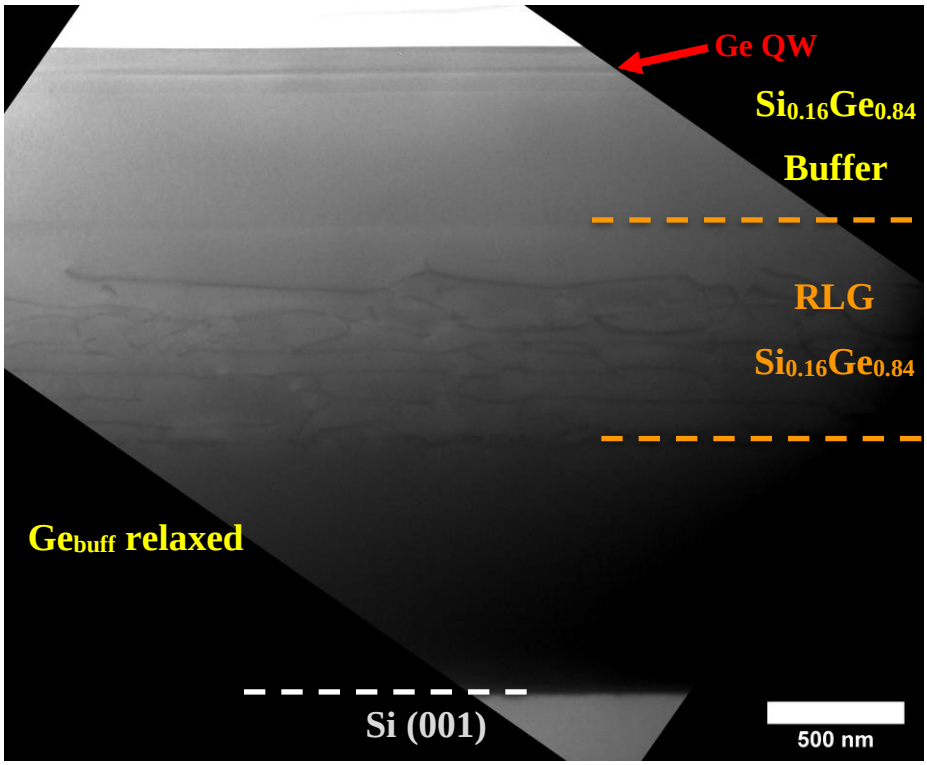

Figure 5.3 TEM image for sample 13-335. Entire heterostructure is 2.4 µm thick. Efficiency of the reverse linear graded region at containing defects is observed. With an observation of a defect free $Si_{0.16}Ge_{0.84}$ buffer layer beneath the Ge QW. This layer structure is shown within Figure 5.2.

The results within Figure 5.4 were produced from Hall and resistivity data collected on a closed cycle cryostat. Sample 13-335 was loaded into an evacuated chamber situated within a homogenous variable magnetic field. A 1 µA current was applied along the Hall bar Mesa while a 100 mT field was applied normal to the sample surface. The orientation of the current and the field are both flipped 180° but not simultaneously. The four measurements are then averaged to provide a value independent of geometric imperfections. The formulas from section 1.4 were used to calculate the sheet density and mobility values presented in Figure 5.4. These values were calculated for 26 different temperatures from RT down to 18 K, one can then observe how the properties of the entire heterostructure vary during cooling. Within Figure 5.4 the plateau in carrier density is confirmation that a 2DHG has been formed within the QW of sample 13-335. At these low temperatures carriers within bulk levels have frozen out, no longer contributing to

conduction. However, within the QW conductive mobile carriers display a high mobility of 836,000 $cm^2V^{-1}s^{-1}$ at 18 K, which continues to increase as temperature is reduced further. The results in Figure 5.4 represent preliminary tests to check the QW presence before completing lower temperature higher field measurements.

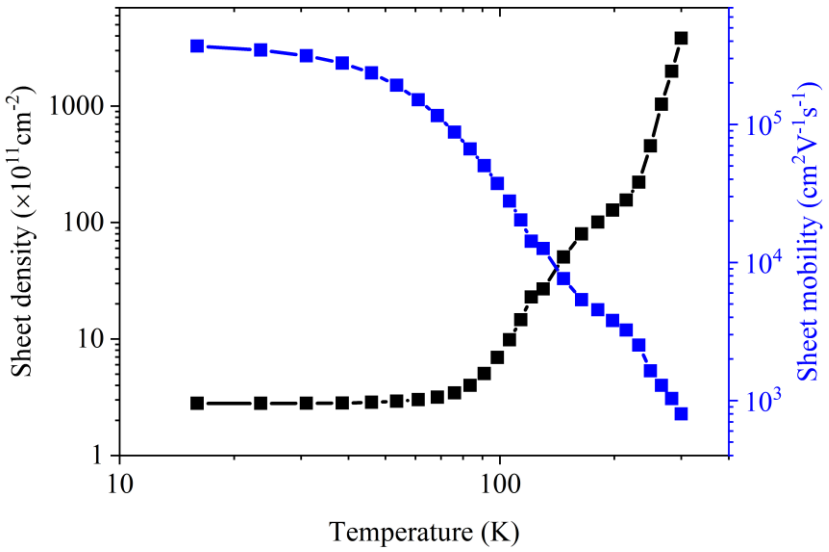

Figure 5.4 Mobility and sheet density values for sample 13-335 plotted as a function of temperature from 300 to 18 K.

The data within Figure 5.5 was measured within a different system to the data within Figure 5.4. This set up contains a superconducting magnet capable of continuous field sweeps. It also utilises a second cooling stage with ^{3}He capabilities to reach down to 370 mK. The results within Figure 5.5 display Shubnikov de Haas (SdH) oscillations for sample 13-335 within a 0 to 1.1 T field sweep at 370 mK. The current applied was 100 nA at 197 Hz.

The high resolution SdH oscillations in Figure 5.5 are added to supplement the magnetic field data presented subsequently. Subsequent low field data is of lower resolution due to equipment limitations at the HFML. The oscillations within Figure 5.5 were analysed, providing the carrier density of $p_s = 3 \times 10^{11} cm^{-2}$ quoted previously. An example of carrier density extraction, including step by step images of data processing is presented subsequently (in section 6.2). The origins and theory of SdH oscillations is described in section 1.4.3. The Zeeman splitting, originating at 0.34 T is clearly visible, identifiable by the splitting of one oscillating period into two.

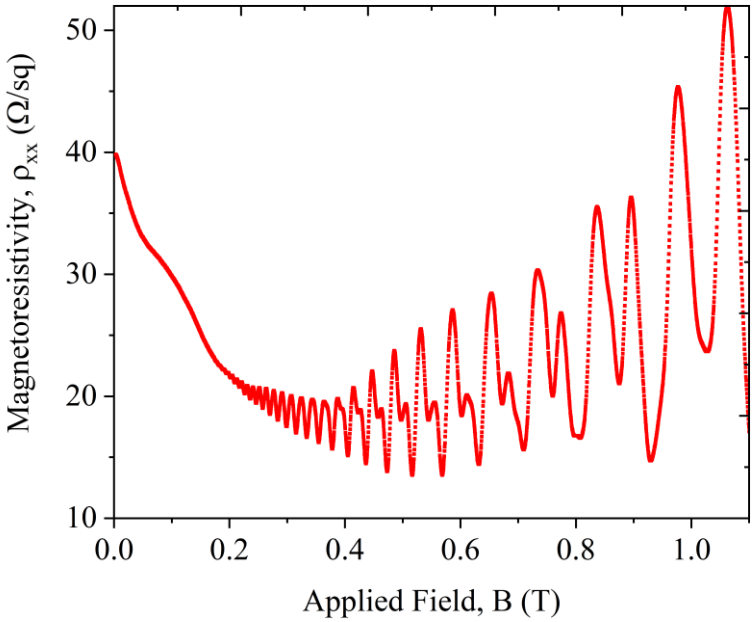

Figure 5.5 Low field SdH oscilations for sample 13-335. Magnetic field sweep ranges from 0 to 1.1 T at a temperature of 370 mK. Zeeman splitting is first observed at 0.34 T and continues to developed towards 1.1 T.

Figure 5.6 displays the XRD results for sample 13-335. The XRD data presented as a RSM within Figure 5.6 includes both the symmetric 004 (left) and asymmetric 224 (right) scans. The primary use for the symmetric scan is to determine that the crystalline layers are not tilted with respect to the substrate, an absence of tilt is shown by Bragg peaks aligning in Q_x. For the asymmetric scan the measured peak positions are compared to where a fully relaxed peak, for identical composition material, would occur. Red crosses are added to display where a fully relaxed Ge and Si peak would be expected. Within reciprocal space, an increase in Q_x equates to a reduction of the in-plane lattice constant. Correspondingly, an increase in Q_z equates to a reduction of the out of plane lattice constant. Compositional changes for fully relaxed SiGe, shift its Bragg peak along the black line within Figure 5.6, with higher Si concentration shifting the peak closer to the elemental Si peak. All Tensile peaks will be located above the black line and all compressive peaks will be located below the black line, as indicated by the red labels. When lattice spacing is reduced within the in-plane orientation it naturally expands in the out of plane direction, producing a tetragonal distortion. Hence strained peaks will move perpendicularly away from the black line within Figure 5.6.

The XRD data of Figure 5.6 shows the compressively strained Ge QW. The Ge QW is fully strained to the SiGe layer, depicted by the QW peak conforming to an identical Q_x value. The peak is weak (compared to the buffer layer peaks) as the QW layer is only 17 nm thick, as verified by TEM measurements. The graded region is shown as a smeared band of high intensity signal between the Ge and SiGe peaks. What is observed from Figure 5.6 is a mismatch between the final composition of the graded SiGe and the constant composition SiGe grown subsequently. If this is too great it can cause issues with initiating new defects at this interface. This can be excluded as the TEM within Figure 5.3 displays a clean interface. The Ge buffer (Ge_{buff}) layer displays a deviation from the inserted red cross. This displays that the Ge_{buff} contains tensile strain, 4% in this case. The Tensile strain originates form the thermal mismatch between Si and Ge_{buff} layers. For a recap of XRD theory including thermal missmatch strain, see page 56 of reference [55].

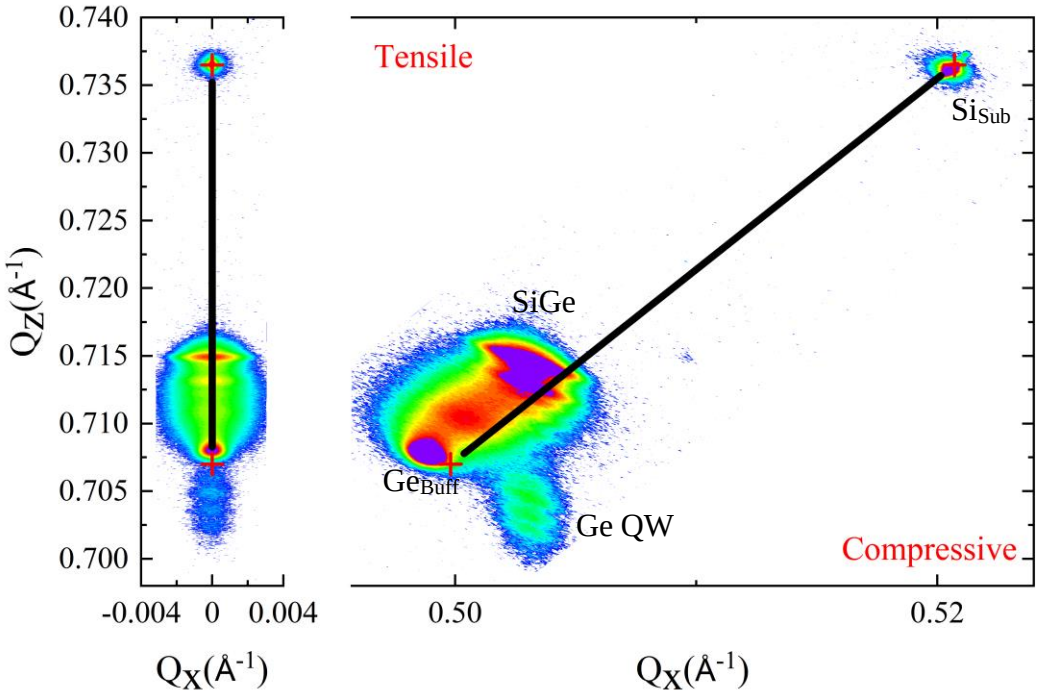

Figure 5.6 XRD reciprocal space map for sample 13-335. Symmetric 004 scan on the left and assymetric 224 scan on the right.

5.1. FQHE measurements varying the angle of applied magnetic field

The results in Figure 5.7 display magnetoresistivity data collected at the HFML using a rotating sample stage. Magnetic field sweeps at 350 mK were repeated eight times, incrementing the sample stage rotation between each measurement. Minima are labelled with their fractional filling factors. Rotating the sample within the homogenous magnetic field varies the parallel and perpendicular components of magnetic field that interact with the sample. This is a powerful experimental technique that is reported in multiple publications [157-160]. Rotated field measurements can probe the spin polarization of each FQHE state. The separation between Landau levels and therefore the gap energy, is solely dependent on the perpendicular component of magnetic field (perpendicular to the sample surface). Whereas, the Zeeman splitting energy varies with the total applied magnetic field. Therefore, by rotating the field we can study each fraction as the Zeeman splitting energy is varied. For an introduction to FQHE theory see section 1.5.

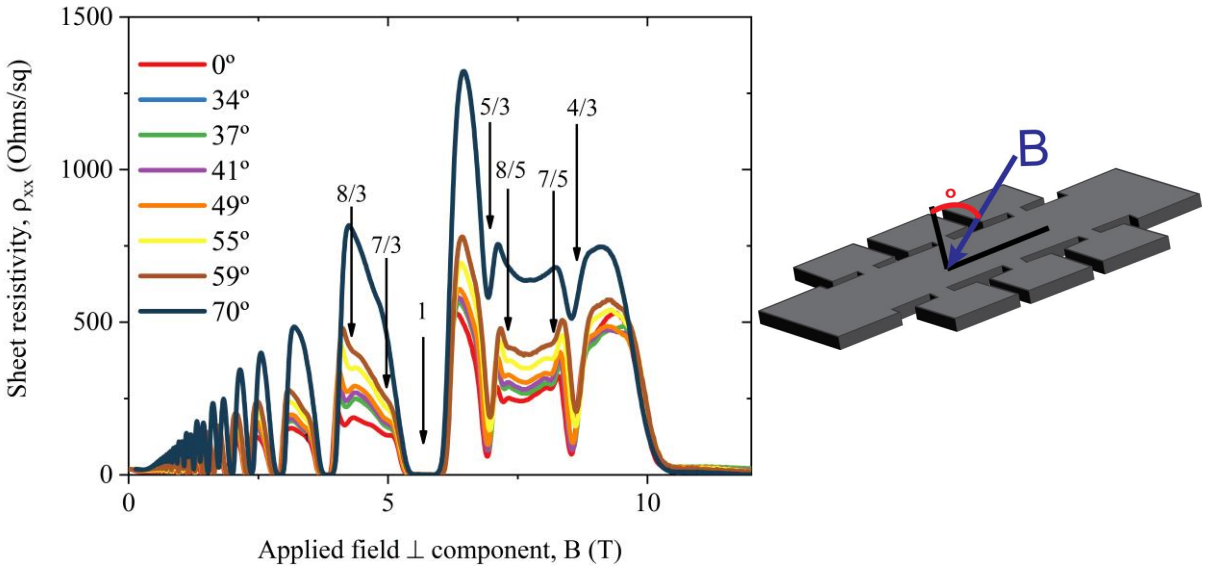

Figure 5.7 (left) FQHE features at different angles of applied magnetic field. The features are normalized by plotting the perpendicular component of magnetic field, resulting in fractions aligning horizontally despite rotation. Sample 13-335 measured at 350 mK with a 100 nA, 13 Hz AC current. (right) schematic diagram displaying convention for measuring angle between hall bar orientation and applied magnetic field orientation, zero degrees rotation descibres the situation where the inpinging field is normal to the sample surface. Ninety degree rotation describes a situation where the magneitc field is alligned along the current path of the hall bar (for a 0 DEG Hall bar alligned along the <110>).

It has been observed [161, 162] that for specific fractions, notably $\upsilon = 2/3\,, 4/3$ and the infamous $\upsilon = 5/2$ [163] that an initially spin unpolarized state will, as the Zeeman energy is increased through field rotation, become fully spin polarized. This is observed through resistivity minima disappearing and reappearing as the rotation angle is increased, termed reentrant peak behaviour. The underlying physics is described by two neighbouring Landau levels that are spin-split, to the extent where the spin up and spin down components, from the neighbouring levels coincide. The features within Figure 5.7 are normalised so that FQHE features align in applied field. This is achieved using the field rotation angle (θ) and the relation $B_{\perp} = 1/\cos(\theta)$. The absence of reentrant peak behaviour, over a broad range of angles, in Figure 5.7 suggests a large effective g factor (g^*_{CF}) for composite fermions, analogous with the g factor of bare charge carriers within a Ge 2DHG. Similar effective g factors for bare carriers and CFs was also reported by Du et al [164] while studying electrons in GaAs around $\upsilon = 3/2$.

An estimation of the g factor can be extracted by comparing the onset of odd and even IQHE oscillations at low field values. A caveat to using this g factor is that the low field g-factor relates to single particle dynamics, whereas the effective g factor in the FQHE regime relates to a many-body system. One cannot conclusively state that these two g factor values will be identical, they are likely to demonstrate some level of variation. However, they are not independent and are commonly assumed to be similar [164]. The extracted value of $g^*_{CF} = 7.4$ has been published previously [165]. The large g^*_{CF} factor (an order of magnitude larger than in GaAs) presents the Ge system as a fully spin polarized system. This feature of the Ge 2DHG system can be advantageous in that it provides a simple system. Material systems with lower g factors contain variations in spin polarization which can mask or be convoluted with other observations. At coincidence points, where spin split Landau levels either cross, with no gap appearing, or anti-cross generating energy gaps, interesting effects have been observed: energy gaps disappear and reappear, and enhanced g factors have been reported [166]. The Ge system is well suited for studying finite thickness effects, energy gap enhancement and other phenomena that could be masked by spin transitions. There is a clear alternative to this positive, the Ge system is incompatible for a study of high field spin transitions. To include a robust g factor value, a collaboration with Mizokuchi et al measured the g factor in an analogous strained Ge QW structure [167]. Mizokuchi fabricated gated 1D quantum wires using the Ge MODQW heterostructure material. Through observing Zeeman splitting of conductance measurements

they calculated an out of plane g^* factor of 11 ± 1. This is larger than the approximated g^* value of $g^* = 7.4$ for sample 13-335, adding weight to the interpretation of a fully spin polarised CF system.

The band structure of a SiGe/Ge/SiGe heterostructure (as represented in Figure 1.3) presents the 2DHG formed as a comparatively simple system. The strain within the Ge QW layer splits the HH and LH bands (as displayed in Figure 1.2), separating the energy bands that are degenerate in relaxed Ge. This energy band separation provides a single band system, avoiding complications that arise from interband scattering. Other material systems, such as GaAs, that contain more complex degenerate band systems, consequently provide more complex FQHE behaviour. One disadvantage of the inter and intra band scattering is that some expected fractions are suppressed or absent from the FQHE results.

This is a possible explanation why the FQHE results, within this chapter, display a multitude of fractions persistent to remarkably high temperatures. It is evident within the literature review, that other material systems, with comparable mobility, do not display a comparable number of fractions to Ge. It is also notable that fractions appear to persist to higher temperatures within Ge, compared to alternative III-V material systems. For a collection of fractions observed in other material systems Table 5.2 is included.

An interesting feature of Figure 5.7 is how the largest rotation angle of 70° appears to show a marked increase in sheet resistivity and reduction in features, compared to the other rotation angles. To investigate further, the resistivity minima values from Figure 5.7 are measured for each rotation angle. These values are normalized to the resistivity value at $\upsilon = 3/2$ and the results are plotted in Figure 5.8.

Figure 5.8 displays that, relative to $\upsilon = 3/2$, each minimum displays a monotonic increase in resistivity with increasing field angle. The enhanced resistance values are normalized by dividing out the resistance value at $\upsilon = 3/2$. Even denominator states, such as (3/2), represent the zero-effective field state for composite fermions, as described in section 1.5.3. This state is a Bose condensate, representing a compressible state. Normalizing by the effective zero point removes the possibility that the observed effect in Figure 5.8 could be due to changes in CF

mobility. It is observed that the fractions get stronger when observed at higher total applied field. This dependence of the resistivity on the total applied field would not be expected in an ideal sample. The perpendicular component of field dictates the energy gaps which are consistent for a specific fraction. Total field should not impact energy gaps it should only impact Zeeman energy. In an ideal sample the minima in ρ_{xx} oscillations would be delta functions when observed at temperatures approaching absolute zero. In this perfect sample the minima would display $\rho_{xx} = 0$ for all angles of applied field. The variation observed in Figure 5.8 occurs due to raised temperatures and sample imperfections.

It is possible that Figure 5.8 is the experimental observation of the theoretical predictions made by Peterson et al [48]. Within spherical systems containing a small number of carriers, Peterson compared the relative overlap of exact Laughlin wavefunctions [45] with exact diagonalized Hamiltonians. Peterson used the degree of overlap as a measure of suitability for confinement models, namely Fang Howard, Infinite square well and Zhang and Das Sarma. Explained another way, Peterson was attempting to model which states are stable, permitting observation, and which states are unstable. The measurement criteria used was to perform modelling using exact diagonalization of few-particle systems. This result was then compared to the empirical wavefunction proposed by Laughlin. The degree of overlap of the results from

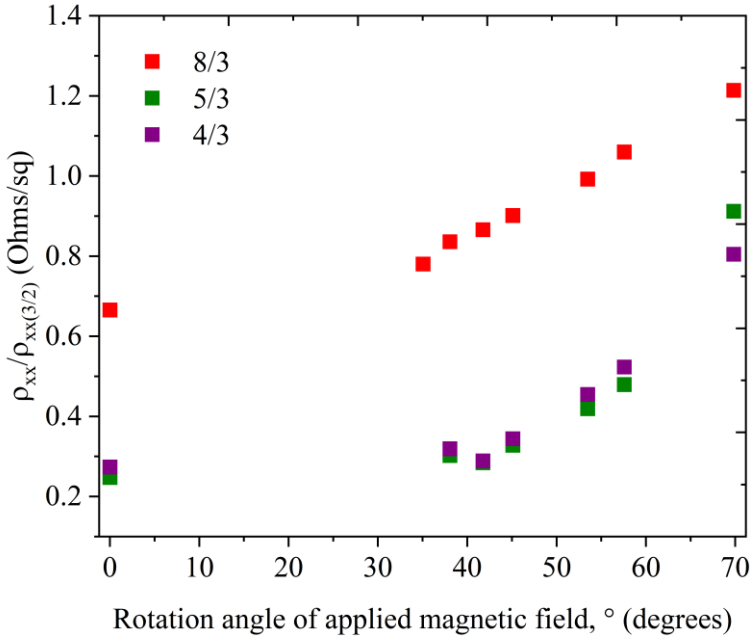

Figure 5.8 Increase in resistivity minima for three states $\upsilon = 8/3, 5/3,$ and $4/3$ caused by rotating sample in magnetic field. Resistivity values are normalized by the resistivity at $\upsilon = 3/2$.

each method was taken as evidence for which fractions would be stable within certain conditions. This method is widely recognised and is in fact how the Laughlin wavefunction was first demonstrated, leading to its current wide acceptance. It was shown that the Laughlin wavefunction had an overlap of essentially unity with the exact small-system numerical wavefunction. This is remarkable, with a large many particle system agreeing exactly with a model that contains only a few particles.

Peterson studied the impact of a tilted field on the carrier motions and Coulomb interactions. Relevant to interpreting Figure 5.8, is Peterson's prediction for a monotonic increase in confinement potential and energy gaps, without any discontinuities, for a rotated field. This agrees with the results presented in Figure 5.8 presenting the coupling of a parallel field component as a likely explanation for the enhanced normalised resistivities. Essentially the in-plane component of field is coupling with the energetics in the system in more ways than was initially predicted. Compressing the carrier wavefunction softens the coulomb repulsion which can suppress fractions, especially in the LLL. Other coupling effects can also take place such as orbital anisotropy, induced by a parallel field on a 2DHG that is not perfectly 2D. It has also been predicted that for higher LLs, specifically the 5/2 state, finite thickness acts to stabilise and enhance the fractional states. This displays that a better understanding of finite thickness effects is essential, especially for higher order fractions.

One factor that differentiates 8/3 from other fractions within Figure 5.8 is the Landau level hierarchy. 8/3 is the only state within Figure 5.8 that is considered to reside in the second LL and not the LLL. The filling factors sequentially fill up Landau levels with: $0 < \upsilon < 2, 2 < \upsilon < 4, 4 < \upsilon < 6$ representing the Lowest LL, Second LL and Third LL respectively. The factor of two accounts for electron spin degeneracy, with each Landau level being filled with both up and down spin electrons. Therefore with 8/3 providing the only fraction >2 it should be clear that this fraction is the only one reported that resides in the 2nd Landau level. More data points are required to investigate potential structure within the data of Figure 5.8. What can be stated conclusively is that, relative to $\nu = 3/2$, a parallel field component increases the ρ_{xx} value of the FQHE minima. Increasing the parallel field component increases the ρ_{xx} value further. The relationship between parallel field and ρ_{xx} is proportional and monotonic, also there is a potential difference in behaviour for states in the lowest and first excited Landau levels. It should be noted

that no increase in the ρ_{xx} value at $B = 0$ was observed, returning identical ρ_{xx} values for all rotation angles.

Without normalizing to $\upsilon = 3/2$ the suppression of the minima for each fraction can be seen. Figure 5.9 shows that as we increase field rotation from 0 to 69° the magneto resistivity increases by a factor of four. It is known that the Landau level spacing is only dependent on the perpendicular component of magnetic field, which is fixed for each fraction. The advantage of germanium is that we can rule out any spin effects due to the large g factor. We can rule out any interband effects as this is a strained single band material system. Any impact on energy gap can be ruled out as the compressible Bose condensate at filling $\upsilon = 3/2$ is displaying the same behavior. Therefore, we can determine that this effect is due to the larger component of parallel magnetic field. Figure 5.9 displays that the behaviour at the highest angle of 69° could potentially fit the trend seen with the other peaks. The trend with higher rotation angles (larger B_{tot}) is an increasing rate of change in ρ_{xx}. This suggests that observing at higher angles would display a large impact on ρ_{xx} values.

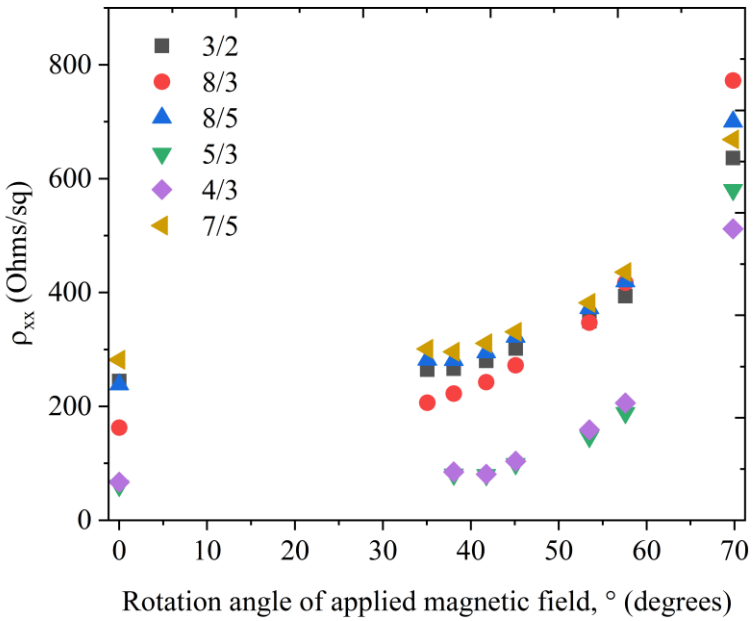

Figure 5.9 Increase in resistivity minima for the six states labelled within the legend, caused by rotating sample in magnetic field. No normalisation has been applied.

Higher field rotation angles initiate the disappearance of the higher order fractions. It can be seen from Figure 5.7 that 8/5,7/5,8/3,7/3,10/3 and 11/3 have all disappeared at the highest rotation angle. The best explanation for this suppression effect is that the parallel field is impacting the energetics of the system. This is most likely due to increased carrier localization and compression of the wavefunction of 2D charge carriers. Papic gave an intuitive semiclassical analysis of the impact of rotated field measurements. He stated that in the perpendicular field situation the cyclotron orbits are circular. However, as the field is rotated electrons orbit the tilted field axis, due to the confinement of electrons to the 2D layer, the true shape of their orbits is a projection of these circles onto the 2D plane, i.e. their shape becomes elliptical [160]. Papic's modelling predicted that at high tilt angles ~70° the system would experience a symmetry breaking, also that Landau level mixing would increase. Our findings would fit within Papic's predictions.

As the field is rotated the in-plane component of magnetic field squeezes the wavefunction in the Z direction, increasing the confinement of the 2DHG, localizing carriers in an area closer to the heterointerface. Chakraborty and Pietiläinen [168] showed that as a consequence, increasing tilt angle increases the gap. This explanation covered experimental evidence shown for $\upsilon = 3/2$ but failed to explain why rotating the field could also result in electron hole symmetry breaking.

Finite thickness corrections may be misinterpreted as merely a correction factor. Many authors compare their experimental results to theoretical modelling and are content with 50% discrepancy. It is common to see most discrepancies validated as Landau level mixing, finite thickness corrections and spin effects, that were not accounted for. With the complex nature of the FQHE this level of agreement is arguably justified. Finite thickness of the 2D system, however, may have a larger role to play in future research than was first envisaged. Peterson et al showed, in his extensive review article, that finite thickness has a different impact on states in the lowest and first Landau level, which could potentially explain the results within Figure 5.8. Furthermore, that finite thickness is in fact an essential component for stabilizing higher order Landau level states. One example was the stabilizing of the $\upsilon = 7/3\ \ (2 + 1/3)$ with increasing d (where d represents the thickness of the quasi 2D layer). This is surprising as within the LLL, finite thickness acts to weaken states, as the results of

Figure 5.7 display. Our results showing suppression of FQHE with rotating field, combined with Petersons results [48] and the discovery that finite thickness is an essential component for observing filling 5/2 [48], displays the importance of improving the understanding of finite thickness and how it couples with 2D systems.

CFs are modelled with great success as a system of non-interacting particles. The dominant length scale within a FQHE system is the magnetic length $l_0 = (h/eB)^{1/2}$. This was evident from the strong field dependence of the extracted value for the CF effective mass. Varying the finite thickness of the 2DHG introduces a new length scale into the problem, the thickness, d, equal to the average z extent of the electron wavefunction. The finite thickness of the 2D system behaves differently depending on the size of the carrier cyclotron orbits. This leads to a simpler quantity being defined, the dimensionless parameter d/l. This parameter dictates the overall impact that finite thickness effects have on a FQHE system. This understanding could present an alternative interpretation of Figure 5.9. It could be possible that a linear regime between 5 and 8 T exists. Under this analogy; above this region the highest field rotation angle has induced the symmetry breaking predicted by Papic [160]. Under this analogy between 8 and 12 T we have crossed a critical ratio of finite thickness to magnetic length. With the magnetic length becoming small compared to the finite thickness of the quasi-2D system. The alternate interpretation highlights the complexities of interpreting FQHE stabilities, there are many pseudopotentials involved. Potential impacts on FQHE states include spin effects, screening effects, finite thickness which leads to elliptical orbit projections, softening of the Coulomb interaction, increased scattering and increased Landau level mixing. Parallel fields can also cause directional anisotropy within the 2D plane and breaking of electron hole symmetries. It is therefore quite astounding the degree of accuracy that modelling achieves, with systems of only a few (<12) particle systems [160], also while not including many of the pseudopotentials impacting the system. This is testament to the fundamental nature of the FQHE. It also demonstrates how the correlated motion of carriers into CFs acts to simplify the system, acting under the motivation of reducing the Coulomb repulsion energy.

Zeeman splitting appears to initiate at 0.6 T in Figure 5.10. The resolution is low for this region of field. The individual SdH oscillation peaks contain too few data points per oscillation, resulting in the squaring of some oscillation peaks. Higher resolution data for this field range is

provided in Figure 5.5. Note, data within Figure 5.5 is collected at 370 mK, higher than the 350 mK field sweep within Figure 5.10. The low resolution occurred due to the ramp rate of the magnetic field, a higher ramp rate was required, due to equipment limitations preventing magnetic field generation for extended time periods. The zero-field sheet resistivity (B = 0) for each rotation angle displays an identical ρ_{xx}. This confirms there have been no shifts in mobility or temperature that could be misinterpreted as finite thickness effects. It can be seen from the low field data that above 0.2 T there is a marked separation between the highest angle and all other rotation angles. This would support Papic's concept of exceeding a critical ratio of magnetic length to finite thickness.

As in Figure 5.10 as the magnetic field is increased from 0° a gradual increase in the sheet resistivity is observed. This is interpreted as a finite thickness effect. A large jump is observed between 59 and 70° applied field. Wu et al [169] observed similar behaviour in an InGaAs/InP system. In this work the discontinuity was explained as a crossing of spin split Landau levels.

Modelling of a single-electron shows that LL crossing should occur for integer ratios of Zeeman energy/ cyclotron energy. This might not always be the case, LL anti-crossing and enhanced g-factors will act to modify this rule.

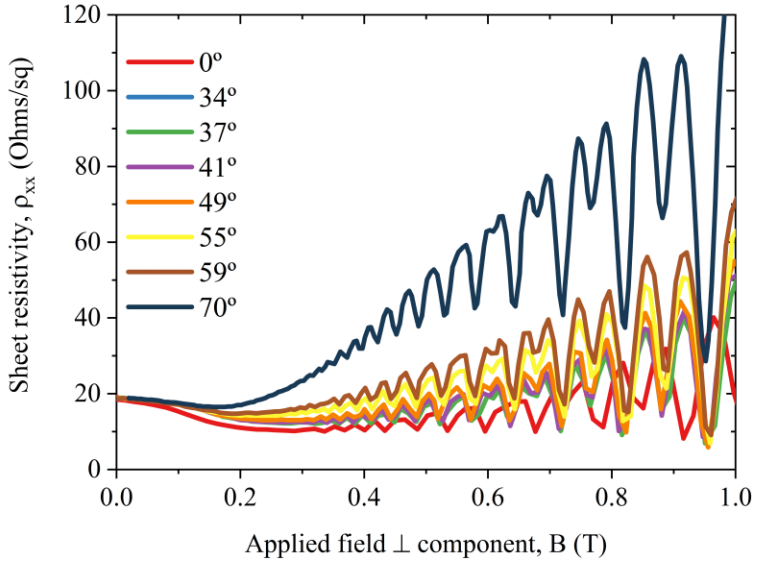

Figure 5.10 Low field SdH oscillations displaying Zeeman splitting. Data for zero-degree HB while magnetic field is rotated. Sweeps were conducted at eight different rotation angles, as shown by the legend. Field sweeps conducted at 350 mK with an applied current of 100 nA.

Thermal activation measurements conducted on this sample previously extracted a CF effective mass of $m^*_{CF} \approx 0.4m_e$. These measurements were conducted on the family of fractions originating from $\upsilon = 3/2$ and have already been published [165].

An approximation for the effective g factor ($g^* \approx 7.4$) within this sample has previously been published [165]. The g^* factor was estimated by comparing the onset of quantum oscillations for even and odd filling factors. The ratios of the magnetic field values at which oscillations began was 2 (as published in [170]). This results in the ratio of the cyclotron energy to the spin splitting energy being approximately equal to 3. The result is the approximation of the g^* factor as $(2m^*_{CF}/m^*)/3 \approx 7.4$ this uses the effective hole mass $m^* \approx 0.09m_e$ [171, 172]. Lu et al conducted thermal activation measurements on a gated Ge QW structure to extract both the in plane and out of plane effective g factor. Values displayed large asymmetry with $g \sim 28$ for out of plane magnetic fields and $g \sim 1.3$ for fields aligned parallel to the 2DHG [173]. This displays that the perpendicular g factor from our Ge MODQW is substantially smaller than reported by Lu. It is not possible to repeat the measurements of Lu to extract the in-plane g factor due to differences in carrier density, however the huge parallel g factor reported deserves validation and opens an interesting question of how this would impact rotated field measurements within Ge. Works completed by Mizokuchi et al with material supplied by the Nano Silicon group, provide measured in plane and out of plane g^* factors on material analogous to sample 13-335. Mizokushi et al fabricated 1D quantum wires from the strained MODQW Ge heterostructure material [167]. Their results return an out of plane g_* factor of 11 ± 1 and an in-plane g^* factor of 1 ± 0.2. The authors suggest that the asymmetry arises from the dominant HH character of the QW system. They also predicted that at vanishing thickness, the lowest subband of the Ge QW would approach pure HH with vanishing in plane g^* and out of plane g^* of approximately $g^* = 21$. Multiple reports of large and highly asymmetric g^* factors for the strained Ge HH system increase confidence in the claim that the system observed within sample 13-335 provides a fully spin polarised system [165, 167, 173].

5.2. Surface Hall bar aligned at 45 degrees to the <110>

Uli Zeitler published results showing that the impact of a parallel field component on a Ge QW varies, depending if it is aligned parallel or perpendicular to the current flow along the HB [174]. Uli found that a parallel field component aligned with the current direction induced a polarisation change. Whereas, a parallel field component perpendicular to the current flow did not induce a polarisation change. It was suggested that the anisotropy could result from domain structure introduced by an anisotropic 2DES.

As seen in Figure 5.2, two Hall bars are located on the sample surface, with a 45° rotational offset. The results in Figure 5.11 are from the 45° Hall bar which is aligned along the <110> orientation. This measurement was simultaneous to the 0° Hall bar data presented in Figure 5.8 with identical temperature and applied current.

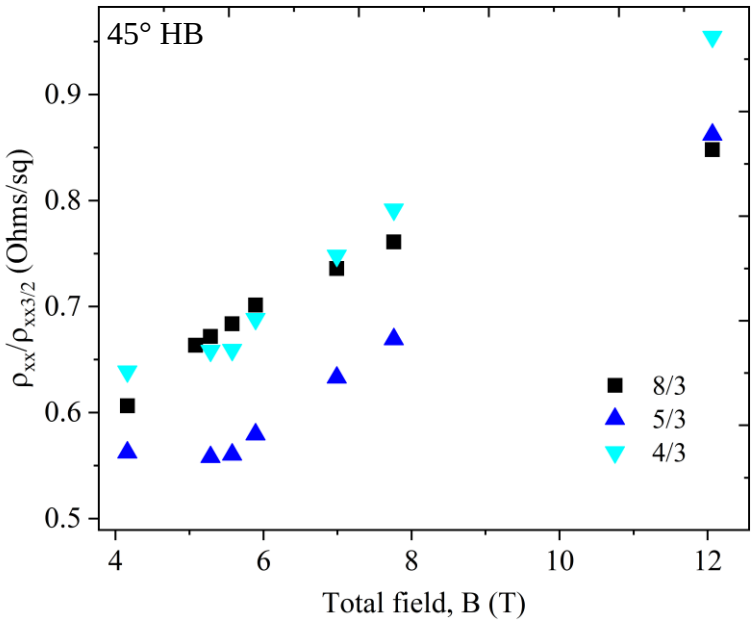

Figure 5.11 Tracking the suppression of minima for three FQHE states, labelled in the legned. Supression induced by rotating the sample within a homogeneous magnetic field. Data recored for a 45-degree Hall bar. Resistivity minima are normalized to the 3/2 fraction.

Again, the suppression of minima, caused by rotating the applied field, is plotted in Figure 5.11. The suppression values are normalised by the suppression that occurs at even denominator filling $\nu = 3/2$ By recording the gradients of each trend from Figure 5.11 and Figure 5.8, it is

possible to compare the minima suppression in the 0 degree and 45-degree Hall bar. The comparison resuls are plotted in Table 5.1.

It is noteworthy that the 0-degree Hall bar shows a two-fold increase in the gradients across all fractions, when compared to the 45-degree orientation. This suggests that the 0° Hall bar shows greater suppression of FQHE minima when field is rotated.

	4/3	5/3	8/3
0 deg	0.07 ± 0.005	0.08 ± 0.005	0.06 ± 0.009
45 deg	0.042 ± 0.002	0.042 ± 0.003	0.028 ± 0.002

Table 5.1 Gradients for each fractional state taken from Figure 5.11 and Figure 5.8. A stronger gradient represents stronger suppression due to rotating the applied magnetic field. Statistical errors added.

0° Hall bar data, shown in Figure 5.10, is from a Hall bar aligned along the <110> direction. The data presented in Figure 5.12, however, is from a 45° Hall bar aligned along the <100> direction. Qualitatively the two orientations appear to show similar results, Other than a more developed 7/3 minimum for the 45-degree orientation. Recent papers report asymmetry in transport properties within strained cubic semiconductor systems [13, 175]. Therefore, it is important to study transport properties in multiple crystal orientations when conducting experiments. The transport asymmetries represent very small signals, easily masked by growth or fabrication imperfections. Only the highest mobility samples demonstrate the FQHE, hence, observations are limited to a small number of material systems. Commonly the systems that display FQHE behaviour are unstrained MODQWs or MOS devices. The Ge system reported in this thesis is a biaxially strained cubic semiconductor, forming a 2DHG in an asymmetric QW. This makes this a unique system compared to the samples that produced the majority of FQHE literature. The origins of transport asymmetry effects [13, 174] in this system have not been conclusively identified. However, structural differences between unstrained zincblende GaAs systems and the strained diamond cubic Ge system will be a prospect. As sample quality continues to improve it is probable that the transport asymmetries in strained cubic 2DHGs will become increasingly visible.

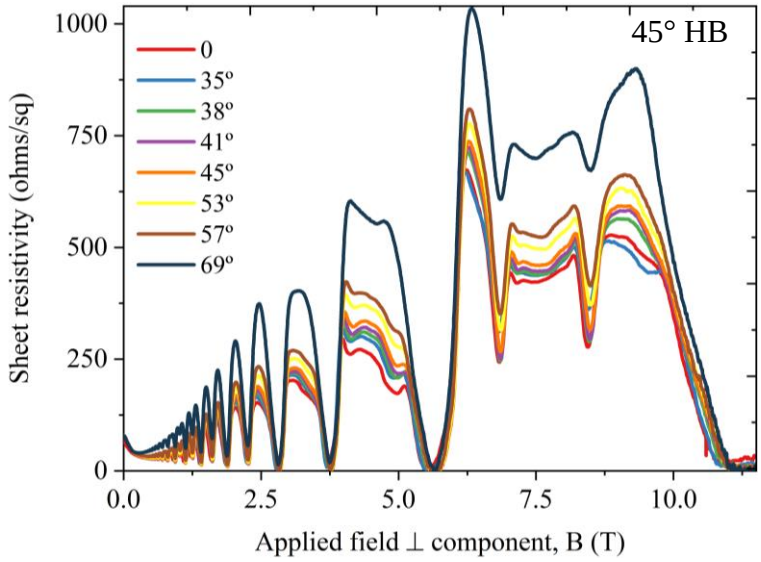

Figure 5.12 Rotated field data for a 45° Hall bar orientation. Resistivity values are plotted for eight field sweeps while incrementing sample rotation within the applied field. All magnetic field sweeps were conducted at 350 mK with an excitation current of 100 nA.

The low field 45° (shown in Figure 5.13) also displays qualitatively similar behaviour to the 0° Hall bar. A divergence in sheet resistivity is observed at 0.2 T for the highest rotation angle. The Zeeman splitting occurs at higher field values for the 45° data, at a value of 0.75 T. This data must be reported with caution, due to low resolution levels and lack of repeat measurements. This variation of 0.5 T in the onset of Zeeman splitting can be ascribed to the error from the low-resolution field scans at low applied field. High resolution results for low field oscillations are supplemented in Figure 5.5, this data places the onset of Zeeman splitting at 0.3 T. These measurements do not display a difference in the low field Zeeman splitting for 45° and 0° Hall bar orientations.

Contrasting Figure 5.13 to Figure 5.10, shows the monotonic components of the zero and 45° Hall bar differ. This cannot be explained as simply an orientationally varied mobility as the peaks from 1.5 T and above overlay each other with high agreement. The resistivity of the 45° Hall bar starts higher and drops down to join the 0° trace. This same formation appears for all temperatures up to and including 4.22 K. Attempting to find a theoretical basis for this anisotropy observation returns the stripe phases observed in GaAs systems. These are observed in high ($2 \leq N \leq 6$) Landau levels within high mobility GaAs systems at low T~ 0.1 K [176-180].

It seems unlikely that the observations made can be explained in the context of stripe phases in GaAs. Doubting the analogy with stripe phase formation is based on the anisotropy appearing in the field region before the onset of quantum oscillations, with oscillations being one of the requirements for observing the stripe phase in GaAs. It may be worth noting some of the differences between the Ge/SiGe system studied and a GaAs system, which makes up much of literature and theory. A GaAs (Ge) system is a Zinc Blende (diamond) crystal structure which lacks (has) an inversion centre. The perpendicular component of the g factor in GaAs is much smaller than in Ge. This gives Ge a larger but *B* parallel independent Zeeman energy. The band structure in the Ge 2DHG is very simple, with only the heavy hole band populated and the light hole pushed down by strain. In this manner a 2DHG in the Ge/SiGe system is closer to a 2DEG than a 2DHG in GaAs/AlGaAs [170]. Trying to find precedent for native anisotropy in high mobility semiconductors, within the literature, naturally leads to comparisons with GaAs, this being the dominant material system reported on. It seems that many of the observations reported here stand to distinguish the anisotropy observed from anything previously reported in GaAs. Sodemann et al stated that with GaAs the native anisotropy results from combining Dresselhaus and Rashba spin-orbit interactions. The Dresselhaus term is not present in Ge, therefore we cannot explain any native macroscopic anisotropy using this analogy.

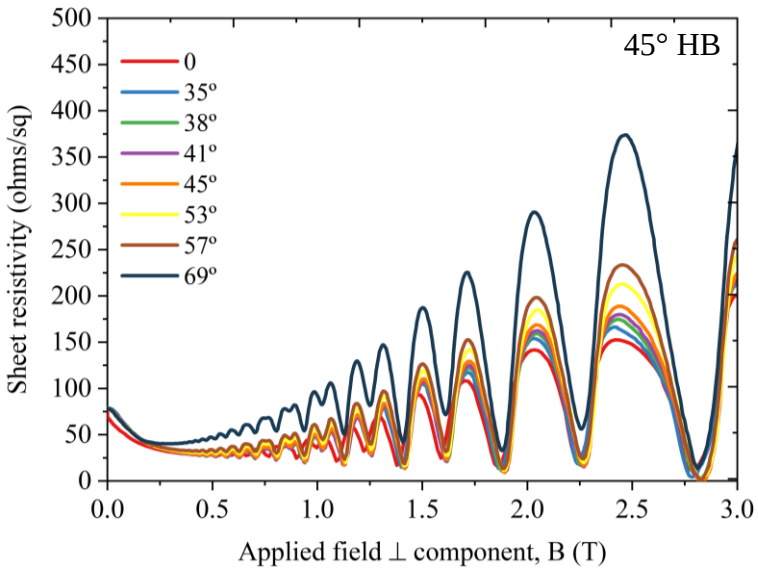

Figure 5.13 Low field (0-3 T) resistivity data for a 45° Hall bar. Eight field sweeps are displayed with incremented values of sample rotation. All magnetic field sweeps conducted at 350 mK with an excitation current of 100 nA.

One possibly theory is that GaAs and Ge 2D systems are impacted in the same manner by tilted fields and parallel components of fields. As is known the tilted fields can cause symmetry breaking effects, leading to anisotropic electrical properties. The difference being that GaAs contains native anisotropy from the interplay of the Rashba and Dresselhaus terms, whereas the Ge system is not expected to contain native anisotropy [170]. This could mean that both systems are subject to the same mechanism under titled fields, the differences occur when this mechanism interacts with the native anisotropy in GaAs and does not experience such an interaction in Ge. This idea is not a definite conclusion, it stands as a possible avenue for further theoretical or experimental work.

Observation of anisotropy within a Ge 2DHG, with a parallel component of applied magnetic field, was also reported by Shi et al [176]. Their observations compared transport properties along the main crystallographic orientations $< 110 >$ and $< 1\bar{1}0 >$ directions orientated 90° to each other. Within a cubic semiconductor these potentials would be considered identical. However, Shi reported a ratio of up to $\rho_{xx}/\rho_{yy} = 11.5$ at rotated field angle of 80° to the sample normal. This perhaps renders the observation of asymmetry between <110> and <001> slightly less surprising, as the potential fluctuation experience on a diagonal path across a cubic unit cell would be altered compared to along an edge. Shi's conclusion supports those presented above, that the observed anisotropy did not conform to all the characteristics of a stripe phase. Shi observed that the anisotropy extends to high temperature and remains after the quantum oscillations are fully suppressed. This is further evidence that the anisotropy does not fit an analogy with the stripe phase seen in GaAs.

5.3. Effective mass of composite fermions within strained germanium

The effective mass of composite fermions bears no relation to the effective mass of charge carriers within the host semiconductor material. Excluding the effects of LL mixing, and nonzero width, the CF mass (m_{CF}) extracted from different material systems are comparable. The CF effective mass is generated entirely from interactions, as such it does not have a bare mass. An advantage of the CF effective mass is that it provides a measure of the energy scales involved in the system. The CF effective mass is sensitive to magnetic field values and disorder. The interaction dependent effective mass and reduced effective field (see section 1.5.3) can raise

questions on how real CFs are. It is reassuring that CFs experience spatial fluctuations in the effective magnetic field, resulting in large-angle scattering, this is believed to be the dominant contribution to resistance [181, 182]. CFs experiencing scattering potentials aids in presenting them as tangible particles instead of a quasi-classical crutch, supporting this interpretation of FQHE phenomena. This is analogous to the zero-field low temperature electron case, where the dominant scattering is Coulomb scattering from impurities. For CFs the fluctuations in field arise from density variation caused by remote ionized impurities [181, 182].

Values reported for the CF effective mass come in different flavours, there is the activation mass, Shubnikov-de Haas mass and the cyclotron mass. The effective mass (m^*) is dependent on electron-electron interactions, this leaves m^* proportional to $e^2/\in l_B$, where $\in$ is the dielectric constant and $l_B = (\hbar c/eB_\upsilon)^{1/2}$. These dependencies explain the relationship between effective mass and effective magnetic field ($m^* \propto \sqrt{B_{eff}}$).

When treating the incompressible ground state at $\nu = 1/2$ as Λ levels of composite fermions. Essentially looking at the FQHE as the IQHE for new CF particles. It naturally leads to taking common analysis techniques from the IQHE and applying them to the FQHE. As such, the exponential decay of Shubnikov-de Haas oscillations around ν = 1/2, with increasing temperature, can be analysed in the same manner as the integer SdH oscillations would be at zero applied field [183].

Evidence exists justifying the treatment of the FQHE as the IQHE for CFs. The number of fractions emanating from υ = 1/2 is itself a justification for the new CF ground state. Experimental evidence exists for fractions up to υ = 10/21 in ρ_{xx} [6]. Large numbers of oscillations appearing symmetrically around $B = 0$ for the IQHE and at $\upsilon = 1/2$ for the FQHE, display the similarity between the high field FQHE and low field IQHE behaviour.

A new effective magnetic field (B_{eff}) is defined by subtracting the applied field value at $\upsilon = ½$, from the total filed (B_{tot}). This B_{eff} has a physical interpretation as this is the applied magnetic field that the CFs experience after flux quantum attachments are considered (see section 1.5.1). A scale for B_{eff} is inserted into Figure 5.14 for clarity. Experiments that probe the

cyclotron radius of charge carriers have been conducted on the region surrounding $\upsilon = 1/2$, the results have been consistent with the effective magnetic field and not the applied magnetic field. Giving tangible evidence supporting the existence of composite fermions experiencing the reduced effective magnetic field [7, 184-186]. Close to $\upsilon = 1/2$ direct measurement of the cyclotron radius can return values that are orders of magnitude larger than would exist for electrons with the same externally applied field. These works provide evidence for the CF picture on a semiclassical level. For a detailed review of CF ballistic transport in semiconductors see reference [3].

An advantage of using low dimensional SiGe/Ge/SiGe systems appears to be the broad range of fractions observed. It is apparent when completing a literature review that Ge systems behave differently to other material systems. Ge systems display fractions at higher temperatures and lower mobilities than is commonly observed in other material systems. Approximately 70 fractional quantum Hall effect states are reported to have been observed experimentally [2, 187, 188], in the n = 0 LLL. Within the second Landau level (SLL) only 10 states have been experimentally observed [189-195]. The SLL states are weaker than the LLL states, requiring lower temperatures and cleaner samples for observation. At temperatures that have an appreciable energy to the gap, the density of thermally excited carriers reaches a critical value. The FQHE features are then washed out [158]. Within the third Landau level (TLL) limited convincing observations of FQH states exist [48, 195, 196].

The upper temperature limit for observing fractions represents the energy gap of the incompressible state. Less broadening or intermixing is one possible answer as this would increase the measured activation energy gap. A reduction in Landau level mixing is predicted for lower effective mass carriers. It is reported that a larger effective mass causes increased Landau Level mixing and reduces the LL separation. In GaAs, holes with a larger m^* have been reported to display a 5 times reduction in energy gap compared to electrons, due to the aforementioned effect [197]. This explanation is favourable for Ge as the bulk material is known to have one of the lowest effective masses among all semiconductor materials.

A striking feature of the data in Figure 5.14 is that a broad range of fractions persist to relatively high temperatures. Comparing to literature it is uncommon to see so many fractions

at comparable temperatures and mobilities within other material systems. A collection of the fractions observed in different material systems, including the carrier mobilities and observation temperatures is included in Table 5.2. One explanation is that this is due to germaniums large g factor and simple valence band structure. The large g factor combined with the carrier density present in the sample provides a fully spin polarized system. There are no coincidence points, where changes in spin polarization can occur, within the fractional regime observed. This helps to simplify the system as the spin degree of freedom can largely be ignored. Due to the biaxial strain removing the LH HH degeneracy of the valence band, this is a single band system. This avoids any complications due to inter band effects. These two factors provide the current best explanation as to the rich and easily accessible phenomena with a low dimensional strained Ge system.

Material (QW)	**Fractions observed**	**Mobility ($cm^2 V^{-1} s^{-1}$)**	**T (mK)**	**Carrier density ($\times 10^{11} cm^{-2}$)**	**Carrier type**	**Field (T)**
SiGe/**Ge**	8/3,7/3,8/5,7/5,2/3,3/5,4/7,5/9,1/2,4/9,3/7,2/5,1/3	1.3×10^{6}	350	2.9	**2DHG**	37.5
AlGaAs/**GaAs**	2/3,3/5,4/7,5/9,6/11,7/13,1/2,6/13,5/11,4/9,3/7,2/5,1/3,2/7,3/11,4/15,5/19,1/4	1×10^{7}	35	2.55	2DEG	45
AlGaAs/**GaAs**	3/5,4/7,1/2,4/9,3/7,2/5	2×10^{6}	30	1.72	2DHG	18
MgZnO/**ZnO**	9/2,11/3,7/2,10/3,8/3,13/5,18/7,5/2,5/3,8/5,11/7,14/9,3/2,13/9,10/7,7/5,4/3	5.3×10^{5}	20	2.3	2DEG	8
SiGe/**Si**/SiGe	2/3/3/5/4/7/4/9/2/5/1/3	2.5×10^{5}	30	2.7	2DEG	45
Graphene	13/3,11/3,10/3,8/3,7/3,4/3,2/3,1/3	3×10^{4}	300			60
AlGaAs/**AlAs**	11/3,7/3,5/3,8/5	1.1×10^{5}	30	6.2	2DEG	6.5
CdMgTe/**CdTe**	2/3		1500	5.7	2DHG	60
AlGaN/**GaN**	5/3	7.5×10^{4}	100	0.2	2DEG	32

Table 5.2 Table comparing observations of the FQHE in different material systems. Layers that contain the QWs are in bold for clarity.

Most high mobility FQHE observations are performed in electron systems. This is due to most high mobility 2D channels being within GaAs systems, which at low field suffer lower mobilities, and complex band effects, in a majority hole carrier system. The GaAs valence band structure is simplified at high field values, where only the lowest LL needs to be considered. One important observation for holes in GaAs is the appearance of an insulating phase between filling 1/3 and 2/5. This observation was made by Santos et al and was explained as a weakly pinned hole Wigner crystal [198]. A Wigner crystal referring to the solid phase of electrons, occurring at low densities when potential energy dominates kinetic energy, first predicted by Eugene Wigner in 1934 [199]. Theoretically the existence of a Wigner crystal was predicted for electrons at filling factors below $\nu = 1/6.5$ [200, 201]. Experimentally a possible electron Wigner crystal state has been observed below filling $\nu = 1/5$ [158]. However, it was only Santos who observed the hole Wigner crystal around $\nu = 1/3$. Santos hypothesized that its appearance might be due to the majority carriers being holes rather than electrons. It was suggested that the larger effective mass of holes in GaAs, that is known to increase Landau level mixing, may be culpable through reducing the energy gap [197].

Looking at our Ge system we do not observe an unaccountably large insulating state between filling 1/3 and 2/5. The insulating peak also appears to display a comparable thermal response to other FQHE peaks in the vicinity and is certainly not reentrant. This permits the firm conclusion of the absence of a Wigner crystal phase around filling $\nu = 1/3$ in our majority hole carrier system. This doesn't contradict the hypothesis of Santos that the critical filling factor for Wigner formation is shifted by Landau level mixing. It is documented that holes within strained Ge have a remarkably low effective mass, lower than electrons within Si [9]. It should also be noted that Pan et al suggested that electron solids will melt away at higher observation temperatures [158], we cannot rule out that our relatively high temperature measurements are not preventative for electron solid observations.

Figure 5.14 displays six magnetic field sweeps from 0 to 37.5 T. Each sweep is conducted at a different temperature from 0.35 up to 4.22 K, as labelled in the color-coded legend. Quantum oscillations in resistance begin at 0.3 T consistent with the IQHE. Minima in resistivity consistent with the FQHE commence at 3 T with filling $\nu = 11/3$. The effective zero field point for the generation of CFs at $\upsilon = ½$ appears at 22.8 T, consistent with the calculated carrier density

of $p_{CF} = 2.7 \times 10^{11}\ cm^{-2}$. A scale bar has been inserted showing the effective field experienced by the CFs, with its zero-point centred on filling υ = ½. Strong fully developed zero resistance plateaus are observed at filling 1/3 and 2/3. We also observe the asymmetric insulating state between integer filling and $\nu = 2/3$, telling of the proximity to states developing in this area. Very few germanium quantum wells exist that display the high quality required to perform these measurements. This leaves the FQHE in Ge as an underdeveloped and underreported area.

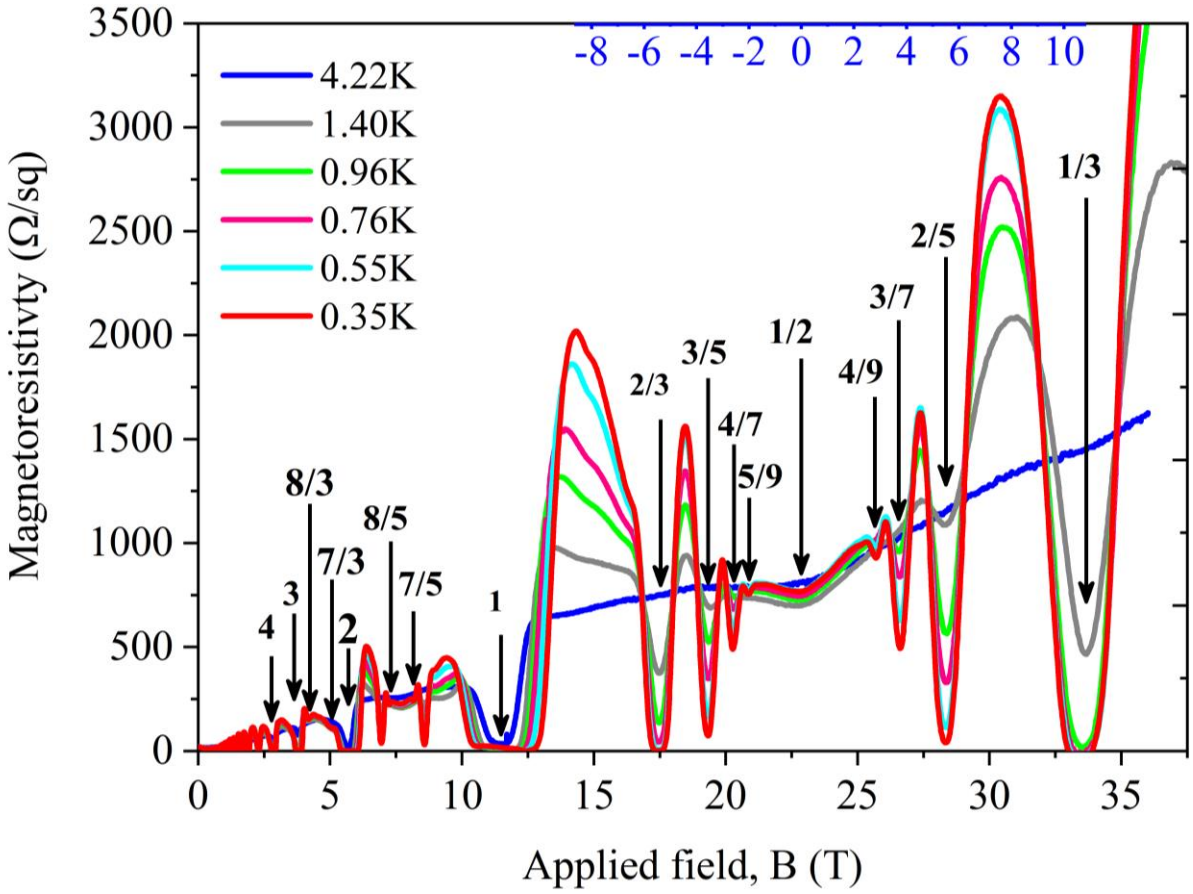

Figure 5.14 Suppression of FQHE minima through stepwise increase in temperature. Blue inserted scale displays B_{eff} for CFs originating from $\upsilon = 1/2$. Six repeated magnetic field sweeps are displayed each at a different tempeature, as indicated by the colour coded legend. The location of the most developed fractional states are labelled for clarity.

In section 1.5 the treatment of the FQHE as the IQHE of CFs was justified. Now the CF effective mass can be extracted using the technique developed for the IQHE. This equivalence is based on the semiclassical composite fermion understanding of the FQHE. It is assumed that

the CFs experience a residual magnetic field $B_{eff} = B - B_{1/2}$, with $B_{1/2}$ the field at half filling. CFs are quantised into their own Γ levels, with corresponding energy gaps. This mirrors the Landau levels and energy gaps of the IQHE. The Shubnikov-de Haas oscillations of the IQHE which appear for electrons when B deviates from $B = 0$ directly translate to the oscillations observed as the effective field B_{eff} deviates from $B_{eff} = 0$. These Oscillations are considered the SdH oscillations of composite fermions, symmetric around $\upsilon = ½$. Similarly, the energy gap (Δ) is considered to represent the cyclotron energy of the CFs, from which we can calculate the CF effective mass m^*_{CF}.

Peak amplitudes for oscillations emanating from $\upsilon = 1/2$ can be extracted by fitting an envelope function and subtracting off the monotonic background increase in resistance. A sequence of diagrams showing the envelope fitting procedure is shown in Figure 6.8. To linearize the exponential decay of peak amplitude (induced by increasing temperature) Figure 5.15 was produced. The figure shows the linearized reduction in peak amplitude for seven peaks which are labelled by the applied field at which they appear. The gradients are seen to vary, with lower field peaks displaying a steeper gradient. The steeper gradients translate into an enhanced CF effective mass.

Using the gradients from Figure 5.15 and equation 5.1 [5] it is possible to extract an effective mass from the thermal activation data.

$$ln\left(\frac{A}{T}\right) = C - \frac{2\pi^2 k_B T}{e\hbar B_{eff}} m^*_{CF} \qquad (5.1)$$

Where A is peak amplitude, T is temperature, B_{eff} is the effective magnetic field, m^*_{CF} is the effective mass and C is a constant. Once an effective mass value was calculated for each B_{eff} the results were plotted in Figure 5.16.

The solid triangles show the m^*_{CF} results for the Ge QW. These are compared to digitised data from the literature, hollow squares represent m^*_{CF} values for multiple GaAs systems. A clear enhancement in effective mass is observed when moving towards zero applied field. This has been observed by other authors [183] although the exact dependence appears to promote some disagreement [5, 202]. Du et al took this divergence in the effective mass to mean that the CF system at $\upsilon = ½$ does not represent an ordinary Fermi system [202]. Du observed an

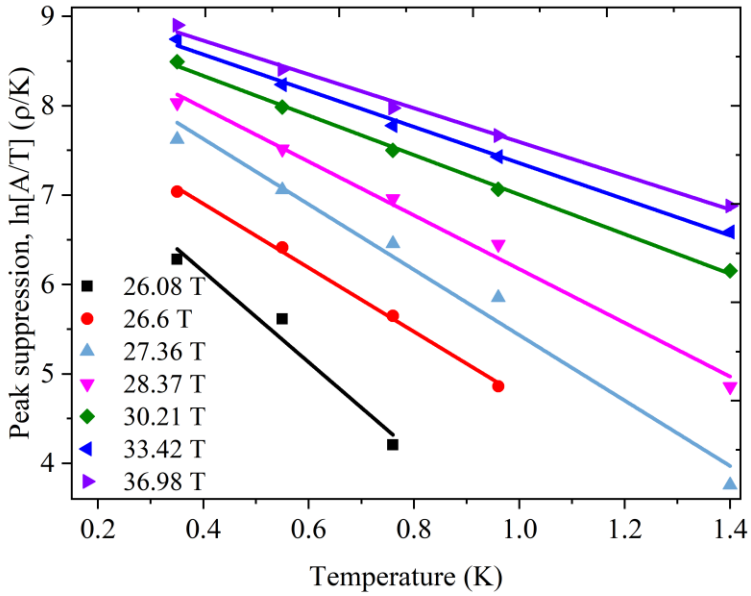

Figure 5.15 Linearized peak amplitude suppression, occurring due to temperature increase. The peaks for which thermal suppression is displayed are located between ν=4/9 and 1/3, they can be indentified by the legend which displays the location in applied magnetic field (B).

enhancement of up to 40% between low and high field m^*_{CF} values, the trend was continuing divergence but the proximity to υ =½ was limited by sample quality at the time.

An asymmetry is observed between positive and negative applied magnetic field directions. This initially seems counter intuitive. A reversed field direction should only induce an identical clock wise or counter clock wise cyclotron orbit for charge carriers within the system. This would render all measured parameters equivalent. Pan et al [203] observed a similar asymmetry around υ =¼ in GaAs, they assigned the asymmetry to an insulating phase at higher fields. An alternative explanation involves inhomogeneous carrier distribution, for a full explanation for this analogy see Figure 5.24 and the explanation that follows it.

The comparison data in Figure 5.16 is recreated from references [5, 202]. The recreated data is from GaAs samples with varied carrier densities. Carrier density values are shown in the legend. All effective mass values are scaled to a carrier density of $1.33 \times 10^{11} cm^{-2}$. Effective mass for CFs must be scaled to a single unifying carrier density. With an m^*_{CF} that is interaction dependent the carrier density will have an impact on the measured effective mass. Plotted values for B_{eff} are the field values where fractions would appear for a sample of carrier density

$1.33 \times 10^{11} cm^{-2}$. For samples of varied carrier density, the fractions will appear in different locations in magnetic field. Therefore, to compare m^*_{CF} in different samples one must scale the field location for carrier density. Although our data shows a good qualitative agreement with the effective mass values from GaAs samples, there is an enhancement in effective mass for every fraction over the entire field range.

We are not confident on the origin of this enhancement in our sample. Clearly the differences in our observation are that this is a Ge system, whereas all other comparison data originates from GaAs systems. The second difference is that we have holes, not electrons, as our majority carrier. Our best interpretation is that the scaling with magnetic field is not fully considering all the underlying physics. As explained values for m^*_{CF} for all samples were scaled to a carrier density of $1.33 \times 10^{11} cm^{-2}$. This means that in the original observations our value for m^*_{CF} was observed at higher total applied fields than the samples it is being compared to. It could be possible that the simple $\sqrt{B}$ scaling relation with field is not fully consistent with the enhancement that applied magnetic field has on the m^*_{CF} of CFs.

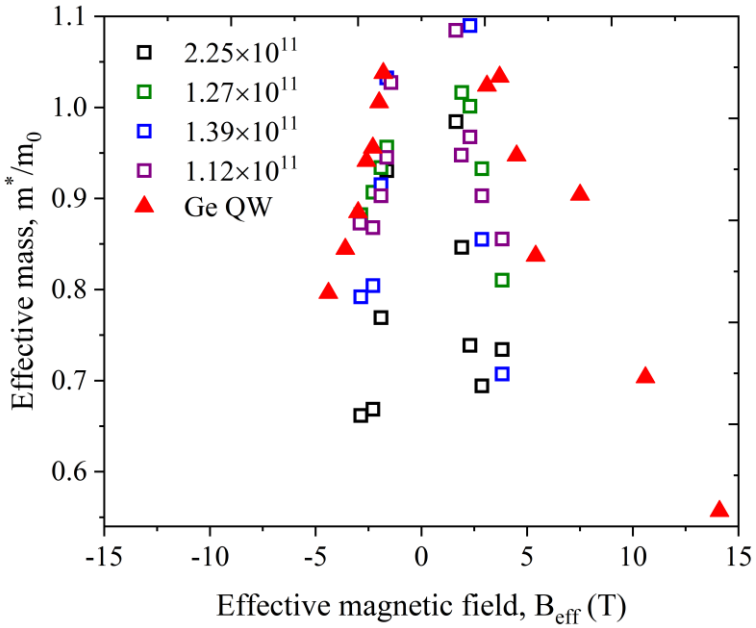

Figure 5.16 Comparison of extracted effective mass (m^*_{CF}), with m^*_{CF}, from GaAs material systems. Results from each sample are scaled to account for variations in carrier density. Comparison (all square data points) are from GaAs MODQW systems, recreated from references [5, 202].

Another method for extracting effective mass is to look at the gap energies. The energy gap between the ground state and its quasiparticle excitation is the foundation of the FQHE. All theories for the FQHE are built on the assumption of ground states, occurring at $p/2 \times n$ fractions (where p and n are positive integers), with energy gaps opening as the effective field moves away from the ground state. Due to the fundamental nature of the energy gaps for the FQHE much of the theoretical work has focused on this area. In a perfectly two-dimensional system the relationship between energy gap and magnetic field is that shown below:

$$\Delta(B) = Ce^2/\in l_0 \qquad (5.2)$$

Where $l_0 = (h/eB)^{1/2}$, representing the magnetic length. Theoretical work using Laughlin's prestigious wave function agreed on a value of $C \approx 0.09$ for the n/3 states [197, 204-210]. It is possible to probe the energy gap (Δ) by measuring the quasiparticle activation energy [211-215]. When comparing theoretical models to experimental results the impact of finite thickness, disorder and Landau level mixing needs to be considered. The finite thickness of a real 2D system reduces the repulsive potential between charge carriers, this effect is increased for high magnetic fields. It is still difficult to provide any models for the impact of disorder, higher quality samples continue to be produced, reducing the impact of disorder. Attempts have been made to include a finite thickness into the theory of the FQHE [216-218] most notable is the contribution from Zhang and Das Sarma [47], using the Fang Howard Model.

The CF model has provided an accessible framework through which to interpret many aspects of the FQHE [2, 3]. It has provided a model through which many experimental developments have been made [157, 165, 202, 219, 220]. Using a rigid analogy of the FQHE as an IQHE for CFs cannot explain all experimental results. The state at filling factor ½ is unlikely to be a Fermi liquid, at least not directly analogous to the bare electron case [181, 221]. Figure 5.16 displays a divergent effective mass as B^* approaches $B^* = 0$, this initiates the question of what exactly is the effective mass of composite fermions at zero effective field? This unknown adds to the uncertainty on how closely the CF picture can be adhered to. Looking back at Figure 5.14 there is a spread in ρ_{xx} at $\nu = 1/2$ caused by increasing temperature. This spread also occurs at $\nu = 3/2$. A temperature instigated change in ρ_{xx} does not occur and is not expected at zero applied field within the IQHE. Indeed, when we check $B^* = 0$ in the IQHE no spread is observed. If this did occur, it would imply a change in mobility. This is exactly how the theoretical argument by Kang et al [222] explains the spread in ρ_{xx} at $B^* = 0$ for CFs.

The two plots within Figure 5.17 are the CF mobility calculated at two points of zero effective magnetic field ($B^* = 0$). To restate what is explained in section 1.5.3, the ($B^* = 0$) points correspond to field values where the CFs behave as if they reside in zero applied field. This involves CFs propagating in straight lines instead of cyclotron orbits. Also, the CF system at ($B^* = 0$) forms a ground state with energy gaps, equivalent to how bare charge carriers behave at zero applied field. The two points correspond to filling factors $\nu = 1/2$ and $3/2$. The formula used for calculating zero field mobility is shown below.

$$\mu = \frac{1}{e \times n_s \times \rho_{xx}(0)} \quad (5.3)$$

Where e is the charge on an electron, n_s the carrier density and $\rho_{xx}(0)$ the magneto resistivity at zero applied field. At first inspection of the results it would be possible to conclude that a strong initial trend is followed by an outlying result. This interpretation is less convincing when both data sets return similar trends. Importantly the data shows high similarity to the results of Kang et al for their GaAs/AlGaAs 2DEG system. When drawing an analogy with the IQHE and electron systems [183], it is known that certain temperature ranges induce a change in dominant scattering effects. This can cause resistance shifts during large temperature sweeps. Figure 5.17 is likely to display a change in the dominant scattering source as the temperature is raised. The most likely shift is from remote ionized impurity effects, which for CFs cause resistance through inducing density fluctuations [223], to acoustic phonon scattering.

It is striking how much lower the mobility for CFs is when compared to the underlying electron mobility. A reduction of over an order of magnitude for the filling factors presented here. The increase in mobility observed from 0.3 to 1.4 K is predominantly ascribed to CF-CF interactions. Kang presented the following formula:

$$\mu_{CF} = c_1 + c_2 T^2 + c_3 lnT \quad (5.4)$$

Where c_1, c_2, c_3 are constants and T is temperature. The final term arises from CF-CF interactions and the first two from impurity scattering. The first two terms hold true for electrons at $B = 0$, however, the final term is interaction dependent and therefore only valid for CFs. With four data points we cannot attempt to fit a model to the low temperature data. However, the knowledge that prior theoretical work predicts an increase in mobility with increasing temperature at low (<1 K) temperatures, confirms this observation has a theoretical basis.

Comparing experimental results to theoretical predictions constitutes much of the published work on the FQHE. The challenge with extensive studies varying a single material variable, within the FQHE, is produced by the extreme difficulty of producing a batch of similar high mobility modulation doped QW heterostructures. In Figure 5.17 the highest temperature data point at 4.2 K displays a dramatic drop in mobility for both data sets. This was also predicted by Kang et al and explained as CF acoustic phonon scattering becoming more dominant. It was shown that CFs would have a $\mu_{CF} \sim T^{-3}$ dependence over several orders of magnitude, this is in contrast with the T^{-5} dependence known for electrons [3, 224, 225]. With one data point in each set, again it is not possible to test this dependence. The steep decrease above 1.4 K agrees with Kang's predictions of a change to a $\mu_{CF} \sim T^{-3}$ dependence around 1 K, However, it is not a confirmation of the T^{-3} dependence.

Comparing gradients for the two low temperature (<1.4 K) regions of Figure 5.17 show that the low mobility plot representing $v = 1/2$ has a gradient ~1/3 as steep as the higher mobility plot, representing $v = 3/2$, this also agrees with the theory of Kang. The magnitude of the mobilities are also in the ratio 1:3, displaying that equation 5.4 still holds for our data. Questioning why mobility is lower at $v = 1/2$ than at $v = 3/2$. Is equivalent to asking why the monotonic background to the FQHE increases with increasing applied magnetic field. If

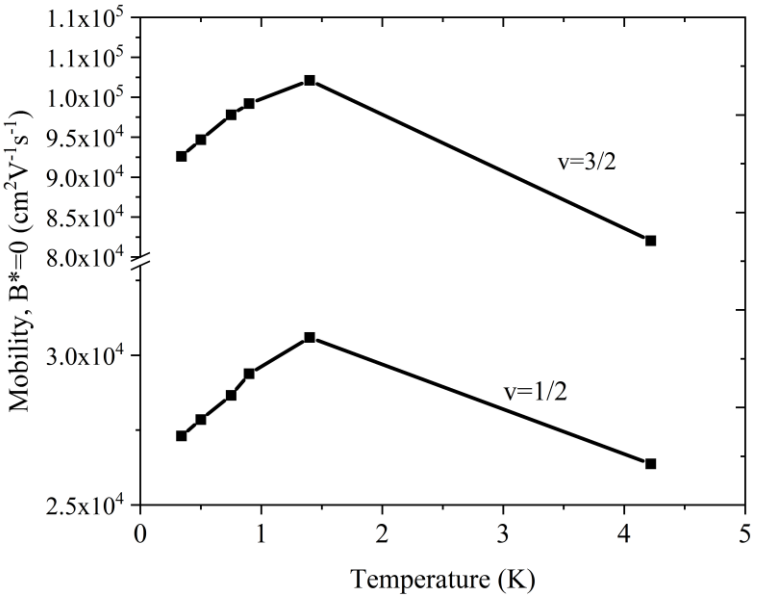

Figure 5.17 CF mobility variation with temperature. Mobilities calculated from ρ_{xx} minima at filling factors $v = 3/2 \ and \ 1/2$.

drawing a direct analogy to the IQHE then each $B^* = 0$ point, representing even denominator filling, would be expected to have the same value of ρ_{xx} and therefore equal mobility. However, this is not observed, with ρ_{xx} at 3/2 larger than ρ_{xx} at ½. Pan et al [226, 227] interpreted this effect as being due to a small unintentional density gradient within the sample. When the even denominator fractions ¾ and ¼ are also visible it is clear that the even denominator fractions show a linear increase in ρ_{xx} with increasing magnetic field [227]. The disparity in mobility between $\nu = 1/2$ and $\nu = 3/2$ shown in Figure 5.17 follow this trend with $\nu = 1/2$ occurring at B = 22.8 T and $\nu = 3/2$ occurring at B = 7.7 T.

5.4. Carrier generation through sample surface illumination

Illuminating the surface of a heterostructure containing a 2DHG can alter the carrier density. Illumination of MODQW samples is commonly utilised to increase transport mobilities. This occurs through increased carrier densities inducing a more effective ionized impurity screening [228]. The increase in carrier concentration are photoexcited electrons, if the modulation doped sample is illuminated at low temperatures the increased carrier densities can persist for many hours or days. This is referred to as the persistent photoconductivity effect (PPE) [229]. The extra donors that contribute carriers upon illumination are referred to as deep level donors, this can include dopants with higher energy barriers to ionisation, defects such as vacancies or interstitials also interacting defect complexes. The increased screening from the increased carrier density reduces the remote ionised impurity scattering and thereby increases mobilities [230].

Sample 13-335 was first cooled to 1.9 K then illuminated using a λ = 950 nm GaAs infrared LED, subsequently the sample was cooled to the base temperature of 350 mK and the field sweep started. The sample was not illuminated at base temperature as the light intensity causes heating that rapidly boils of the condensed ^{3}He. Figure 5.18 displays a change in the magnetoresistivity spectrum after illumination. There is a notable shift of recognizable features to higher values of applied magnetic field. This confirms an increase in carrier density within the 2DHG. An increase in resistivity is also observed with oscillations translating up the y axis. This indicates the increase in carrier density impacted scattering processes, this interpretation is confirmed when comparing the zero-field resistance, which displays a mobility reduction for the illuminated sample. An unexpected effect of illumination is the apparent deepening of the

$\nu = ½$ minima in resistance, for this an explanation cannot currently be provided, however, it would seem more likely that this feature is an increase in resistance either side of $\nu = ½$ rather than a deepening FQHE state at $\nu = ½$.

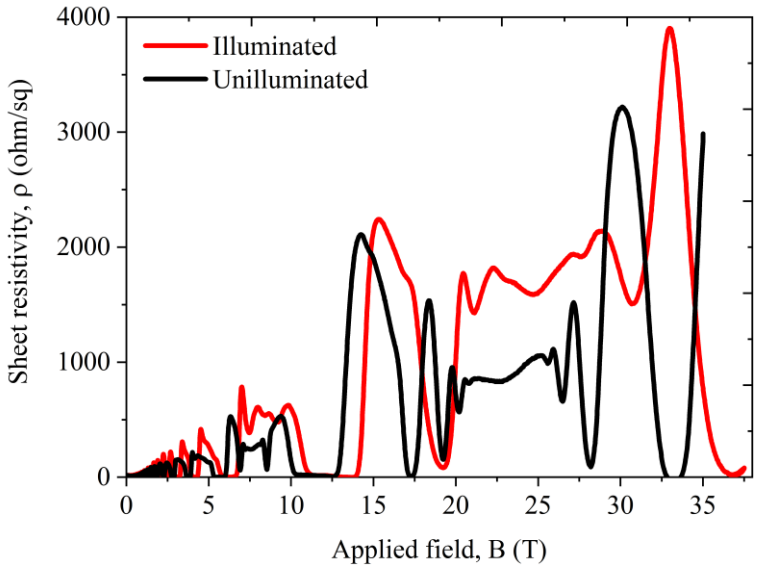

Figure 5.18 Comparison of illuminated vs un-illuminated magneto resistivity spectrum. Data taken at base temperature (340 mK) and perpendicular magnetic field for sample 13-335.

To ascertain the quantitative effect of the LED on the 2DHG carrier density, formula 5.5 was used, inputting the gradients of the Hall resistance data from Figure 5.19.

$$p_{Hall} = \frac{1}{e \times R_H} \qquad (5.5)$$

Where e represents the charge on an electron and $R_H = \Delta\rho_{xy}/\Delta B$ is the Hall coefficient. The origins of these equations are first displayed in section 1.4.2.

The Hall resistance plots in Figure 5.19 display results for both 0 and 45-degree orientation Hall bars. The figure compares the small gradient change caused by illuminating the sample surface. This gradient is proportional to the 2DHG carrier density, as shown by equation 5.5. The Gradient of each data set within Figure 5.19 is measured for the range 0 to 0.5 T. The low field region is used to avoid the Hall plateaus impacting the recorded gradient. The measured gradients and calculated carrier densities are shown in Table 5.3.

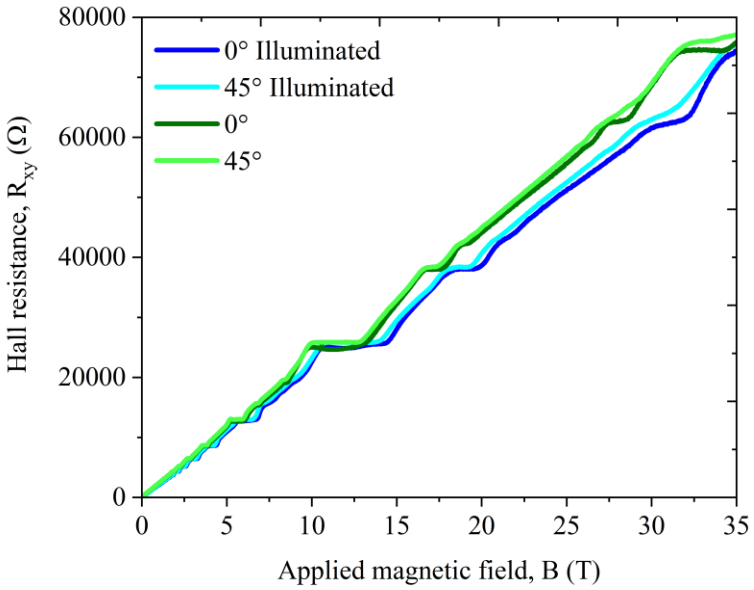

Figure 5.19 Hall resistance plateaus for both 0 and 45-degree surface orientation Hall bars. Data highlights a change in gradient for the Hall bar after it is illuminated with an infrared LED.

The results in Table 5.3 show a 17% increase in carrier density for both orientations of Hall bar. This approximately corresponds to an extra 45 million carriers per square millimetre. No temperature activation measurements were completed on the sample with increased carrier density, due to illumination. This would be an area of interest for further work. Thermal activation data would permit calculation of the energy gap. Comparison between two carrier densities within the same sample would show what the impact of carrier density is on the energy gap. This may aid in designing new samples with increased energy gaps and therefore better defined and more stable FQHE states. The observation of a reduction in mobility induced by an increase in carrier density it not consistent with the common theory of the PPE. Commonly increased carrier density provides enhanced screening returning higher mobility. This is not the first report of a decrease in mobility during the PPE. Elharmi et al [231] and Antoszewski et al [232] both reported similar findings for AlGaN/GaN MODQW systems. It cannot be conclusively determined what the source for the mobility reduction is within the Ge QW system. The increasing carrier density is no longer reducing the remote ionised impurity scattering. However, three strong possible origins are firstly: increased surface roughness scattering. As the carrier density increases the carrier wavefunction moves closer to the heterointerface, increasing the contribution of surface roughness scattering. Secondly: a similar origin with a

shifted wavefunction but instead considering interface charge scattering. Thirdly as suggested by Elharmi et al [231] as the wavefunction is translated towards the interface it spreads into the barrier, increasing the contribution of alloy disorder scattering.

	0 DEG	45 DEG	0 DEG illuminated	45 DEG illuminated
R_H	2431 ± 32	2484 ± 36	2084 ± 7	2104 ± 14
P_{Hall} ($\times 10^{11}$ cm^{-1})	2.57 ± 0.04	2.51 ± 0.05	2.99 ± 0.01	2.96 ± 0.02

Table 5.3 Hall coefficient (R_H) and carrier density (P_{Hall}) before and after illumination with an infrared LED. Both 45 and 0-degree surface orientations are included. Statistical errors are included.

The data of Figure 5.20 show qualitatively similar results to rotated field measurements for the unilluminated sample. Figure 5.20 displays rotated field data for 0° HBs. The top graph shows the illuminated data with a 17% increase in carrier density. The lower graph is the unilluminated data Both field sweeps are conducted at 350 mK with a 100 nA, 13 Hz applied current. The 17% increase in carrier density, caused by sample illumination, has impacted the results. The outcome is clearest when observing the lower field region of the trace in Figure 5.20. The complete suppression of fractions 7/3 and 8/3 that appears as the field is rotated occurs at 54° for the higher carrier density. While the lower carrier density suppression is incomplete up until 70°. The illuminated sample displays an increase in the insulating phase masking filling 5/3, Carrier density appears to be a dominant driving force behind the high angle field effects that are suppressing the FQHE states. With increased carrier density the disturbance to the FQH system at high angles is increased. This result means that reduced density samples will be optimum for studies investigating rotated field measurements, such as spin polarisation or finite thickness investigations.

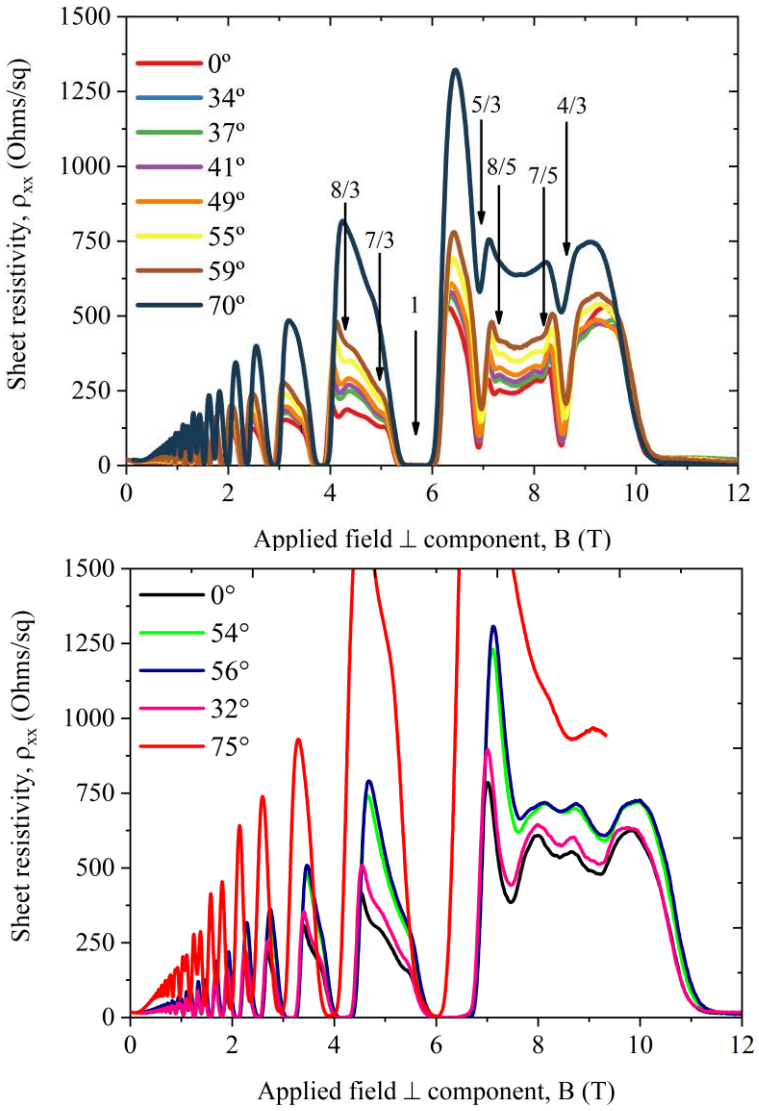

Figure 5.20 Resistivity measurements with varied angles of sample rotation within an applied magnetic field. Conparison of results for illuminated (bottom) and un-illuminated (top) data both taken using sample 13-335. Both graphs represent 0° HBs measured at 350 mK with a 100 nA 13 Hz applied current.

Figure 5.21 displays the low field region of sample 13-335, the blue data is before illumination and the red data is after sample illumination. The illumination resulted in a 17% increase in carrier density. The region between 0 and 0.3 T, before the onset of oscillations shows carrier density dependent variation. Figure 5.23 shows that for the higher carrier density sample the initial decrease in magnetoresistance, with increasing field, is reduced. The magnitude of this reduction in $\Delta\rho_{xx}$ between 0 and 0.3 T is 30%, caused by a ~ 17% increase in carrier density. Due to the location of this region prior to the onset of quantum oscillations, it

seems appropriate to look for a macroscopic source for the variation. A literature review for similar effects returns the results of Bykov et al [233, 234].

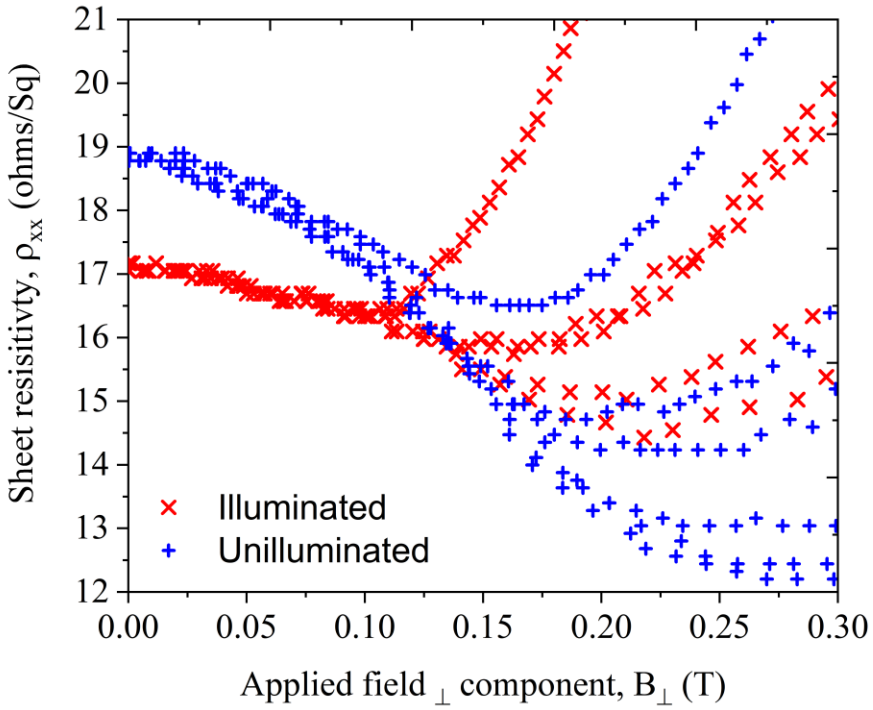

Figure 5.21 Low field (0 - 0.3 T) comparison of rotated field measurements for illuminated (red) and un-illuminated (blue) measurements for sample 13-335. Repeated curves for illuminated and unillluminated represent varied rotation angles. The area of interest is below 0.125 T where all angles are displaying analogous behaviour.

The schematic diagram of Figure 5.22 (a) displays the Hall bar used in Bykov's work, it comprises a mesa that is half smooth and half corrugated (figure taken from [233]). By measuring either contact pairs 2-3 or 3-4 Bykov could measure a 2DEG with either a smooth or corrugated heterointerface. The results of Bykov are displayed in Figure 5.22 (b) with trace 1 showing the corrugated measurement and 2 the smooth measurement. We can see that Bykov has observed a similar result to the data shown in Figure 5.21 between 0 and 0.3 T. These results are not identical to our situation, but they do stimulate an interesting interpretation. Firstly, Bykov's results display a larger initial drop in ρ_{xx} with a corrugated surface. Secondly, Bykov's variation in low field magnetoresistivity behaviour differs between smooth and corrugated heterointerfaces, whereas ours occurs due to different carrier densities. To respond to the first point, the height of corrugations was 30 nm, in comparison the RMS roughness of our sample is ~3 nm. Therefore, if the two effects are driven by the same process it is not prohibitive that the magnitude of our response is reduced. For the second point, it is possible that our results are

also driven by variations in scattering from the heterointerface, however, in our case the change in surface scattering is varied by changing the carrier density. Interpreted in this manner our results show that the increased carrier density reduces the scattering from the heterointerface.

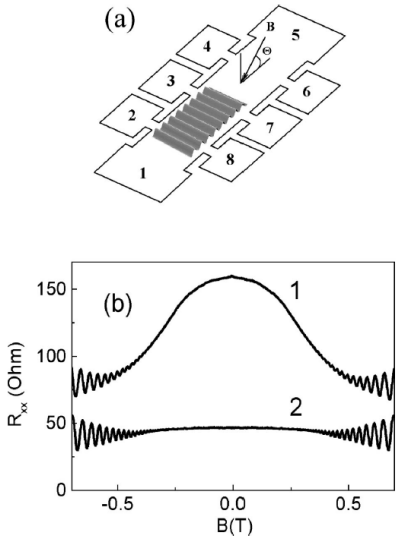

Figure 5.22 (a) Schematic diagram of Hall bar samples used in the work of Bykov et al. (b) Results of Bykov et al. Firgure taken from reference [233, 234].

The sample surface was illuminated with a GaAs LED. This caused a 17% increase in carrier density, as displayed in Figure 5.19. To return the sample to the original carrier density the temperature was increased to 100 K and returned to base temperature (300 mK). As 100 K is above the temperature at which background impurity conduction freezes out it was assumed that this annealing step would return the carrier density to its as cooled state. It is an interesting but little understood fact that SiGe/Ge heterostructures produce highly repeatable results over different cooling cycles. This contrasts with GaAs material systems that can show variation with each cooling cycle. What was observed after annealing the illuminated sample at 40 K and returning to base was an improvement in the FQHE spectrum. With subtle improvements in minima and clearer plateaus in Hall resistance. There was an immeasurably small difference in the carrier density. Similar results have also been observed by Samani et al within a GaAs system [235] where they repeated illumination and annealing, varying the length of time the temperature was raised. Samani et al discovered that the carrier density saturated after only four minutes at 2.6 K, longer anneals however continued to improve the energy gap, with no further variations in carrier density. The suggested conclusion was that the continued annealing instead reflected improvements in sample homogeneity. Applying this theory back to the SiGe/Ge

sample reported here, it appears that the annealing, post illumination has redistributed the density fluctuations. Prior to annealing, the system may have included a spatially varying charge density. In this situation measurement results represented an average over many minutely different areas within the sample, each with a different filling factor. The annealing and cooling evened the density fluctuation, increasing homogeneity. This is the best explanation for the enhancement in FQH features observed, with a negligible shift in carrier density.

5.5. Searching for the exotic state ν = 4/11

The empirical resistance rule states that the dependence of the Hall resistance R_{xy} and the longitudinal resistance R_{xx} is given by:

$$R_{xx} = C \times B\left(\frac{dR_{xy}}{dB}\right) \quad (5.6)$$

Where dR_{xy}/dB is the differential of the Hall voltage with respect to the applied magnetic field and C is a constant [226, 236]. The resistance rule has been demonstrated experimentally in many other material systems [236-238]. However, an all-encompassing model accounting for every element, has not been conceived. The most established model is based on the concept of density fluctuations [239]. To compare how well our system conforms to this rule, the differential of the Hall resistance is multiplied by the value for applied field and plotted against applied field. Numerous published works exist that use this technique [236-238], providing precedent for creating Figure 5.23 using equation 5.6. Studying the differentiated Hall signal is advantageous. Weak developing states first appear in the Hall signal before appearing in the ρ_{xx} signal. This is how many higher order fractions were first discovered, before advances in sample production lead to these exotic fractions becoming common observations.

Within Figure 5.23 the blue trace is the unaltered ρ_{xx}. The red trace is the differentiated Hall resistance, scaled by the applied magnetic field. The traces overlay with high conformity, matching the period and often the amplitude of oscillations. Note that the scales on opposing axes are different, having been scaled to overlay the two traces. Pan et al [226] explained the difference as occurring due to the density gradient between each Hall voltage probe. The difference for this sample ~ 40 which gives $1/20 = \Delta n/n$, resulting in a density gradient of 2.5% between Hall voltage probes. This result is a reasonable order of magnitude compared to

the results of Pan, confirming that the scaling difference between the two axes in Figure 5.23 is reasonable.

The points at which the differentiated trace diverges, from ρ_{xx}, show that minima for developing fractions have been observed in the R_{xy} signal but not in the R_{xx} signal. It is likely that lower temperature measurements, of the order 10 mK, will further develop these fractions at $\upsilon = 9/7\,, 7/9\,, 5/7$ and $4/11$ as developed fractional minima in the R_{xx} trace.

The appearance of 4/11 in dR_{xy}/dB is an important result. This observation cannot be overstated as conclusive evidence of a FQHE state. This is solely an indication from the Hall resistance data that this sample is on the edge of developing a state at the field value where 4/11 would occur. Thermal activation data is required to conclusively prove that this is a full FQHE state at 4/11. Thermal activation data can measure the energy gap. If an energy gap is demonstrated, then there is an incompressible state, and this would be conclusive proof of a full FQHE state at 4/11. However, this indication of 4/11 is still an exciting prospect. All initial observations of exotic fractions have been on the fringes of what is physically observable. After the initial observation further work proceeds to prove the existence of new fractions. To my knowledge filling factor 4/11 has been observed experimentally by two other groups, both observations within a GaAs/GaAlAs 2DEG, and written up over three publications [240-242].

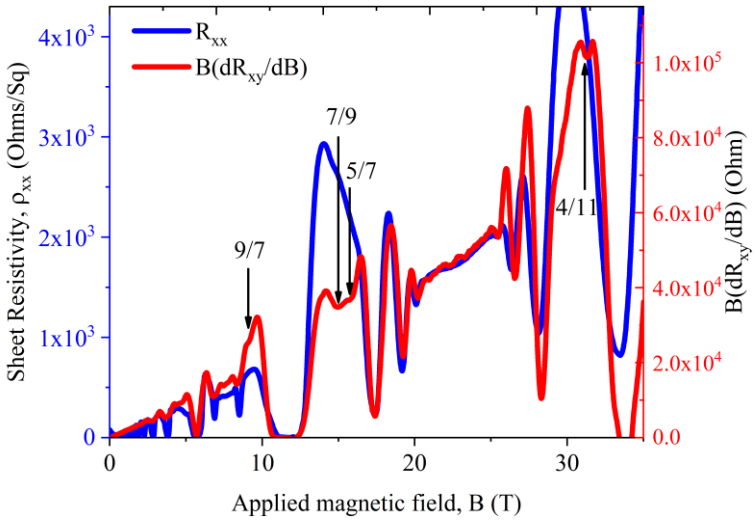

Figure 5.23 Differential of Hall signal (dR_{xy}/dB) multiplied by the applied field, compared to the Sheet resistivity. Plot tests conformity to the empirical resistance rule (equation 5.6). The red differentiaed data overlays the raw (blue) data with convincing conformity.

The first conclusive evidence, including gap extraction though thermal activation, was provided by Pan. W et al in 2015 [240]. Although experimental observations remain limited, many theoretical publications regarding $\nu = 4/11$ exist [243-247]. The reason for the interest in filling $\nu = 4/11$ lies with its complex origins. The core FQHE states appear in sequence according to the hierarchical model [248, 249]. For example, the positive effective field states, emanating from $\nu = ½$, are $\nu = 1/3,\ 2/5, 3/7\ and\ 4/9$. These fractions make up the family $\nu = p/(2p \pm 1)$. Filling $\nu = 4/11$ appears in the filling range $2/5 > \upsilon > 1/3$. Fractions are not predicted to appear in this region and $\nu = 4/11$ cannot be explained by the Laughlin wavefunction [45] or hierarchical system. A strong analogy can be drawn here with the enigmatic $\nu = 5/2$ system [189, 190]. This system also cannot be explained by the fundamental principles governing the FQHE of electrons. To explain the $\nu = 5/2$ state, paring of CFs, similar to cooper pairing within superconductivity, is used [250]. Under this analogy the 5/2 state is predicted to obey non-Abelian statistics and is therefore a prospect for future applications in quantum computing [251]. It is believed that the 4/11 state will also obey non-Abelian statistics. The novel feature of the 4/11 state is that it resides in the LLL. Until its discovery, observations of non-Abelian FQHE states had been limited to the second Landau level.

The discovery of energy gaps below integer filling of the LLL originally caused much debate. The phenomena now known as the FQHE initially incited multiple explanations. The creation of the CF analogy provides an intuitive semiclassical interpretation. The strength of the CF picture is that it takes the IQHE theory, for which many readers have a grounding, then applies it to the new composite particles. One explanation for the origins of filling $\nu = 4/11$ adds another level to the current understanding. It is believed that, just as the FQHE can be interpreted as the IQHE for CFs, $\nu = 4/11$ can be understood as the FQHE for CFs. From here on this will be referred to as FQHE^{CF}. The driver for the initial formation of CFs is the reduction of the Coulomb interaction through correlated electron motion. It was originally believed, potentially incorrectly, that CFs comprised a system of non-interacting particles [160]. Indeed, many models have achieved highly accurate results through simulations based on non-interacting systems [48]. For the FQHE^{CF} to be realized there must be a remnant interaction between CFs, albeit weak. This has been hinted at previously, Stormer et al hypothesized back in 1998 that distortions in ρ_{xx} maxima may be due to residual interactions between CFs [4].

The understanding that the residual CF-CF interaction is weak agrees with the theoretical work completed by C-C Chang et al [252]. Chang performed calculations that gave the energy gap for $\nu = 4/11$, he found the gap to be an order of magnitude less than the gaps for $\nu = 2/5$ and $\nu = 1/3$ The weak CF-CF interaction also agrees with experimental findings, it explains why the $\nu = 4/11$ state is so fragile and easily destroyed by thermal effects or disorder.

The initial theoretical work [243, 245, 246, 253, 254] predicted that $\nu = 4/11$ would be a spin unpolarized state, even at the high magnetic field values. This disagreed with the experimental findings of Pan and Samkharadze [6, 240, 242]. Pan's findings displayed full spin polarization through rotated field measurements. It was Wojs, Yi and Quinn that first produced numerical simulations to show that a spin-polarized FQHE^{CF}, with potential non-Abelian behaviour, could exist at filing $4/11$. The state has been termed a (WYQ) state.

The results of Figure 5.23 analysed in accordance with the work of Pan et al [226] would suggest that a density gradient exists along the length of the Hall bar, due to the axis scaling required to overlay ρ_{xx} and dR_{xy}/dB. This possibility can be investigated further by comparing magnetic field sweeps with positive and negative orientations. The fundamental equations for

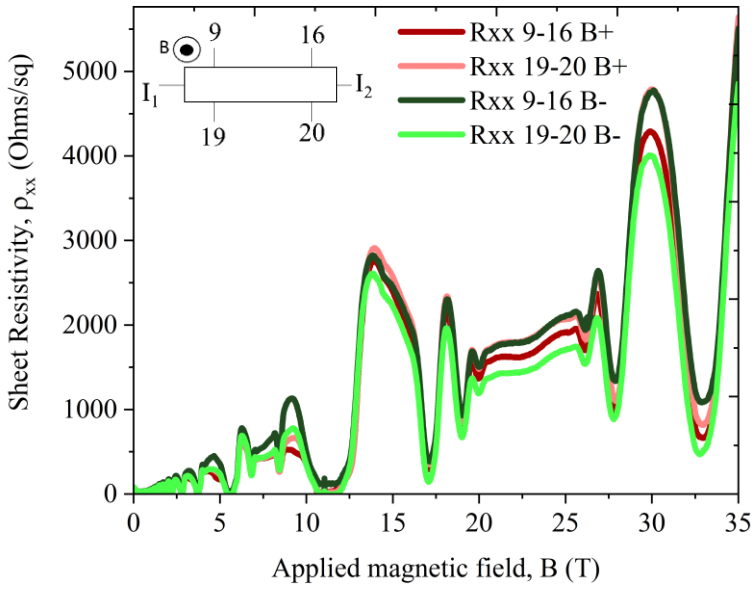

Figure 5.24 Comparing positive and negative applied magnetic fields for two pairs of contact pads on the same 45° Hall bar. Insert displays contact pad layout and field orientation. Positive magnetic field sweeps are labelled B+ and negative magnetic field sweeps are labelled B-.

Hall bar geometry measurements assume that an electric field applied along the Hall bar results in a uniform current density. This is only true if a uniform background carrier density is present.

For a 2DHG within a perfect Hall bar, reversing the field direction should have no impact on results. Carriers would switch from a clockwise to anticlockwise cyclotron motion, the Hall voltage would reverse sign but the ρ_{xx} signal should remain unchanged. This does not hold true if a carrier density gradient is present within the sample. To investigate this, positive and negative field orientations were swept and are overlaid within Figure 5.24.

Results from two pairs of contacts are shown in Figure 5.24 R_{xx}^{9-16} between contacts 9 and 16 and R_{xx}^{19-20} between contacts 19 and 20, the insert shows the contact locations. The contact pairs are located either side of the Hall bar mesa. Initially when experiencing the same field orientation each pair is already displaying different magnetoresistance values. This is shown by the offset between the red and pink data within Figure 5.24. When the field orientation is reversed the magnetoresistance for both contact pairs changes, with R_{xx}^{9-16} increasing and R_{xx}^{19-20} decreasing.

Ponomarenko et al [256] also observed field orientation dependent asymmetry in longitudinal magnetoresistance. Friedland et al [257] verified Ponomarenko's results by forming a 2DHG with a curved mesa, this acted to vary the perpendicular field component and therefore the filling factor along the mesa. This reproduced the density gradient Ponomarenko was investigating using predictable topological methods. Friendland's findings agreed with Ponomarenko with the density gradient being responsible for the field orientation asymmetry.

Ponomarenko found that reversing the field direction caused the contact pairs to exchange values. In our situation this would refer to pairs 9-16 and 19-20 displaying different values initially. On reversal of field orientation, the two pairs would swap results, displaying the value that the opposite pair showed in the previous field orientation. This is like the results observed in Figure 5.24, but not identical. R_{xx}^{19-20} for positive field and R_{xx}^{9-16} for negative field do display this behaviour, with each pair showing the same value for opposite field orientations. This result alone would produce strong agreement with the results of Pan et al. However, the same result

does not occur for the remaining data within Figure 5.24, displayed by the dark red and light green lines not overlaying each other.

Alternative explanations for non-ideal behaviour of Hall bars include geometry and contact imperfections. As explained by Haug et al [258] even ideal ohmic contacts will induce scattering, especially with thin probe arms. This common issue is increased by any disparity in contact resistances, with higher resistance contacts causing greater reflection of incoming chemical potentials. For clarity, an ideal contact is expected to provide a reservoir, with the contact potential set at an average between the incoming and outgoing potentials. This ideal contact would not cause any reflection of the incoming potential. What Haug discovered is that even an ideal contact will cause some reflection and the commonly narrow arm between the mesa and contact will always provide some scattering. Haug et al [258] also explains various experiments performed by Klaus von Klitzing and others where a gate over an unused contact pad could be used to isolate the contact electrically. This group of experiments concluded that even contacts not actively involved in measurements can impact measured magneto transport results. In summary our results support the work of Pomerenko with the Caveat that we have a contact issue. This was already discovered during initial testing and is the reason data from contacts 9-16 is not included anywhere else in this chapter.

5.6. Conclusion

This report covering a strained SiGe/Ge QW system represents the only sample structure to have returned FQHE features from a Ge QW, adding to only a handful of publications that make up the literature of the FQHE within Ge. As such the results open multiple avenues for further research efforts into the FQHE within a strained Ge system.

Multiple trips to the High Magnetic Field Laboratory in Nijmegen (Netherlands) provided the data for this chapter. Rich, highly developed FQHE spectra were observed from field sweeps that extend the highest magnetic field range previously reported up to 37.5 T. Rotating the sample relative to the applied magnetic field varies the parallel and perpendicular components of field incident on the sample, in turn this varies the total field and Zeeman splitting that a particular fraction is observed under. A resistance increase of the FQHE minima was observed

relative to the effective zero field point at $\nu = 3/2$. The origin of this was interpreted as a finite thickness effect, induced as the parallel field component compresses the carrier wavefunctions, producing a system closer to the idealised 2D state. This result highlights the advantages of the simplicity of the strained Ge system. This system is demonstrated to contain fully spin polarised composite fermions with a large effective g factor of ~7.4. Due to strain effects removing the degeneracy of the LH HH bands, the system also populates only a single band, demonstrated through analysis of SdH oscillations. The simplicity of the Ge system demonstrates it as a suitable candidate for further investigation of finite thickness effects, its suitability lies in reduced spin transitions and interband scattering that complicate analysis. Ge is well suited for investigating finite thickness effects through field rotation and contributing to FQHE modelling attempts [47, 48].

Magnetic field sweeps from 0 to 37.5 T conducted at multiple temperatures facilitated thermal activation measurements. Through this an effective mass for the composite fermions was extracted, which increased from 0.6 m_o up to 1 m_o when approaching zero effective field. The effective mass and its magnetic field dependence was compared to values quoted for multiple GaAs systems within the literature. A good agreement was returned especially for negative values of applied field. A possibility remains of an unexpected dependence with higher field observations, with our Ge measurements at high field deviating from the m^* relationship quoted within the literature.

Plotting CF mobility, from the zero effective magnetic field points at $\nu = 3/2$ and $\nu = 1/2$, against temperature suggests two separate dependences in the temperature range 0.3 to 4.2 K. Results show that CF mobility is impacted to a greater extent by increased temperature when compared to its bare electron counterpart. This system in particular displays a large drop in mobility when the temperature is raised above the 1 K limit, due to increasing acoustic phonon scattering.

Insitu illumination of the sample surface, with an LED, is commonly used within GaAs and AlGaN systems to improve mobility [230-232]. The primary mechanism through which this enhancement occurs is via smoothing of the periodic surface potential (essentially a form of shielding from increased carrier density). A secondary advantage of adding carriers via

photoexcitation rather than modulation doping is that the number of ionised donors that act as remote impurity scattering centres is not increased. However, what was observed in the case of Ge opposed expectations. The 17% increase in carrier density reduced mobility and was detrimental to the FQHE features observed. Increased suppression of fractions upon sample rotation was also observed. This was especially pronounced for higher order fractions such as $\nu = 7/3$ and $\nu = 8/3$, which reside within the 2nd Landau level. These results link back into the study of finite thickness effects and display a dependence of finite thickness on carrier density, with increased carrier density requiring a greater finite thickness correction.

Differentiating the Hall signal to uncover weak fractions on the cusp of developing in the ρ_{xx} trace is a practise used by multiple authors [165, 236]. The feature that made this technique particularly exciting was the potential observation of a fraction at filling $\nu = 4/11$. To our knowledge this fraction has only been observed twice before and is reported on over three publications [240, 242, 246]. Both observations were made within unstrained GaAs/AlGaAs systems. The intrigue surrounding filling 4/11 is that it is believed to obey non-Abelian statistics, only one other fraction of this nature has been reported, at filling 5/2, residing in the second excited Landau level. Little is understood about filling $\nu = 4/11$ and it does not fit neatly within the Laughlin wavefunction or CF theories of the FQHE. One possible theory for $\nu = 4/11$ is that it originates from the very weak residual interactions between CFs. Intriguing, as CFs are usually modelled as a non-interacting many particle system, to great effect. Unquestionably the presence of $\nu = 4/11$ within a strained Ge system demands further investigation. Ideally a dilution refrigerator with base temperatures of 10 mK will be utilised. If the presence of $\nu = 4/11$ is validated, the initial observation of such a fraction at the relatively high temperature of 350 mK will be confirmed as truly remarkable.

Chapter 6. Room temperature mobility transport results

Quantum transport phenomena are low energy processes, resulting in easy loss of signal within noise. Sources of noise include thermal carrier activation, lattice vibrations, impurity scattering and surface roughness scattering. Advances in the last 70 years have mainly been due to the production of higher quality samples. Observing quantum phenomena using macroscopic transport measurements, requires low temperatures, high quality samples and in some cases very high magnetic fields (15-100 T). Technological developments achieving lower temperatures (down to the millikelvin range) and higher magnetic fields (up to 100 T in pulsed magnetic fields) have also furthered observations of quantum phenomena [259]. To further the 2DHG research at Warwick University we have been working on incremental improvements to the modulation doped heterostructure design shown in Figure 6.1. Areas of interest include increasing low and room temperature mobilities. Reducing surface roughness and threading dislocation densities is also a constant motivation within the semiconductor community. The high mobilities (>100,000 $cm^2V^{-1}s^{-1}$) quoted for QW devices are measured at low temperatures (<1 K). When considering the future commercial impact of high mobility structures, it seems unlikely devices required to operate below 1 k will be widely implemented. Reaching cryogenic

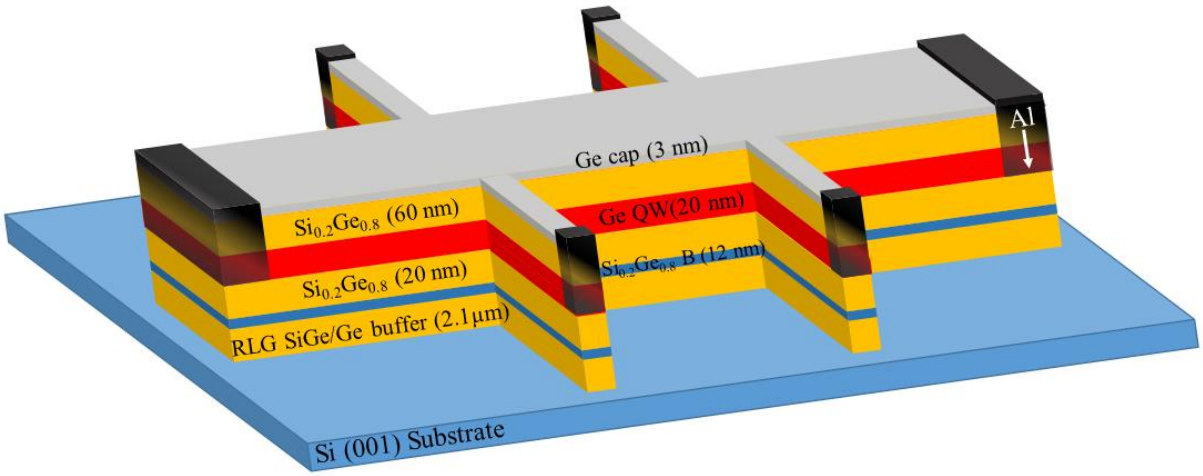

Figure 6.1 Hall bar device geometry, black faded regions shows, the standard process of Al diffusion into heterostructure, forming contact pads. Heterostructure layer compositions and thicknesses are labelled. The Hall bar geometry is produced by depositing a protective stencil of photoresist on the sample surface, the unwanted material is then etched away using reactive ion etching. Once the etching reaches the Si_{sub} the process is terminated. The layer structure represnts the inverted doping geometry of sample 15-247.

temperatures requires cryogens such as ^{3}He which is a rare, expensive and finite resource. Applications for cryogenically cooled QW transistors can however be envisaged for quantum computing or aerospace applications. Regarding the commercial market, RT mobility becomes a more practical and desirable quantity, as opposed to low temperature mobility. Within the research group the ethos is to produce samples on industry standard Si substrates, irrespective of the added difficulty due to increased lattice mismatch. This method presents the devices produced as a viable option for integration into current industry practice, the motivation is that this will narrow the gap between academic research and commercial impact. Another advantage of using industry standard Si substrates for research is their relatively low cost and wide availability.

6.1. Contact processing for inverted doping semiconductor heterostructures, demonstrated to produce high mobility RT results

Improving electrical contacts is a constant motivation for most applied semiconductor physicists. Heterostructures like sample 15-247 (shown in Figure 6.1) present added difficulty, with the QW one is trying to contact buried ~80 nm below the sample surface. At low temperatures the material between the QW and the surface is designed to become insulating. Which would render a standard metal surface contact high resistance at low temperatures. A basic method of contact formation to Ge is to evaporate aluminium onto the sample surface and encourage the metal to diffuse down to the QW layer using short 5-minute anneals, in an argon atmosphere, at 250°C. Al is an optimal contact metal for P-type Ge, it acts as a P-type dopant, providing increased doping concentrations at the metal semiconductor interface. The increased doping biases the energy bands at the interface, reducing the thickness of the barrier carriers must tunnel through. High doping at the metal-semiconductor interface is a common method used in industry, predominantly achieved by ion implantation of dopants beneath the contact area.

As a contact material Al also includes disadvantages. Al can suffer from spiking during metal diffusion into Si [260]. Voids appear in the Si which the Al preferentially fills, the result is that the Al diffuses in spikes causing nonuniform metal diffusion. In Chapter 4, wet chemical etching is performed using TMAH. This rapidly etches Al, preventing the use of Al contacts on such

structures. With the goal of finding an improved contact formation method, many contact processes were tested for the P type Ge heterostructures. The methods trailed are listed in Table 6.1.

Method	Notes
Al sputtering	Good, lacks reliability
Al thermal evaporation	Good, lacks reliability (spiking)
Evaporation antimony	Schottky characteristics
Evaporation Ga/Au	Evaporating Ga unreliable, high chamber contamination
Wet etch pits, Al thermal evaporation	Difficult to clean pits, adhesion issues
Argon milling, E-Beam Al/Au	On annealing Al and Au form purple gold
Argon milling, E-Beam Ag/Au	ICP etching reacts with silver
Argon milling, E-Beam Al/Ti/Au	Low resistance and repeatable

Table 6.1 Contact formation methods and comments on the difficulties encountered

Instead of including multiple similar I-V plots displaying poor contact resistances and Schottky like characteristics, the table sums up contact methods attempted and the most prominent difficulty that arose with each one. The proceeding text then goes on to explain the best method in detail. There are many variables affecting contact formation, this table does not dictate which methods emphatically will not work on buried P-type Ge, the table represents the experiences of the author with the methods described. There are many factors involved, including surface contamination, insufficient metal diffusion down to the buried layer and many other issues within subsequent Hall bar fabrication steps. With many variables causing processing issues, it was challenging to ascertain with certainty which variable was the dominant cause of poor electrical contact. Attempts to simplify the problem by forming contacts on bulk Ge material failed. Contact techniques that returned good results on bulk material would fail when attempted on a full heterostructure. Similar issues were found by Taylor et al and Koop et al. These authors reported that forming contacts to buried high mobility channels within GaAs is a very sensitive and volatile process [261, 262].

The motivation for etching through the surface layers, contacting the QW layer directly was twofold. Firstly, direct contact removes the variability that occurs when diffusing metal down through the surface layers to contact a buried layer. Reliability for this process relies on the

annealing temperature and time, surface contaminants and in the case of Al, spiking. Wet etching was a natural choice, providing the most delicate process, combined with the relative ease of etch depth calibration for various SiGe concentrations. The challenge that appeared, with wet etching, was stubborn surface contaminants inside the etch pits prior to metal deposition. Also, when using isotropic wet etchants, under etching occurs which appeared to cause issues with side wetting when depositing metals. Using wet etching prior to contact metal deposition, to improve electrical properties, has been reported previously in GaAs/AlGaAs systems by Mak et al [263] and Taneja et al [264]. Taneja reported that the side wall profile and side wetting was of crucial importance to success with wet etch contact processes [264]. Mak reported that using a microwave ashing process between etching and deposition dramatically improved contact performance [263]. This could explain the difficulties discovered with the wet etch contact process for the buried Ge QW.

A dry etching trial, involving argon milling, proceeding evaporation of Ag/Au by E-Beam was conducted. The aim was that by selecting Ag in place of Al, issues with Al spiking would be avoided. Also, as seen in Chapter 4, suspended devices formed using the etchant TMAH are desirable and processing in TMAH etches Al contacts rapidly, hence finding an alternative material would be advantageous. The difficulty found with Ag is that when using inductively coupled plasma etching, as the Hall bar fabrication process in this work does, the sulphur hexafluoride and oxygen mix reacts with the Ag preventing a straight sided etch profile, as seen in Figure 6.2 (right). The device shown in Figure 6.2 was created with both Ag/Au and Al/Au contacts to highlight the different responses to ICP etching. The dry etching process is required to define the mesa, as displayed in Figure 6.1. The mesa and contact pad surfaces are protected with photoresist and the surrounding material is etched away, down into the Si_{sub}. Removing this material improves RT measurements by reducing parallel conduction paths, it also defines the current path and Hall bar geometry. The desired profile for the mesa and contacts edges is straight uniform sides. Within Figure 6.2 (right), the contact pad with straight edges is composed of Al capped with Au, displaying a clean edge profile. The contact pad with non-uniform undulating edges is composed of Ag capped with Au. As etchants progress down, removing surface layers, a reaction with the Ag is retarding the etching process. The result is that the contact pad sidewall extends further from the centre line of the contact pad as the etch progresses down.

Using Al capped with Au produced an unforeseen issue, during annealing of Al capped with Au, purple gold formed. Which is bright purple in colour, it also contains the unfavourable contact properties of being high resistance and brittle [265].

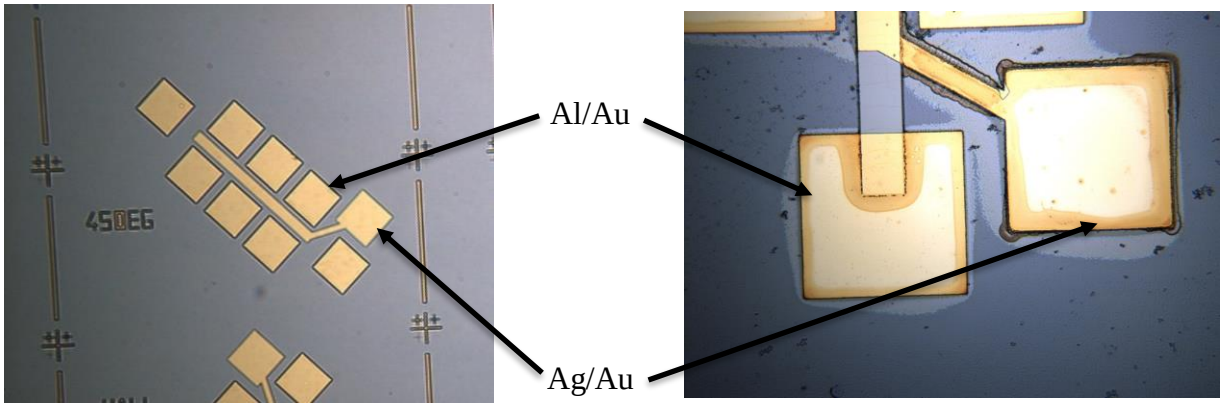

Figure 6.2 (left) Image of gated Hall bar with Ag/Au and Al/Au contacts before ICP etching in SF_6 and O_2. Two types of contacts introduced to clearly display variation in response to ICP etching. (right) Ag retarding etch process, forming irregular sidewall profile, for Ag/Au contacts during ICP etching in SF_6 and O_2.

The final contact solution was to Argon mill down to the Ge layer. The pit was back filled with Al/Ti/Au. The titanium produced a stable layer to prevent the Al and Au forming high resistance purple gold. Ar milling reduced any issues of surface contamination, under etching, side-wetting and metal diffusion calibration or spiking. The E-Beam deposition system used is an SVS 8 pocket electron beam evaporator. This system contains a built-in ion beam gun for in-situ etching prior to metal deposition. The argon beam uses an accelerating voltage of 5 KV providing an etch rate of 7 nm per minute for $Si_{0.3}Ge_{0.7}$, with a small amount of variation in etch rate with SiGe composition. Etching was performed normal to the sample surface to provide straight etch pit side walls. Al deposition followed argon milling, Al was deposited while oscillating the sample ±15°. This aided in side wetting of contact metals on the etch pit walls. The subsequent Ti and Au deposition was conducted without oscillation. This contact arrangement was discovered to be the best for the buried Ge 2DHG samples.

Figure 6.3 displays resistance values for the dry etched Al/Ti/Au contact process. The plotted 2-point resistance values within Figure 6.3 show that at 15 K the measured resistance is 25 Ω. This is the first contact process to produce acceptable resistance values for the inverted doping structure of 15-247. It also displays good ohmic contact behaviour over the full temperature range. Presenting this dry etching Al/Ti/Au as unquestionably the best method discovered for sample 15-247 (structure shown in Figure 6.5). Four-point resistivity values are presented within Figure 6.4 for the same sample. With the etch pits the metal is deposited directly in contact with the QW, resulting in a shorter anneal time for germanide formation between the Al and Ge. This reduces the thermal budget and prevents the need for extensive annealing temperature and time calibration. Al diffusion through silicon is known to cause "spiking", this is where the Si rapidly diffuses into the Al leaving voids which are filled by Al [260]. Reduced annealing times assist in preventing this effect. The dry etching contact process was used to form electrical contacts for sample 15-247. The results of electrical measurements on this sample are displayed in Figure 6.4.

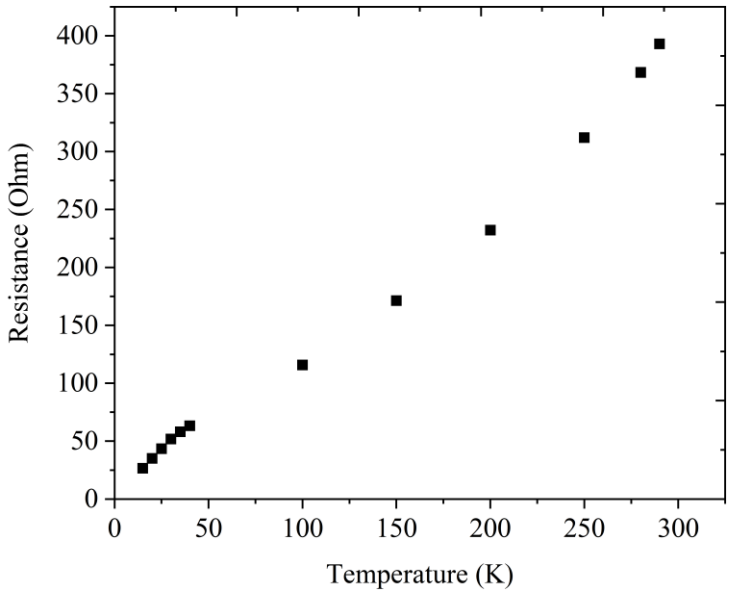

Figure 6.3 Plot showing the impact of temperature on two-point resistance IV measurements. The resistance reduces dramatically as the temperature is reduced. Contacts are dry etched pits back filled with Al/Ti/Au.

6.2. High RT mobility transport results

As shown within Figure 6.4, sample 15-247 displays remarkably high room temperature (RT) mobility. The mobility at RT (293 K) is 4,900 $cm^2V^{-1}s^{-1}$ this is the highest RT value ever reported within germanium. Previously the highest value was 4,500 $cm^2V^{-1}s^{-1}$ reported in 2015 [12]. Crucially this previously published value was extracted using mobility spectrum analysis (MSA), meaning that the quoted value would be above the value that was actually measured [266-268]. Comparing the structures of the previous RT record holder and the sample reported here shows similarities. Both contain reverse linearly graded SiGe buffer layers and strained Ge QWs. Both samples aimed to introduce a high doping density of 2×10^{18} cm^{-3}. The result in both cases was that the boron doping level exceeded the metal insulator transition. This means that

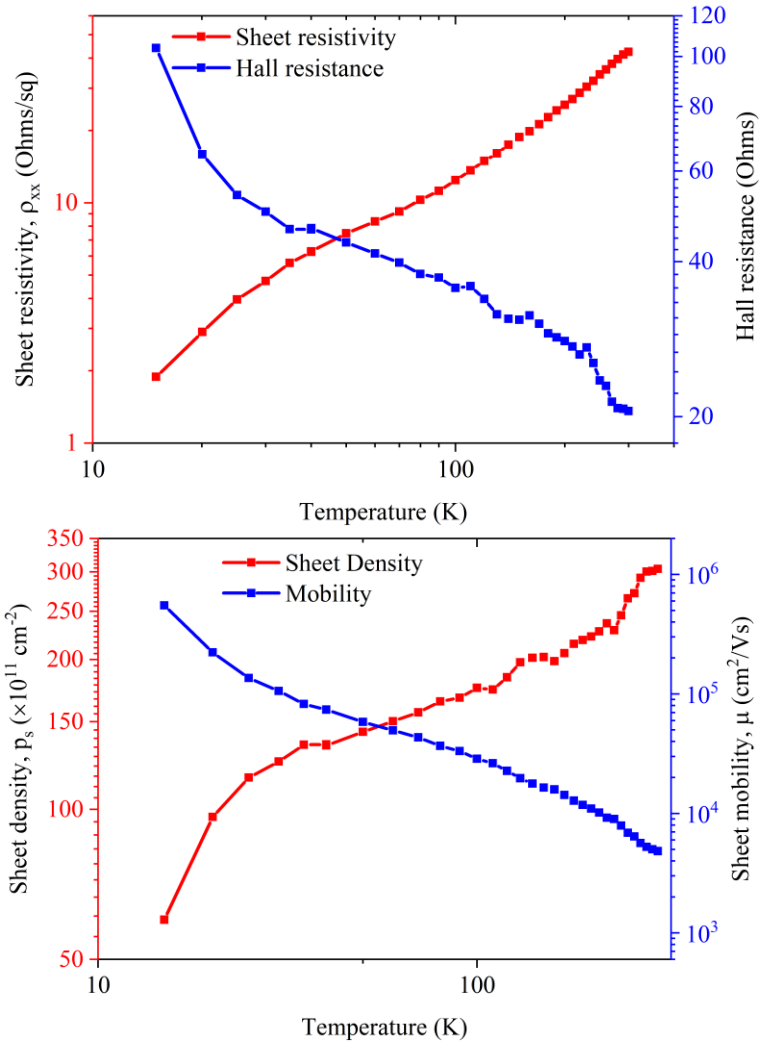

Figure 6.4 Transport results from 15 K to 293 K for sample 15-247, contacts formed by dry etching followed by Al/Ti/Au deposition. Applied field 100 mT, applied current 1 µA.

the doping layer will remain conductive even at cryogenic temperatures, causing anomalies in the magnetoresistance and Shubnikov de-Haas oscillations. The data in Figure 6.4 display the preliminary results, from 15 K to 293 K, including the high RT mobility. These measurements were conducted using an applied magnetic field of 100 mT and an excitation current of 1 μA. the properties plotted within Figure 6.4 were extracted using the formulas described in section 1.4. Subsequently the sample was loaded into a cryostat with ^{3}He cooling, providing lower temperature capabilities down to 300 mK. As can be seen in Figure 6.5 the sheet resistivity continued to decrease, during sample cooling, eventually reaching a plateau, displaying 2D carrier confinement.

The graph within Figure 6.5 displays results from four-point resistivity measurements conducted while cooling from 300 K to 1.6 K. Results from two different contact pairs are shown. They agree well, with a small discrepancy of 0.16 Ohms/Sq at 1.6 K. The layer structure for sample 15-247 is displayed at the top of Figure 6.5. Importantly it represents an inverted doping structure, where the doping layer lies beneath the QW layer. This is opposed to normal orientation doping, where the supply layer lies above the QW layer. Inverted doping can be advantageous, especially for samples where top gates are likely to be added subsequently. Inverted doping avoids gate leakage issues that occur with normal orientation doping [269]. The main reported difficulty with inverted doping is dopant segregation and surface diffusion [270]. The early results were mainly for n type GaAs systems doped with phosphorous, this dopant is known to suffer greater segregation and auto-doping than the P type, Boron dopants reported on in this chapter. It is unexpected to have measured such high mobilities from the inverted structure 15-247, we would still expect to have some level of dopant surface segregation. Dopants would move up through the 20 nm spacer layer towards the high mobility QW channel, causing increased remote impurity scattering, or potentially direct scattering once dopants reach the Ge QW layer.

Ge	3 nm
$Si_{0.3}Ge_{0.7}$	60 nm
Ge QW	20 nm
$Si_{0.3}Ge_{0.7}$	20 nm
B(2×10^{18} cm^{-3}): $Si_{0.3}Ge_{0.7}$	10 nm
$Si_{0.3}Ge_{0.7}$	50 nm
Graded to $Si_{0.3}Ge_{0.7}$	
Ge	~1050 nm
n^- - Si (001)	

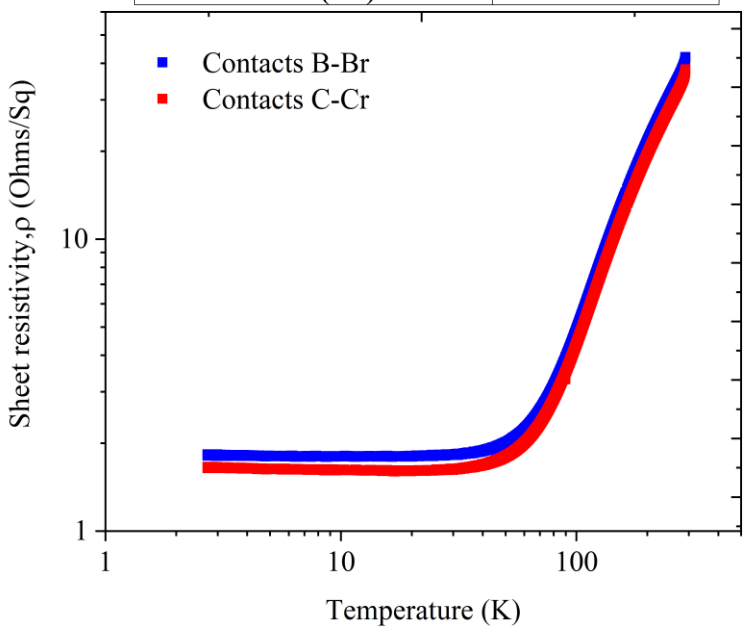

Figure 6.5 (bottom) Monitoring sheet resistivity during cooling cycle, for two contact pairs. (top) Schematic diagram of the layer structure for sample 15-247. Applied current 100 nA, 13 Hz.

Figure 6.6 displays SdH oscillations, confirming that 2D carrier confinement has been achieved. These measurements were conducted using a superconducting magnet capable of continuous magnetic field ramping up to ±12 T. The field sweeps are repeated at multiple temperatures, as stated in the legend. The expected suppression of peak amplitude with increasing temperature is clearly observed. The applied current during the measurements is 100 nA at 13 Hz. If a carrier is not confined within a 2D plane the extra degree of freedom for movement (in the Z axis) can add any amount of energy to the system, meaning that the characteristic Landau levels, with fixed energy gaps, cannot form and SdH oscillations would not be observed. Therefore, an observation of SdH oscillations confirms 2D confinement is present.

The oscillations in ρ_{xx} are displayed in Figure 6.6, both positive and negative field orientations have been swept, with opposite polarities displaying a slight asymmetry in the monotonic background component, often ascribed to small gradients in the carrier density [256]. Peak amplitude is suppressed as the temperature is increased, as would be expected [44]. An unexpected feature is seen at field values above 3 T. Alternate peaks begin to display different amplitudes. Looking at the graph at the bottom of Figure 6.6 it appears there are two individual sets of oscillations, expanding from different starting points along the X axis. The dashed

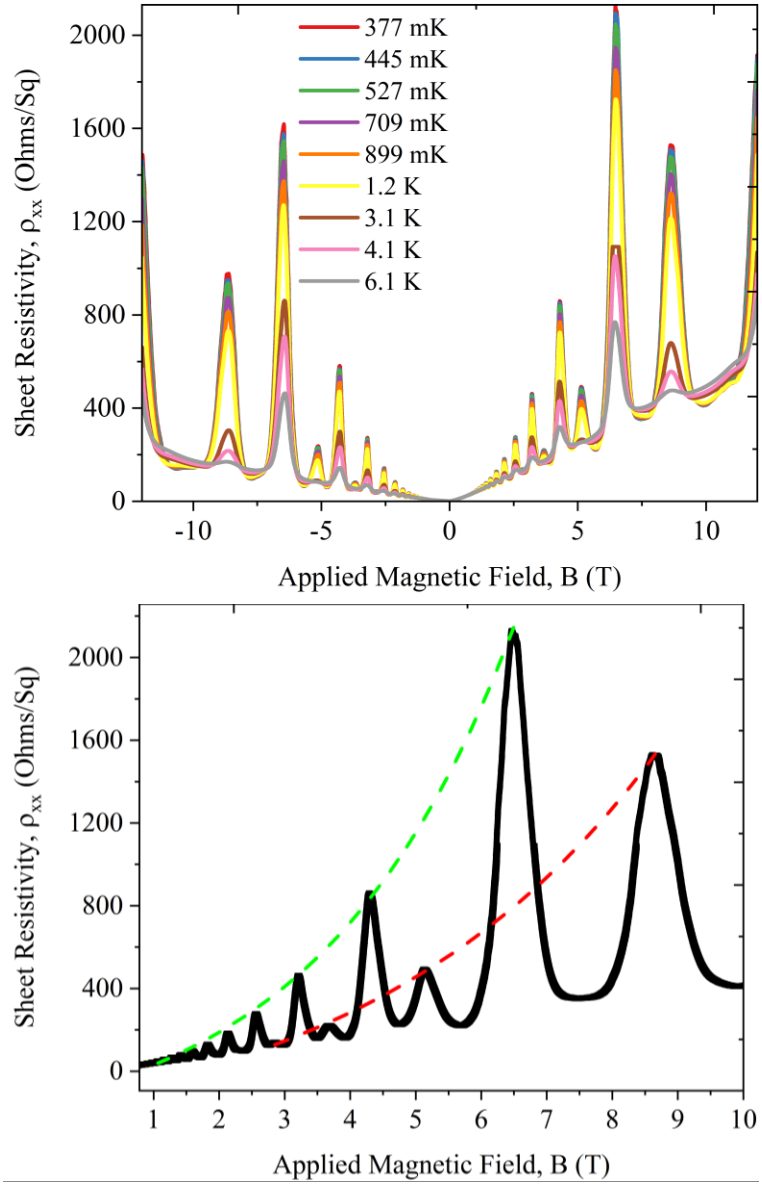

Figure 6.6 (top) Magnetic field sweeps from +12 T to -12 T, measurement repeated at nine different temperatures ρ_{xx} displays oscillations in magnetoresistance, consistent with 2D carrier confinement. (bottom) exponential growth curves fitted to the two separate peak growth features. Sample 15-247.

exponential fit lines are added as a guide for the eye. This displays the effect of a Zeeman split energy level.

The magnetoresistance oscillations observed in Figure 6.6 confirm that the charge carriers are confined within a two-dimensional plane. Once two-dimensional confinement is confirmed (at cryogenic temperatures and high mobilities) one expects results to conform to IQHE theory. IQHE theory states that when the fermi level resides in a forbidden energy gap, resistivity and conductivity tend to zero, an interesting consequence of edge conduction via chiral carrier motion (see section 1.4). Through plotting the magnetoconductance (Figure 6.7) it is possible to extract an estimation of the conductance contribution from parallel conducting layers. This is achieved by recording the non-zero background magnetoconductance value. This extraction method is displayed in Figure 6.7 for the base temperature (377 mK). The dashed blue line represents the contribution of parallel conducting layers (0.2 mS). This is the conductance of layers conducting parallel to the 2DHG at 377 mK. The parallel conduction contributes 0.2% of the conductance of the entire heterostructure. The value for total heterostructure conductance is calculated from the inverse of the zero-field longitudinal resistance for the sample $1/R_0^{xx}$.

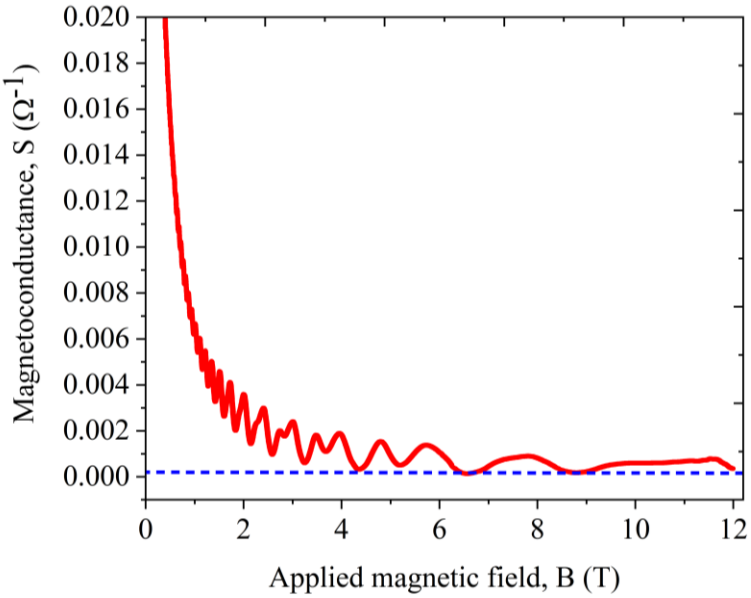

Figure 6.7 Magnetoconductance at 377 mK, the dashed blue line marks the contribution from the parallel conduction layer, resulting in a background conductance level. The background conductance is 0.2 mS wheareas the conductance of the heterostructure is 100 mS, meaning the parallel conduction only contributes 0.2% of the total conductance.

The $Si_{0.3}Ge_{0.7}$ and Ge layers within the buffer and spacer layers are intentionally undoped. This leads to these layers displaying carrier freeze out as temperature is reduced, with no carriers free to contribute to conduction. It is believed to be highly likely that the parallel conduction observed in sample 15-247 is located within the boron doped supply layer. The supply layer is approximately doped with 2×10^{18} cm^{-2} boron atoms. This increases the valence band energy above the Fermi energy, resulting in persistent conduction within this layer at low temperatures.

The carrier density of the 2DHG can be extracted from the period of the SdH oscillations, in inverse magnetic field coordinates. The parallel conducting layer is not 2D, therefore it does not produce SdH oscillations. The parallel conducting layer is not expected to impact the 2DHG carrier density extracted using this method. This is the most accurate method for determining the carrier density of a 2DHG. Equation 6.1 outputs the carrier density, the only input required is the period of the SdH oscillations in inverse magnetic field.

$$p_{sdh} = \frac{e}{\pi \times \hbar \times \Delta(B^{-1})} \qquad (6.1)$$

Where $\Delta(B^{-1})$ is the period of the SdH oscillations in inverse magnetic field and e represents the charge on an electron. The data analysis steps performed to extract carrier density from SdH oscillations are displayed in Figure 6.8. The raw data is a 0 to 1.5 T field sweep performed at 380 mK on sample 15-247. The first step is to remove the monotonic background component. This is performed by fitting an envelope function to the raw data (top left). The upper and lower envelopes are then averaged. The averaged function represents the monotonic background increase and is subtracted from the raw data (top right). The oscillations are then plotted in the inverted field coordinates (bottom left). Finally, a FFT is completed on the oscillations, displaying a narrow peak at the location of the oscillation frequency (bottom right). Observing a single period and a 2× harmonic of ρ_{xx} in 1/B confirms that Zeeman splitting of the lowest heavy hole subband has occurred (in this field range), this in turn confirms the lifting of the degeneracy of the light and heavy hole bands, caused by the compressive strain within the Ge channel [271].

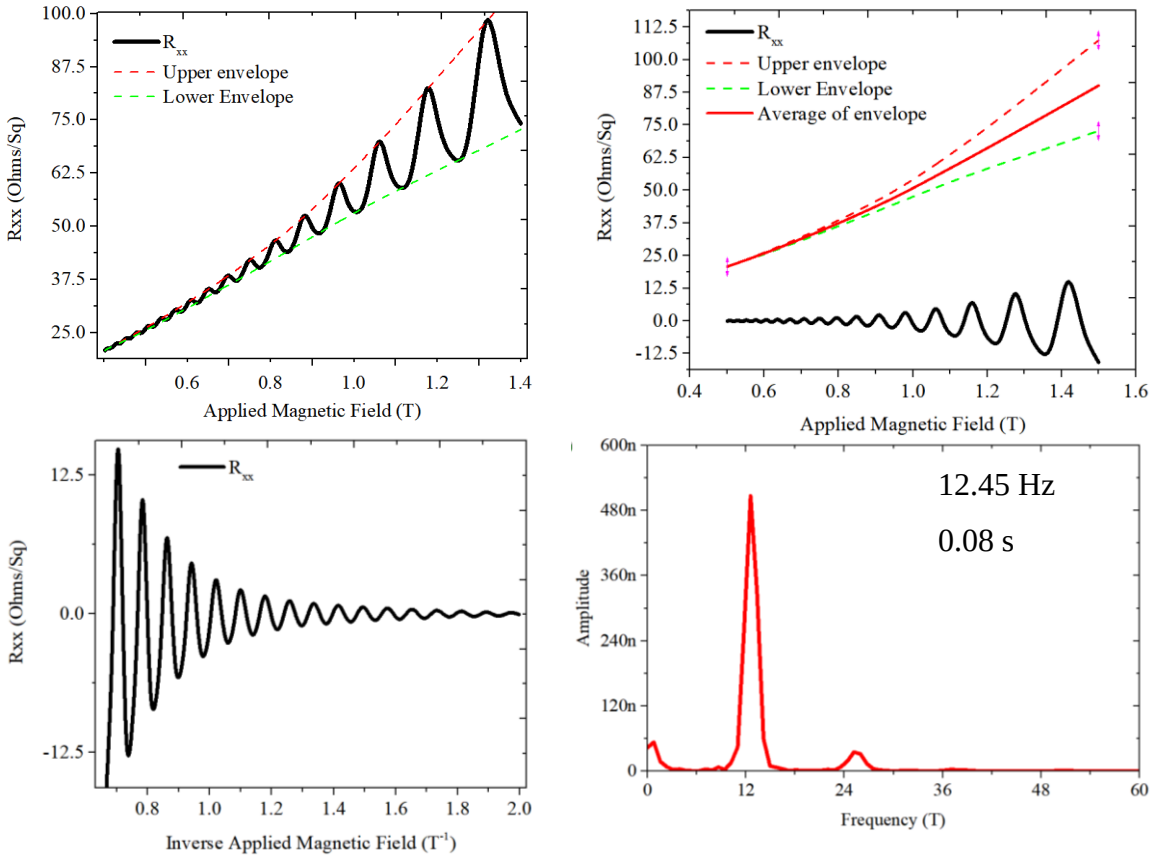

Figure 6.8 (Top left) Fitting an envelope function to the SdH oscillations between 0.5 and 1.5 T, raw data is a 380 mK field sweep for sample 15-247. (Top right) Averaging the upper and lower envelope functions, subtracting averaged monotonic background component away from SdH oscillations. (Bottom left) SdH oscillations plotted with inverted magnetic field on X axis, data is also reduced to evenly spaced X for subsequent FFT. (Bottom right) Frequency peak from FFT completed on SdH oscillations. All images represent analysis steps to extract carrier density.

Inverting the frequency gives the required period. The period produced by the FFT in Figure 6.8, inputted to equation 6.1 produces a carrier density of $p_s = 6 \times 10^{11}\mathrm{cm}^2\mathrm{V}^{-1}\mathrm{s}^{-1}$. This value is three times higher than the previous highest RT mobility Ge QW sample, with equivalent doping density. This displays a relatively high transferal of carriers from the doping layer into the QW. Heterostructures of SiGe/Ge/SiGe are not a new concept. Devices of this type, hosting a 2DHG have been used to demonstrate crystallographic anisotropy of electrical properties [272], Spin orbit interaction effects [171, 273] and the IQHE[274, 275]. These publications all relate to SiGe/Ge/SiGe QWs and span over a 30-year period, interestingly the carrier density in all samples lies between 2 and $6 \times 10^{11} cm^{-2}$, a relatively narrow window. This places the extracted carrier density for 15-247 at the higher end of the Ge 2DHG carrier density window.

The magnetoresistance minima within Figure 6.10 are labelled with selected filling factors. The first well defined oscillation is $\nu = 44$ at a magnetic field value of $B = 0.56$ T. Plotting filling factor (ν) against inverse field (1/B) provides a method for verifying the value for sheet carrier density (p_s). This plot is displayed in Figure 6.9 with the odd and even minima distinguish as different symbols and labelled within the legend. Total conformity to a single gradient shows that every oscillation arises from the existence of Landau levels within one individual energy level, in the QW. The gradient of the linear fit within Figure 6.9 is equal to:

$$\frac{\Delta \upsilon}{\Delta B^{-1}} = \frac{h \times p_s}{e} \qquad (6.2)$$

Where h is planks constant, e the charge on an electron and p_s is the sheet carrier density. The gradient within Figure 6.9 returns a sheet carrier density of 6.0×10^{11} cm^{2}V^{-1}s^{-1}. This value matches the sheet carrier density extracted from the period of SdH oscillations before the onset of Zeeman splitting. The agreement of values confirms correct recognition of filling factors within Figure 6.10, also that all oscillations are generated from a single carrier population within one 2D layer.

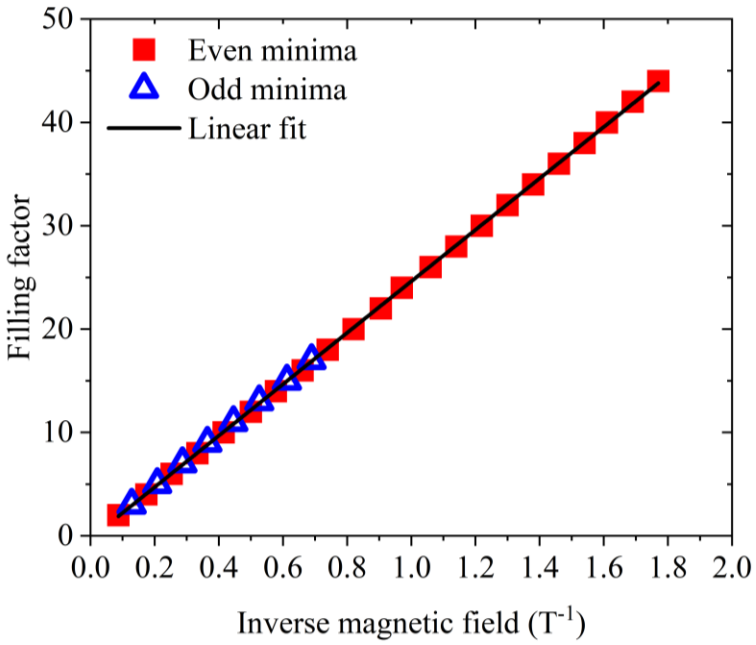

Figure 6.9 Filling factor for each minima from 3 to 44 plotted against inverse of the magnetic field locations for each minima. Magnetoresistance data used to find field value for each filling factor is displayed in Figure 6.10, with selected filling factor labels. Data was collected at 377 mK. The carrier density extracted using the linear fit is 6.0×10^{11}cm^{2}V^{-1}s^{-1}.

Figure 6.6 (top) displays magnetic field sweeps for sample 15-247 at multiple temperatures. The extent of the peak amplitude suppression caused by increasing temperature is dependent on the effective mass of the charge carriers within the system, as explained in detail in section 1.4.3. Using formula 6.3 [5] that models SdH oscillations an effective mass value can be calculated from the peak suppression.

$$ln\left(\frac{A}{T}\right) = C - \frac{2\pi^2 k_B T}{e\hbar B_{eff}} m^* \qquad (6.3)$$

Where A is peak amplitude, T is temperature, B_{eff} is the effective magnetic field, m^* is the effective mass and C is a constant.

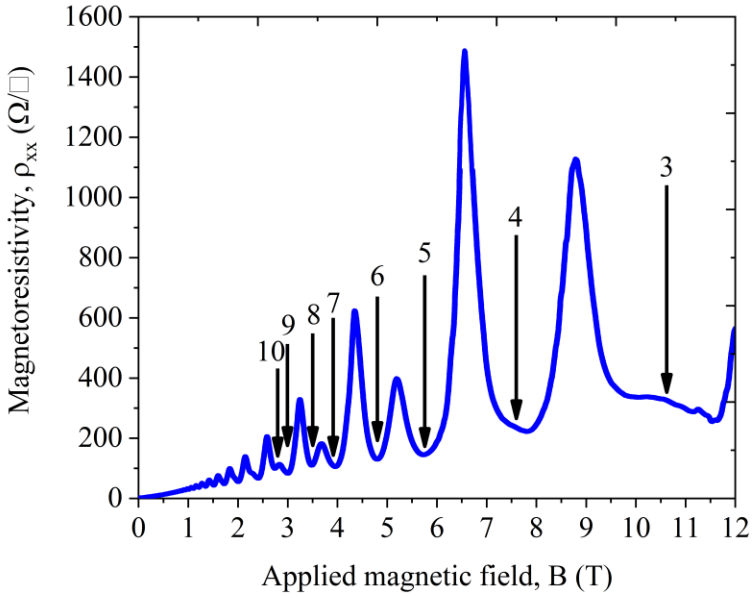

Figure 6.10 Magnetorestiance oscilations for base temperature 377 mK field sweep. Filling factor labels added up to $\nu = 10$. Zeeman split peaks are observed from the onset of odd filling at $\nu = 17$.

The plot of ln(A/T) vs temperature can, when considering formula 6.3, be shown to have a gradient equal to $-\frac{2\pi^2 k_B}{e\hbar B_{eff}}$. By dividing out the constants and the magnetic field value an effective mass is calculated for each SdH oscillation peak. The values are plotted in the bottom of Figure 6.11. The errors are propagated from the SE of the gradient fits, with smaller SdH oscillations, from lower field values, displaying a larger error. An increase in the calculated effective mass with applied magnetic field is observed, this occurs due to the nonparabolicity of the Ge valence band. The non-parabolicity of the Ge valence band causes an effective mass that

varies with carrier density and with magnetic field. The band mass of carrier holes can also be impacted by confinement potential [276] and strain [277].

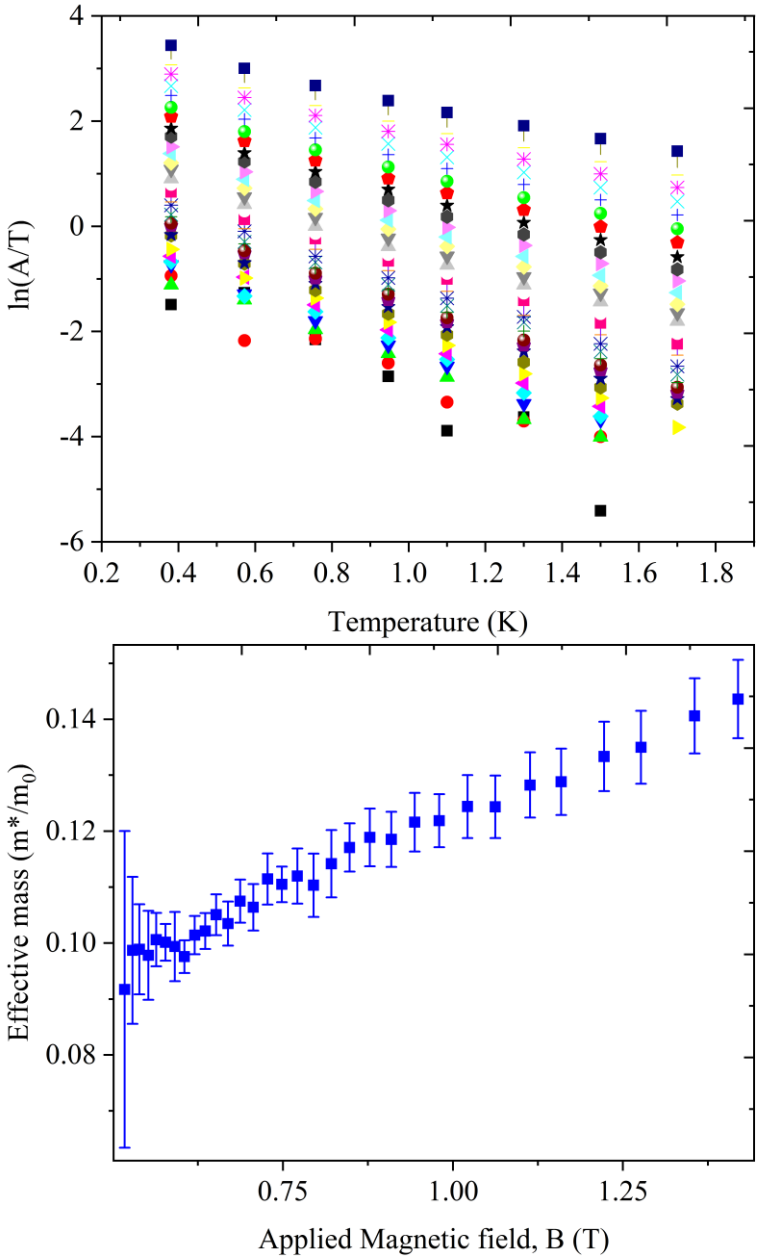

Figure 6.11 Extraction of effective mass *m** from thermal suppression of SdH oscillation peaks. (top) natural log of peak amplitude divided by temperature. (bottom) effective mass normalized by free electron mass plotted against magnetic field location of SdH oscillations.

6.3. Conclusion

Improving high RT operation of MODQW heterostructures is important, particularly for commercial impact. With the goal of improving RT mobility, an inverted doping structure may not initially appear as the obvious choice. Inverted doping is prone to issues with surface diffusion of dopants, approaching or entering the high mobility channel. This will reduce mobility through increased carrier scattering. One advantage of inverted doping is that one can produce electrical contacts directly connected to the channel layer, yet isolated from the doping layer. This aids in reducing parallel conduction at room temperature. This advantage is enhanced by the contact process developed for low resistance inverted structures, comprising an argon milling process followed by backfilling the etch pit with Al/Ti/Au. The Ar mill adds tuneable control of the contact depth, with the aim of contacting the high mobility channel and not the doping layer.

The RT mobility reported is 4,900 $cm^2V^{-1}s^{-1}$, representing the highest RT mobility recorded in Ge to date. This sample contains a small amount of parallel conduction, contributing 0.2% of the total conductance of the heterostructure. Therefore, the true RT mobility of the QW layer would be higher than this measured value. The parallel conduction is likely to originate from the doping layer which will contain a notably lower value of mobility. This will cause a disproportionately large reduction in the measured total RT mobility value. This sample containing a record high RT mobility and the previous record holder both contained a high level of Boron doping 2×10^{18} cm^{-3}, both samples also suffer from parallel conduction. The future of high RT mobility MODQW structures appears to hinge on finding a method of reducing parallel conduction to permit higher carrier densities.

Chapter 7. Further work

The potential observation of a state at fractional filling $\nu = 4/11$ deserves further investigation. Lower temperatures requiring a dilution refrigerator may help to further stabilise the state. To confirm the presence of the fraction one must measure the presence of an energy gap. This can be achieved using large sets of repeated field sweeps with temperature increments. Thermal activation data would confirm the presence of an energy gap and the presence of a fractional state.

A natural progression from a Ge QW suspended within the microwire geometry, is a suspended device. Adding the electrical contacts includes additional complications, if one adds them pre-suspension then contact metals must be resistant to the TMAH etchant. It has proven challenging to produce ohmic contacts to a Ge QW using a metal that is resistant to TMAH. Alternatively post suspension contact deposition, which adds the difficulty of photolithography processing involving delicate suspended microwires. Once these challenges are overcome, suspended devices provide an ideal means for reducing parallel conduction and remote scattering. The current etching technique only removes the Si_{sub}, however, a secondary etch that also removes the Ge_{buff} and part of the SiGe buffer layer could remove a much larger percentage of defects within the device. Annealing material that has been suspended is also an area of further interest. Observing how defects behave once the misfits pinning them at interfaces have been removed has not yet been investigated within group IV materials.

Attempts at producing thinner buffer layers, facilitating relaxed SiGe deposition on a Si_{sub}, returned compressive Ge_{buff} layers and RLG as the prime options. This method of tuning the correct amount of compression within the Ge_{buff} to induce a fully relaxed SiGe epilayer merits investigation. The potential to fabricate relaxed, sub-micron SiGe on Si_{sub} buffer layers provides advantages for low dimensional systems, increased thermal dissipation and avoiding microcracks. If required this system could permit subsequent thick overgrowth, with the possibility of exceedingly low TDD.

Chapter 8. References

[1] Q. J. Liu, Z. T. Liu, L. P. Feng, and H. Tian, "First-principles study of structural, elastic, electronic and optical properties of rutile GeO2 and alpha-quartz GeO2," (in English), *Solid State Sciences*, Article vol. 12, no. 10, pp. 1748-1755, Oct 2010.

[2] J. K. Jain, *Composite Fermions*. Cambridge University Press, 2007.

[3] O. Heinonen, *Composite fermions a unified view of the quantum Hall regime*. New York: World Scientific, 1998.

[4] H. L. Stormer *et al.*, "Composite fermions at different levels " *Physica E: Low-dimensional Systems and Nanostructures* vol. 3, no. 1, pp. 38-46, 1998.

[5] P. T. Coleridge, Z. W. Wasilewski, P. Zawadzki, A. S. Sachrajda, and H. A. Carmona, "Composite-fermion effective masses," *Physical Review B*, vol. 52, no. 16, 1995.

[6] W. Pan, H. L. Stormer, and D. C. Tsui, "Fractional quantum Hall effect of composite fermions," *Phyical Review Letters*, vol. 90, no. 1, 2003.

[7] W. Kang, H. L. Stormer, L. N. Pfeiffer, K. W. Baldwin, and K. W. West, "How real are composite fermions," *Phyical Review Letters*, vol. 71, no. 23, 1993.

[8] H. L. Stormer, "The Fractional Quantum Hall Effect," Nobel Letcture1998.

[9] S. M. Sze, *Physics of semiconductor devices*, 2nd ed. Wiley, 1981.

[10] R. People *et al.*, "Modulation doping in Ge_xSi_{1-x}/Si strained layer heterostructures," *Applied Physics Letters*, vol. 45, no. 11, p. 1231, 1984.

[11] S. Subramanian, "High electron mobility transistors," *Bulletin of Materials Science*, vol. 13, no. 1-2, pp. 121-133, 1990.

[12] M. Myronov, C. Morrison, J. Halpin, S. Rhead, J. Foronda, and D. Leadley, "Revealing high room and low temperatures mobilities of 2D holes in a strained Ge quantum well heterostructures grown on a standard Si(001) substrate," *Solid-State Electronics*, vol. 110, pp. 35-39, 2015.

[13] C. Morrison and M. Myronov, "Electronic transport anisotropy of 2D carriers in biaxial compressive strained germanium," *Applied Physics Letters*, vol. 111, no. 19, 2017.

[14] J. K. M. Failla, G. Scalari, C. Maissen, J. Faist, C. Reichl, W. Wegscheider, O. J. Newell, D. R. Leadley, M. Myronov, J. Lloyd-Hughes, "Terahertz quantum Hall effect for spin-split heavy-hole gases in strained Ge quantum wells," *New Journal of Physics*, vol. 18, no. 11, 2016.

[15] C. G. Tuppen and C. J. Gibbings, "Misfit Dislocations in Annealed SiGe/Si Heterostructures," *Thin Solid Films*, vol. 183, no. 1-2, pp. 133-139, 1989.

[16] D. C. Houghton, "Nucleation rate and glide velocity of misfit dislocations in $Si_{1-x}Ge_x$/(100) Si heterostructures," *Applied Physics Letters*, vol. 57, no. 20, 1990.

[17] R. Hull, J. C. Bean, D. Bahnck, L. J. P. Jr, K. T. Short, and F. C. Unterwald, "Interpretation of dislocation propagation velocities in strained Ge_xSi_{1-x}/Si(100) heterostructures by the diffusive kink pair model," *Applied Physics Letters,* vol. 70, no. 4, 1991.

[18] R. Hull, J. C. Bean, L. J. Peticolas, D. Bahnck, B. E. Weir, and L. C. Feldman, "Quantitative analysis of strain relaxation in Ge_xSi_{1-x}/Si(110) heterostructures and an accurate determination of stacking fault energy in Ge_xSi_{1-x} alloys," *Applied Physics Letters* vol. 61, no. 23, 1992.

[19] R. People and J. C. Bean, "Calculation of critical layer thickness versus lattice mismatch for Ge_xSi_{1-x}/Si strained-layer heterostructures," *Applied Physics Letters,* vol. 47, no. 3, 1985.

[20] P. M. J. Marée, J. C. Barbour, and J. F. v. d. Veen, "Generation of misfit dislocations in semiconductors," *Journal of Applied Physics,* vol. 62, no. 11, 1987.

[21] D. J. Eaglesham, E. P. Kvam, D. M. Maher, C. J. Humphreys, and J. C. Bean, "Dislocation nucleation near the critical thickness in GeSi/Si strained layers," *Philosophical Magazine A,* vol. 59, no. 5, pp. 1059-1073, 1989.

[22] S. V. Kamat and J. P. Hirth, "Dislocation injection in strained multilayer structures," *Journal of Applied Physics,* vol. 67, no. 11, 1990.

[23] W. Hagen and H. Strunk, "A new type of source generating misfit dislocations," *Journal of Applied Physics,* vol. 17, no. 1, pp. 85-87, 1978.

[24] F. K. LeGoues, B. S. Meyerson, J. F. Morar, and P. D. Kirchner, "Mechanism and conditions for anomalous strain relaxation in graded thin films and superlattices," *journal of Applied Physics,* vol. 71, no. 9, 1992.

[25] M. A. Capano, "Multiplication of dislocations in $Si_{1-x}Ge_x$ layers on Si(001)," *Physical Review B,* vol. 45, no. 20, 1992.

[26] B. J. Spencer, P. W. Voorhees, and S. H. Davis, "Morphological instability in epitaxially strained dislocation-free solid films," *Physical Reivew Letters,* vol. 67, no. 26, 1991.

[27] W. H. Yang and D. J. Srolovitz, "Cracklike surface instabilities in stressed solids," *Physics Review Letters,* vol. 71, no. 10, 1993.

[28] D. E. Jesson, S. J. Pennycook, and J. M. Baribeau, "Direct imaging of surface cusp evolution during strained-layer epitaxy and implications for strain relaxation," *Physical Review Letters,* vol. 71, no. 11, 1993.

[29] J. Tersoff and F. K. LeGoues, "Competing relaxation mechanisms in strained layers," *Physical Review Letters,* vol. 72, no. 22, 1994.

[30] E. A. Stach, R. Hull, R. M. Tromp, F. M. Ross, and M. C. Reuter, "In-situ transmission electron microscopy of the interaction between dislocations " *Philosophical Magazine A,* vol. 80, no. 9, 1999.

[31] P. M. Mooney, "Strain relaxation and dislocations in SiGe/Si structures," *Materials Science and Engineering,* vol. 17, no. 3, pp. 105-146, 1996.

[32] A. D. Capewell, "Novel grading of silicon and germanium for high quality virtual substrated," PhD Thesis, Univesity of Warwick, 2002.

[33] A. G. Cullis, D. J. Robbins, S. J. Barnett, and A. J. Pidduck, "Growth ripples upon strained SiGe epitaxial layers on Si and misfit dislocation interactions," *Journal of Vacuum Science and Technology,* vol. 12, no. 4, 1994.

[34] A. G. Cullis, "Strain-Induced Modulations in the Surface Morphology of Heteroepitaxial Layers," *MRS Bulletin,* vol. 21, no. 4, pp. 21-26, 1996.

[35] Y. H. Xie *et al.*, "Semiconductor Surface Roughness: Dependance on Sign and Magnitude of Bulk Strain," *Physical Review Letters,* vol. 73, no. 22, 1994.

[36] D. K. Schroder, *Semiconductor Material and Device Characterisation,* 3rd ed. New Jersey: Wiley, 2006.

[37] F. Schaffler, "High-mobility Si and Ge structures," *Semiconductor Science and Technology,* Review vol. 12, no. 12, pp. 1515-1549, Dec 1997.

[38] E. Simoen *et al.*, "Challenges and opportunities in advanced Ge pMOSFETs," *Materials Science in Semiconductor Processing,* vol. 15, no. 6, pp. 588-600, 2012.

[39] T. Chidambaram *et al.*, "Interface trap density and mobility extraction in InGaAs buried quantum well metal-oxide-semiconductor field-effect-transistors by gated Hall method," *Applied Physics Letters,* vol. 104, no. 13, p. 4, 2014.

[40] T. Ebner, K. Thonke, R. Sauer, F. Schaeffler, and H. J. Herzog, "Electroreflectance spectroscopy of strained $Si_{1-x}Ge_x$ layers on silicon," *Physical Review B,* vol. 57, no. 24, 1998.

[41] P. Blood and J. W. Orton, *The electrical characterization of semiconductors: majority carriers and electron states.* Cambridge: Academic press, 1992.

[42] T. Ando, A. B. Fowler, and F. Stern, "Electronic properties of two-dimensional systems," *Reviews of Modern Physics,* vol. 54, no. 2, 1982.

[43] A. Isihara and L. Smrcka, "Density and magnetic field dependences of the conductivity of two-dimensional electron systems," *Journal of Physics C-Solid State Physics,* vol. 19, no. 34, pp. 6777-6789, 1986.

[44] Y. F. Komnick, V. V. Amdrievskii, I. B. Berkutov, S. S. Kryachko, M. Myronov, and T. E. Whall, "Quantum effects in hole-type Si/SiGe heterojunctions," *Low Temperature Physics,* vol. 26, no. 8, pp. 609-614, 2000.

[45] R. B. Laughlin, "Anomalous Quantum Hall Effect: An Incompressible Quantum Fluid with Fractionally Charged Excitations," *Physical Review Letters,* vol. 50, no. 18, 1983.

[46] F. F. Fang and P. J. Stiles, "Effects of a Tilted Magnetic Field on a Two-Dimensional Electron Gas," *Physical Review,* vol. 174, p. 823, 1968.

[47] F. C. Zhang and S. Das Sarma, "Excitation gap in the fractional quantum Hall effect: Finite layer thickness corrections," *Physical Review B,* vol. 33, no. 4, 1986.

[48] M. R. Peterson, T. Jolicoeur, and S. D. Sarma, "Orbital Landau level dependance of the fractional quantum Hall effect in quasi-two-dimensional electron layers: Finite-thickness effects," *Physical Review B,* vol. 78, no. 15, 2008.

[49] J. Hampton and J. P. Eisenstein, "Capacitance of Two-Dimensional Electron Systems Subject to an In-Plane Magnetic Field," *Solid State Communications,* vol. 94, no. 7, pp. 559-562, 1995.

[50] R. J. Haug, K. von Klitzing, R. J. Nicholas, J. C. Maan, and G. Weimann, "Fractional quantum Hall effect in tilted magnetic fields," *Physical Review B,* vol. 36, no. 8, 1987.

[51] V. Halonen, P. Pietiläinen, and T. Chakraborty, "Subband-Landau-level coupling in the fractional quantum Hall effect in tilted magnetic fields," *Physical Review B,* vol. 41, no. 14, 1990.

[52] T. Chakraborty, *The Quantum Hall Effects*. Berlin: Springer, 1988.

[53] J. E. Furneaux, D. A. Syphers, and A. G. Swanson, "Fractional Quantum Hall Effect with an Added Parallel Magnetic Field," *Physical Review Letters,* vol. 63, no. 10, 1989.

[54] J. Halpin, "Silicon Germanium Materials for Terahertz Emission," PhD Thesis, University of Warwick, 2014.

[55] V. A. Shah, "Reverse-graded high germanium content (x>0.75) Si1-xGex virtual substrates," PhD Thesis, University of Warwick, 2009.

[56] A. J. Ying, C. E. Murray, and I. C. Noyan, "A rigorous comparison of X-ray diffraction thickness measurement techniques using silicon-on-insulator thin films," *Journal of Applied Crystals,* vol. 42, pp. 401-410, 2009.

[57] P. F. Fewster, *X-ray scattering from semiconductors.* London: Imperial College Press, 2000.

[58] W. Massa, *Crystal Structure Determination*. Berlin: Springer, 2004.

[59] P. Main, W. Clegg, A. J. Blake, and R. O. Gould, *Crystal Structure Analysis: Principles and Practice*. Oxford: Oxford Science Publications, 2002.

[60] P. Allred, "The development and optimization of potential germanium on silicon single photon avalanche diodes," PhD Thesis, University of Warwick, 2016.

[61] D. Bowen, *High resolution X-ray diffractometry and topography*. Oxford: Taylor and Francis, 1998.

[62] K. J. S. Sawhney *et al.*, "A test Beamline on Dimond Light Source," *AIP Conference Proceedings,* vol. 1234, no. 1, 2010.

[63] J. Stangl, C. Mocuta, A. Diaz, T. H. Metzger, and G. Bauer, "X-Ray Diffraction as a Local Probe Tool," *ChemPhysChem,* vol. 10, no. 17, pp. 2923-2930, 2009.

[64] A. Snigirev, V. Kohn, I. Snigireva, and B. Lengeler, "A compound refractive lens for focusing high-energy X-rays," *Nature,* vol. 384, no. 6604, pp. 49-51, 1996.

[65] C. Mocuta *et al.*, "Beyond the ensemble average: X-ray microdiffraction analysis of single SiGe islands," *Physics Review B,* vol. 77, no. 24, 2008.

[66] M. Hanke *et al.*, "Scanning x-ray diffraction with 200 nm spatial," *Applied Physics Letters,* vol. 92, no. 19, 2008.

[67] D. Chrastina *et al.*, "Patterning-induced strain relief in single lithographic SiGe nanostructures studied by nanobeam x-ray diffraction," *Nanotechnology,* vol. 23, no. 15, 2012.

[68] J. M. Hartmann, B. Gallas, J. Zhang, and J. J. Harris, "Gas-source molecular beam epitaxy of SiGe virtual substrates: II. Strain relaxation and surface morphology," *Semiconductor Science and Technology,* vol. 15, no. 4, pp. 370-377, 1999.

[69] D. Misra, P. Srinivasan, N. Rahim, and N. A. Chowdhury, "Interface characterization of high-k dielectrics on Ge substrates," *Materials Science in Semiconductor Processing,* vol. 9, no. 4-5, pp. 741-748, 2006.

[70] C. O. Chui *et al.*, "A Sub-400 degrees C germanium MOSFET technology with high-kappa dielectric and metal gate," (in English), *International Electron Devices 2002 Meeting, Technical Digest,* Proceedings Paper pp. 437-440, 2002.

[71] C. Morrison and M. Myronov, "Strained germanium for applications in spintronics," *Physica Status Solidi,* vol. 213, no. 11, 2016.

[72] S. Lee, S. T. Choi, and Y. Y. Earmme, "Analysis of vertical cracking phenomena in tensile-strained epitaxial film on a substrate: Part I. Mathematical formulation," *International Journal of Solids and Structures,* vol. 45, no. 3-4, pp. 746-756, 2006.

[73] D. J. Dunstan, "Strain and strain relxation in semiconductors," *Journal of Materials Science: Materials in Electronics,* vol. 8, no. 6, pp. 337-375, 1997.

[74] D. Calvez, F. Roqueta, S. Jacques, L. Bechou, Y. Ousten, and S. Ducret, "Crack Propagation Modeling in Silicon: A Comprehensive Thermomechanical Finite-Element Model Approach for Power Devices," *Institute of Electrical and Electronic Engineers,* vol. 4, no. 2, pp. 360-366, 2014.

[75] R. T. Murray, C. J. Kiely, and M. Hopkinson, "Crack formation in III-V epilayers grown under tensile strain on InP(001) substrates," *Philosophical Magazine A,* vol. 74, no. 2, pp. 383-393, 2006.

[76] J. Kim and Y.-H. Xie, "Fabrication of dislocation-free tensile strained Si thin films using controllably oxidized porous Si substrates," *Applied Physics Letters,* vol. 89, no. 15, 2006.

[77] M. Yamaguchi, "Dislocation density reduction in heteroepitaxial III-V compound films on Si substrates for optical devices," *Journal of Materials Research,* vol. 6, no. 2, 2011.

[78] K. Hartman, M. Bertoni, J. Serdy, and T. Buonassisi, "Dislocation density reduction in multicrystalline silicon solar cell material by high temperature annealing," *Applied Physics Letters,* vol. 93, no. 12, 2008.

[79] K. W. Shin, S. H. Park, S. Park, and E. Yoon, "Reduction in Threading Dislocation Density in Ge Epitaxial Layers Grown on Si(001) Substrates by Using Rapid Thermal Annealing," *Journal of the Korean Physical society,* vol. 67, no. 9, 2015.

[80] W. Li *et al.*, "Effect of rapid thermal annealing on threading dislocation density in III-V epilayers monolithically grown on silicon," *Journal of Applied Physics* vol. 123, no. 21, 2018.

[81] M. Nemoz, R. Dagher, S. Matta, A. Michon, P. Vennéguès, and J. Brault, "Dislocation densities reduction in MBE-grown AlN thin films by high-temperature annealing," *Journal of Crystal Growth,* vol. 461, pp. 10-15, 2017.

[82] G. Capellini *et al.*, "Strain relaxation in high Ge content SiGe layers deposited on Si," *Journal of Applied Physics,* vol. 107, no. 6, 2010.

[83] V. Sivadasn, "Strain relaxation study of $Si_{1-x}Ge_x$ & Ge buffer layers on Si(001) and InSb on Ge/Si(001) virtual substrates," PhD Thesis, University of Warwick, 2016.

[84] X.-C. Liu, R. J. H. Morris, M. Myronov, A. Dobbie, and D. R. Leadley, "Silicon–germanium interdiffusion in strained Ge/SiGe multiple quantum well structures," *Journal of Physics D-Applied Physics,* vol. 43, no. 50, 2010.

[85] J. Bharathan, H. Zhou, J. Narayan, G. Rozgonyi, and G. E. Bulman, "Thermal Misfit Strain Relaxation in Ge/(001) Si Heterostructures," *Journal of Electronic Materials* vol. 43, no. 9, 2014.

[86] N. E. B. Cowern, P. C. Zalm, P. Van Der Sluis, D. J. Gravesteijn, and W. B. de Boer, "Diffusion in strained Si(Ge)," *Physical Review Letters,* vol. 72, no. 16, 1994.

[87] S. D. Theiss, F. Spaepen, and M. J. Aziz, "Pressure-enhanced interdiffusion in amorphous Si/Ge multilayers," *Applied Physics Letters,* vol. 68, no. 9, 1996.

[88] B. Hollander, R. Butz, and S. Mantl, "Interdiffusion and thermally induced strain relaxation in strained SiGe/Si superlattices," *Physical Review B,* vol. 46, no. 11, 1992.

[89] W. P. Gilling and D. J. Dunstan, "Strain and Interdiffusion in Semiconductor Heterostructures," *Physical Review B,* vol. 50, no. 11, 1994.

[90] J. M. Baribeau, "X-ray scattering analysis of interface roughness and diffusion," *Journal of Vacuum Science & Technology B,* vol. 16, no. 3, 1998.

[91] D. B. Aubertine and P. C. McIntyre, "Influence of Ge concentration and compressive biaxial stress on interdiffusion in Si-rich SiGe alloy heterostructures," *Journal of Applied Physics,* vol. 97, no. 1, 2005.

[92] D. B. Aubertine *et al.*, "Observation and modeling of the initial fast interdiffusion regime in Si/SiGe multilayers," *Journal of Applied Physics,* vol. 92, no. 9, 2002.

[93] G. R. Xia, M. Canonico, and J. L. Hoyt, "Interdiffusion in strained Si/strained SiGe epitaxial heterostructures," *Semiconductor Science and Technology,* vol. 22, no. 1, 2007.

[94] G. R. Xia, J. L. Hoyt, and M. Canonico, "Si–Ge interdiffusion in strained Si/strained SiGe heterostructures and implications for enhanced mobility metal-oxide-semiconductor field-effect transistors," *Journal of Applied Physics,* vol. 101, no. 4, 2007.

[95] D. Yuanwei, W. Chern, P. M. Mooney, J. L. Hoyt, and G. R. Xia, "On the role and modeling of compressive strain in Si-Ge interdiffusion for SiGe heterostructures," *Semiconductor Science and Technology,* vol. 29, no. 1, 2013.

[96] P. Fahey, S. S. Iyer, and G. J. Scilla, "Experimental evidence of both interstitial- and vacancy-assisted diffusion of Ge in Si," *Applied Physics Letters,* vol. 54, no. 9, 1989.

[97] M. J. Aziz, "Thermodynamics of diffucion under presssure and stress: Relation to point defect mechanisms," *Applied Physics Letters,* vol. 70, no. 21, 1997.

[98] Y.-M. Chang, C.-L. Dai, T.-C. Cheng, and C.-W. Hsu, "Effect of annealing temperature for $Si_{0.8}Ge_{0.2}$ epitaxial thin films," *Applied Surface Science,* vol. 254, no. 10, 2008.

[99] J. W. Matthews, "The observation of dislocations to accommodate the misfit between crystals with different lattice parameters," *Philosophical Magazine,* vol. 6, no. 71, pp. 1347-1349, 1961.

[100] J. W. Matthews, "Accommodation of misfit across the interface between single-crystal films of various face-centred cubic metals," *Philosophical Magazine,* vol. 13, no. 126, pp. 1207-1221, 1965.

[101] J. Nyeki, C. Girardeauxa, G. Erde´lyib, A. Rollanda, and J. Bernardinia, "Equilibrium surface segregation enthalpy of Ge in concentrated amorphous SiGe alloys," *Applied Surface Science,* vol. 212-213, pp. 244-248, 2003.

[102] C. Tetelin, X. Wallart, D. Shevenard, J. P. Nys, and D. J. Gravesteijn, "Evidence of Ge island formation during thermal annealing of SiGe alloys: Combined atomic force microscopy and Auger electron spectroscopy study," *Journal of Vacuum and Science Technology B,* vol. 16, no. 1, 1998.

[103] D. E. Jesson, *Handbook of thin film process technology. Part F. Superlattices and multilayered structures, F1 Growth Phenomena in Superlattices*. Bristol: I. O. P publishing, 1997.

[104] P. Wynblatt and R. C. Ku, "Surface energy and solute strain energy effects in surface segregation," *Surface Science,* vol. 65, no. 2, pp. 511-531, 1977.

[105] P. Treglia, B. Legrand, and P. Maugain, "Surface segregation in CuNi and AgNi alloys formulated as an area-preserving map," *Surface Science,* vol. 225, no. 3, pp. 319-330, 1990.

[106] D. A. Grützmacher *et al.*, "Ge segregation in SiGe/Si heterostructures and its dependence on deposition technique and growth atmosphere," *Applied Physics Letters,* vol. 63, no. 18, 1993.

[107] J. Nyeki *et al.*, "AES study of surface segregation in amorphous $Si_{1-x}Ge_x$ thin film alloys," *Surface Science,* vol. 495, no. 3, pp. 195-203, 2001.

[108] C. J. Gibbings, C. G. Tuppen, and M. Hockly, "Dislocation nucleation and propagation in SiGe layers on silicon," *Applies Physics Letters,* vol. 54, no. 2, 1989.

[109] D. D. Perovic, G. C. Weatherly, J. M. Baribeau, and D. C. Houghton, "Heterogeneous nucleation sources in molecular beam epitaxy-grown GeSi/Si strained layer superlattices," *Thin Solid Films,* vol. 183, no. 1-2, pp. 141-156, 1989.

[110] C. W. Leitz, M. T. Currie, A. Y. Kim, J. Lai, E. Robbins, and E. A. Fitzgerald, "Dislocation glide and blocking kinetics in compositionally graded SiGe/Si," *Journal of Applied Physics,* vol. 90, no. 6, 2001.

[111] E. A. Fitzgerald, S. B. Samavedam, Y. H. Xie, and L. M. Giovane, "Influence of strain on semiconductor thin film epitaxy," *Journal of Vacuum Science and Technology A,* vol. 15, no. 3, 1997.

[112] I. Yonenaga, S. H. Lim, and D. Shindo, "Dislocation dissociation and stacking-fault energies in GeSi alloys," *Philosophical Magazine Letters*, vol. 80, no. 4, 2000.

[113] J. Parsons, "Relaxation of strained silicon on virtual substrates," PhD Thesis, University of Warwick, 2007.

[114] D. Hull and D. J. Bacon, *Introduction to Dislocations*. Oxford: Elsevier, 2011.

[115] B. Shi, Q. Li, and K. M. Lau, "Self-organized InAs/InAlGaAs quantum dots as dislocation filters for InP films on (001) Si," *Journal of Crystal Growth*, vol. 464, pp. 28-32, 2016.

[116] H. Ye, P. Lu, Z. Yu, S. Zhou, and Y. Liu, "Analysis of strained nitride quantum dots as threading dislocation filters," *Solid State Sciences*, vol. 13, no. 9, 2011.

[117] E. A. Fitzgerald and S. B. Samavedam, "Line, point and surface defect morpohology of graded, relaxed GeSi alloys on Si substrates," *Thin Solid Films*, vol. 294, no. 1-2, pp. 3-10, 1997.

[118] T. Ward *et al.*, "Design rules for dislocation filters," *Journal of Applied Physics*, vol. 116, no. 06, 2014.

[119] R. Kumar *et al.*, "Evaluation of Vertical Coherence Length, Twist and Microstrain of GaAs / Si Epilayers Using Modified Williamson-Hall Analysis," *Journal of Nano- and Electronic Physics*, vol. 6, no. 2, 2014.

[120] J. E. Ayers, "The measurement of threading dislocation densities in semiconductor crystals by X-ray diffraction," *Journal of Crystal Growth*, vol. 135, no. 1-2, pp. 71-77, 1994.

[121] S. R. Lee *et al.*, "Effect of threading dislocations on the Bragg peakwidths of GaN, AlGaN, and AlN heterolayers," *Applied Physics Letters*, vol. 86, no. 24, 2005.

[122] V. S. Kopp *et al.*, "X-ray determination of threading dislocation densities in GaN/Al_2O_3(0001) films grown by metalorganic vapor phase epitaxy," *journal of Applied Physics*, vol. 115, no. 07, 2014.

[123] K. Maeda *et al.*, "On optimum design of dislocation filters for reduction of misfit dislocations," *Journal of Crystal Growth*, vol. 127, no. 1-4, pp. 451-455, 1993.

[124] B. W. Dodson, "Dislocation filtering: why it works, when it doesn't," *Journal of Electronic Materials*, vol. 19, no. 6, 1990.

[125] C. H. Simpson and W. A. Jesser, "On the Use of Low Energy Misfit Dislocation Structures to Filter Threading Dislocations in Epitaxial Heterostructures," *Physics Status Solidi*, vol. 149, no. 9, 1995.

[126] J. W. Matthews and A. E. Blakeslee, "Defects in epitaxial multilayers. I. Misfit dislocations," *Journal of Crystal Growth*, vol. 32, pp. 118-125, 1976.

[127] Y. Shiraki and A. Sakai, "Fabrication technology of SiGe hetero-structures and their properties," *Surface Science Reports*, vol. 59, no. 7-8, pp. 153-207, 2005.

[128] M. T. Currie, S. B. Samavedam, T. A. Langdo, C. W. Leitz, and E. A. Fitzgerald, "Controlling threading dislocation densities in Ge on Si using graded SiGe layers and chemical-mechanical polishing," *Applied Physics Letters*, vol. 72, no. 14, pp. 1718-1720, 1998.

[129] D. M. Isaacson, C. L. Dohrman, and E. A. Fitzgerald, "Deviations from ideal nucleation-limited relaxation in high-Ge content compositionally graded SiGe/Si," *Journal of Vacuum and Science Technology B,* vol. 24, no. 6, 2006.

[130] E. A. Fitzgerald, A. Y. Kim, M. T. Currie, T. A. Langdo, G. Taraschi, and M. T. Bulsara, "Dislocation dynamics in relaxed graded composition semiconductors," *Materials Science and Engineering B,* vol. 67, no. 1-2, pp. 53-61, 1999.

[131] E. A. Fitzgerald *et al.*, "Relaxed GeSi structures for III–V integration with Si and high mobility two-dimensional electron gases in Si," *Journal of Vacuum and Science Technology B,* vol. 10, no. 4, 1992.

[132] E. A. Fitzgerald and S. B. Samavedam, "Line, point and surface defect morphology of graded, relaxed GeSi alloys on Si substrates," *Thin Solid Films,* vol. 294, no. 1-2, pp. 3-10, 1997.

[133] S. B. Samavedam and E. A. Fitzgerald, "Novel dislocation structure and surface morphology effects in relaxed Ge/Si-Ge(graded)/Si structures," *Journal of Applied Physics,* vol. 81, no. 7, 1997.

[134] V. T. Gillard, W. D. Nix, and L. B. Freund, "Role of dislocation blocking in limiting strain relaxation in heteroepitaxial films," *Journal of Applied Physics,* vol. 76, no. 11, 1994.

[135] V. A. Shah, A. Dobbie, M. Myronov, and D. R. Leadley, "Reverse graded SiGe/Ge/Si buffers for high-composition virtual substrates," *Journal of Applied Physics,* vol. 107, no. 6, 2010.

[136] V. A. Shah, A. Dobbie, M. Myronov, D. J. F. Fulgoni, L. J. Nash, and D. R. Leadley, "Reverse graded relaxed buffers for high Ge content SiGe virtual substrates," *Applied Physics Letters,* vol. 93, no. 19, 2008.

[137] M. Myronov, A. Dobbie, V. A. Shah, X.-C. Liu, V. H. Nguyen, and D. R. Leadley, "High Quality Strained Ge Epilayers on a $Si_{0.2}Ge_{0.8}$ Ge/Si (100) Global Strain-Tuning Platform," *Electrochemial and Solid-State Letters,* vol. 13, no. H388, 2010.

[138] A. Sakaia, N. Taoka, O. Nakatsuka, and S. Zaima, "Pure-edge dislocation network for strain-relaxed SiGe⁄Si(001) systems," *Applied Physics Letters,* vol. 86, no. 22, 2005.

[139] S. Cecchi *et al.*, "Thin SiGe virtual substrates for Ge heterostructures integration on silicon," *Journal of Applied Physics,* vol. 115, no. 9, 2014.

[140] D. Chrastina *et al.*, "Quantum-confined Stark effect at 1.3 μm in $Ge/Si_{0.35}Ge_{0.65}Ge/Si_{0.35}Ge_{0.65}$ quantum-well structure," vol. 37, no. 19, pp. 3960-3962, 2012.

[141] D. Chen *et al.*, "Ultralow temperature ramping rate of LT to HT for the growth of high quality Ge epilayer on Si (100) by RPCVD," *Applied Surface Science,* vol. 299, pp. 1-5, 2014.

[142] J. W. Gardner, V. K. Varadan, and O. O. Awadelkarim, *Microsensors, MEMS and smart Devices*. New York: Wiley, 2001.

[143] V. A. Shah *et al.*, "Electrical isolation of dislocations in Ge layers on Si(001) substrates through CMOS-compatible suspended structures," *Science and Technology of Advanced Materials,* vol. 13, no. 5, p. 7, 2012.

[144] K. A. Shaw, Z. L. Zhang, and N. C. MacDonald, "SCREAM I: a single mask, single-crystal silicon, reactive ion etching process for microelectromechanical structures," *Sensors and Actuators,* vol. 40, no. 1, pp. 63-70, 1994.

[145] M. Elwenspoek and H. Hansen, *Silicon Micromachining*. Cambridge: Cambridge University Press, 1998.

[146] D. Nam *et al.*, "Strained germanium thin film membrane on silicon substrate for optoelectronics," *Optics express,* vol. 19, no. 27, pp. 25866-25872, 2011.

[147] R. M. Audet *et al.*, "Surface-Normal Ge/SiGe Asymmetric Fabry–Perot Optical Modulators Fabricated on Silicon Substrates," *Journal of Lightwave Technology,* vol. 31, no. 24, pp. 3995-4003, 2013.

[148] V. A. Shah *et al.*, "High quality single crystal Ge nano-membranes for opto-electronic integrated circuitry," *Journal of Applied Physics,* vol. 115, no. 14, 2017.

[149] S. D. Rhead *et al.*, "Tensile strain mapping in flat germanium membranes," *Applied Physics Letters,* vol. 104, no. 17, p. 5, 2014.

[150] C. Riddet *et al.*, "Hole Mobility in Germanium as a Function of Substrate and Channel Orientation, Strain, Doping, and Temperature," *IEEE Transactions on Electron Devices,* vol. 59, no. 7, pp. 1878 - 1884, 2012.

[151] V. A. Shah *et al.*, "Flat single crystal Ge membranes for sensors and opto-electronic integrated circuitry," *Solid-State Electronics,* vol. 98, pp. 93-98, 2017.

[152] V. A. Shah, A. Dobbie, M. Myronov, and D. R. Leadley, "High quality relaxed Ge layers grown directly on a Si(001) substrate," *Solid-State Electronics,* vol. 62, no. 1, pp. 189-194, 2011.

[153] G. Colston *et al.*, "Mapping the strain and tilt of a suspended 3C-SiC membrane through micro X-ray diffraction," *Materials & Design,* vol. 103, pp. 244-248, 2016.

[154] A. Yoichi, "Topological Insulator Materials," *Journal of the Physical Society of Japan,* vol. 82, no. 10, 2013.

[155] W. Hongming, Y. Rui, H. Xiao, D. Xi, and F. Zhong, "Quantum anomalous Hall effect and related topological electronic states," *Advances in Physics,* vol. 64, no. 3, 2015.

[156] J. Schliemann, "Spin Hall Effect," *International Journal of Modern Physics B,* vol. 20, no. 9, 2006.

[157] R. R. Du, A. S. Yeh, H. L. Stormer, D. C. Tsui, L. N. Pfeiffer, and K. W. West, "g factor of composite fermions around v=1/2 from angular-dependent activation-energy measurements," *Physical Review B,* vol. 55, no. 12, 1996.

[158] W. Pan, H. L. Stormer, D. C. Tsui, L. N. Pfeiffer, K. W. Baldwin, and K. W. West, "Transition from an Electron Solid to the Sequence of Fractional Quantum Hall States at Very Low Landau Level Filling Factor," *Phyical Review Letters,* vol. 88, no. 17, 2002.

[159] Y. Yu and S. Yang, "Effect of the tilted field in fractional quantum Hall systems: Numerical studies for the solid-liquid transition," *Physical Review B,* vol. 66, no. 24, 2002.

[160] Z. Papic, "Fractional quantum Hall effec in a tilted magnetic field," *Physical Review B,* vol. 87, no. 24, 2013.

[161] R. G. Clark *et al.*, "Spin configurations and quasiparticle fractional charge of fractional-quantum-Hall-effect ground states in the N=0 Landau level," *Physics Review Letters,* vol. 62, no. 13, 1989.

[162] R. G. Clark and P. Maksym, "Fractional Quantum Hall effect in a spin," *Physics World,* vol. 2, no. 9, 1989.

[163] R. L. Willet, "The quantum Hall effect at 5/2 filling factor," *Reports on Progress in Physics*, vol. 76, no. 7, 2013.

[164] R. R. Du, A. S. Yeh, H. L. Stormer, D. C. Tsui, L. N. Pfeiffer, and K. W. West, *Phyical Review Letters,* vol. 55, p. 7351, 1997.

[165] Q. Shi, M. A. Zudov, C. Morrison, and M. Myronov, "Spinless composite fermions in an ultrahigh-quality strained Ge quantum well," *Physical Review B,* vol. 91, no. 24, 2015.

[166] T.-Y. Huang, Y.-M. Cheng, C.-T. Liang, G.-H. Kim, and J. Y. Leem, "Exchange-enhanced Landé g-factor, effective disorder and collapse of spin-splitting in a two-dimensional GaAs electron system," *Physica E: Low-dimensional Systems and Nanostructures,* vol. 12, no. 1-4, pp. 424-427, 2002.

[167] R. Mizokuchi, R. Maurand, F. Vigneau, M. Myronov, and S. D. Franceschi, "Ballistic One-Dimensional Holes with Strong g-Factor Anisotropy in Germanium," *Nano Letters,* vol. 18, no. 8, 2018.

[168] T. Chakraborty and P. Pietiläinen, "Fractional quantum Hall effect in tilted magnetic fields," *Physical Review B,* vol. 39, no. 11, 1989.

[169] X.-J. Wu, T.-X. Li, C. Zhang, and R.-R. Du, "Landau level crossing in a spin-orbit coupled two-dimensional electron gas," *Applied Physics Letters,* vol. 106, no. 1, 2015.

[170] Q. Shi, M. A. Zudov, C. Morrison, and M. Myronov, "Strong transport anisotropy in Ge/SiGe quantum wells in tilted magnetic fields," *Physical Review B,* vol. 91, no. 20, 2015.

[171] C. Morrison, P. Wisniewski, S. D. Rhead, J. Foronda, D. R. Leadley, and M. Myronov, "Observation of Rashba zero-field spin splitting in a strained germanium 2D hole gas," *Applied Physics Letters,* vol. 105, no. 18, 2014.

[172] M. A. Zudov, O. A. Mironov, Q. A. Ebner, P. D. Martin, Q. Shi, and D. R. Leadley, "Observation of microwave-induced resistance oscillations in a high-mobility two-dimensional hole gas in a strained Ge/SiGe quantum well," *Physical Review B,* vol. 89, no. 12, p. 125401, 2014.

[173] T. M. Lu, C. T. Harris, S.-H. Huang, Y. Chuang, J.-Y. Li, and C. W. Liu, "Effective g factor of low-density two-dimensional holes in a Ge quantum well," *Applied Physics Letters,* vol. 11, no. 10, 2017.

[174] U. Zeitler *et al.*, "Exchange interaction effects in the crossing of spin-polarized Landau levels in a silicon-germanium heterostructure: transition into a ferromagnetic state," *Physica E,* vol. 6, pp. 288-292, 2000.

[175] J. Xia, J. P. Eisenstein, L. N. Pfeiffer, and K. W. West, "Evidence for a fractionally quantized Hall state with anisotropic longitudinal transport," *Nature Physics,* vol. 7, pp. 845-848, 2011.

[176] Q. Shi, M. A. Zudov, C. Morrison, and M. Myronov, "Transport anisotropy in Ge quantum wells in the absence of quantum oscilations," *Physical Review B,* vol. 92, no. 16, 2015.

[177] A. A. Koulakov, M. M. Fogler, and B. I. Shklovskii, "Charge Density Wave in Two-Dimensional Electron Liquid in Weak Magnetic Field," *Phyical Review Letters,* vol. 76, no. 3, 1999.

[178] M. P. Lilly, K. B. Cooper, J. P. Eisenstein, L. N. Pfeiffer, and K. W. West, "Evidence for an Anisotropic State of Two-Dimensional Electrons in High Landau Levels," *Physical Review Letters,* vol. 82, no. 2, 1999.

[179] R. R. Du, D. C. Tsui, H. L. Stormer, L. N. Pfeiffer, K. W. Baldwin, and K. W. West, "Strongly anisotropic transport in higher two-dimensional Landau levels," *Solid State Communications,* vol. 109, no. 6, pp. 389-394, 1999.

[180] E. Fradkin and A. Kivelson, "Liquid-crystal phases of quantum Hall systems," *Physical Review B,* vol. 59, no. 12, 1999.

[181] B. I. Halperin *et al.*, "Theory of the half-filled Landau level," *Physical Review B,* vol. 47, no. 12, p. 7312, 1993/03/15 1993.

[182] V. Kalmeyer and S. C. Zhang, "Metallic phase of the quantum Hall system at even-denominator filling fractions," *Physical Review B,* vol. 46, no. 15, 1992.

[183] D. R. Leadley, R. J. Nicholas, C. T. Foxon, and J. J. Harris, "Measurements of the effective mass and scattering times of composite fermions from magnetotransport analysis," *Physical Review Letters,* vol. 72, no. 12, p. 1906, 1994.

[184] D. Weiss, M. L. Roukes, and A. Menschig, "Electron pinball and commensurate orbits in a periodic array of scatterers," *Phyical Review Letters,* vol. 66, no. 21, 1991.

[185] V. H. Houten, C. W. J. Beenakker, and J. G. Williamson, "Coherent electron focusing with quantum point contacts in a two-dimensional electron gas.," *Physical Review B,* vol. 39, no. 12, 1989.

[186] J. H. Smet, R. Fleischmann, and D. Weiss, "Evidence for quasi-classical transport of composite fermions in an inhomogeneous effective magnetic field," *Semiconductor Science and Technology,* vol. 11, 1996.

[187] S. Das Sarma and A. Pinczuk, *Perspectives in Quantum Hall Effects*. John Wiley and Sons, 1997.

[188] R. E. Prange and S. M. Girvin, *The Quantum Hall effect*. New York: Springer-Verlag, 1990.

[189] R. L. Willet, J. P. Eisenstein, H. L. Stormer, D. C. Tsui, A. C. Gossard, and J. H. English, "Observation of an even-denominator quantum number in the fractional quantum Hall effect," *Phyical Review Letters,* vol. 59, no. 15, 1987.

[190] W. Pan *et al.*, "Exact Quantization of the Even-Denominator Fractional Quantum Hall state at v=5/2 Landau Level Filling Factor," *Physical Review Letters,* vol. 83, no. 17, 1999.

[191] J. P. Eisenstein, K. B. Cooper, L. N. Pfeiffer, and K. W. West, "Insulating and Fractional Quantum Hall States in the First Excited Landau Level," *Physical Review Letters,* vol. 88, no. 7, 2002.

[192] J. S. Xia *et al.*, "Electron Correlation in the Second Landau Level: A Competition Between Many Nearly Degenerate Quantum Phases," *Physical Reivew Letters,* vol. 93, no. 17, 2004.

[193] G. A. Csathy *et al.*, "Tilt-Induced Localization and Delocalization in the Second Landau Level," *Phyical Review Letters,* vol. 94, no. 14, 2005.

[194] H. C. Choi, W. Kang, S. D. Sarma, L. N. Pfeiffer, and K. W. West, "Activation gaps of fractional quantum Hall effect in the second Landau level," *Physical Review B,* vol. 77, no. 8, 2008.

[195] W. Pan *et al.*, "Experimental studies of the fractional quantum Hall effect in the first excited Landau level," *Phyical Review B,* vol. 77, no. 7, 2008.

[196] G. Gervais *et al.*, "Competition between a Fractional Quantum Hall Liquid and Bubble and Wigner Crystal Phases in the Third Landau Level," *Physical Review Letters,* vol. 93, no. 26, 2004.

[197] R. L. Willet, H. L. Stormer, D. C. Tsui, A. C. Gossard, and J. H. English, "Quantitative experimental test for the theroretical gap energies in the fractional quantum Hall effect," *Physical Review B,* vol. 37, no. 14, 1988.

[198] M. B. Santos, Y. W. Suen, M. Shayegan, Y. P. Li, L. W. Engel, and D. C. Tsui, "Observation of a Reentrant Insulating Phase near the 1/3 Fractional Quantum Hall Liquid in a Two-Dimensional Hole System," *Phyical Review Letters,* vol. 68, no. 8, 1992.

[199] E. Wigner, "On the Interaction of Electrons in Metals," *Physical Review,* vol. 46, no. 11, pp. 1002-1011, 1934.

[200] P. K. Lam and S. M. Girvin, "Erratum: Liquid-solid transition and the fractional quantum-Hall effect," *Physical Review B,* vol. 31, no. 1, 1984.

[201] D. Levesque, J. J. Weiss, and A. H. MacDonald, "Crystallization of the incompressible quantum-fluid state of a two-dimensional electron gas in a strong magnetic field," *Physical Review B,* vol. 30, no. 2, 1984.

[202] R. R. Du, H. L. Stormer, D. C. Tsui, A. S. Yeh, L. N. Pfeiffer, and K. W. West, "Drastic Enhancement of Composite Fermion Mass near Landau Level Filling," *Physical Review Letters,* vol. 73, no. 24, p. 3274, 1994 1994.

[203] W. Pan, H. L. Stormer, D. C. Tsui, L. N. Pfeiffer, K. W. Baldwin, and K. W. West, "Effective mass of the four-flux compositve fermion at v=1/4," *Physical Review B,* vol. 61, no. 8, 1999.

[204] D. Yoshioka, B. I. Halperin, and P. A. Lee, "Ground State of Two-Dimensional Electrons in Strong Magnetic Fields and 1/3 Quantized Hall Effect," *Physics Review Letters,* vol. 50, no. 16, 1983.

[205] F. D. M. Haldane and E. H. Rezayi, "Finite-Size Studies of the Incompressible State of the Fractionally Quantized Hall Effect and its Excitations," *Physics Review Letters,* vol. 54, no. 3, 1985.

[206] R. Morf and B. I. Halperin, "Monte Carlo evaluation of trial wave functions for the fractional quantized Hall effect: Disk geometry," *Physical Review B,* vol. 33, no. 4, 1986.

[207] R. Morf and B. I. Halperin, " Monte Carlo Evaluation of Trial Wavefunctions for the Fractional Quantized Hall Effect: Spherical Geometry," *Z Phys,* vol. B68, no. 391, 1987.

[208] W. P. Su, "Higher-order fractional quantum Hall effect," *Physical Review B,* vol. 32, no. 4, 1985.

[209] G. Fano, F. Ortolani, and E. Colombo, "Configuration-interaction calculations on the fractional quantum Hall effect," *Physical Review B,* vol. 34, no. 4, 1986.

[210] A. H. MacDonald and G. C. Aers, "Size dependence in small-system calculations for fractional quantum Hall states," *Physical Review B,* vol. 34, no. 4, 1986.

[211] A. M. Chang, M. A. Paalanen, D. C. Tsui, H. L. Stormer, and J. C. M. Hwang, "Fractional quantum Hall effect at low temperatures," *Physical Review B,* vol. 28, no. 10, 1983.

[212] G. S. Boebinger, A. M. Chang, H. L. Stormer, and D. C. Tsui, "Magnetic Field Dependence of Activation Energies in the Fractional Quantum Hall Effect," *Physical Review Letters,* vol. 55, no. 16, 1985.

[213] J. Wakabayashi, S. Kawaji, J. Yoshino, and H. Sakaki, "Activation Energies of the Fractional Quantum Hall Effect in GaAs/AlGaAs Heterostructures," *Journal of the Physical Society of Japan,* vol. 55, no. 4, pp. 1319-1326, 1986.

[214] V. I. Kukushkin and V. B. Timofeev, "Activation gaps in the energy spectrum and influence of disorder under fractional quantum Hall effect in silicon MOSFET," *Suface Science,* vol. 170, no. 1-2, pp. 148 -153, 1986.

[215] R. G. Clark, R. J. Nicholas, and A. Usher, "Odd and even fractionally quantized states in GaAs-GaAlAs heterojunctions," *Surface Science,* vol. 170, no. 1-2, pp. 141-147, 1986.

[216] D. Yoshioka, "Effect of the Landau Level Mixing on the Ground State of Two-Dimensional Electrons," *Journal of the Physical Society of Japan,* vol. 53, no. 11, pp. 3740-3743, 1984.

[217] A. H. MacDonald and G. C. Aers, "Inversion-layer width, electron-electron interactions, and the fractional quantum Hall effect," *Physical Review B,* vol. 29, no. 10, 1984.

[218] D. Yoshioka, "Excitation Spectrum of the Fractional Quantum Hall Effect: Two Component Fermion System," *Journal of the Physical Society of Japan,* vol. 55, no. 11, pp. 3960-3968, 1986.

[219] R. R. Du, A. S. Yeh, H. L. Stormer, D. C. Tsui, L. N. Pfeiffer, and K. W. West, "Fractional Quantum Hall Effect around $\nu = 3/2$: Composite Fermions with a Spin," *Phyical Review Letters,* vol. 75, no. 21, 1995.

[220] A. S. Yeh, H. L. Stormer, D. C. Tsui, L. N. Pfeiffer, K. W. Baldwin, and K. W. West, "Effective Mass and g factor of Four-Flux-Quanta Composite Fermions," *Physical Review Letters,* vol. 82, no. 3, 1998.

[221] Y. B. Kim, P. A. Lee, X.-G. Wen, and P. C. E. Stamp, "Influence of gauge-field fluctuations on composite fermions near the half-filled state," *Physical Review B,* vol. 51, no. 16, 1995.

[222] W. Kang, S. He, H. L. Stormer, L. N. Pfeiffer, K. W. Baldwin, and K. W. West, "Temperature Dependant Scattering of Composite Fermions," *Physics Review Letters,* vol. 75, no. 22, 1995.

[223] B. I. Halperin, P. A. Lee, and N. Read, "Theory of the half-filled Landau Level," *Physical Review B,* vol. 47, no. 12, 1993.

[224] P. J. Price, "Low temperature two-dimensional mobility of a GaAs heterolayer," *Suface Science,* vol. 143, no. 1, 1984.

[225] H. L. Stormer, L. N. Pfeiffer, K. W. Baldwin, and K. W. West, "Observation of a Bloch-Gruneisen regime in two-dimensional electron transport," *Physical Review B,* vol. 41, no. 2, 1990.

[226] W. Pan *et al.*, "Quantization of the Diagonal Resistance: Density Gradients and the Empirical Resistance Rule in a 2D System," *Physical Review Letters,* vol. 95, no. 06, 2005.

[227] W. Pan, H. L. Stormer, and D. C. Tsui, "Resistance scaling for composite fermions in the presence of a density gradient," *arXiv Condensed Matter,* vol. arXiv:cond-mat/0601627 2006.

[228] T. J. Drummond, W. Kopp, R. Fischer, H. Morkoç, R. E. Thorne, and A. Y. Cho, "Photoconductivity effects in extremely high mobility modulation-doped (Al,Ga)As/GaAs heterostructures," *Journal of Applied Physics,* vol. 53, no. 2, 1982.

[229] J. H. Davies, *The physics of low dimnesional semiconductors an introduction* (Cambridge). Cambridge University Press 1998.

[230] E. Arslan, S. Bütün, S. B. Lisesivdin, M. Kasap, S. Ozcelik, and E. Ozbay, "The persistent photoconductivity effect in AlGaN/GaN heterostructures grown on sapphire and SiC substrates," *Journal of Applied Physics,* vol. 103, no. 10, 2008.

[231] S. Elhamri *et al.*, "Persistent photoconductivity study in a high mobility AlGaN/GaN heterostructure," *Journal of Applied Physics,* vol. 88, no. 11, 2000.

[232] J. Antoszewski, M. Gracey, J. M. Dell, L. Faraone, and T. A. Fisher, "Scattering mechanisms limiting two-dimensional electron gas mobility in $Al_{0.25}Ga_{0.75}N$/GaN modulation-doped field-effect transistors," *Journal of Applied Physics,* vol. 87, no. 8, 2000.

[233] A. A. Bykov, A. K. Bakarov, A. V. Goran, A. V. Latyshev, and A. I. Toropov, "Anisotropy of Magnetic Transport and Self Organization of Corrugated Heterointerfaces in Selectively Doped Structures on GaAs(100) Substrates," *JETP Letters,* vol. 74, no. 3, 2001.

[234] A. A. Bykov *et al.*, "Hall effect in a spatially fluctuating magnetic field with zero mean," *Physical Review B,* vol. 61, no. 8, 1999.

[235] M. Samani *et al.*, "Low-temperature illumination and annealing of ultra-high quality quantum wells," *Physical Review B,* vol. 90, no. 12, 2014.

[236] A. M. Chang and D. C. Tsui, "Experimental observation of a striking similarity between quantum Hall transport coefficients," *Solid State Communications,* vol. 56, no. 1, pp. 153-154, 1985.

[237] H. L. Stormer, K. W. Baldwin, L. N. Pfeiffer, and K. W. West, "Strikingly linear magnetic field depedance of the magnetoresistivity in high quality two-dimensional electron systems," *Solid State Communications,* vol. 84, no. 1-2, pp. 95-98, 1992.

[238] W. Pan *et al.*, "Quantization of the Diagonal Resistance: Density Gradients and the Empirical Resistance Rule in a 2D system," *Physical Review Letters,* vol. 95, no. 6, 2005.

[239] S. H. Simon and B. I. Halperin, "Explanation for the Resistivity Law in Quantum Hall Systems," *Phyical Review Letters,* vol. 73, no. 24, 1994.

[240] W. Pan, K. W. Baldwin, K. W. West, L. N. Pfeiffer, and D. C. Tsui, "Fractional quantum Hall effect at Landau level filling v = 4/11," *Physical Review B,* vol. 91, no. 4, 2015.

[241] W. Pan, H. L. Stormer, D. C. Tsui, L. N. Pfeiffer, K. W. Baldwin, and K. W. West, "Fractional Quantum Hall Effect of Composite Fermions," *Phyical Review Letters,* vol. 90, no. 1, 2003.

[242] N. Samkharadze, I. Arnold, L. N. Pfeiffer, K. W. West, and G. A. Csathy, "Observation of incompressibility at v = 4/11 and v = 5/13," *Physical Review B,* vol. 91, no. 08, 2015.

[243] K. Park and J. K. Jain, "Mixed states of compsite fermions carrying two and four vortices," *Physical Review B,* vol. 62, no. 20, 2000.

[244] C.-C. Chang, S. Sudhansu, Mandal, and J. K. Jain, "Partially spin-polarised quantum Hall effect in the filling factor range 1/3 < v < 2/5," *Physical Review B,* vol. 67, no. 12, 2003.

[245] A. Wojs, K.-S. Yi, and J. J. Quinn, "Fractional quantum Hall states of clustered composite fermions," *Physical Review B,* vol. 69, no. 20, 2004.

[246] S. Mukherjee, S. S. Mandal, Y.-H. Wu, A. Wojs, and J. K. Jain, "Enigmatic 4/11 state: A Prototype for Unconventional Fractional Quantum Hall Effect," *Physical Review Letters,* vol. 112, no. 1, 2014.

[247] A. C. Balram, C. Toke, A. Wojs, and J. K. Jain, "Phase diagram of fractional quantum Hall effect on composite fermions in multicomponent systems," *Physical review B,* vol. 91, no. 04, 2015.

[248] F. D. M. Haldane, "Fractional Quantization of the Hall effect: A Hierarchy of Incompressible Quantum Fluid States," *Physical Review Letters* vol. 51, no. 7, 1983.

[249] B. I. Halperin, "Statistics of Quasiparticles and the Hierachy of Fractional Quantized Hall states," *Physical Review Letters,* vol. 52, no. 18, 1984.

[250] G. Moore and N. Read, "Nonabellions in the fractional quantum Hall effect," *Nuclear Physics B,* vol. 360, no. 2-3, pp. 362-396, 1991.

[251] C. Nayak, S. H. Simon, A. Stern, M. Freedman, and S. D. Sarma, "Non-Abelian anyons and topological quantum computation," *Reviews of Modern Physics,* vol. 80, no. 3, 2008.

[252] C.-C. Chang and J. K. Jain, "Microscopic Origin of the Next-Generation Fractional Quantum Hall Effect," *Phyical Review Letters,* vol. 92, no. 19, 2004.

[253] C.-C. Chang, S. S. Mandal, and J. K. Jain, "Partially spin-polarized quantum Hall effect in the filling factor range 1/3<v<2/5," *Physical Review B,* vol. 67, no. 12, 2003.

[254] A. Wójs, G. Simion, and J. J. Quinn, "Spin phase diagram of the ν_e = 4/11 composite fermion liquid," *Physical Review B,* vol. 75, no. 15, 2007.

[255] A. Wojs, K.-S. Yi, and J. J. Quinn, "Fractional qunautm Hall states of clustered composite fermions," *Physical Review B,* vol. 69, no. 20, 2004.

[256] L. A. Ponomarenko *et al.*, "The effect of carrier density gradients on magnetotransport data measured in Hall bar geometry," *Solid State Communications,* vol. 130, pp. 705-710, 2004.

[257] K. J. Friedland, A. Siddiki, R. Hey, H. Kostial, A. Riedel, and D. K. Maude, "Quantum Hall effect in a high-mobility two-dimensional electron gas on the surface of a cylinder," *Physical Review B,* vol. 79, no. 12, 2009.

[258] R. J. Haug, "Edge-state transport and its experimental consequences in high magnetic fields," *Semiconductor Science and Technology,* vol. 8, pp. 131-153, 1993.

[259] J. Bears *et al.*, "Design and Tests of the 100-T Triple Coil at LNCMI," *IEE Transactions on Applied Superconductivity,* vol. 28, no. 3, 2018.

[260] K. Dressler, M. Kratt, P. A. Voss, S. Ebert, A. Herguth, and G. Hahn, "Influence of Al Particle Size and Firing Profile on Void Formation in Rear Local Contacts of Silicon Solar Cells," *IEEE Journal of Photovoltaics,* vol. 6, no. 1, pp. 68-73, 2016.

[261] E. J. Koop *et al.*, "On the annealing mechanism of AuGe/Ni/Au ohmic contacts to a two-dimensional electron gas in GaAs/$Al_xGa_{1-x}As$ heterostructures," *Semiconductor Science and Technology,* vol. 28, no. 2, 2013.

[262] R. P. Taylor, P. T. Coleridge, M. Davies, Y. Feng, J. P. McCaffrey, and P. A. Marshall, "Physical and electrical investigation of ohmic contacts to AlGaAs/GaAs heterostructures," *journal of Applied Physics,* vol. 76, no. 12, 1994.

[263] W. Y. Mak, K. D. Gupta, H. E. Beere, I. Farrer, F. Sfigakis, and D. A. Ritchie, "Distinguishing impurity concentrations in GaAs and AlGaAs using very shallow undoped heterostructures," *Applied Physics Letters,* vol. 97, no. 24, 2010.

[264] D. Taneja *et al.*, "N-type ohmic contacts to undoped GaAs/AlGaAs quantum wells using only frontsidedprocessing: application toambipolar FETs," *Semiconductor Science and Technology,* vol. 31, no. 6, 2016.

[265] C. Cretu and E. v. Lingen, *Coloured gold alloys*. Berlin: Springer Verlag, 1999.

[266] M. Myronov, K. Sawano, K. M. Itoh, and Y. Shiraki, "Room-temperature Transport Properties of High Drift Mobility Two-dimensional Electron Gas Confined in a Strained Si Quantum Well," *Applied Physics Express,* vol. 1, no. 2, 2008.

[267] I. Vurgaftman *et al.*, "Improved quantitative mobility spectrum analysis for Hall characterization," *Journal of Applied Physics,* vol. 84, no. 9, 1998.

[268] S. Kiatgamolchai, M. Myronov, O. A. Mironov, V. G. Kantser, E. H. C. Parker, and T. E. Whall, "Mobility spectrum computational analysis using a maximum entropy approach," *Physical Review E,* vol. 66, no. 3, 2002.

[269] M. A. Sadeghzadeh, "Top-gating of p-Si/SiGe/Si inverted modulation-doped structures," *Applied Physics Letters,* vol. 76, no. 3, 2000.

[270] W. Walukiewicz and E. E. Haller, "Effect of scattering by native defects on electron mobility in modulation-doped heterostructures," *Applied Physics Letters,* vol. 58, no. 15, 1991.

[271] T. Irisawa *et al.*, "Hole density dependence of effective mass, mobility and transport time in strained Ge channel modulation-doped heterostructures," *Applied Physics Letters,* vol. 84, no. 9, 2003.

[272] A. H. A. Hassan *et al.*, "Anisotropy in the hole mobility measured along the [110] and [110] orientations in a strained Ge quantum well.," *Applied Physics Letters,* vol. 104, no. 13, 2014.

[273] R. Moriya *et al.*, "Cubic Rashba Spin-Orbit Interaction of a Two-Dimensional Hole Gas in a Strained-Ge/SiGe Quantum Well," *Physics Review Letters,* vol. 113, no. 8, 2014.

[274] Q. Shi, Q. A. Ebner, and M. A. Zudov, "Hall field-induced resistance oscillations in a p-type Ge/SiGe quantum well," *Physical Review B,* vol. 90, no. 16, 2014.

[275] P. J. Newton *et al.*, "Magnetotransport in p-type Ge quantum well narrow wire arrays," *Applied Physics Letters,* vol. 106, no. 17, 2015.

[276] T. M. Lu, Z. F. Li, D. C. Tsui, M. J. Manfra, L. N. Pfeiffer, and K. W. West, "Cyclotron mass of two-dimensional holes in (100) oriented GaAs⁄AlGaAs heterostructures," *Applied Physics Letters,* vol. 92, no. 01, 2008.

[277] K. Sawano *et al.*, "Magnetotransport properties of Ge channels with extremely high compresssive strain," *Applied Physics Letters,* vol. 89, no. 16, 2006.